(2)

NAVAL POSTGRADUATE SCHOOL
Monterey, California

DISSERTATION

EFFECTS OF TAIWAN OROGRAPHY
ON THE MOTION AND STRUCTURE OF TYPHOONS

by

Tien-Chiang Yeh

December, 1992

Dissertation Co-supervisor: Russell L. Elsberry
Dissertation Co-supervisor: Chih-Pei Chang

Approved for public release; distribution is unlimited

REPORT DOCUMENTATION PAGE

1a. REPORT SECURITY CLASSIFICATION Unclassified	1b. RESTRICTIVE MARKINGS
2a. SECURITY CLASSIFICATION AUTHORITY	3. DISTRIBUTION/AVAILABILITY OF REPORT Approved for public release; distribution is unlimited.
2b. DECLASSIFICATION/DOWNGRADING SCHEDULE	
4. PERFORMING ORGANIZATION REPORT NUMBER(S)	5. MONITORING ORGANIZATION REPORT NUMBER(S)
6a. NAME OF PERFORMING ORGANIZATION Naval Postgraduate School 6b. OFFICE SYMBOL (*If applicable*) 35	7a. NAME OF MONITORING ORGANIZATION Naval Postgraduate School
6c. ADDRESS (*City, State, and ZIP Code*) Monterey, CA 93943-5000	7b. ADDRESS (*City, State, and ZIP Code*) Monterey, CA 93943-5000
8a. NAME OF FUNDING/SPONSORING ORGANIZATION 8b. OFFICE SYMBOL (*If applicable*)	9. PROCUREMENT INSTRUMENT IDENTIFICATION NUMBER
8c. ADDRESS (*City, State, and ZIP Code*)	10. SOURCE OF FUNDING NUMBERS Program Element No. / Project No. / Task No. / Work Unit Accession Number

11. TITLE (*Include Security Classification*)
Effects of Taiwan orography on the motion and structure of typhoons (unclassified)

12. PERSONAL AUTHOR(S) Yeh, Tien-Chiang

13a. TYPE OF REPORT	13b. TIME COVERED	14. DATE OF REPORT (*year, month, day*)	15. PAGE COUNT
PhD. Dissertation	From To	December, 1992	307

16. SUPPLEMENTARY NOTATION
The views expressed in this thesis are those of the author and do not reflect the official policy or position of the Department of Defense or the U.S. Government.

17. COSATI CODES			18. SUBJECT TERMS (*continue on reverse if necessary and identify by block number*)
FIELD	GROUP	SUBGROUP	spun-up vortex, blocking effect, asymmetric gyre, track deflection, track discontinuity, secondary vortex

19. ABSTRACT (*continue on reverse if necessary and identify by block number*)

Effects of steep island terrain on typhoon motion and structure changes are studied by both observational analyses and numerical simulations. The analyses involve calculation of center position deviations from a second-order polynomial curve fitted to the best tracks, and an empirical orthogonal function analysis to determine the terrain-induced surface structures. The simulation use a limited-area model with a elliptical-shaped barrier and a 'spun-up vortex' to represent the typhoon, to demonstrate the sensitivity on track and structure relative to vortex intensity, approach direction and translation speed. Both observational and simulation studies show that the orography induces significant track deflections and structure distortions, especially for a weaker and slowly moving typhoon approaching the central or southern Taiwan. As the typhoon approaches, the outer edge of the circulation accentuates the blocking effect of the barrier. Asymmetric gyres are induced by a vortex-terrain interaction as the vortex moves closer to the barrier, which accounts for the significant track deflections from a simple barrier effect. The simulations suggest that a center-following algorithm focus on the wind field would be more representative than on the pressure field. A track discontinuity occurs when the secondary vortex created from flow deflections around the barrier becomes the primary center downstream.

20. DISTRIBUTION/AVAILABILITY OF ABSTRACT	21. ABSTRACT SECURITY CLASSIFICATION	
☒ UNCLASSIFIED/UNLIMITED ☐ SAME AS REPORT ☐ DTIC USERS	Unclassified	
22a. NAME OF RESPONSIBLE INDIVIDUAL Russell L. Elsberry	22b. TELEPHONE (*Include Area code*) (408)6462373	22c. OFFICE SYMBOL MR/Es

Approved for public release; distribution is unlimited

Effects of Taiwan Orography
on the Motion and Structure of Typhoons

by

Tien-Chiang Yeh
B.S., National Central University, Taiwan, 1977
M.S., National Central University, Taiwan, 1979

Submitted in partial fulfillment of the
requirements for the degree of

DOCTOR OF PHILOSOPHY IN METEOROLOGY

from the

NAVAL POSTGRADUATE SCHOOL
December 1992

Author: Tien-Chiang Yeh
Tien-Chiang Yeh

Approved by:

Chih-Pei Chang
Professor of Meteorology
Dissertation Co-supervisor

Russell L. Elsberry
Professor of Meteorology
Dissertation Co-supervisor

Chin-Hwa Lee
Professor of Electrical
and Computer Engineering

Dr. Chi-Sann Liou
Naval Research Laboratory

Neil C. Rowe
Associate Professor of Computer Science

Roger T. Williams
Professor of Meteorology

Approved by: Robert L. Haney, Chairman, Department of Meteorology

Approved by: Richard S. Elster, Dean of Instruction

ABSTRACT

Effects of steep island terrain on typhoon motion and structure changes are studied by both observational analyses and numerical simulations. The analyses involve calculation of center position deviations from a second-order polynomial curve fitted to the best tracks, and an empirical orthogonal function analysis to determine the terrain-induced surface structures. The simulations use a limited-area model, with a elliptical-shaped barrier and a 'spun-up vortex' to represent the typhoon, to demonstrate the sensitivity on track and structure relative to vortex intensity, approach direction and translation speed. Both observational and simulation studies show that the orography induces significant track deflections and structure distortions, especially for a weaker and slowly moving typhoon approaching central or southern Taiwan. As the typhoon approaches, the outer edge of the circulation accentuates the blocking effect of the barrier. Asymmetric gyres are induced by a vortex-terrain interaction as the vortex moves closer to the barrier, which accounts for the significant track deflections from a simple barrier effect. The simulations suggest that a center-following algorithm based on the wind field would be more representative than on the pressure field. A track discontinuity occurs when the secondary vortex created from flow deflections around the barrier becomes the primary center downstream.

TABLE OF CONTENTS

LIST OF TABLES

LIST OF FIGURES

ACKNOWLEDGMENTS

I would like to thank my dissertation co-advisors, Professors R.L Elsberry and C.-P. Chang for their invaluable guidance throughout all phases of this study. I also wish to thank the other members of my committee: Professors C.-H. Lee, C.-S. Liou, N.C. Rowe and R.T. Williams, for their suggestions that enhanced the dissertation. I am also grateful to Professors R.J. Renard and R.L. Haney for their comments and continuous support.

Dr. S.W. Chang of the Naval Research Laboratory kindly provided the numerical model used in the simulation research. Professors J.M. Chen and M.S. Peng provided their analysis and interpolation programs, that were very useful in the analysis of data and output fields. All the computations were performed in the Interactive Digital Environmental Analysis Laboratory of the Department of Meteorology.

In addition, I am also grateful to the National Science Council and the Central Weather Bureau of R.O.C. for providing various support and data used in this study, especially to Mr. T.-Y. Wu, Dr. C.-Y. Tsay, Mr. S.-T. Wang and Mr. H.-M. Wang for their assistance and valuable discussions.

This work is supported in part by the National Science Foundation, under Grants ATM-9106495 and INT-9012409.

A special note of thanks goes to my wife, Hsin-Chung and daughter Cheu-Hong for their love, patience and understanding which made this work possible. This dissertation is dedicated to my parents.

I. INTRODUCTION

Tropical cyclones are one of the most severe weather systems in the world. Anthes (1983) reported that an average of 80-100 tropical cyclones occurred annually during 1964-1978 and caused an annual average of 20,000 deaths and a total economic loss of $US6-7 billion. Some of this property damage, and most of the loss of life, can be avoided if we have better track and intensity forecasts that allow people to prepare before the strike. Although each tropical cyclone has its individual detailed characteristics of wind, precipitation and pressure distributions (Willoughby 1990), the general axisymmetric framework given in Frank (1977) and Holland (1987) provides a good description of the typical structure of a tropical cyclone. The tropical cyclone has the lowest surface pressure in the center, and maximum wind speeds about 30 to 50 km from the center, which is also the area that has the largest precipitation. Outward from this area, the surface pressure increases, and the wind speed decreases. It is in this inner area that the strong wind and heavy precipitation cause the greatest damage. Therefore, the major focus of a tropical cyclone forecast is the location of this inner core of about 100 km radius.

Elsberry (1987) summarized the tropical cyclone track prediction techniques into three categories: simple track prediction techniques, statistical models and dynamical models. The annual mean track forecast errors that he showed indicate very small improvements on the track forecast during the last decade. Lack of adequate

observations makes the tropical cyclone forecast difficult. Near the coast, interactions between the tropical cyclone and the orography may make the track forecast even more difficult.

When a tropical cyclone encounters a flat coast, a surface wind discontinuity is reported by Powell (1982). He showed that smaller wind speeds and larger inflow angles over land occurred when Hurricane Federic made landfall on the Alabama-Mississippi coast. Mean winds immediately inland from the coast were 20% less than mean winds immediately offshore. Therefore, convergence was found on the right side and divergence on the left side of the coastal area. Wind asymmetries were also reported when Hurricane Alice made landfall on the Texas coast (Powell 1987). However, convergence was found on both sides of the coastal area. The landfall of tropical cyclones on a flat plain has also been studied in several numerical simulations (e.g., Tuleya and Kurihara 1978, Tuleya et al. 1984, and Jones 1987). The simulated low-level winds, moisture and precipitation fields become notably asymmetric relative to the coastline at landfall. The major filling of the storm generally occurs several hours after landing, primarily due to the suppression of the surface moisture flux. Although a landing without high orography generally produces relatively little change in the vortex track, some exceptions have also been reported. For example, Tuleya et al. (1984) did not detect a track change before landing. However, Jones (1987) showed that the storm is located at about 20 km to the left of the control simulation by the time of landing.

As a storm enters a more complex coastal terrain, more complex changes in the track and structure may be expected. One of the most significant areas where this

situation arises frequently is over the island of Taiwan, which is dominated by the Central Mountain Range (CMR). Because the horizontal scale of the CMR is comparable to the core of damaging winds and heavy precipitation of a typical typhoon, and has peaks higher than 3900 m, typhoon-terrain interactions produce many interesting features and forecast difficulties. Hsu (1960) found that a shallow or weak typhoon will dissipate after contact with the Taiwan terrain. For typhoons with maximum sustained winds of about 25-50 m/s, or if the vertical extent of the circulation is not much more than 6 km, one or more secondary lows may form on the opposite side of the CMR from the landfalling typhoon. One of the secondary lows may later dominate the circulation. When this occurs, the track of the typhoon center may appear to leap across the island. For a deeper (circulation extending to higher than 10.7 km) or a stronger (maximum sustained wind greater than 50 m/s) typhoon, the typhoon center appears to follow a continuous track even when secondary lows are formed. Hsu's (1960) results and the findings of Li (1963) were summarized by Brand and Blelloch (1974) into forecast rules for tropical cyclones approaching or crossing Taiwan.

Brand and Blelloch (1974) also studied the tracks of 22 typhoons during 1960-1972 that crossed Taiwan on a general westward heading. They found that the average intensity of typhoons increases during the period 48 h to 24 h prior to hitting Taiwan. The intensity is then about constant until 12 h prior to landfall and then decreases for about 12 h. For the period beginning from 6 h prior to hitting Taiwan until 6 h after leaving, the average intensity decreases by about 41% (from about 47 to 28 m/s). The average translation speed increases from -48 h to -24 h, then it levels off prior to a slight

acceleration just as the typhoon center is about to cross the island. Based on average 24-h right-angle track forecast errors of the Joint Typhoon Warning Center (JTWC) in Guam, Brand and Blelloch suggested that the storms start to veer toward the northwest 48 h to 24 h prior to landfall, and then maintain a basically east-to-west direction until landfall. After leaving the island, the right-angle forecast error is 94 km to the north, which reflects an average southward displacement of the storms. They also classified the storms into two groups according to the average initial intensity. They found that the more intense storms (maximum wind greater than or equal to 50 m/s) move faster, and experience more weakening in intensity (45% vs 40%) than do less intense storms.

The most comprehensive study of the Taiwan topography effect on typhoons was by Wang (1980). After examining the behavior of 120 typhoons that threatened Taiwan between 1949 and 1977, he classified these typhoons into eight categories according to their motion direction and the way the storm center passed the island. Wang's study provides strong evidence that the low-level structure and the movement of typhoons experience significant modifications as they encounter the Taiwan orography.

For typhoons approaching Taiwan from the east, Wang showed the storm center can either cross Taiwan continuously, or have a discontinuous track due to the formation of a secondary low that replaces the terrain-blocked low-level center. He further classified the track-continuous typhoons into three categories: (i) the track of typhoons has only minor deflections when it crosses the mountain; (ii) the center of the storm has a cyclonic circular motion just before it reaches the east side of the mountain, and then crosses the mountain gradually; and (iii) the upper part of the system is able to cross the

mountain and induces a center in the lower levels even though the lower-level center has been blocked on the east side of the mountain.

Other westward-moving typhoons include the formation of one or several induced lows on the west side of the mountain when the typhoon approaches the mountain. These typhoons were classified into three additional categories: (i) the dominant secondary low is located to the south of the original center; (ii) the dominant secondary low is located to the north of the original center; and (iii) dual centers exist, with the secondary low developing and traveling away from the island while the original center is traveling parallel to the developed secondary center after having crossed the mountain. The original center in categories (i) and (ii) dissipates and does not cross the mountain.

In addition to the observational studies, several numerical modeling studies addressed the effect of the terrain on typhoons crossing Taiwan. Using a 60 km resolution model and including an idealized topography, Chang (1982) showed that the mountain-induced flow is mainly confined to the lower levels. The basic (easterly) flow in the lower levels is blocked so that most of the parcels are unable to go over, and thus must pass around the mountain. In the upper levels, the flow has only minor deflections. Due to the different influences in lower and upper levels, the center of vortex is not vertically aligned. The upper-level center experiences little change as it passes the mountain ridge. The low-level center accelerates and moves northward as it approaches the mountain, decelerates and moves southward after it passes the mountain ridge. Chang suggests that the cumulus heating near and over the mountain is responsible for generating and maintaining a cyclonic circulation around the topography. This cyclonic

circulation then steers the low-level center to pass the mountain in a cyclonic direction. In a experiment without cumulus heating, Chang showed the circulation around the mountain is mostly anticyclonic. The secondary vortex centers form over the leeside when the low-level vortex center is blocked by the mountain range. One of the secondary centers develops when it is in phase with the upper-level vortex center.

Bender et al. (1987) used a triply-nested high resolution (1/6° lat.) model to study the effects of island terrain on tropical cyclones in three regions of the tropics: the Caribbean Sea, Taiwan, and Luzon in the Philippines. As in previous studies, track deflections are found, with the most prominent upstream northward deflection occurring when the simulated storm approaches Taiwan. They suggested that the enhanced and deflected steering flow as well as some unknown vortex-barrier interactions cause the vortex motion change. The distortion effect on the tropical cyclone structure is also most conspicuous over Taiwan, and especially, with the formation of secondary lows. The secondary low is absent in the numerical experiments of the other two regions. Compared to Chang (1982), the Bender et al. high-resolution simulations produced more realistic intensity changes during the typhoon approach, landfall and departure from Taiwan. They found that a region of dry air, which is due to the descending flow over the land, is advected into the storm and is responsible for the filling of the system before landfall. According to this mechanism, a slow-moving typhoon may start weakening several hours earlier before landing than a fast-moving one.

The important scientific problems related to the mountainous topography effects on typhoon motion and structure, and the approaches that are taken to address these

problems, are first discussed in Chapter II. The numerical model that is used in conducting the experiments is described in Chapter III. Both observational studies and numerical modeling simulations showing significant terrain-induced track deflections are given in Chapter IV. Chapter V is an observational study to analyze the terrain effects on the typhoon structure based on a 20-year data set. The observational studies also serve to validate a numerical study of the terrain effects on typhoon structure changes. Demonstration of the formation of secondary low and secondary vortex from the model simulations is given in Chapter VI. Finally, a summary is given in Chapter VII.

II. SCIENTIFIC PROBLEMS AND STUDY METHODOLOGIES

The previous observational and numerical studies (e.g., Brand and Blelloch 1974; Wang 1980; Chang 1982; Bender et al. 1987) have shown significant intensity, structure and movement changes occur when typhoons approach or cross the island of Taiwan. These studies provide explanations on the mechanisms causing typhoon filling when it is nearby or landing on Taiwan. However, some important problems are still not well understood. Some examples are the 'track deflection' upstream of the mountain, the modification of the flow structure when a typhoon is nearby, the mechanism that produces the secondary lows, and the structure of the secondary lows. These problems are discussed in the following sections.

A. UPSTREAM TRACK DEFLECTIONS

For a westward-approaching typhoon, poleward track deflections upstream of Taiwan island have been emphasized in both observational (e.g., Brand and Blelloch 1974) and numerical simulations (e.g., Chang 1982; Bender et al. 1987) studies. However, diverse conclusions have been found as to the magnitude of the deflections and the upstream range of the terrain effect. For example, Brand and Blelloch showed a leftward track forecast error of 33 km between -48 h and -24 h prior to a typhoon making landfall, and a rightward forecast error of 41 km in the period from -24 h to landfall. If the initial veering of 33 km prior to -24 h can be interpreted as an upstream

terrain-induced deflection, a cross-track velocity of 0.38 m/s is implied. However, if the net deflection is interpreted as only 25 km in 48 h, the average cross-track velocity is only 0.14 m/s. Moreover, Chang showed that the average cross-track velocity component of the storm center in his simulation was northward at 0.8 m/s during the 18 h prior to encountering the terrain, while Bender et al. found that the upstream vortex deflection in their simulation started relatively close (about 8 h prior to landfall) to the terrain and the center was deflected more northward. Although the average cross-track velocity obtained by Bender et al. was about 3.1 m/s, the track deflection was sensitive to the storm translation speed. A translation speed increase from 5 m/s to 10 m/s almost eliminated the northward deflection.

The different results on the track deflections between the observational and numerical simulation studies may be due to the storm structure and the environmental flow being much more complicated in nature than in the simplified simulations. Moreover, Brand and Blelloch used the JTWC forecast tracks as a reference to calculate the deviations. As a result, the calculated deviation may not be due only to the Taiwan topography effect. Variations due to the large-scale environment flow change and forecast skill differences may also be involved. Bias may also be introduced because relatively few cases (22) were examined. In the present study, more cases are included and a redefinition of the reference track is used.

Bender et al. suggested that the terrain-induced steering flow modification is the main cause of the typhoon track deflection. According to this conclusion, different magnitudes of deflections will be expected for typhoons approaching different portions

of Taiwan. The previous studies have not considered such suggestions. If the track deflection does depend on the landfall region, then the magnitude of the track deflection may be underestimated by averaging all approaching storms. Large forecast errors are expected if a forecaster simply applies the average 'poleward deflection' to a typhoon approaching the southern portion of Taiwan.

The track deflection upstream of the barrier depends on the intensity of the approaching vortex (Chang 1982). In addition, Bender et al. showed that the track deflection was sensitive to the vortex translation speed. The terrain-induced cyclonic circulation was suggested by Chang to explain the vortex motion near the barrier. However, it is unclear how the vortex track and the terrain-induced circulation are related. Bender et al. examined the influence of the mountain range on the basic flow as a contributor to the vortex motion change. Their Fig. 9 suggests that an unknown factor contributed to the large vortex track deflections in relation to the steering flow. More studies are required to understand the physics involved in the upstream track deflections caused by Taiwan, and the dependence of these track deflections on the vortex intensity and the translation speed.

This study of the Taiwan terrain effect on typhoon tracks will be focused on the upstream region and for the generally westward-moving cases. The JTWC best-tracks of 103 typhoons that approached Taiwan between 1947-1990 are analyzed in Chapter IV. A polynomial curve-fitting technique is applied to obtain a smooth track for each typhoon. Position deviations from the smooth track will be referred to as the Taiwan terrain effect. Cases are also separated into storms that landed on the northern and on

the southern region to isolate differences in the upstream track deflections. Numerical modeling simulations are also employed to study the upstream track deflections. Discussion of the numerical model and the simulation procedure are given in Chapter III. The simulation results are discussed in Chapter IV.

B. STRUCTURE MODIFICATIONS

As mentioned, interesting structure modifications when a typhoon approaches Taiwan have been noticed by Taiwan scientists since the 1960s (e.g., Hsu 1960; Li 1963). Wang (1980) collected one of the most complete sets of observations of the surface pressure and winds over the island when a typhoon was nearby. Many cases of the formation of a secondary low(s) over the western coast when a storm approached Taiwan from the east have been shown by his subjective analyses. For example, Wang observed a secondary low near the northwestern coast at 03 UTC (Fig. 2.1a) prior to the landfall of Typhoon June on eastern Taiwan. This secondary low was located inland three hours later (not shown) and became the dominant center at 09 UTC when Typhoon June was blocked on the east slope of the CMR (Fig. 2.1b). Another secondary low center was analyzed near the southwestern coast. In another example, three secondary lows were analyzed when Typhoon Louise (Fig. 2.1c) made landfall on the northern portion of Taiwan. Later, the secondary low near the west-central coast developed and became the dominant center (Fig. 2.1d). However, the interpretation of these examples may be significantly different if an objective analysis is carried out, because most of the small-scale low centers in Fig. 2.1 are not easy to resolve from the rather sparse

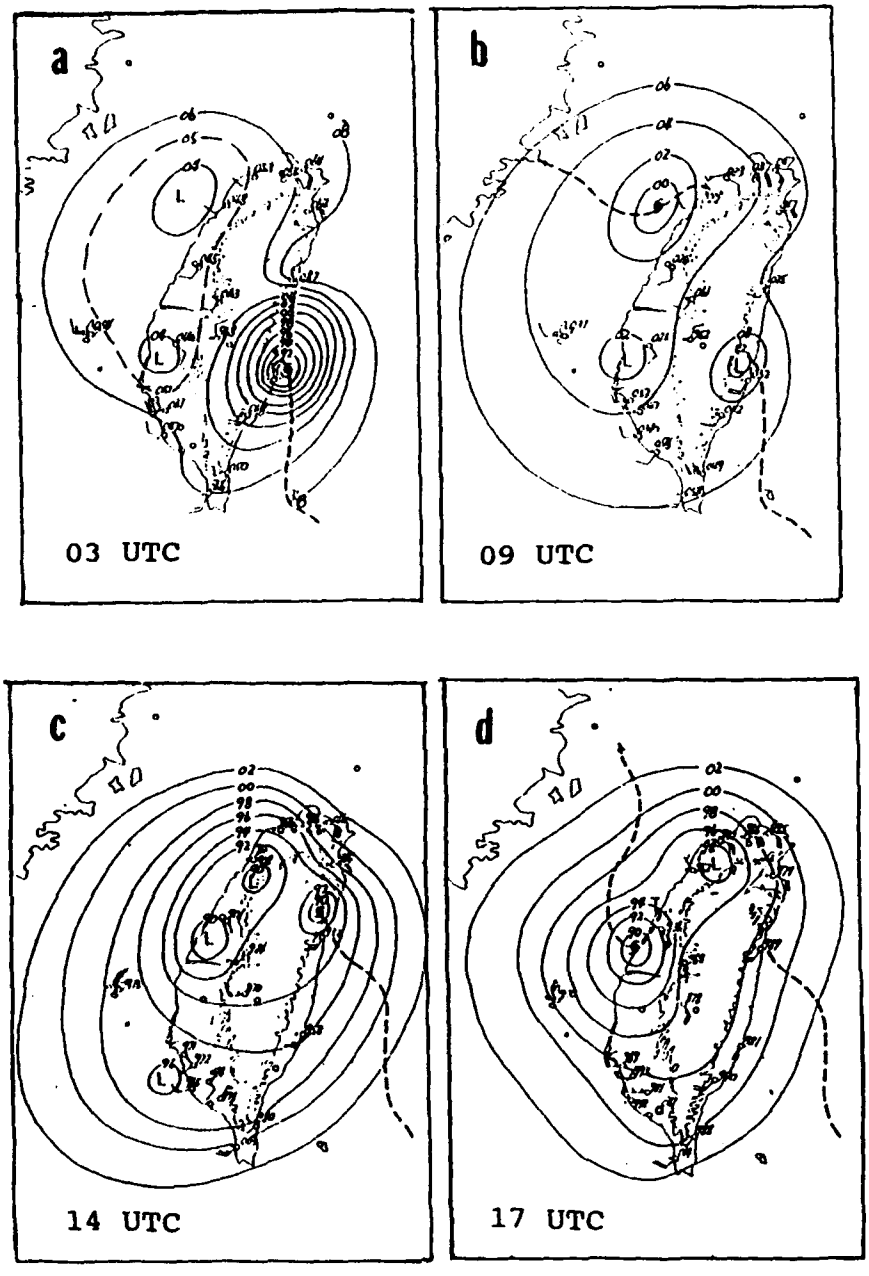

Fig. 2.1 Sea-level pressure analyses as Typhoon June (a) made landfall at 03 UTC 7 August 1961 and (b) six hours later when the lowest central pressure was northwest of Taiwan; and Typhoon Louise (c) made landfall at 14 UTC 3 September 1959 and (d) three hours later. Dashed line indicates the track (from Wang 1980).

observations. The gradient wind relationship to infer the pressure field from the wind distribution was used by Wang to identify the low center in the absence of observations. More studies are required to verify such an approach and the nature of any balance between wind and pressure fields.

The few observations from the central Taiwan region are very valuable to the determination of the typhoon structure over Taiwan. Unfortunately, three observation sites in the south-central Taiwan were generally neglected in the previous studies (e.g., Wang 1980) because of the difficulty of reducing the surface pressure at these high mountain stations to sea level. Proper use of the observations in the central Taiwan may help in clarifying whether: (i) a trough or two secondary lows were produced on west side of CMR (Fig. 2.1a) when Typhoon June was located on the eastern coast at 03 UTC; and (ii) whether the original center was blocked near the east coast or was located farther inland at 09 UTC (Fig. 2.1b). New observation stations in the north-central CMR may be required to identify the separation of the secondary low near the northwestern coast from the typhoon center on the east, such as in the example in Fig. 2.1c from Wang when Typhoon Louise moved over Taiwan at 14 UTC.

Wang also reported three favorable locations in the north, center and south sections along the west side of Taiwan (e.g., Fig. 2.1c) for secondary lows to form when a typhoon approaches. The typhoon approach direction (incident angle) and the wind direction in northern Taiwan were suggested by Wang to be important factors in the formation of secondary lows. Some cases indicated that the formation of the northern and central centers was related to the incident wind direction, whereas the formation of

the third center was related to the horizontal wind shear in southern Taiwan. The extent to which these conclusions may be applied is unknown. No detailed upper-air observations are available to study the terrain-induced structures in three dimensions. Without knowledge of the vertical structure, an understanding of how the secondary lows are formed, and whether a secondary low will later become the tropical cyclone center, is lacking.

In a numerical simulation study, Chang (1982) showed that two secondary centers were induced and one of the secondary lows developed to form a discontinuous track when a weak vortex encountered an idealized mountain range. One secondary center was produced at a location south of the barrier and another secondary center was produced about 300 km downstream of the barrier. Both center locations were different from the 'favorable positions' suggested by Wang (1980). Formation of secondary lows was also simulated by Bender et al. One secondary center was located much closer to the mountain peak as compared to the location suggested by Wang (1980), and the other center formed over the ocean. Bender et al. simulations also suggest that the formation of the secondary center is sensitive to the vortex translation speed. These diverse conclusions regarding the initial location of the secondary low requires further clarification, especially since the numerical studies of Chang and Bender et al. have not examined the secondary low in detail.

In summary, significant modifications of the precipitation, wind and pressure distributions when typhoons encountered Taiwan island have been reported in both observational and numerical simulation studies. However, general conclusions on the

cause and the structure of these modifications have not been reached. This provided the motivation for this study. Due to the data sparsity, a detailed observational case analysis is not pursued in this study. Rather, a statistical approach is used to describe the general features of the Taiwan terrain effect on the surface structure of typhoons. The observational study is described in Chapter V.

Numerical simulations have been successfully used to study the mountainous terrain effects on different flow environments (e.g., Smolarkiewicz et al. 1988; Sun et al. 1991). A similar approach is used here to examine the CMR effects on typhoon structure. Comparison of the simulations with observational results, simulations of the three-dimensional structure of the terrain effects, and the mechanisms involved in the formation of the secondary center are described in Chapter VI.

III. NUMERICAL MODEL AND EXPERIMENT DESIGN

A. NUMERICAL MODEL

A version of the Limited-Area Weather Prediction Model of the Naval Research Laboratory (Madala et al. 1987; Chang et al. 1989; Holt et al. 1990) is employed in this study. The model physics include internal diffusion, dry convective adjustment, latent heat release in nonconvective clouds and in convective clouds based on the modified Kuo-type cumulus parameterization (Kuo 1974; Anthes 1977). A high-resolution turbulent kinetic energy closure planetary boundary parameterization is also included. The radiation processes are not considered due to their computational complexity and the relatively short integration period of these simulations of the terrain-typhoon interaction.

The model has been installed in the VAX computer system in the Interactive Digital Environmental Analysis Laboratory of the Department of Meteorology after minor modifications of the input/output modules. Another modification is the calculation of the ground temperature. The original model prognostic equation for predicting the ground temperature follows Blackadar (1976) and Chang (1979), in which, diurnal insolation, cloud amounts, and ground wetness are all required for calculating the net radiation, the sensible and the latent heat fluxes. Since the radiation processes are not included in the model, and the precipitation and cloud processes are all simplified, the difference between the ground surface temperature and the temperature of the lowest model layer is assumed to be equal to the mean temperature difference over the ocean surface. This

simplified procedure speeds up the calculation and also eliminates the dependence on the diurnal cycle. Effects due to the differential heating between the ground and ocean surfaces, such as the land-sea breeze, are minimized. This simplified approach apparently produces no significant differences as long as the wind speed is not too much smaller than 5 m/s.

The complete set of equations on the sigma coordinate (Phillips 1957) are approximated by finite difference methods with a split-explicit time integration scheme (Madala 1981). A Brown and Campana (1978) temporal filter, and the Perkey and Kreitzberg (1976) lateral boundary blending technique are included. Details of the model and computational procedures are given in the above-mentioned references.

B. EXPERIMENT DESIGN

The main purpose of this study is to understand the major mechanisms causing the general track and structure modifications when a typhoon approaches Taiwan not to predict the actual typhoon track and structure changes caused by the details of the Taiwan topography. Therefore, the experiments are based on idealized cases and with the Coriolis parameter that is assumed constant to exclude the complexity of the beta effect on the typhoon motion and structure (Elsberry 1987). Simulations are examined for typhoons approaching different sections (from north to south) of Taiwan with three translation speeds: 2.5 m/s, 5 m/s and 10 m/s. Comparisons are also made for weak and intense typhoons. Details of the model domain, gridpoint arrangement, and initial condition specification are discussed in the following sections.

1. Model Domain and Grid Arrangement

A 45 km resolution in the horizontal is employed over a domain of 3600 km by 2250 km in the east-west and north-south directions respectively. In the vertical, eight of the 16 sigma layers are in the lower 200 mb to allow higher resolution near the surface. The vertical model levels are shown in TABLE I. The time increment for the simulation is two minutes. Under these arrangements, the model requires about seven mega bytes of computer memory and about 21 hours of central processing unit time on the VAX 3500 workstation for a 24-hour simulation.

2. The Topography

The topography of Taiwan is greatly simplified such that it is represented by a smooth, elliptical barrier. All other nearby terrain such as the China mainland, Philippine islands and islands of Japan are not included. The idealized topography is centered at (x_c,y_c) with the height $h(x,y)$ specified as

$$h(x,y) = h_{max} * \cos(\pi/2 * R/r_{size}) \qquad \text{for } R < r_{size}$$

$$= 0 \text{ (ocean)} \qquad \text{for } R \geq r_{size}$$

Here, h_{max} is the maximum terrain height, and r_{size} is a parameter to control the size of the terrain. An elliptical-shaped barrier is produced by defining a weighted distance (R) between a location (x,y) and the barrier center (x_c,x_c) as

$$R = ((x-x_c)^2 + ((y-y_c)/e)^2)^{1/2}$$

where e is the ratio of the horizontal scaling lengths. In this study, h_{max}=2500 m, r_{size}=160 km, and e = 205/160. Therefore, the elliptical-shaped barrier extends 320 km in the E-W direction and 410 km in the N-S direction with a peak equal to 2500 m. This

TABLE I VERTICAL MODEL LEVELS.

Model level	Sigma level	Approximate pressure (mb)
1	0.05	50
2	0.15	150
3	0.25	250
4	0.35	350
5	0.45	450
6	0.55	550
7	0.65	650
8	0.75	750
9	0.82	820
10	0.86	860
11	0.90	900
12	0.93	935
13	0.96	960
14	0.9775	977
15	0.99	990
16	0.9975	997

isolated barrier is slightly lower and larger than the CMR of Taiwan. Notice that the cosine function produces a well-defined coast line and a steeper terrain slope near the coast line than does the exponential function that has been used for many theoretical studies.

3. Initial Condition Specifications

The initial conditions include a specified zonal wind field and a conditionally unstable vertical profile of temperature and relative humidity (TABLE II). An initial geopotential height field is derived from the geostrophic equation and the hydrostatic relation using the layer thicknesses from the specified temperature profile. The initial surface pressure on the terrain is interpolated vertically assuming hydrostatic balance. Fields on the constant pressure surfaces are interpolated to the sigma surfaces prior to the integrations. Since these fields are not in balance, an adjustment occurs during the first few hours of the simulation.

A typhoon is implanted in the model by adding a "spun-up vortex" to the background wind, temperature and humidity fields on the constant pressure surfaces. This vortex is fully three-dimensional and is the result of a 72-h simulation beginning from an initial wind field with a maximum wind v_{max} (see values in TABLE II) at the radius of maximum wind r_{max}. The initial radial structure is defined following Chan and Williams (1987) as

$$v(r) = v_{max}(r/r_{max})exp[(1-(r/r_{max})^b)/b].$$

Two spun-up vortices are examined in this study. A smaller and weaker vortex, which is close to a steady state after 72 h of simulation, is generated by assigning r_{max}=90 km

TABLE II INITIAL PROFILES. The initial temperature (T), relative humidity (RH) and maximum wind speed (v_{max}) profiles for the numerical model.

Level (mb)	T (K)	RH (%)	v_{max} (m/s)
50	216.7	30	0
70	216.7	30	0
100	216.7	30	0
150	216.7	30	-15
200	217.4	30	-30
250	221.0	30	-15
300	228.6	30	0
350	235.5	30	6
400	241.5	40	9
500	251.9	50	21
600	260.8	60	30
700	268.6	80	30
850	278.7	80	30
925	287.4	90	30
1000	287.4	90	30
sea surface temperature = 301.0 (K)			

and $b=1.2$. A more intense vortex is generated with $r_{max}=135$ km and $b=1.0$. The more intense vortex is still slightly deepening at the end of the 72-h pre-integration spin-up period. Some properties of these two spun-up vortices are summarized in TABLE III and are discussed in Chapter IV. The development of the sea-level pressure and the lower-troposphere height and wind fields of the two vortices in an ocean-only 5 m/s zonal flow are discussed in Chapter IV and Chapter VI, respectively.

TABLE III VORTEX STRUCTURE. The minimum sea surface pressure (P_{min}), the maximum averaged wind speed (v_{max}), the radius of maximum wind (r_{max}) and the size (R_{size}, radius of 15 m/s wind) of the weak and intense spun-up vortices. In the table, the maximum averaged wind speed, the radius of maximum wind and the size are determined from the 900 mb level.

vortex	P_{min} (mb)	v_{max} (m/s)	r_{max} (km)	R_{size} (km)
weak	1001	19	135	200
intense	985	33	135	450

The barrier-modified wind, temperature and relative humidity fields are also included in the initial fields. These barrier-modified fields are the 48-h model simulation results beginning from the specified zonal flow and the conditionally unstable atmosphere in TABLE II. After the 48-h simulation, the flow structure reaches a quasi-steady state except downstream of the barrier where shedding vortices are found. These barrier-modified fields are similar to other simulations (e.g., Smolarkiewicz et al. 1988;

Sun et al. 1991; Li 1992). Although the barrier-induced flow structure is sensitive to the imposed flow, detailed discussion of these modifications caused by the barrier is not included. Deep-layer mean wind fields for a 5 m/s (Fig. 4.13) and a 10 m/s (Fig. 4.16) zonal flow are discussed later in Chapter IV. These barrier-modified mean flows are related to the upstream deflections of an approaching vortex.

For a vortex in a 5 m/s basic flow, the barrier is centered 1350 km east of the western model boundary and the vortex is located 810 km farther upstream. This arrangement prevents the vortex from being too close to the lateral boundaries at both the initial and the final stages of the integration. This arrangement also allows about 36 h before the vortex center makes landfall on the barrier. For simulations of a vortex in a 10 m/s (2.5 m/s) basic flow, the initial vortex is placed 1125 km (585 km) upstream of the barrier. This interval requires about 27 h (48 h) for the faster (slower) flow case to make landfall. North-south displacements of the initial vortex center are used to simulate typhoons making landfall on different portions of the CMR (Chapter IV). In all cases, both the barrier and the vortex are kept near the center of the computational domain.

IV. TERRAIN EFFECTS ON THE MOTION OF VORTEX

A. OBSERVATIONAL EVIDENCE

1. Track Stratifications

Many additional cases of typhoons striking Taiwan have become available since the Brand and Blelloch (1974) study. All 103 typhoons between 1947-1990 that entered a domain (Fig. 4.1) slightly larger than the island of Taiwan were selected. Locations from the JTWC best tracks at 6-h intervals were utilized. The landing (departing) time was defined as the first (last) time the typhoon was inside the domain shown in Fig. 4.1.

The incident angle is defined as the track direction relative to the domain edge at the landing position. As suggested by Wang (1980), this incident angle will be used to stratify the cases. In this report, only the storms approaching the eastern domain edge with an incident angle between 45° and 135° will be considered. That is, these are generally westward-moving storms that will strike Taiwan relatively perpendicular to the CMR. This choice of incident angles also will make comparisons with the numerical model simulations more straight-forward. Only 58 of the 103 typhoons satisfy the 45°-135° incident angle criterion. If the upstream track deflections are due to a blocking effect of CMR, they should be different for a storm approaching the northern and southern ends of Taiwan. Thus, 33 typhoons landing north of 23.5° N will be considered separately from 25 storms with a landing position to the south of this latitude.

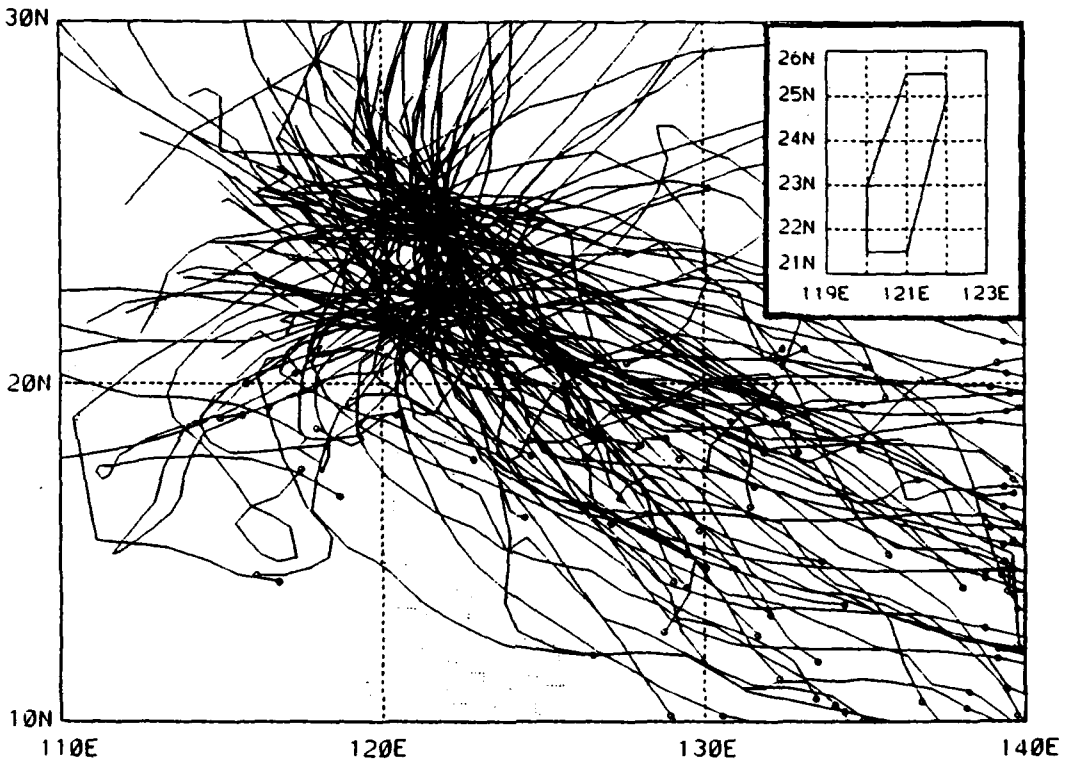

Fig. 4.1 Tracks of 103 typhoons that passed through a trapezoidal selection box (see insert) surrounding Taiwan. The initial position of each track is indicated by a circle.

2. Cross-track and along-track calculations

Notice that many of the tracks in Fig. 4.1 have a curvature that might be incorrectly interpreted as a track deflection caused by the Taiwan terrain. Thus, a second-order polynomial curve was fitted to the 6-h track positions from about 72 h before landing to about 18 h after landing. Holland and Lander (1991) have used a similar approach to study track oscillations on a number of time scales. A polynomial fit of the sequence of longitudes in terms of the latitudes and a polynomial fit of the latitudes as a function of the longitudes were calculated by a least squares method. The polynomial with the smaller fitting error was selected. Nevertheless, some very irregular tracks had large fitting errors. A somewhat subjective criteria of 1.0° lat./long. RMS error was used to reject those tracks that were not well represented by the second-order polynomial fit. This resulted in a rejection of two and three cases from the northern and southern landing samples respectively, so that the final sample sizes are 30 and 23 respectively.

Some examples of the polynomial fit of typhoon tracks are in Fig. 4.2. Typhoon Yancy (storm number 13 during 1990) was a large storm that had some small track oscillations about 36-72 h prior to the landfall (Fig. 4.2a). A significant track deflection to the north began about 24 h prior to landfall. However, Yancy resumed a more westward track just 12 h later and struck northern Taiwan. Detailed surface center positions near Taipei revealed by the Doppler radar data (Jong-Dao Jou, personal communication) were not available to JTWC and thus are not included in the 6-h best track positions. A similar upstream track deflection seemed to be present in Tropical

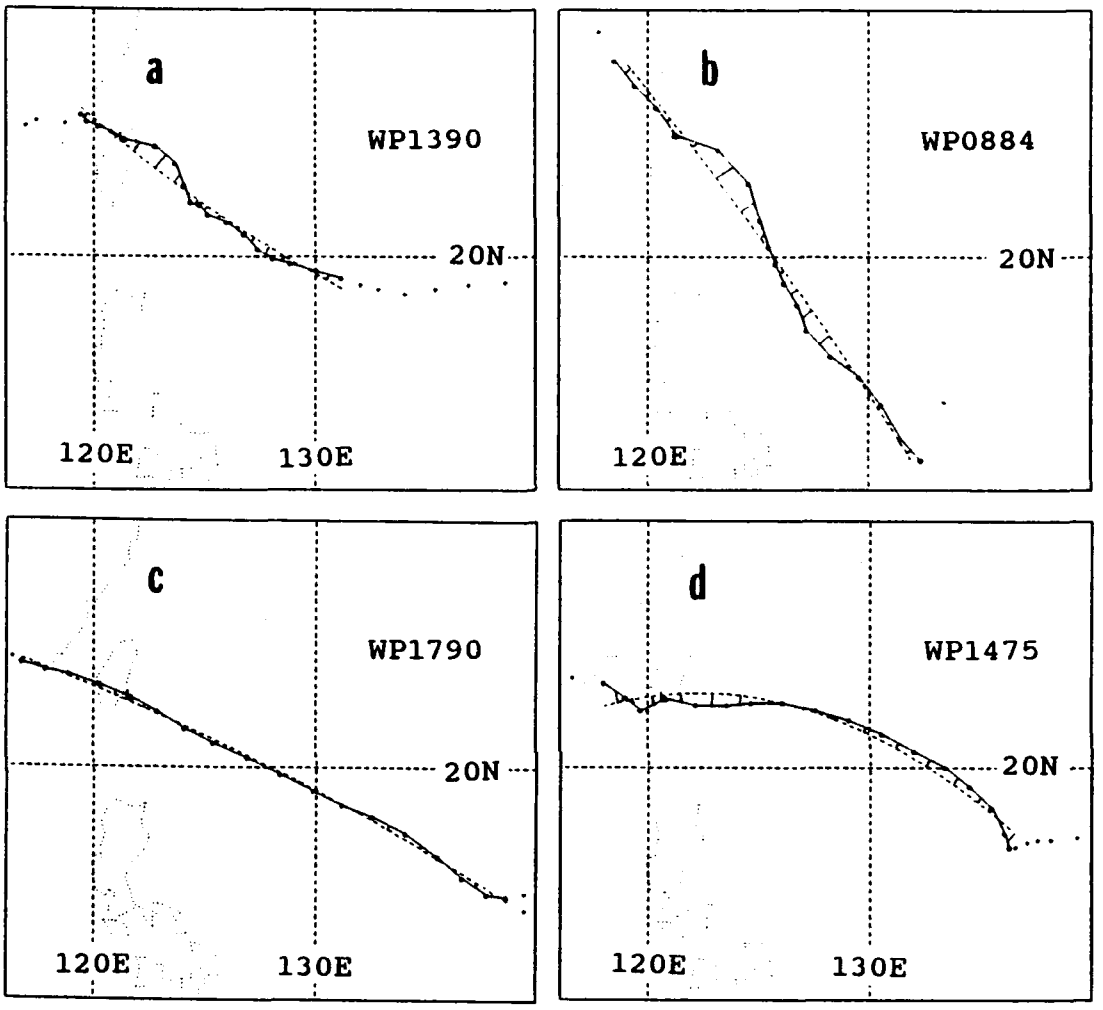

Fig. 4.2 Positions each 6 h, actual track (solid) and second-order polynomial track (dashed) within 72 h of landfall and 18 h after leaving Taiwan for (a) Typhoon Yancy (WP1390); (b) Tropical storm Freda (WP0884); (c) Typhoon Dot (WP1790); and (d) Typhoon Betty (WP1475). Cross-track displacements and along-track speeds are calculated from the perpendicular line segments at +3 h and -3 h from the 6-h position.

Storm Freda during 1984 (Fig. 4.2b). However, this deflection may be part of a longer time scale oscillation about the polynomial fit. Typhoon Dot (1990) had a long smooth track toward a landing position on the southern end of Taiwan (Fig. 4.2c). The northward track deflection just upstream of Taiwan was no larger than the small oscillations about the polynomial track during the prior 72 h. The JTWC 6-h positions do not indicate the discontinuous nature of the track across Taiwan, which was associated with one or more secondary low pressure centers and was revealed only in hourly surface analyses (G. Chen, private communication). Typhoon Betty (Fig. 4.2d) during 1975 approached the southern part of Taiwan along a curved path. A southward deflection upstream of Taiwan may be due to an interaction with the CMR. An alternate interpretation is that this deflection is part of longer term oscillation about the polynomial track.

Along-track speeds are calculated by constructing the shortest distance between the track at +3 h and -3 h and the fitted curve (Fig. 4.2). Thus, the along-track speeds at the original synoptic time (00, 06, 12 and 18 UTC) are the displacements per six hours between these + 3 h and -3 h points. Instead of defining a cross-track speed, cross-track deflections will be calculated with positive (negative) deflections defined to be to the right (left) of the polynomial fitted track.

Notice that the -72 h to +18 h time interval is much longer than the time interval of the upstream track deflections that are to be detected, which should then appear as perturbations to the smooth track. If all of these 6-h positions are used, the positive (negative) cross-track deflections that are being sought will be balanced by

negative (positive) offsets over the remainder of the track to minimize the deviations relative to the smoothed track in the least-squares fitting routine. Thus, an alternate approach of excluding the 6-h positions during the period of expected deflections was tested. That is, only the far upstream positions (-54, -60, -66 and -72 h) and the positions after leaving Taiwan (+6, +12 and +18 h) were used in the second-order polynomial curve fitting.

3. Mean Along-track Component

The average along-track speeds relative to the second-order polynomial fit using all of the 6-h positions between -72 h and +18 h are shown in Fig. 4.3a for the 53 typhoons that approached Taiwan with a westward track within +45° and -45° of a normal incidence. As in Brand and Blelloch (1974), a downstream acceleration is noted with along-track speed increases from about 4.5 m/s at 72 h prior to landfall to about 6 m/s at landfall. The total speed (not shown) has a very similar variation with time, but is slightly larger than the along-track component. The approximate one third increase in along-track speed from -72 h to the landfall speed of 6 m/s would seem to be a significant factor for the forecaster to consider.

Some numerical model simulations do indicate an acceleration prior to landfall. For example, Chang (1982) obtained a speed increase of 0.8 m/s in a 24 h period prior to landfall of a storm in a 5 m/s basic flow. Bender et al. (1987) also obtained an acceleration of the tropical cyclone in their high resolution simulations. For example, the increase in translation speed begins only 8 h prior to landfall in a simulation

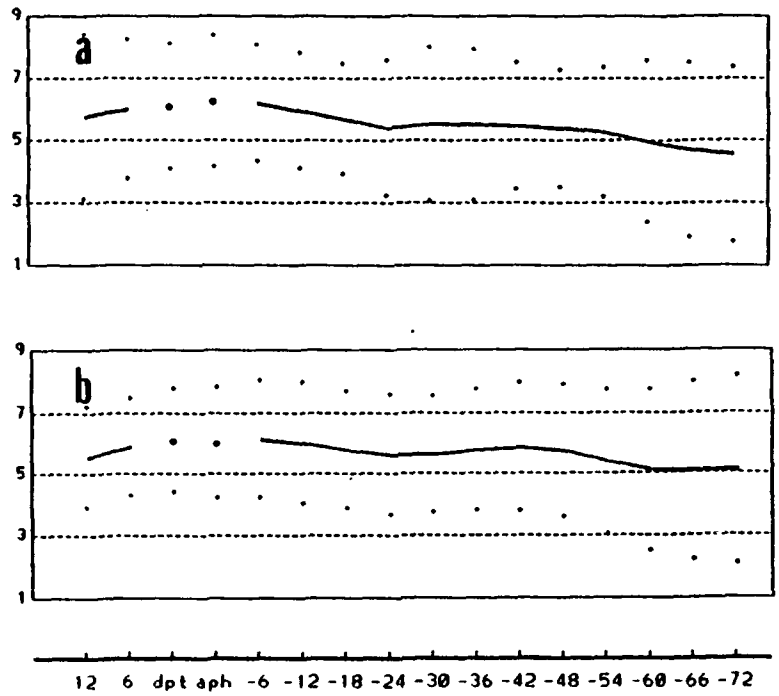

Fig. 4.3 (a) Average along-track speeds (m/s) and ± one standard deviation (dots) from -72 h prior to landfall (right side) to 12 h after leaving Taiwan (left side). Open circles indicate approximate speeds while over Taiwan. (b) As in (a), except for 60 storms passing through a trapezoidal box (see inset of Fig. 4.1) displaced 6° long. to the east and 2° lat. to the south of the box around Taiwan.

with a 5 m/s basic flow. Prior to this time, the translation speed with a mountain included in the simulation was slower than for the ocean-only control.

Chang (1982) attributed the translation speed increase in his numerical simulation to an interaction between the terrain and the tropical cyclone that caused enhanced easterlies around the north end of the mountain. Bender et al. demonstrated that the acceleration of the tropical cyclone was greater than the basic flow deflection around the topography, so they suggested some additional interaction between the storm circulation and the mountain range.

Notice that the increase in along-track speed in Fig. 4.3a is rather steady (rather than just prior to landfall). Thus an alternate explanation may be that the large-scale environmental flow is accelerating in this general region near the east Asian trough. Consequently, a separate set of typhoon tracks was obtained by displacing the trapezoidal box in Fig. 4.1 to the east by 6° long. and to the south by 2° lat. The along-track speeds of 60 typhoons passing through the displaced box are shown in Fig. 4.3b. A general downstream increase is observed from about 5.0 m/s to about 6.0 m/s over a 72-h period. Consequently, the acceleration near Taiwan in Fig. 4.3a, and in Brand and Blelloch (1974), is likely to be due to environmental flow changes rather than to interaction with the topography of Taiwan.

Other possibilities are that large, short-term deflections near the coast would not be detected with existing observation platforms, or not be considered representative during the construction of the best track in the post-storm analysis at JTWC. The

cancellations between different categories of storms may also obscure the CMR effect in Fig. 4.3a.

As Chang (1982) indicated, the storm track may be sensitive to the storm intensity. Consequently, a separation of the 103 typhoons into two groups according to the maximum wind speed is examined. Among the 50 typhoons in which the maximum wind speed 12 h prior to landfall was less than 40 m/s, 18 typhoons approached Taiwan with a westward track within +45° and -45° of a normal incidence. The along-track speeds of the weaker typhoons (Fig. 4.4a) are not increased from about 48 h prior to landfall. For the remaining 35 more intense westward-moving typhoons (Fig. 4.4b), the gradual increase of the along-track speeds is relatively similar to those in Fig. 4.3. These results suggest the CMR has a relatively small effect on the along-track speed of the more intense storms, but slows the weaker storm.

The storm tracks in the Bender et al. simulation were sensitive to the translation speed. A similar dependency of the along-track speed on the storm translation speed is sought in Fig. 4.5, in which two groups are determined according to whether the translation speed of the typhoon 12 h prior to landfall was smaller or larger than 6.0 m/s. The 27 slower-moving typhoons had an average along-track speed slightly smaller than 5 m/s from -54 h to -6 h (Fig. 4.5a). The remaining 26 faster-moving typhoons had an acceleration of along-track speed similar to Fig. 4.3. These results suggest the CMR decelerates the approaching slower-moving storms and has a relatively small effect on the along-track speed of the faster-moving typhoons.

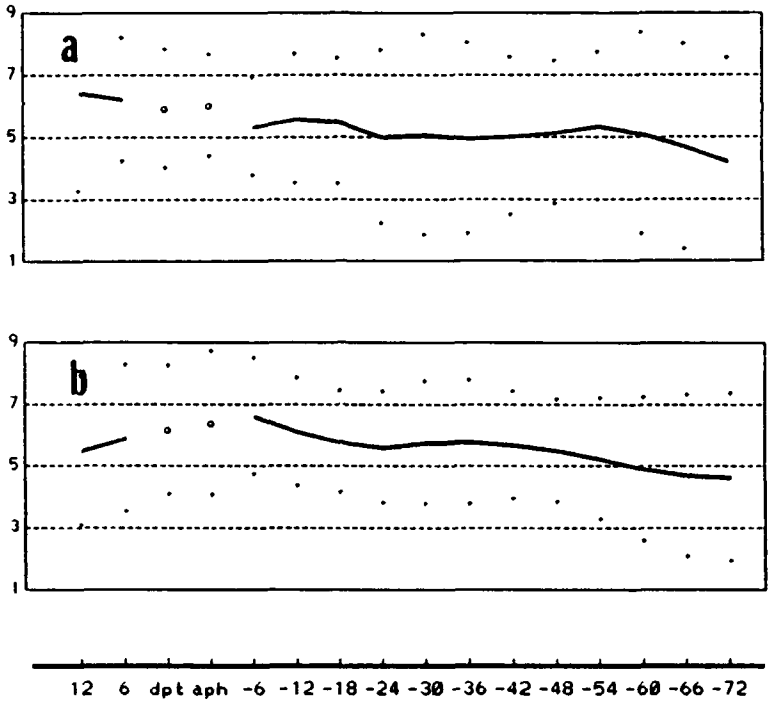

Fig. 4.4 Similar to Fig. 4.3(a), except for (a) 18 weaker typhoons in which the maximum wind 12 h prior to landfall was less than 40 m/s; and (b) 35 more intense typhoons in which the maximum wind 12 h prior to landfall was larger than 40 m/s.

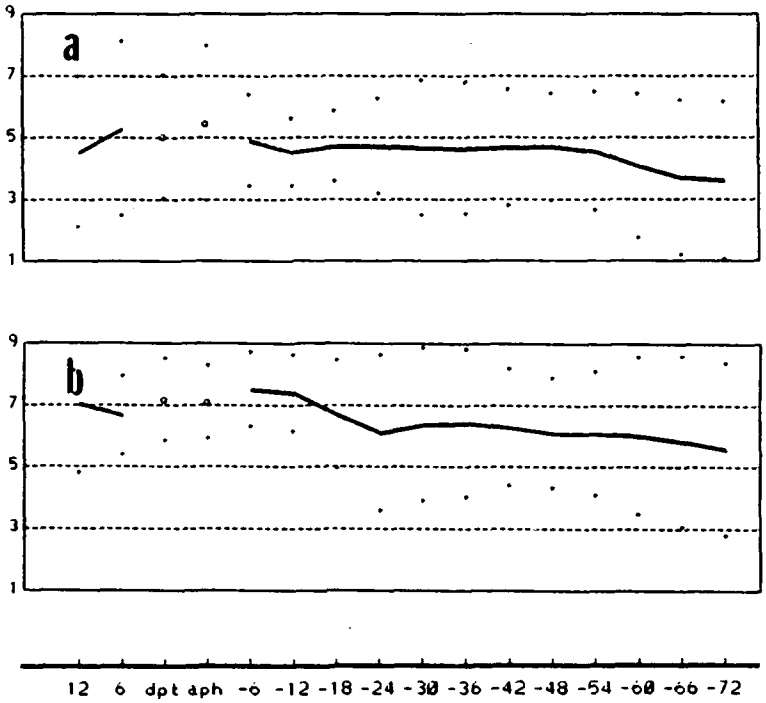

Fig. 4.5 Similar to Fig. 4.3(a), except for (a) 27 slower-moving typhoons in which the translation speed 12 h prior to landfall was less than 6.0 m/s; and (b) 26 faster-moving typhoons in which the translation speed 12 h prior to landfall was larger than 6.0 m/s.

4. Mean Cross-track Component

When the polynomial curve fit includes all of the 6-h positions, the sum of the cross-track deflections from -72 h to +18 h tends to zero in the least-squares fitting routine. The alternative is to include only the positions on either end and exclude the positions expected to have upstream deflections. Cross-track deflections relative to a second-order polynomial curve that includes only the -54 h through -72 h and the +6 h through +18 h positions are shown in Fig. 4.6. As expected, the curve fits to these end positions is relatively good, as indicated by the near-zero mean values and standard deviations of about 25 km. The mean values depart from zero and have much larger standard deviations (not shown if they exceed 50 km) about the mean values for the intermediate times that have been excluded in the polynomial fitting.

The mean cross-track deflections are positive (northward) relative to the polynomial curve for storms to the north (Fig. 4.6a) and are negative (southward) for storms to the south (Fig. 4.6c). Surprisingly, the largest cross-track deflections occur about 24 h prior to landfall rather than at landfall. The combined sample (Fig. 4.6b) has smaller mean values due to the tendency for cancellation between the northern and southern storms. Thus, these cross-track deflections generally appear to be consistent with a hypothesis of blockage of the low-level steering flow around the island leading to northward (southward) deflections for storms approaching the northern (southern) ends of the CMR.

Significant northward (southward) deflections are found for the weaker typhoons (Fig. 4.7a) approaching northern (southern) Taiwan. By contrast, the more

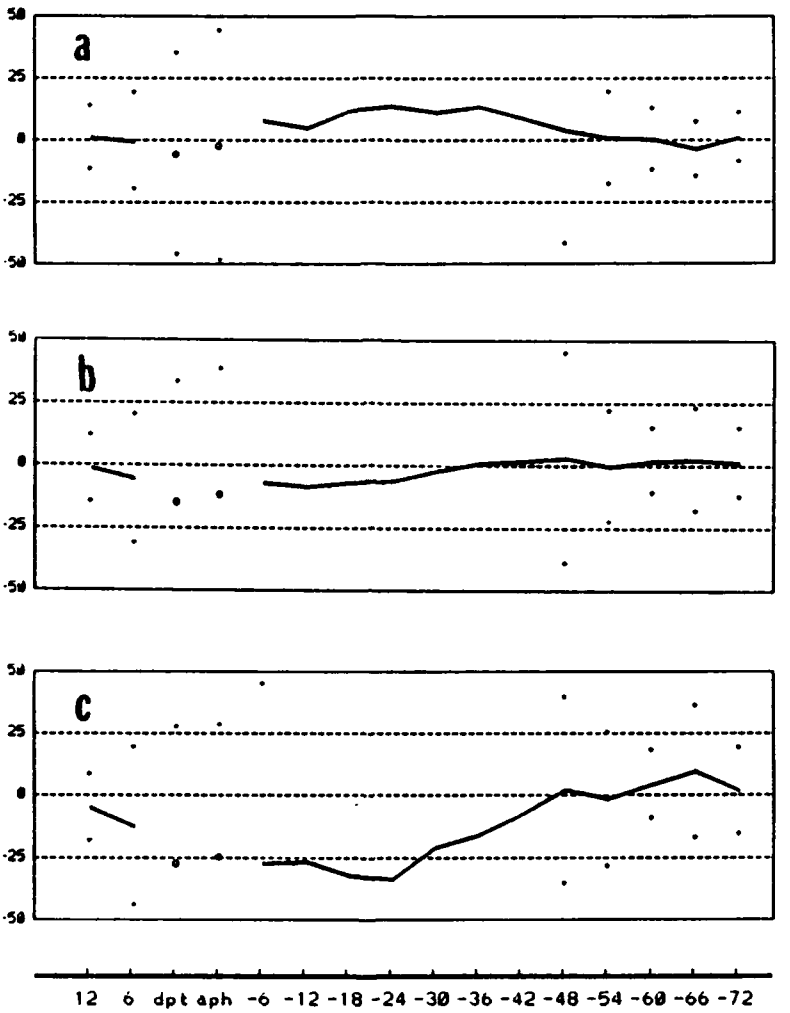

Fig. 4.6 Similar to Fig. 4.3, except cross-track displacements (km) relative to a second-order polynomial curve between end points of track (-54 h to -72 h and +6 h to +18 h) for (a) 26 west-moving storms landing north of 23.5° lat; (b) all west-moving storms; and (c) 19 west-moving storms landing south of 23.5° lat.

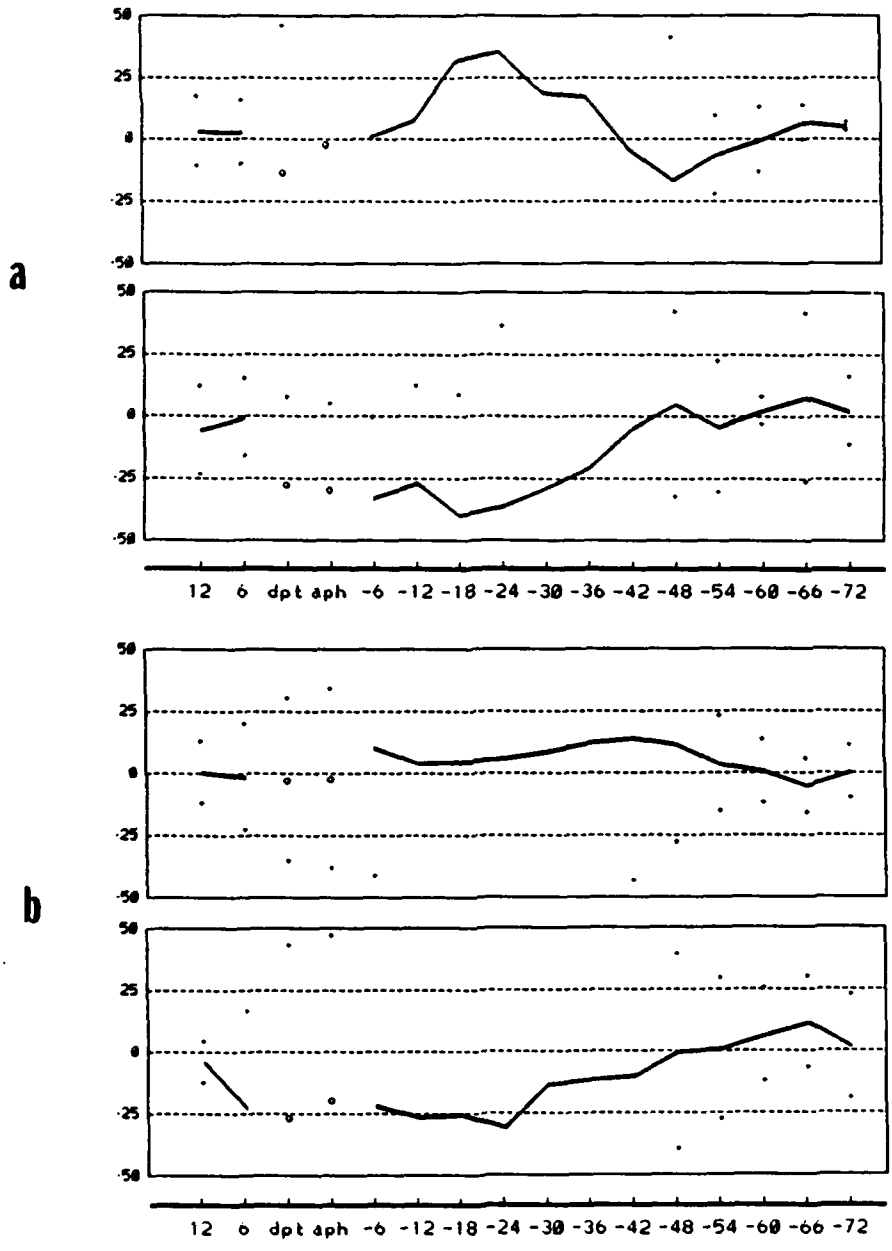

Fig. 4.7 Similar to Fig. 4.6, except for cross-track displacements of (a) seven weaker storms to the north (upper panel) and nine weaker storms to the south (lower panel) of Taiwan; and (b) 19 more intense storms to the north (upper panel) and 10 more intense storms to the south (lower panel) of Taiwan.

intense storms (Fig. 4.7b) experienced relatively small deflections. Notice that the largest cross-track deflections in the weaker typhoons are located closer to the CMR than for the more intense typhoons, for which the deflections start farther upstream.

The cross-track deflections of the slower-moving typhoons (Fig. 4.8a) have a similar magnitude as the faster-moving typhoons (Fig. 4.8b), except the faster-moving typhoons passing through the southern Taiwan have slightly larger southward deflections. More significant differences between Fig. 4.8a and Fig. 4.8b may be that the large deflections occurred somewhat closer to Taiwan for the slower-moving storms.

The extent to which these averaged cross-track deflections are caused by the CMR effect is not known. Relatively large standard deviations are found in all the calculations. The large variations may due to more complicated environmental flows in the nature. Numerical model simulations with simplified flow structures will be studied in the following sections to compare with the observations.

B. SIMULATIONS

1. Design of Experiments

As mentioned, the variability in the upstream track deflections in the above data analysis requires further verification to reach a conclusion. Numerical model simulations are applied in this section to promote the general understanding of how the track may be influenced by an idealized terrain. The model has been described in Chapter III. Studies include:

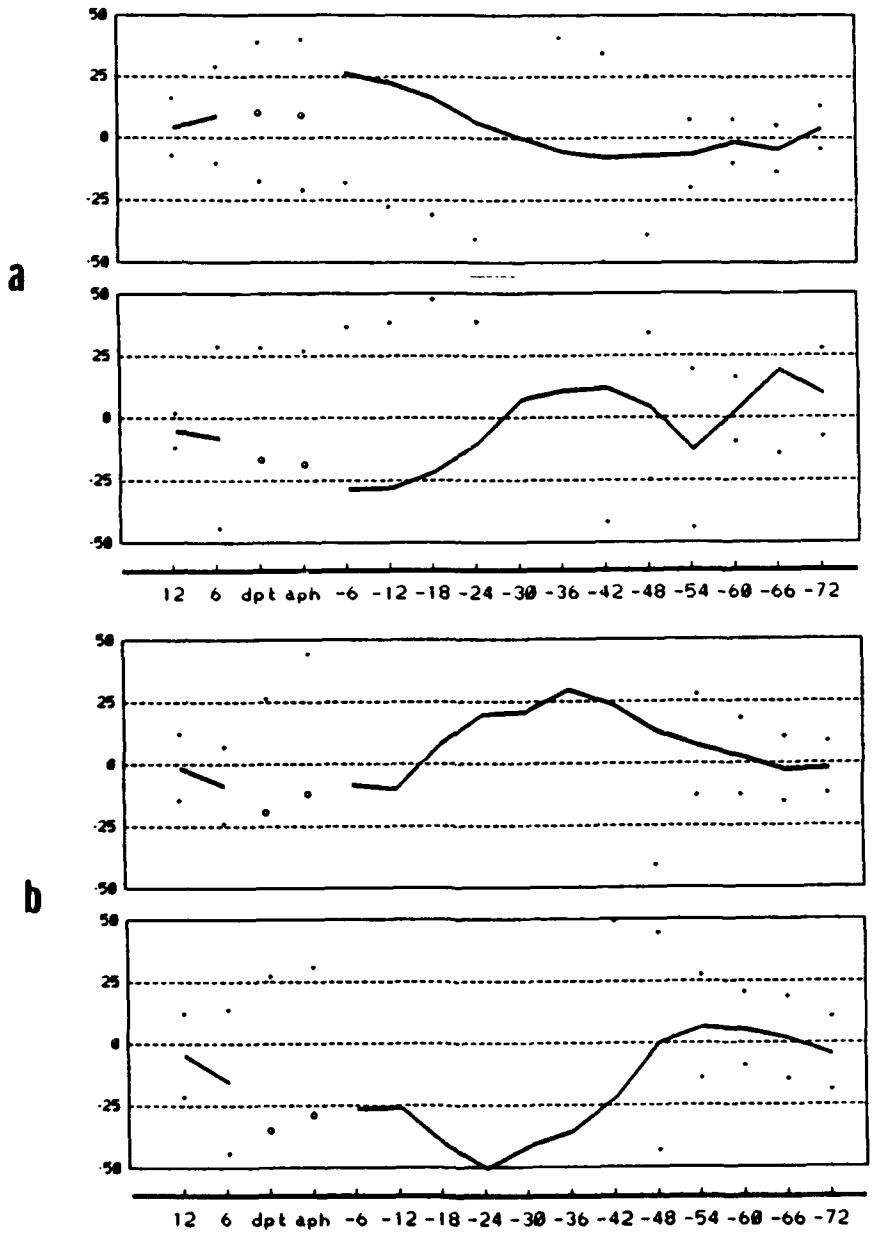

Fig. 4.8 Similar to Fig. 4.6, except for cross-track displacements of (a) 12 slower-moving storms to the north (upper panel) and eight slower-moving storms to the south (lower panel) of Taiwan; and (b) 14 faster-moving storms to the north (upper panel) and 11 faster-moving storms to the south (lower panel) of Taiwan.

i) How does the track behavior depend on the upstream approach (e.g., northern, central or southern portions of the terrain)?

ii) How does the upstream track deflection depend on the intensity of storm?

iii) How does the track behavior depend on the translation speed of the storm?

The dependence of the track behavior on the storm intensity will be examined with two spun-up vortices representing weak and intense typhoons (Chapter III). TABLE III provides a list of the minimum sea-level pressure, the maximum wind speed, the radius of maximum wind and the size (radius of 15 m/s wind, following Fiorino and Elsberry 1989) of the two spun-up vortices. In the table, the maximum wind speed, the radius of maximum wind (r_{max}) and the size are determined at the 900 mb level. Due to the model resolution (45 km), the r_{max} (135 km) is slightly larger than the 100 km values in the barotropic studies of Chan and Williams (1987) and Fiorino and Elsberry (1989). The size of the weak (intense) vortex is smaller (larger) than that of the basic vortex (300 km) used by Fiorino and Elsberry (1989), and would be classified as a smaller (medium) size tropical cyclone according to the study of Merrill (1984). Merrill used the average radius of the outer closed isobar to define the size of the western North Pacific tropical cyclones between 1961-1969. He found the average cyclone size was about 4.4° lat. with a standard deviation of 2.0°, and more than 15% of the tropical cyclones had a size smaller or equal to 2.0°. Therefore, the weak and intense vortices used in the study are similar to the small tropical storm and the medium typhoon, respectively, as defined by Elsberry (1987).

The initial procedure to start a simulation is to superpose a spun-up vortex on a background flow. The details about the model and the starting procedure are given in Chapter III.

In this sensitivity study, the intensity of the spun-up vortex, the starting location of the vortex, and the zonal speed of the background flow will be varied. A code convention of four characters has been designed to identify each simulation. The first character of the code indicates the intensity of the spun-up vortex, where W and I represent the weak and intense vortices, respectively. The second and third characters of the code indicate the starting location of the spun-up vortex when the mountain barrier is included, where nN (nS) represents an initial vortex position n grid intervals to the north (south) of the central plane of the barrier. When the mountain barrier is not included (ocean-control), OC are the second and third characters. The fourth character indicates the zonal flow speed, where s is for a slower (2.5 m/s) zonal flow, f is for a faster (10 m/s) zonal flow. The fourth character is omitted if the simulation is with the standard zonal flow equal to 5 m/s.

a. Barrier-control

As indicated in Fig. 4.3a, the average along-track speed of the westward-moving typhoons upstream of Taiwan is about 5 m/s. Therefore, the background flow for the standard simulation will be a 5 m/s zonal flow that will initially be perpendicular to an idealized, north-south mountain barrier that is similar to Taiwan island. The deep-layer mean streamlines in the simulation with the standard 5 m/s

background flow and no vortex are displayed in Fig. 4.9. The deep-layer mean (V_{mean}) is calculated directly on sigma coordinates as

$$V_{mean} = \frac{1}{\sigma_2 - \sigma_1} \int_{\sigma_1}^{\sigma_2} V(\sigma)\ d\sigma \qquad (4.1)$$

where $V(\sigma)$ is the velocity at level σ and the integration interval (σ_1, σ_2) is from sigma level 0.4 to the surface. This vertical average may be interpreted as the deep-layer mean through the low and middle troposphere.

The near-surface disturbances generated in the lee of the barrier (e.g., Smolarkiewicz and Rotunno 1989) are not clearly shown in the deep-layer streamlines in Fig. 4.9 because these leeside disturbances are limited to the lower layers. Significant flow deflections are found on the upstream of the barrier in the deep-layer mean, especially near or over the island. To the north of the center-plane through the barrier, the flow deflections are to the north. Conversely, the flow to the south of the center-plane is deflected to the south. Notice that the deflections are not symmetrical even through the flow is on an f-plane. The deep-layer mean flow is a little stronger around the northern barrier. Near the surface (not shown), a larger fraction of the upstream flow is deflected southward to pass around the southern barrier than to the north, which is similar to Sun et al. (1991). They found an anticyclonic circulation (or ridge) is produced at the surface level over the mountain barrier when the Coriolis force is included in the simulation.

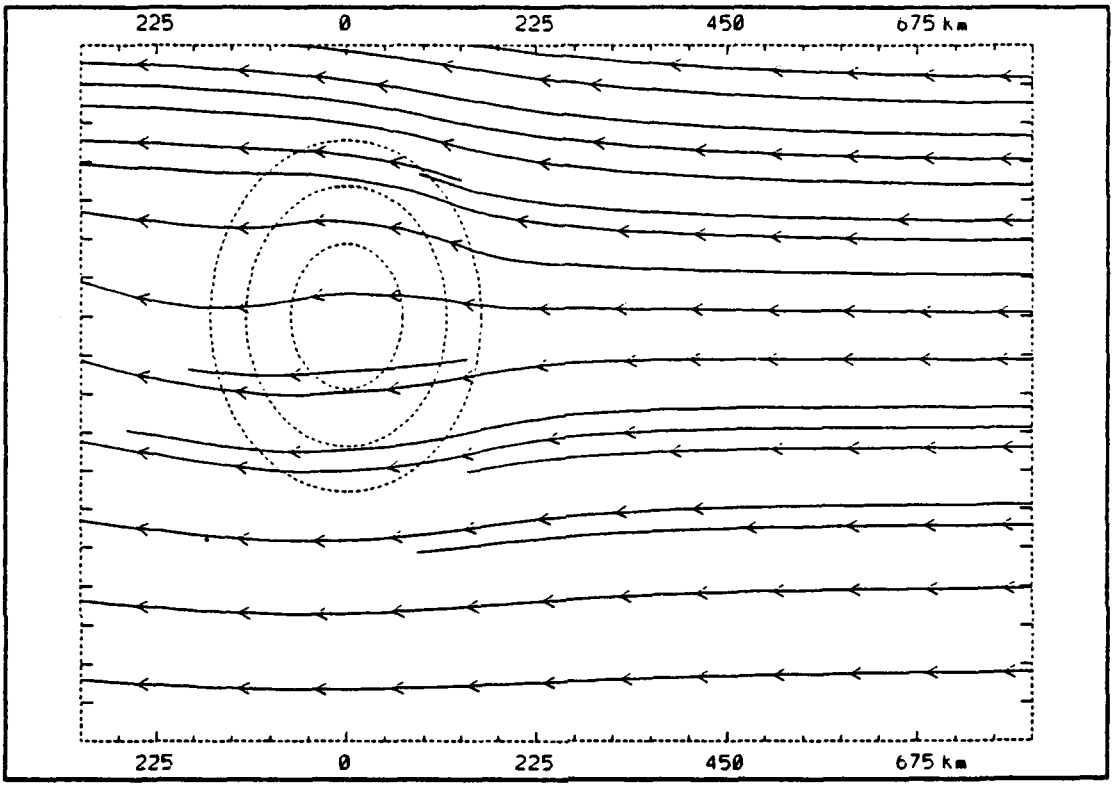

Fig. 4.9 Deep-layer mean (see text) streamlines after 48 h in the simulation of a 5 m/s easterly zonal flow encountering the mountain barrier (dashed lines indicate terrain boundary and altitudes of 1,000 m and 2,000 m). The grid intervals are equal to the model resolution (45 km), with east-west distances (km) relative to the mountain center. The domain shown (26 X 19 grid points) only covers a portion of the model domain (71 X 51 grid points) near the mountain barrier.

If the tropical cyclone moved with the deep-layer mean flow (as a 'cork in the stream'), the track would follow the streamlines in Fig. 4.9. That is, a cyclone would tend to be deflected northward (southward) around the barrier. Track deviations from this barrier-control steering simulation will be explored below.

b. Ocean-control

The second control simulation is the superposition of the vortex on the 5 m/s basic current without a barrier being present. The tracks and the time variations of the minimum sea surface pressures of the simulation with the weak vortex in a 5 m/s environmental flow and only open ocean (WOC) are shown in Fig. 4.10. Because the spun-up vortex is a near-equilibrium vortex solution from a prior model simulation, the minimum pressure of the spun-up vortex maintains about the same level (1003 mb) throughout the simulation.

Rather large amplitudes of track fluctuations in the early period of the simulation are shown in Fig. 4.10, which indicates an adjustment process is taking place after the spun-up vortex has been superposed into a new environment. Throughout the simulation, the two low-level centers (700 mb and surface) are very close to each other. However, the 500 mb center is slightly to the south of the low-level centers. Even through this solution is on a f-plane, the low-level centers move slightly faster and to the north of the mean flow as in beta-plane solutions (e.g., Elsberry 1987). At 60 h, the center is located about 70 km to the north and 45 km to the west of the location due only to the imposed zonal flow. If the first 15 h is considered to be the adjustment period, then the averaged northward (westward) speed is 0.6 (5.2) m/s for a 45 h period.

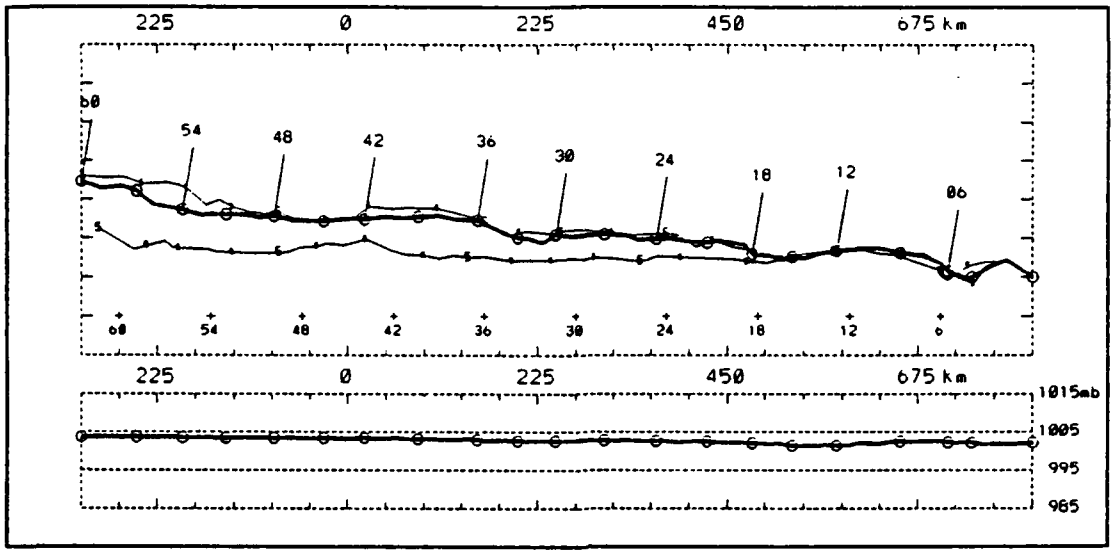

Fig. 4.10 Track (top panel, from right to left) and minimum sea-level pressure (bottom, mb) for the weak-vortex, ocean-control simulation (WOC). Three-hourly positions of the height centers at 500 mb and 700 mb and the sea-level pressure centers are shown with lines connecting '5', circles and 's', respectively. The 700 mb center locations are also labeled in 6-h intervals. The cross (+) signs with number (in h) indicate the center positions if the vortex was being advected by the zonal flow. The abscissa is labeled as in Fig. 4.9 even though no mountain barrier is included.

Since the simulation is on a constant f-plane, these northward and westward accelerations are clearly not due to the beta-effect (Chan and Williams 1987; Fiorino and Elsberry 1989). In the barotropic model without horizontal wind shear, diabatic and friction effects, the vortex would be simply advected along with the background flow. Thus, these departures must be due to the combination of diabatic and friction effects that cause asymmetric circulations and propagation relative to the mean flow. For example, the frictional effects in the planetary boundary layer may promote an asymmetric distribution of low-level convergence, which would lead to clouds in the parameterization scheme, and thus an asymmetric heating distribution. At the end of the simulation, the 500 mb center is located about 80 km to the south and slightly behind the lower-level centers. This result indicates the upper-level center has less northward and westward acceleration than the lower-level circulation.

After the 15-h adjustment period, small track oscillations with a period of about 12 h continue (Fig. 4.10). This phenomenon is better shown in the simulation of an intense, slow-moving vortex (IOCs, Fig. 4.40). These short-time scale track oscillations appear to be related to the asymmetric latent heating effects, and will be discussed in Section F.

In summary, the vortex motion is different from the steering flow in which it is embedded due to the inclusion of friction and diabatic effects. To isolate the mountain effects on the vortex motion, these faster and rightward track deviations in the ocean-control must be subtracted from the cases including the mountain barrier. The 'barrier-induced deflections' (or simply track deflections) will be defined as the track

difference between the case result and its corresponding ocean-control. Part of this track deflection may be due to the change of steering flow (zonal flow is deflected by the mountain barrier, e.g., Fig. 4.9). By a linear assumption, that portion of the track deflection that is not associated with the steering effect (e.g., Fig. 4.9) must be produced by the vortex-barrier interaction. The term 'vortex-barrier deflection' will be used to describe this part of the track deflection.

2. Vortex Tracks under the Influence of a Mountain Barrier

The mountain barrier is now inserted 810 km downstream of the vortex initial position. A group of simulations that start the vortex at different north-south distances from the center-plane is performed. To simulate the track behavior of a typhoon approaching the northern or southern mountain barrier, the initial vortex positions will be varied from 180 km to the north of center-plane (code named W4N) to 360 km to the south of the center-plane (W8S). For example, the track of the vortex started 45 km to the south (W1S) is examined in detail in Fig. 4.11. In the figure and all subsequent discussions, the vortex center will refer to the 700 mb height center unless otherwise specified. Similar to the simulations of Bender et al., significant northward deflections and an increased westward speed are found in the W1S case as the vortex approaches the barrier from the east. The largest displacement at 45 h is about 100 km to the north relative to the ocean-control when the vortex center is about to pass the long-axis of the barrier. After the vortex passes over the long-axis of barrier, southward deflections and decelerations are found. At the end of the simulation (60 h), the center is located only about 10 km north of the ocean-control.

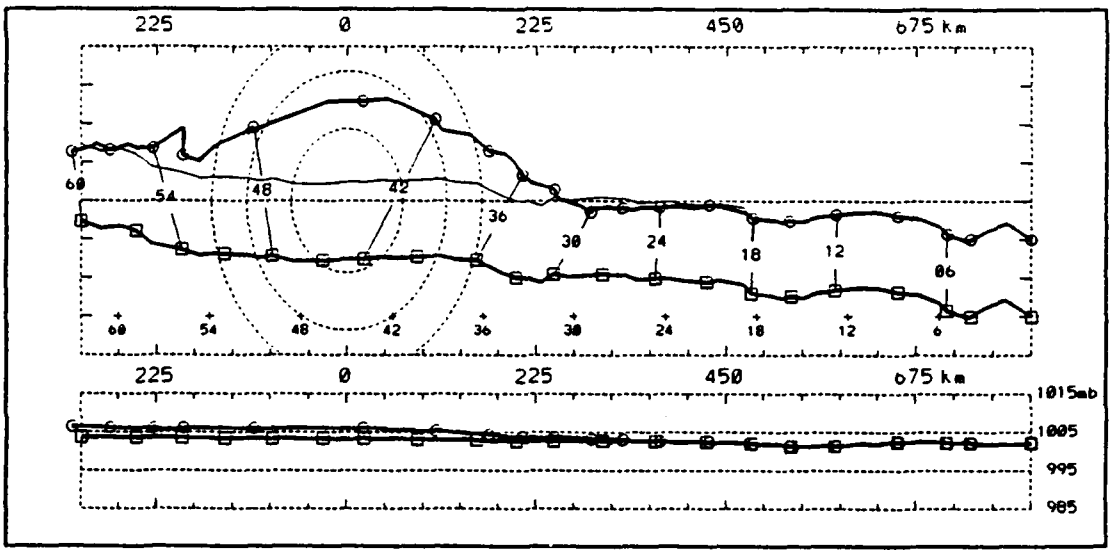

Fig. 4.11 Tracks (top panel) and the minimum sea-level pressures (bottom as in Fig. 4.10) for simulation W1S (line with circles) and the ocean-control simulation WOC (line with boxes, shifted in north-south direction, in light solid line for the same initial position as W1S). The dashed lines indicating the mountain barrier are as in Fig. 4.9, and the barrier center-plane (dashed line in east-west direction passing through the mountain center) is also plotted.

Bender et al. explained the northward deflection and acceleration of the typhoon upstream of the barrier as being due to the topographical effect that changes the basic flow that advects the typhoon. However, significant differences between the velocity of the background flow and the movement of the vortex existed. As shown in Fig. 9 of Bender et al., the typhoon moved with a speed about twice as fast (about 12 m/s) as the mean flow (6 m/s) near the time of landfall. Chang (1982) simulated a similar cyclonic path, but the displacements were smaller in his coarse resolution (60 km) model that also included a larger scale mountain barrier than in Bender et al. Chang proposed that an increased cyclonic circulation around the mountain barrier may cause the cyclonic deflection of the storm track. However, a detailed examination of how this circulation change could affect the typhoon motion has not been given.

Other effects besides the advection may be contributing to the vortex motion. Well upstream of the region in which the vortex has been deflected to the north, both Fig. 4.11 and the simulations of Bender et al. (their Fig. 6 and Fig. 10) show the vortex is located slightly to the south and to the east of ocean-control. This southward displacement and deceleration of the vortex motion well upstream of the barrier has not been discussed previously by Bender et al. As this phenomenon persisted for more than nine hours, it is not likely to be a small error arising from computational problems.

Tracks from other simulations (Fig. 4.12) also indicate these systematic southward displacements for vortices approaching the southern portion of the island. All six simulations are started with the same procedure, same weak spun-up vortex, same 5 m/s background flow and same initial distance (810 km) to the east of the mountain

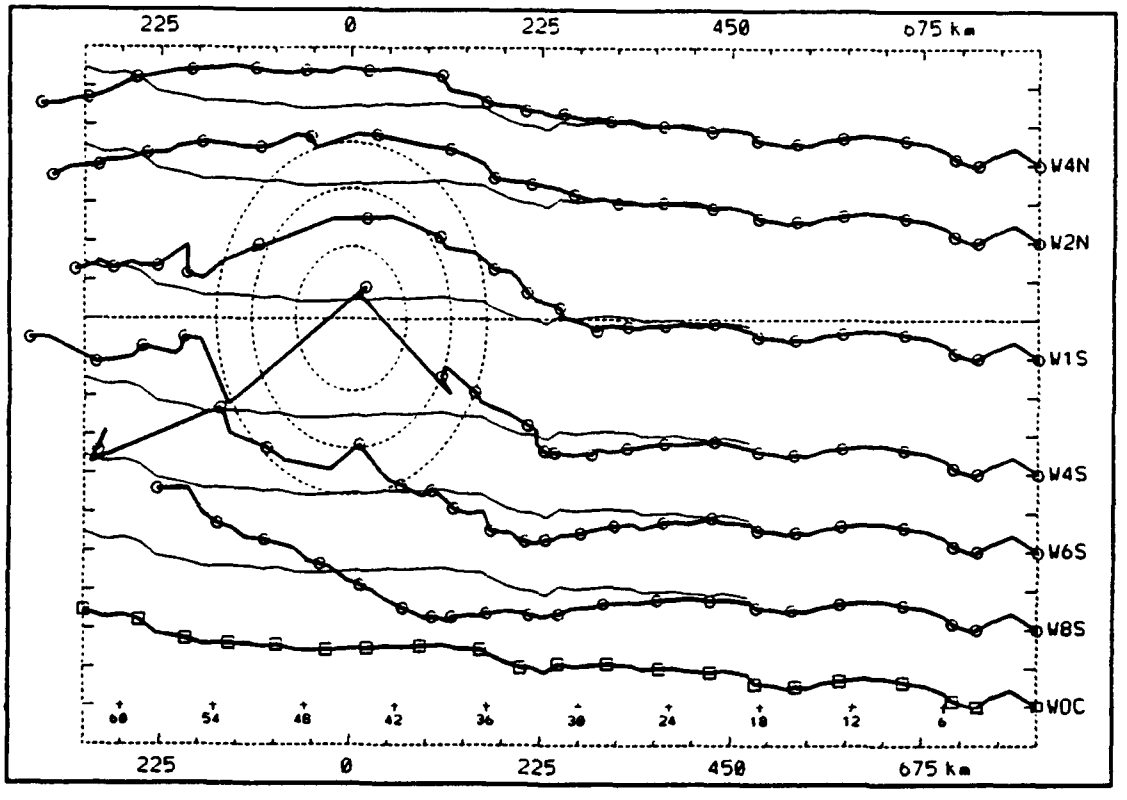

Fig. 4.12 Tracks as in Fig. 4.11 of six simulations (lines with circles each 3 h) and the ocean-control (line with boxes at bottom and also thin lines shifted to initial positions) of the weak vortex in 5 m/s easterly zonal flow. The code (see text) of each simulation is indicated on the right side of their initial location.

barrier center. The only differences are in the initial distance from the center-plane. From north to south, the vortices have been displaced four grid intervals to the north (W4N), two grid intervals to the north (W2N), one grid interval to the south (W1S), etc. from the center-plane. The track of ocean-control (WOC) has been superposed in seven locations for easy reference.

As the vortices approach different portions of the mountain barrier from the east, different track deflections (compared to the ocean-control) are found. Similar to W1S, the other two northern vortices (W4N and W2N) turn cyclonically as they move close to the barrier. Vortex W2N initially approaches the northern island where the terrain is relatively low (less than 1,000 m). Due to the smaller northward movement than vortex W1S, the center passes the northern coast without a landfall. Vortex W4N starts farther north of the barrier center-plane so that a path along the ocean-control will not directly pass over the island. Nevertheless, the terrain still has an influence on the vortex motion. The center of W4N is deflected to the north, but the displacements are smaller compared to W2N. Southward displacements far upstream are not found for vortices W2N and W4N as in W1S. However, decelerations in the zonal component are found when these northern vortices are still far upstream of the island. The westward speeds only increase after the vortices turn to the north. These speed changes become larger as the vortices are closer to the barrier center-plane. At the end of the simulation, the center of W1S is behind the other two northern vortices.

The other three vortices that approach the southern portion of the island also have systematic track deflections. As in W1S, all of them have southward displacements

starting about 400 km upstream of the mountain barrier. These southward displacements persist longer for the more southern vortices. For example, the southward motion in W8S lasts about one day, from about 18 h to about 42 h. During this 24-h period, the center moves about 60 km to the south of the ocean-control. However, these southward motions do not continue as expected from the deep-layer mean steering flow (Fig. 4.9). Rather, all of the southern vortices are deflected to the north beginning about 150 km upstream of the coastline.

Similar track deflections are observed in Fig. 4.6c, which shows the average cross-track deflections of 19 storms landing south of 23 °N. The southern storms are first deflected southward about 48 h prior to landfall, but then turn back toward the island 24 h prior to landfall.

Notice that the center of W8S continues to move toward the north in a rather smooth path around the southern end of the barrier (Fig. 4.12). However, large fluctuations in the center positions for W4S and W6S are found after the landfall. These fluctuations when the vortex is over or near the mountain barrier are due to other effects besides the advection, and will be discussed separately later.

Decelerations in the westward translation speed also are found in Fig. 4.12 as the southern vortices are far upstream of the island. The westward speeds start to accelerate only when the vortices are very close to the island. For W8S, the very long period of deceleration upstream of the barrier results in the center being significantly behind the ocean-control at the end of the simulation. By contrast, the center of W4S is about 70 km to the west of the ocean-control at 60 h. The track of W6S is very

irregular at 60 h as adjustment processes are still occurring after the vortex has moved to the southwest of the island. More studies are required to explain this irregular track.

In summary, this group of simulations provides a more complete view of how the storm tracks are influenced by the mountain barrier. Distinct differences are found as each vortex approaches a different portion of the mountain barrier. These different track behaviors may be a reason (large-scale flow changes are another) for the large deviations in the storm speeds and cross-track displacements in the observations (Fig. 4.3a and Fig. 4.6). In general, the vortices approaching the northern island experienced northward deflections, and the vortices approaching the southern island first experienced southward deflections and then moved toward the north. Similar track deflections appear in the observations (Fig. 4.6). Although the northern storms (Fig. 4.6a) are first deflected northward beginning about 48 h prior to landfall, the cross-track deflections decrease (beginning about 24 h prior to landfall) toward zero prior to striking Taiwan. Similarly, the southern storms (Fig. 4.6c) are first deflected southward but then turn back toward the island prior to landfall. The physical processes involved in these track deflections are to be examined in the following sections.

From the forecaster's point of view, it is important to know when the southward-deflected storm will turn back to the north. The observations in Fig. 4.6c suggest the average maximum southward displacement of the center occurs about 24 h before landfall. These model simulations with idealized terrain, zonal flow equal to 5 m/s and simplified vortex structure, suggest the maximum southward displacement is

about 12 h before landfall. How this timing may vary due to the intensity and the translation speed of the vortex will be examined with more simulations later.

C. UPSTREAM TRACK DEFLECTIONS

As mentioned above, Bender et al. (1987) suggested the northward deflection and the acceleration of the typhoon when it approaches a mountain barrier may be explained by the topographical effect on the environmental flow that advects the typhoon. In their study, the steering flow was selected from a particular layer. Many studies (see Elsberry 1987) have found that a deep-layer mean is best related to the typhoon motion. Therefore, a deep-layer mean as defined by equation (4.1) will be used to examine whether the vortex motion under the influence of a mountain barrier can be explained in terms of the mean steering flow modifications.

The deviations (or barrier-modified mean steering flow) from the 5 m/s zonal flow due to the inclusion of the mountain barrier (barrier-control simulation in Fig. 4.9) is shown in Fig. 4.13. In general, the mean easterly flow (Fig. 4.13a) is reduced over the mountain and increased to the north and to the south. The maximum decelerations exceeding 3 m/s occur west of the island where the return flow in the low-level leeside vortices is found. Upstream of the barrier, the mean zonal flow decelerations are mainly limited to a zone with a north-south length that is about equal to the width of the mountain. An area with more than 0.4 m/s deceleration (which would cause a reduction of about 35 km in vortex motion per day) extends to about 200 km east of the east coast. Beyond 400 km from the east coast, the deceleration is less than 0.2 m/s. The areas of

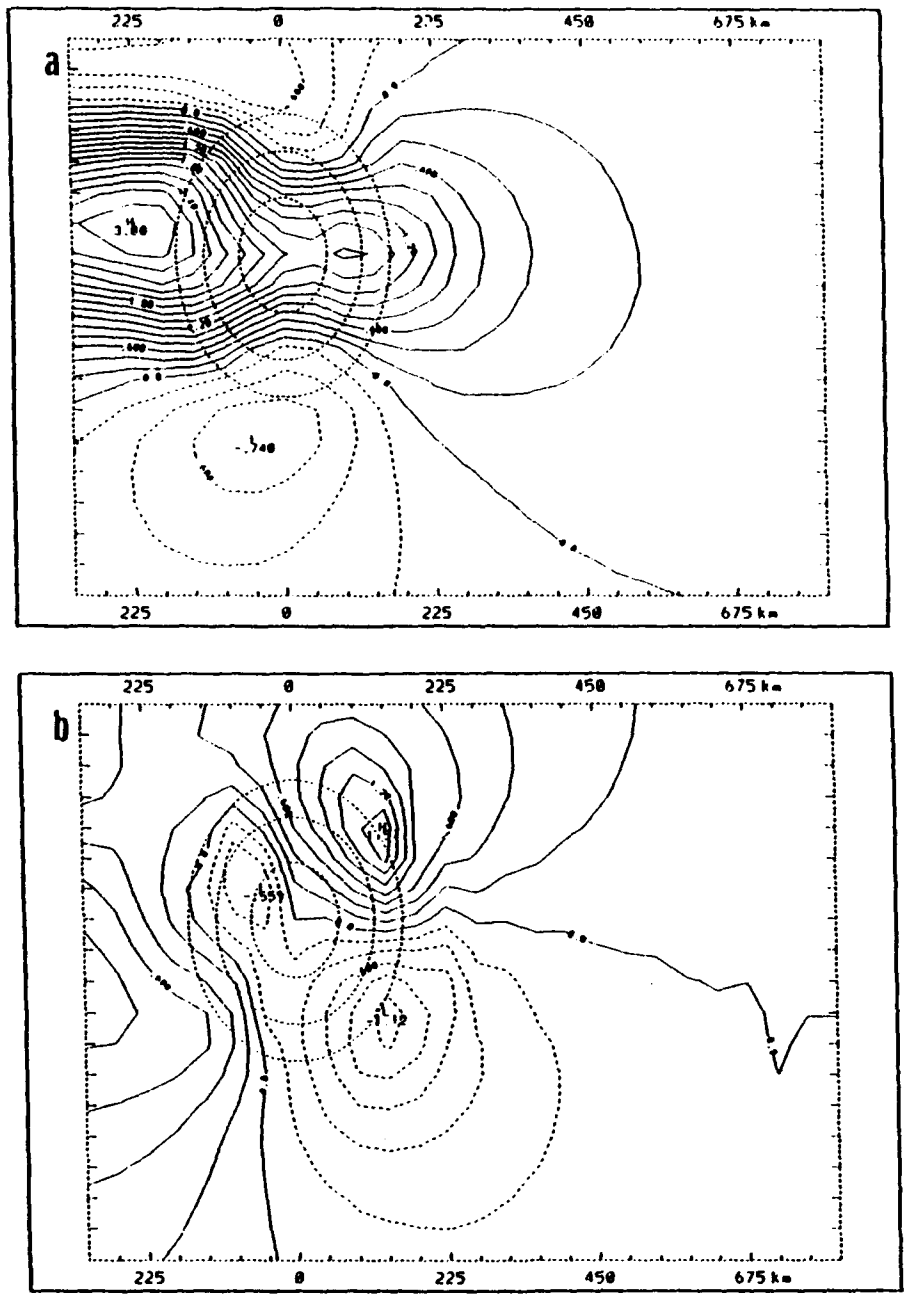

Fig. 4.13 Deviations (contour interval, 0.2 m/s) of the deep-layer mean flow of simulation with mountain included (Fig. 4.9) from the 5 m/s easterly zonal flow. A positive (solid line) value for the east-west (u-) component in (a) indicates the easterly flow has been slowed down by the mountain, and for the north-south (v-) component in (b) indicates a northward deflection relative to the mean flow. The map background is similar to Fig. 4.9, except on a different scale.

easterly acceleration extend from the island tips to the nearby ocean. A maximum of 0.75 m/s is located about 50 km to the south of the south coast. As found in previous simulations (e.g., Sun et al. 1991), the Coriolis effect causes the flow patterns to not be symmetric with respect to the barrier center-plane.

The large north-south (v-) deviations (Fig. 4.13b) on the west side of the island are associated with the shedding of the lee vortices. Because of the highly time-dependent nature of these vortices, the pattern may be different at other times. Upstream of the island, which is the focus of this study, the flow pattern is relatively steady. East of the mountain, the zero contour line is generally very close to the barrier center-plane. North (south) of the center-plane, the flows are deflected around the barrier with maximum deviations on the coast. Notice that the maximum flow deflections of 1.6 m/s northward and 1.1 m/s southward are not equal due to the Coriolis effect. The area in which the southward flow deflections are more than 0.4 m/s is within 200 km from the coast. The area with northward deflections is slightly larger and extends farther to the north.

If the north-south track deflections are to be explained by this barrier-modified mean steering flow, significant northward (southward) deflections of the vortex tracks should be found within a distance 200 km from the coast. The vortex translation velocity is computed as the mean of velocities calculated in 2-h, 4-h and 6-h intervals by central difference. Even in the case of the ocean-control with a constant background flow, the vortex center does not move with a constant speed (Fig. 4.10). The average $u(v)$-component speed of the WOC simulation during 18 h to 57 h is -5.2 (0.6) m/s with a standard deviation of 0.5 (0.7) m/s.

Prior to 18 h, all of the vortices shown in Fig. 4.12 have a similar track as the ocean-control, even though a mountain barrier is included in the downstream. After 18 h, the distance between the center from the ocean-control and the center from a simulation with the mountain included may exceed 100 km. Because the translation speeds in the ocean-control are not constant, and the vortex centers may be displaced from that of the ocean-control, the computation of the vortex deflections due to the inclusion of the mountain barrier becomes a little complicated. If a constant velocity is subtracted, the short time-scale variations (especially in the early period of the simulations) may be incorrectly interpreted as mountain effects. If the difference between the vortex translation velocity with mountain barrier included and that of the ocean-control is calculated at a given time, an error may be introduced because the two centers are not at the same location. In the following sections, the track deflection due to the inclusion of the mountain barrier is calculated as the difference between the translation velocities of the case and the corresponding ocean-control before 18 h. After 18 h, the mean translation velocity of the ocean-control (5.2 m/s westward and 0.6 m/s northward) is subtracted from the case translation velocity.

Differences between the track deflections for the six simulations and the barrier-modified mean steering flow (Fig. 4.13) are shown in Fig. 4.14. In Fig 4.14a, the vector differences are calculated hourly, and the results are shown as vectors originating at the vortex centers from 12 h to 56 h. These vectors indicate the direction and speed of the vortex motion deviations from the mean flow steering (vortex-barrier deflections). In regions where the vectors are small, the changes of vortex motion when

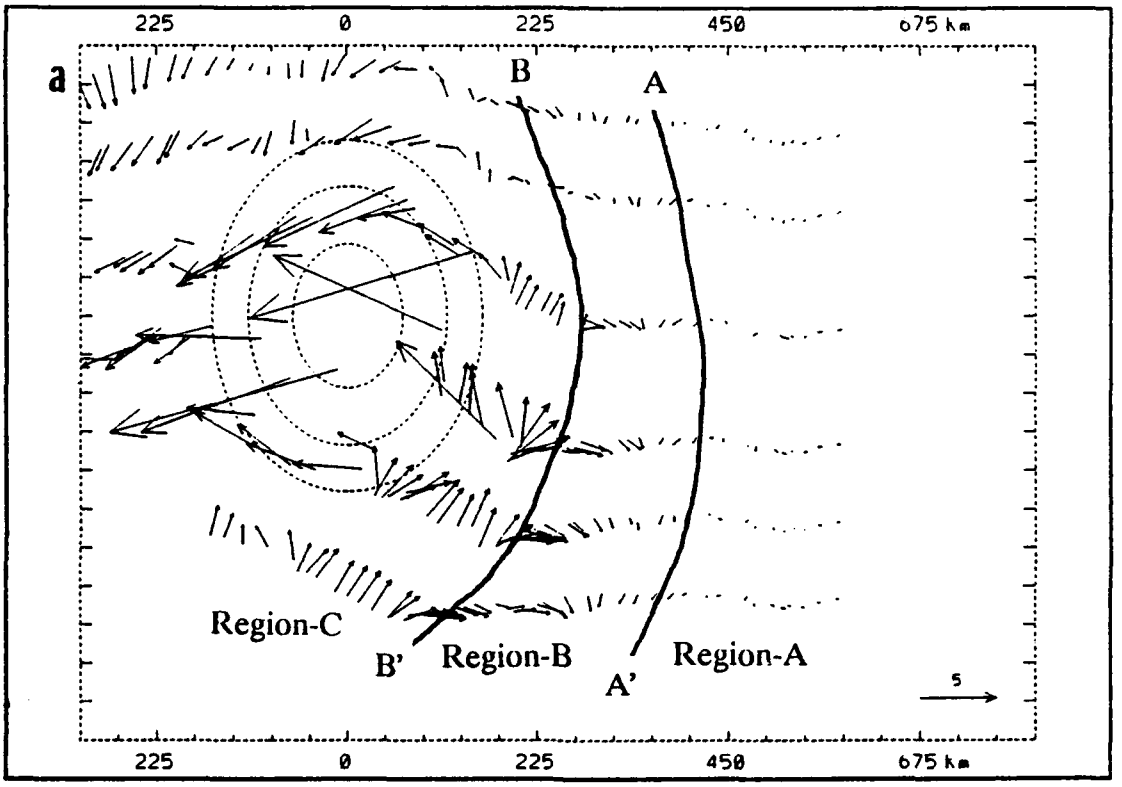

Fig. 4.14 Hourly vectors of the vortex-barrier deflections (see text) for the six simulations in Fig. 4.12 from 12 h to 57 h. Deflections are shown for (a) the total vectors originating from the position each hour; (b) east-west (u-) components; and (c) north-south (v-) components. Plots (b) and (c) are on a smaller scale and the values are given in 2-h intervals. The scale for the vectors in (a) is shown in the lower right corner of the figure. A positive value in (b) indicates the vortex moves slower than the mean steering flow, and in (c) indicates the vortex moves to the north of the mean steering flow. Lines AA' and BB' divide the domain into three regions (Region-A, Region-B and Region-C) discussed in the text.

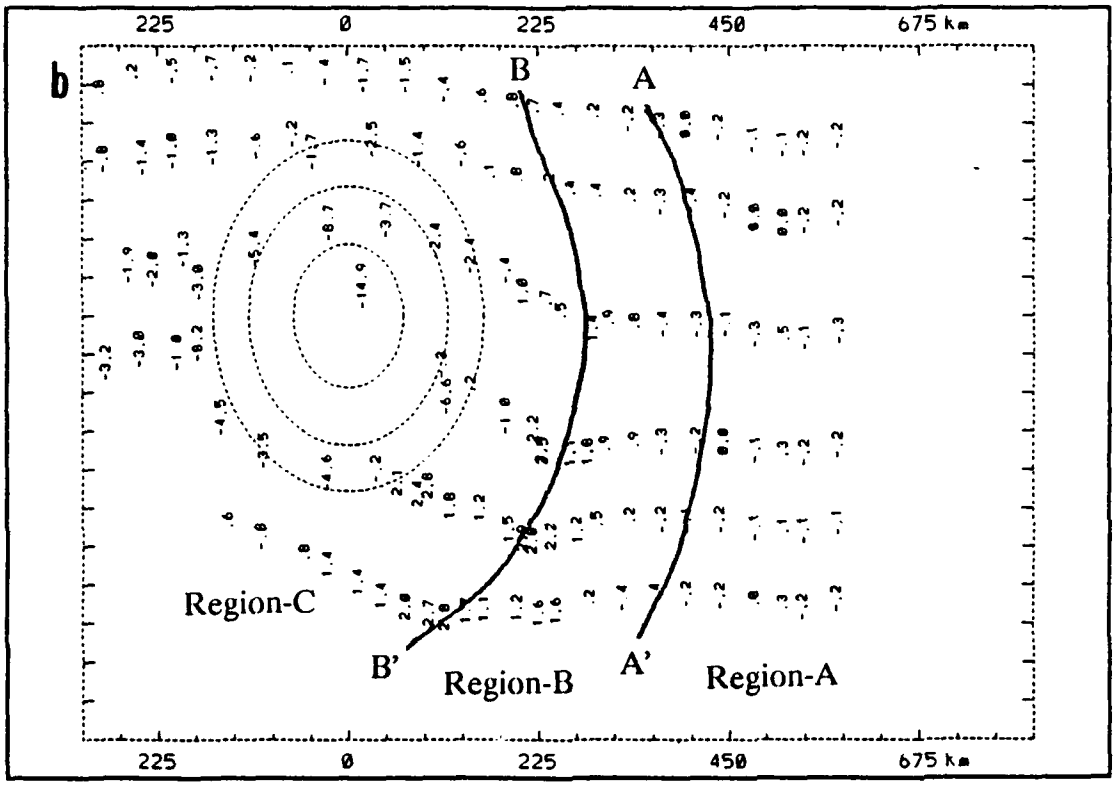

Fig. 4.14 (Continued)

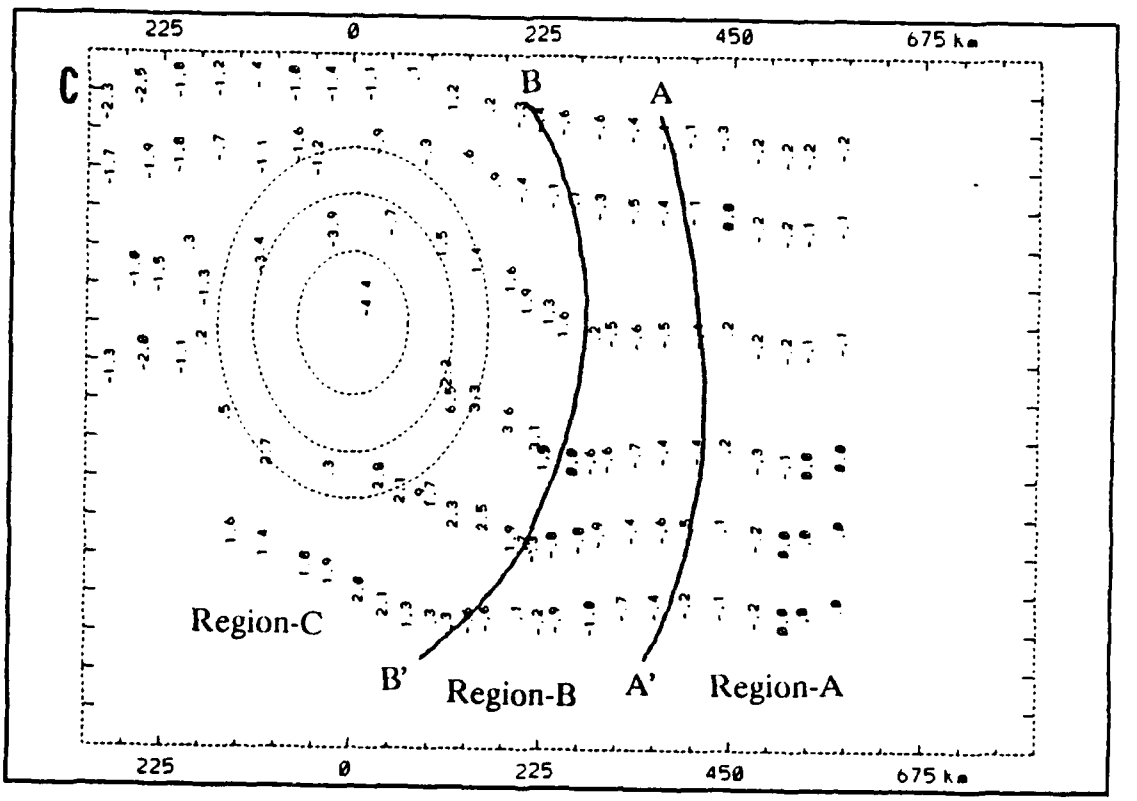

Fig. 4.14 (Continued)

the mountain barrier is included can be attributed to the barrier-modified mean steering flow. The *u*- and *v*- component speed differences (Figs. 4.14b and 4.14c, respectively) illustrate the magnitudes of the speed differences.

1. Region-A

Lines AA' and BB' in Fig. 4.14 separate the domain into three regions. To the east of line AA', the vortex-barrier deflections in both *u*- and *v*-components are relatively small. Although the values range from -0.3 m/s to 0.5 m/s, most of the magnitudes (absolute value) are close to or smaller than 0.2 m/s. Such a speed difference of 0.2 m/s would only produce a vortex displacement of 8.8 km in a 12-h period. If the signs are changing along the track within this period, then the position differences would be even smaller. In this region (Region-A), advection by the background steering flow is the dominant factor in the vortex motion.

2. Region-B

In Region-B between line AA' and line BB', the vortex-barrier deflections are generally larger than those in Region-A. The *u*-components in Fig. 4.14b are negative (positive) on the east (west) side of Region-B, which shows the vortices undergo a small westward acceleration (relative to the steering) before a larger deceleration. For the *v*-component motion (Fig. 4.14c), the vortices move toward the south with a magnitude of about 0.5 m/s relative to the steering flow. In the southern areas of Region-B, the southward speeds relative to the steering flow reach about 1.0 m/s. These deflections produced by the vortex-barrier interactions are as large as the deviations

associated with the mean steering flow in Region-B. In some of the southern areas, the former is larger than the latter. For example, the mean steering flow in W6S at 30 h is about 0.2 m/s slower than a zonal flow without the mountain barrier (Fig. 4.13a). The vortex-barrier deflections cause a easterly speed decrease of about 1.2 m/s. In v-component, the southward speed produced by the mean steering flow and the vortex-barrier interactions are 0.4 (Fig. 4.13b) and 0.8 m/s, respectively.

To investigate the physics involved in the cause of the vortex-barrier deflections, the deep-layer mean winds from simulation W6S at 24 h are displayed in Fig. 4.15. About 10 m/s easterly components are associated with the northeasterly winds along the east coast. Therefore, the speeds at the outer edge of the vortex circulation just reaching the mountain barrier are about the same magnitude as the background flow. Interactions of these vortex-related winds with the orography may enhance the barrier effect and may produce a significant influence on the vortex motion.

To test this hypothesis, the barrier-modified mean steering flow at 48 h for a simulation with a 10 m/s easterly zonal flow is calculated (Fig. 4.16a and b). The differences of the barrier-modified mean steering flows between the simulation with a 10 m/s easterly zonal flow (Fig. 4.16a and 4.16b) and the simulation with a 5 m/s easterly zonal flow (Fig. 4.13) are shown in Fig. 4.16c (u-component) and Fig. 4.16d (v-component). To the east of the barrier, the easterlies are slowed more and the southward motions are stronger with a 10 m/s easterly zonal flow than with a 5 m/s easterly zonal flow. The differences are not symmetric to the barrier center-plane, with larger southward (eastward) changes near the southern (northern) regions of the barrier.

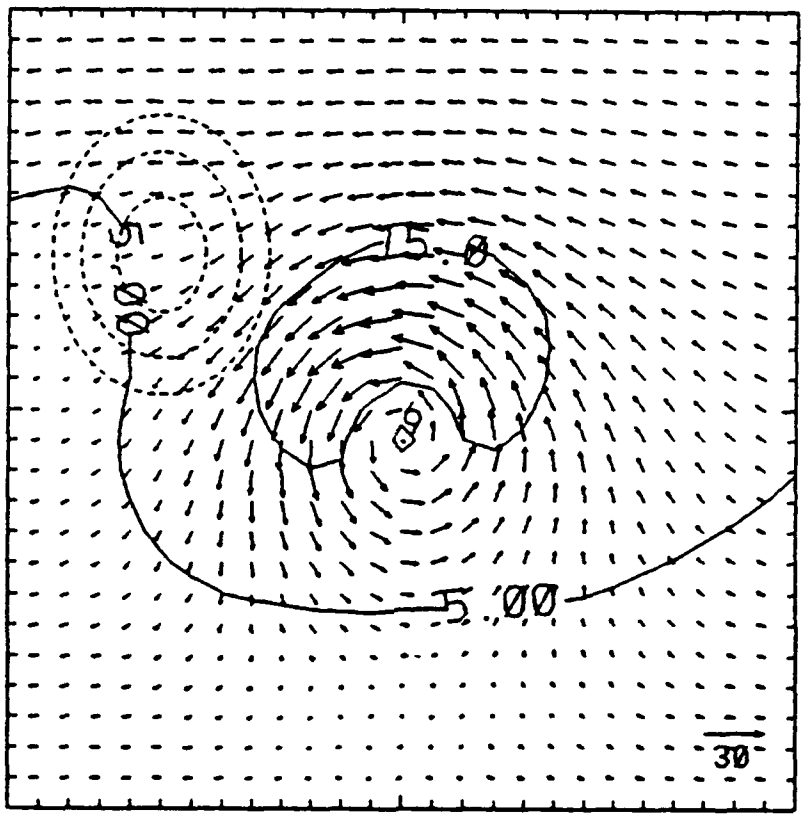

Fig. 4.15 Deep-layer mean winds of simulation W6S at 24 h with scale in the lower right corner. The contour lines indicate the isotachs in 10 m/s intervals. The typhoon symbol indicates the vortex center location. The grid distances are the same as the model resolution (45 km), and the domain shown (1,170 km square) only covers a portion of the model domain (3,600 X 2,250 km).

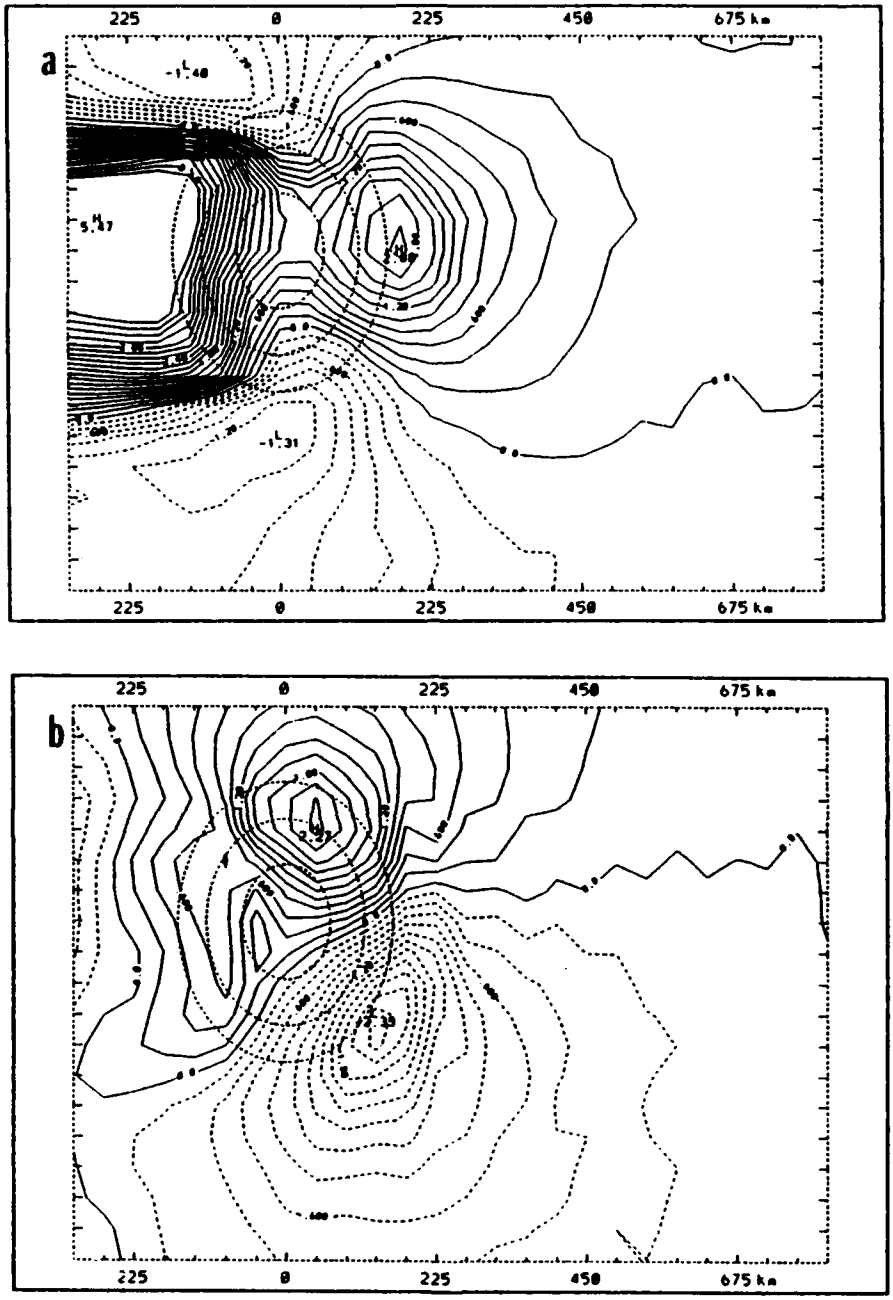

Fig. 4.16 (a) and (b) as in Fig. 4.13, except for the deviations of the deep-layer mean flow of simulation with mountain included in the 10 m/s easterly zonal flow. The additional zonal and meridional deflections of (a) and (b) compared to that for a 5 m/s zonal flow (Fig. 4.13) are in (c) and (d), respectively. The typhoon symbol in (c) and (d) is the center position of W6S at 24 h.

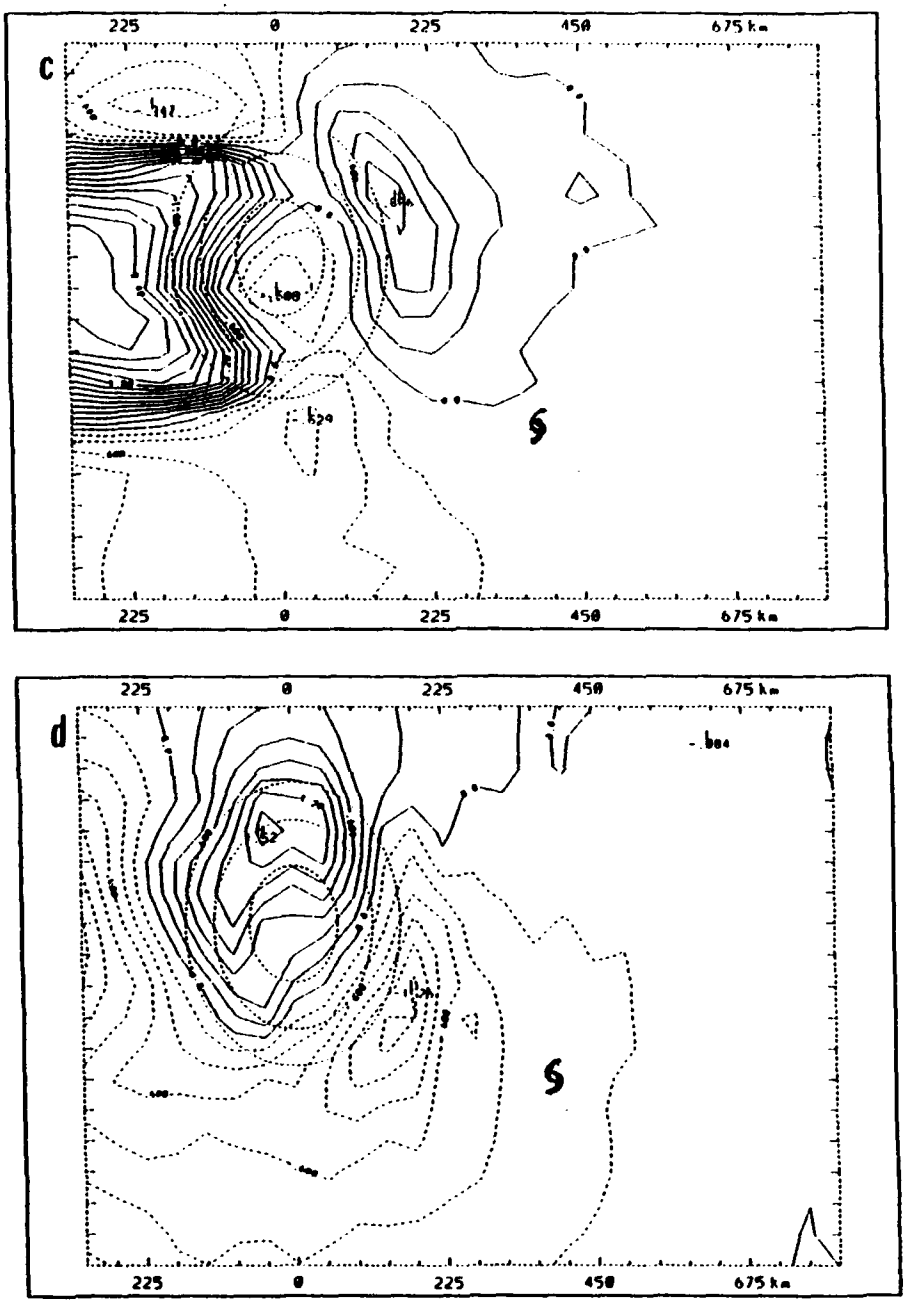

Fig. 4.16 (Continued)

The asymmetric response to the increase in the zonal flow is similar to the result by Sun et al. (1991). Their Figs. 3e and 5a show the northward deflections increase significantly near the northern barrier when they increased the zonal westerly from 5 m/s to 10 m/s. At the position of W6S at 24 h (indicated by a typhoon symbol in Fig. 4.16c and 4.16d), the eastward difference is close to 0.0 m/s and the southward speed difference is larger than 0.3 m/s, which is similar to the magnitudes in Fig. 4.14b and 4.14c that are calculated relative to the 5 m/s basic current. For example, the value at 24 (26) h in Fig. 4.14b and 4.14c are 0.2 (-0.2) m/s eastward and 0.6 (0.4) m/s southward, respectively. As the vortex moves closer to the barrier in Region-B, further deceleration and southward deflections are expected from Fig. 4.14b and 4.14c.

The above example suggests that an external forcing is produced in Region-B when the outer edge of the vortex circulation is encountering the mountain barrier, and the resulting track deflection is as large as that associated with the mean flow steering. This external forcing is interpreted as being generally similar to an enhanced zonal flow encountering a mountain barrier. On the upwind side of the mountain barrier, a pressure ridge is produced that decelerates and deflects the flow to pass around the barrier, and therefore changes the vortex motion. The ridge will be to the north and the west of the vortex center when the vortex is east of the mountain and not too far north from the barrier center-plane. Therefore, a southeastward forcing is produced to slow the westward motion and advect the vortex to the south. When the vortex is located to the east of the northern end of the mountain, the outer edge of the vortex circulation will have a direction about parallel to the long-axis of the mountain. As in Fig. 4.13, an

increase of flow speed and an outward motion from the center-plane will be found on both sides of the barrier. In this case of a northerly flow encountering the barrier, increases of northerly and westerly components on the east side of the barrier are expected. As in the situation when the vortex is located to the southeast of the island, a deceleration of the zonal speed and deflection of the vortex to the south is predicted.

3. Region-C

The separation of the blocking effect on vortex motion into one associated with the mean steering flow and an accentuated effect due to the superposition of the vortex circulation gradually becomes unsuitable as the vortex moves closer to the mountain. Near or inside the line BB', very large decelerations of the vortex westward motion are found (Fig. 4.14b). The v-component is no longer toward the south. Indeed, the vortex turns back toward the north (Fig. 4.14a), which increases the likelihood of a landfall. In this subsection, it will be shown that the interaction of the inner region storm circulation with the mountain barrier becomes so significant within the Region-C (inside the line BB') that the vortex motion is determined as a result of these interactions.

In the barotropic study of the beta-effect on vortex motion, Fiorino and Elsberry (1989) decomposed the vortex structure into the wave spectrum in the azimuthal direction. They found that the gradient of the Coriolis force induced an asymmetric wavenumber one circulation that produced a ventilation flow through the center that significantly affected the vortex motion. A similar idea is used here to investigate the vortex motion in Region-C, except the deep-layer mean wind field is decomposed into steering, symmetric (relative to the vortex center) and asymmetric components. The

steering component is assumed to be the zonal basic flow for ocean-control simulations. For simulations with the mountain included, the deep-layer mean basic flow such as in Fig. 4.9 is used so that this steering component includes the horizontal shear produced by the barrier effects.

The averaged asymmetric flow through the center will be treated as the 'ventilation flow'. Examples of the asymmetric wind of the weak vortex ocean-control simulation (WOC) at 18 h and 36 h are given in Fig. 4.17a and 4.17b, respectively. Although the total winds have a smooth cyclonic circulation with maximum speeds larger than 20 m/s around the center (Fig. 4.17 left panel), counter-rotating gyres are found in the asymmetric component. The magnitude of the asymmetric flow near the center is about 3.0 m/s, and the direction varies from southwest (18 h) to southeast (36 h). The cause of these gyres may be related to the asymmetric diabatic heating, as one of the heavy precipitation cells (Fig. 4.17a and b) is co-located with the wind cell. This phenomenon is better shown in a simulation including the intense vortex, which will be discussed in Section F.

To illustrate how the asymmetric circulation is related to the vortex motion, a radial band between 22.5 km (0.5 grid interval) to 180 km (4.0 grid intervals) is used for calculating the ventilation flow (averaged asymmetric wind) near the center. In the WOC simulation, the vortex is moving generally westward at 5 m/s with a speed deviation of about 1.0 m/s (Fig. 4.18). The steady cyclonic shift of the motion deviation direction, especially between 24 h to 48 h, indicates the center is looping cyclonically relative to the steering flow with a period of about 13 h. Throughout the period in Fig.

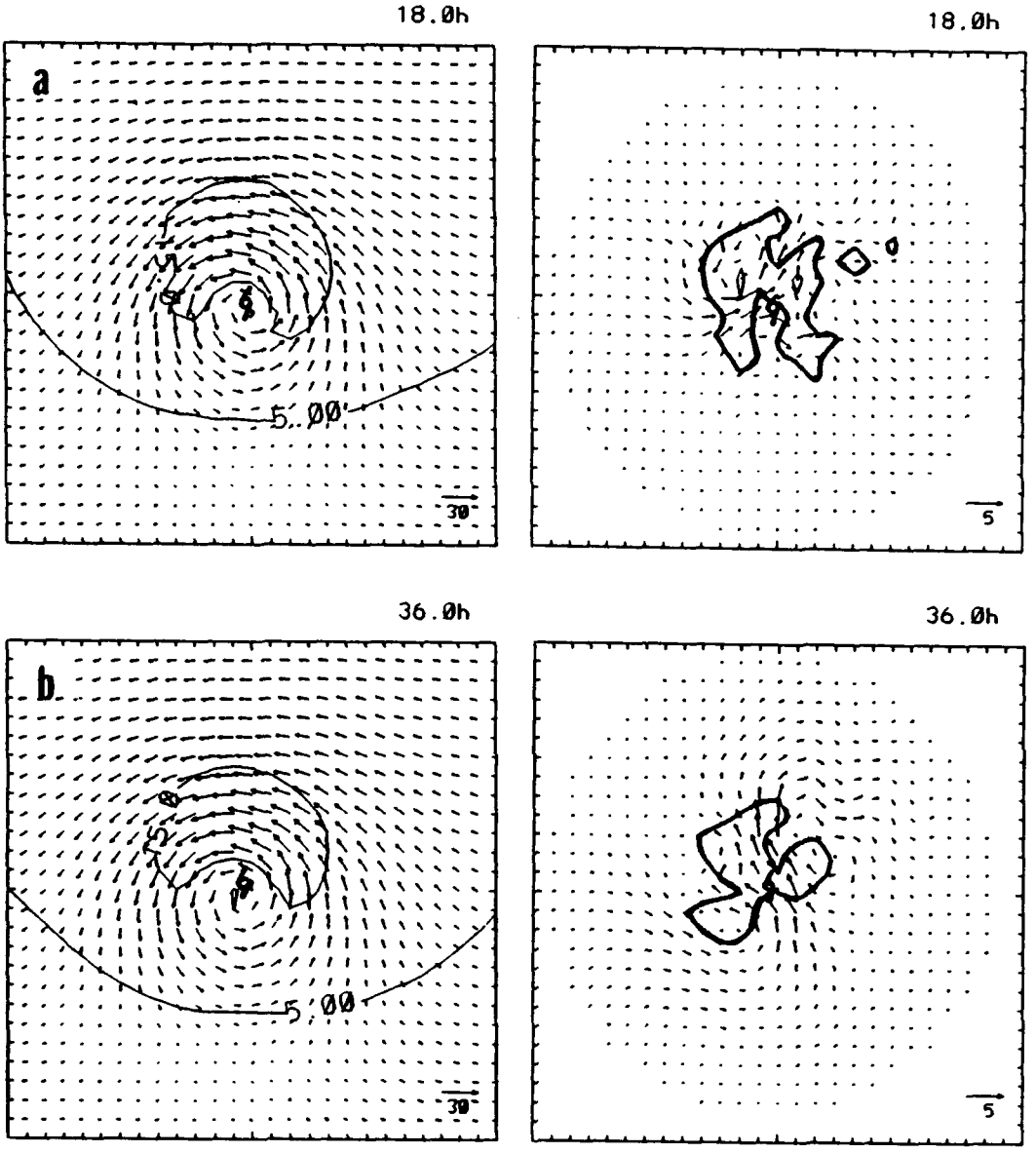

Fig. 4.17 The deep-layer mean wind vectors (left) and the asymmetric winds (right) from simulation WOC at (a) 18 h and (b) 36 h. Different wind vector scales (m/s, lower right corner) are used in the two panels, and the 5 m/s and 15 m/s isotachs of the total wind (covers 1,170 km square) are also shown. The asymmetric winds are calculated relative to the vortex center (shown in typhoon symbol) within a circle of radius equal to 12 grid intervals. Hourly accumulated precipitation contours (in 5 mm intervals beginning from 2 mm) are overlaid.

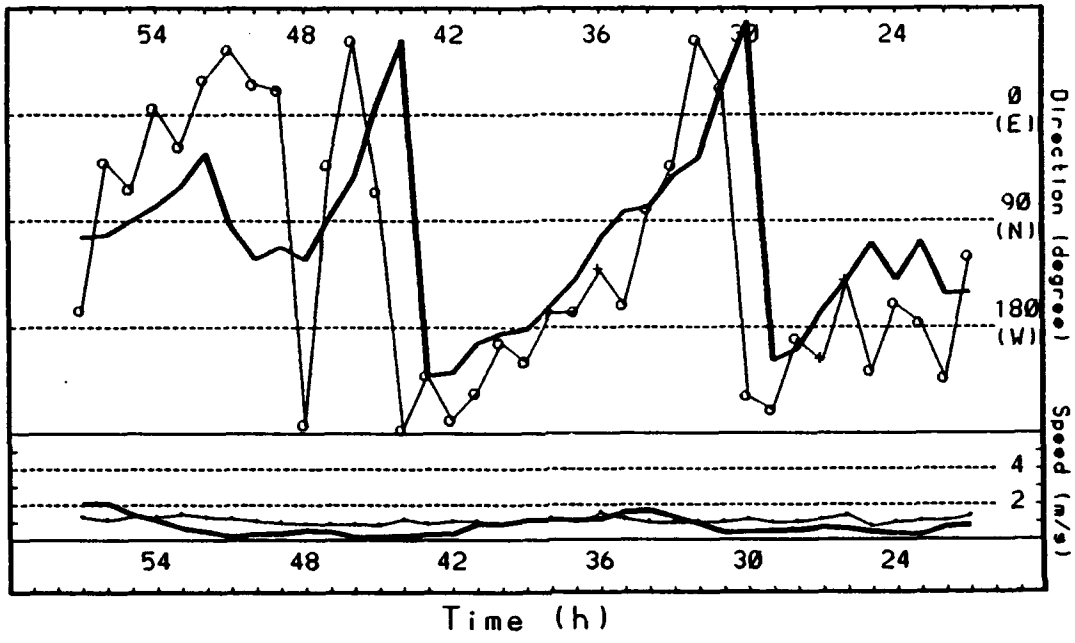

Fig. 4.18 Time variations (increasing time from right to left) of the ventilation flow and the vortex motion deviation (m/s) from the steering flow in simulation WOC. In the top panel, the ordinate is the asymmetric flow direction (thin solid) and vortex motion deviation (thick solid), with 0° defined as eastward, 90° as northward, 180° as westward and 270° as southward. Symbols (*, x, + and o) indicate different levels of consistency of the ventilation flow direction: Star (*) indicates there are less than 10 % of grid points (in the averaging circle band) that deviate by more than 22.5° from the ventilation flow direction; Symbol 'x' indicates the percentage is between 10 % and 30%; symbol '+' is for between 30 % and 50%; and symbol 'o' indicates the percentage is greater than 50 %. In the bottom panel, the thick solid line is the vortex translation speed deviation from the zonal easterly flow, and the thin line connecting dots is the asymmetric ventilation flow speed.

4.18, the ventilation flow direction consistency check is relatively low due to the existence of small-scale gyres near the center (e.g., Fig. 4.17). Nevertheless, the direction changes of the ventilation flow are highly correlated with the vortex motion deviations. The speed differences between the ventilation flow and the motion deviation are generally less than 1.0 m/s. Larger differences occur only in the final period of the simulation when the vertical separation of the centers (Fig. 4.10) is large. Consequently, the deep-layer mean fields with the symmetric vortex removed will be used to infer how the upstream deflections of the tropical cyclone occur when a mountain barrier is included.

The calculation of the ventilation flow is sensitive to the definition of the vortex center when the lower-level and upper-level centers are separated. The evolution of the ventilation flow calculated relative to the center defined by averaging the positions of the sea-level pressure center and 700 mb height center is given in Fig. 4.19. Including the surface center location slightly improves the estimation of the vortex motion direction and the direction consistency check. The ventilation flow magnitude changes also agree better with the vortex translation speed variations. Since the objective of this study is not to estimate the vortex motion in fine detail, further testing to determine which definition of the center (it may be the wind center) will result in a best estimation of the vortex motion has not been pursued. The center defined as the average position of the sea-level pressure center and 700 mb height center will be used in subsequent diagrams.

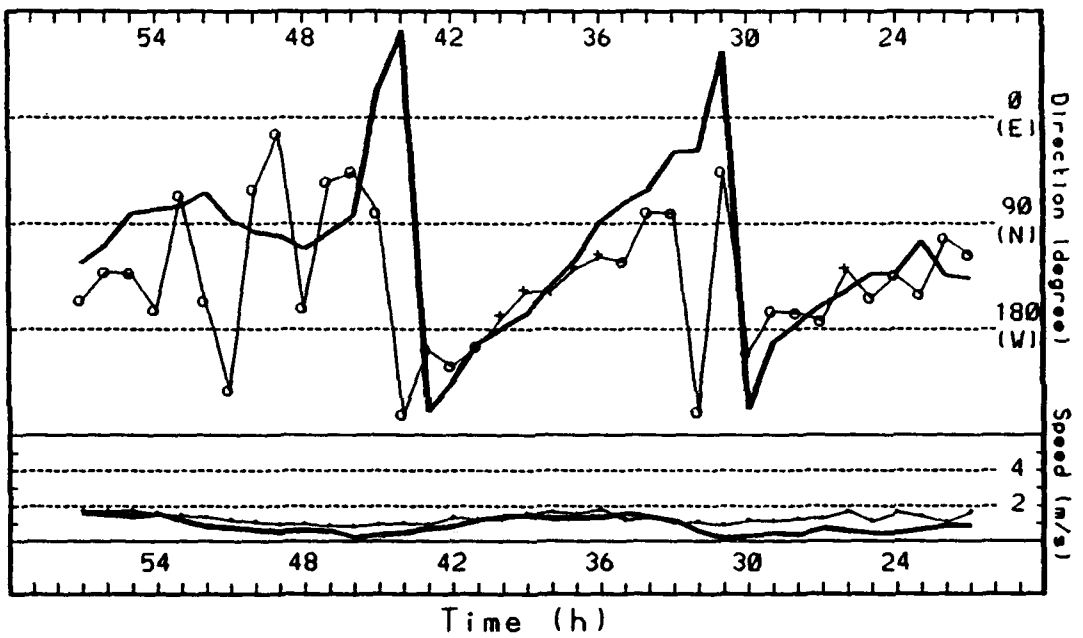

Fig. 4.19 As in Fig. 4.18, except the calculations of asymmetric winds and the vortex motion deviations are relative to an averaged position of the sea-level pressure center and the 700 mb height center.

The ventilation flow and the vortex motion deviation of the simulation with the weak vortex initially six grid points south of the center-plane (W6S) are shown in Fig. 4.20. By 36 h, the center is about to pass line BB' and enter Region-C. The calculation is ended when the center landfalls on the southeastern coast 12 h later because the vertical separation of the centers becomes so significant. When the center is still in Region-B at 24 h (Fig. 4.20), the vortex motion deviations have relatively large differences from the ventilation flow, and the wind direction consistency checks are also lower. However, the deviation of the vortex translation speed from the steering flow (bottom panel, Fig. 4.20) is relatively small, especially in the earlier periods around 24 h. This result is consistent with the earlier conclusion as the steering effect dominates the vortex motion far upstream of the barrier. The deviations from the steering flow then increase as the vortex moves closer to the barrier. The deviations exceed 2.5 m/s when the vortex is in Region-C, and the direction shifts from northeast (at 36 h) to north (at 48 h). Over this period, the ventilation flow is highly correlated with the vortex motion deviation from the steering flow. Along with this shift in the direction, an increased translation speed is indicated.

The deep-layer mean wind and the asymmetric component for W6S at 42 h is given in Fig. 4.21. When the averaged vortex center is about 50 km southwest of the island, a strong cyclonic (weak anticyclonic) asymmetric gyre is found on the west (east) side of the center. These gyres produce a strong northerly ventilation flow through the center. Since the heavy precipitation cell is to the south of the barrier and is not co-located with the asymmetric wind gyres, these gyres must be caused by different

AD-A261 819 EFFECTS OF TAIWAN OROGRAPHY ON THE MOTION AND STRUCTURE OF TYPHOONS(U) NAVAL POSTGRADUATE SCHOOL MONTEREY CA T C YEH DEC 92 XB-NPS 2/4

UNCLASSIFIED NL

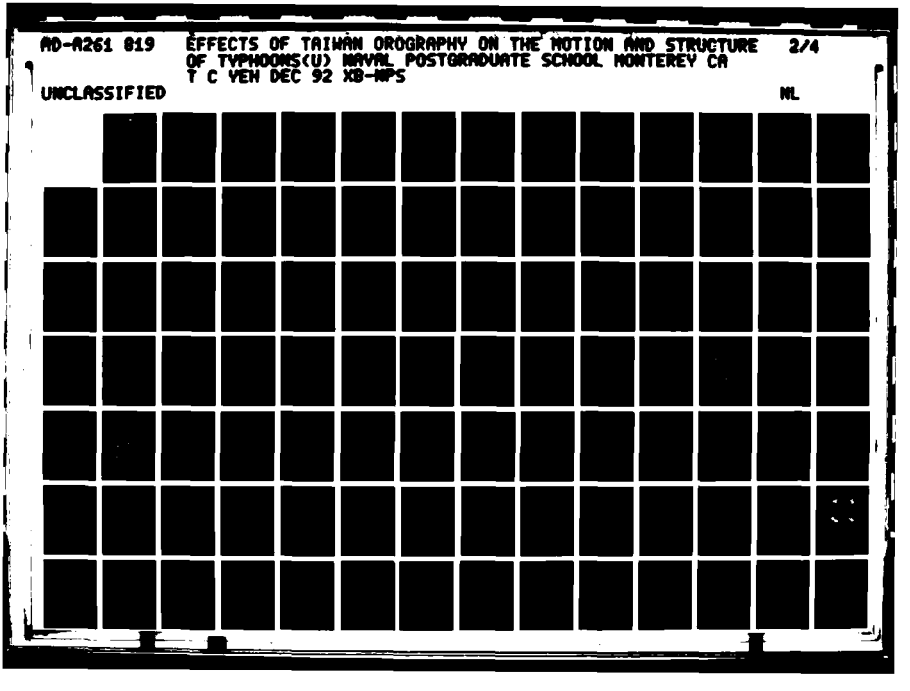

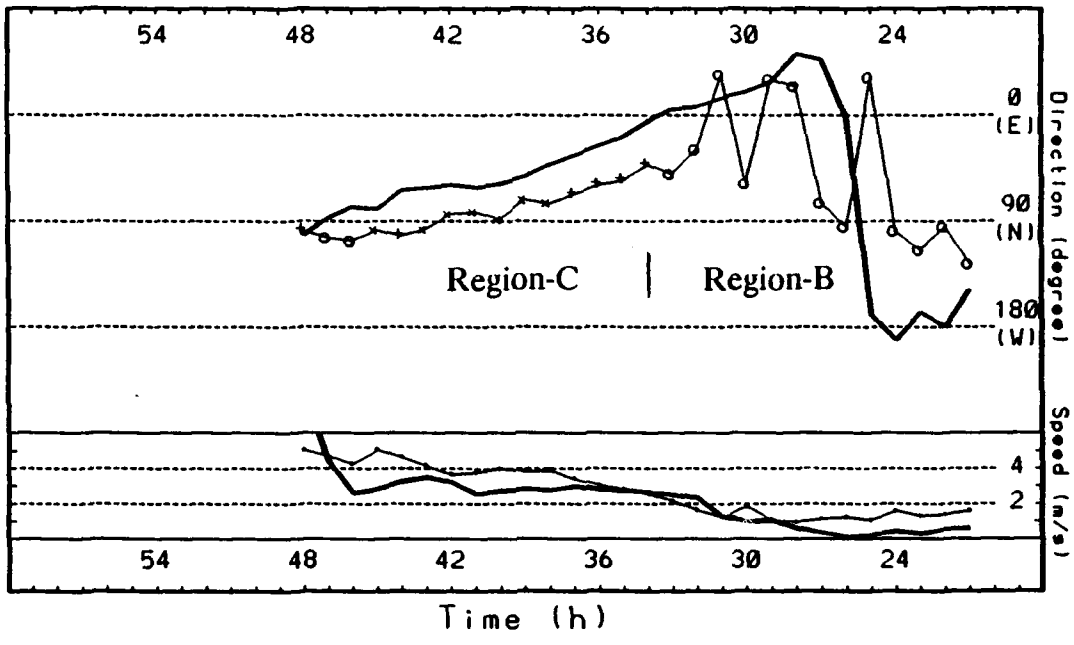

Fig. 4.20 As in Fig. 4.19, except for the ventilation flow and the vortex motion deviations (thick solid) for simulation W6S. The calculations are ended after 48 h because of the large separation of the 700 mb center from the surface center. Regions B and C are defined (see text).

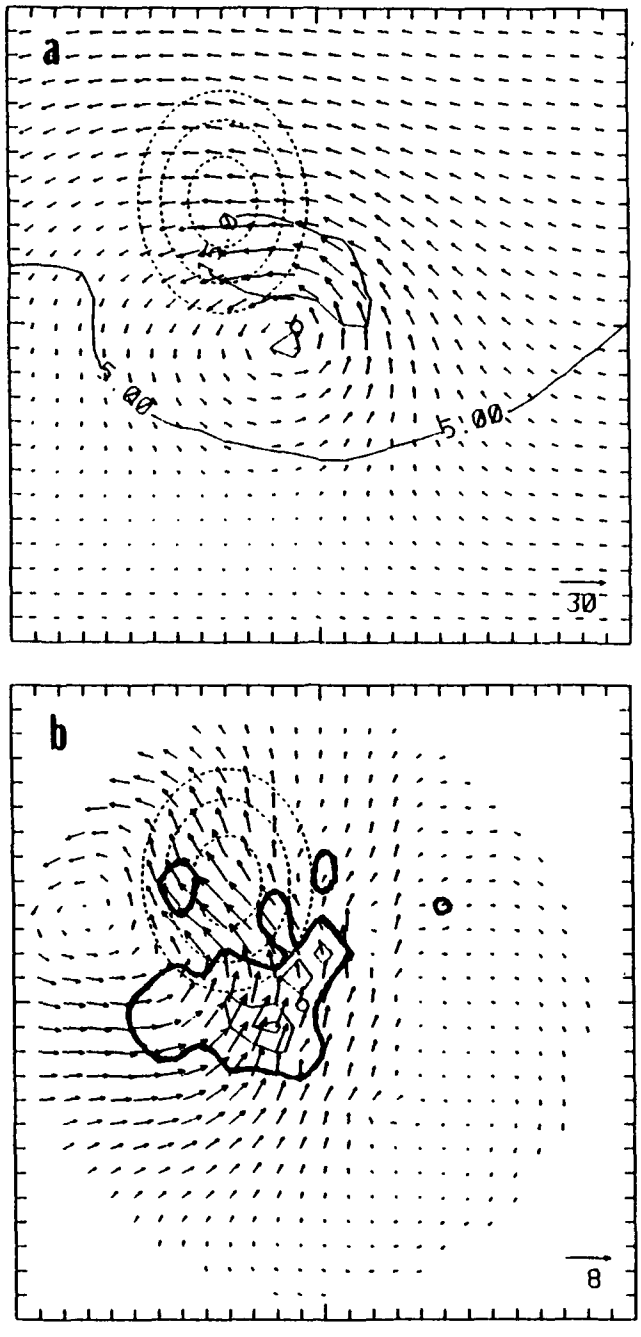

Fig. 4.21 Similar to Fig. 4.17a, except for the deep-layer mean wind (top panel) and the asymmetric winds and the hourly accumulated precipitation (bottom panel) of simulation W6S at 42 h plotted on a different scale and map orientation.

physical mechanisms than in the simulation WOC, or the mechanisms proposed by Holland and Lander (1991) and Willoughby (1992). The interaction of the deep-layer mean flow (top panel of Fig. 4.21) with the mountain barrier has significantly changed the inner structure of the vortex and resulted in the asymmetric wind distributions. On the west side of the center, the cyclonic flow components are blocked and deflected by the barrier, and therefore are significantly smaller than those on the east side of the center. This decrease of the cyclonic flow on the west side of the vortex produces strong northward asymmetric flow across the center, and moves the vortex toward the north. Therefore, the terrain blocking and deflection effects from the vortex-barrier interaction are the major factor for the formation of the asymmetric gyres and the motion of the vortex in Region-C.

A sequence of deep-layer mean flows and their asymmetric components from simulation W6S are shown in Fig. 4.22 to display how the inner vortex circulation is changed by the interaction with the mountain barrier, and to explain how these changes are related to the vortex motion. When the vortex center is located far upstream of the mountain barrier (Fig. 4.22a), only the outer edge of the vortex circulation reaches the island. The inner circulation (defined as the radius from center to the outer-most point with 15 m/s wind speed) is relatively unaffected by the terrain at this time. The asymmetric wind field has a similar pattern as the ocean-control (Fig. 4.17a). In the earlier periods (e.g., 18 h) of the simulation, the accumulated precipitation pattern (Fig. 4.22) is similar to the results from the ocean-control (Fig. 4.17a).

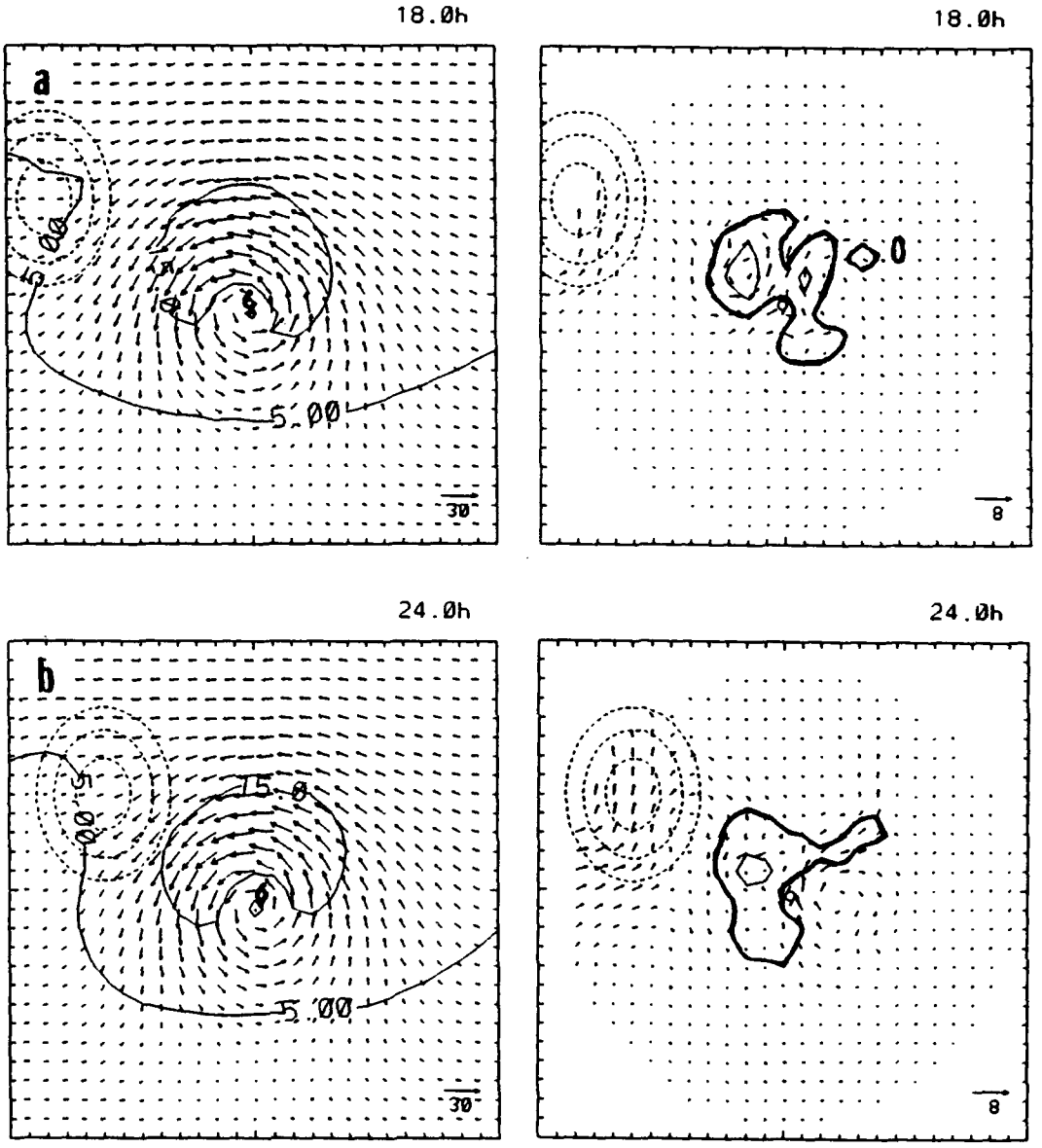

Fig. 4.22 As in Fig. 4.17, except for the deep-layer mean wind (left) and the asymmetric winds and the hourly accumulated precipitation (right) of W6S at (a) 18h, (b) 24 h, (c) 30 h and (d) 36 h.

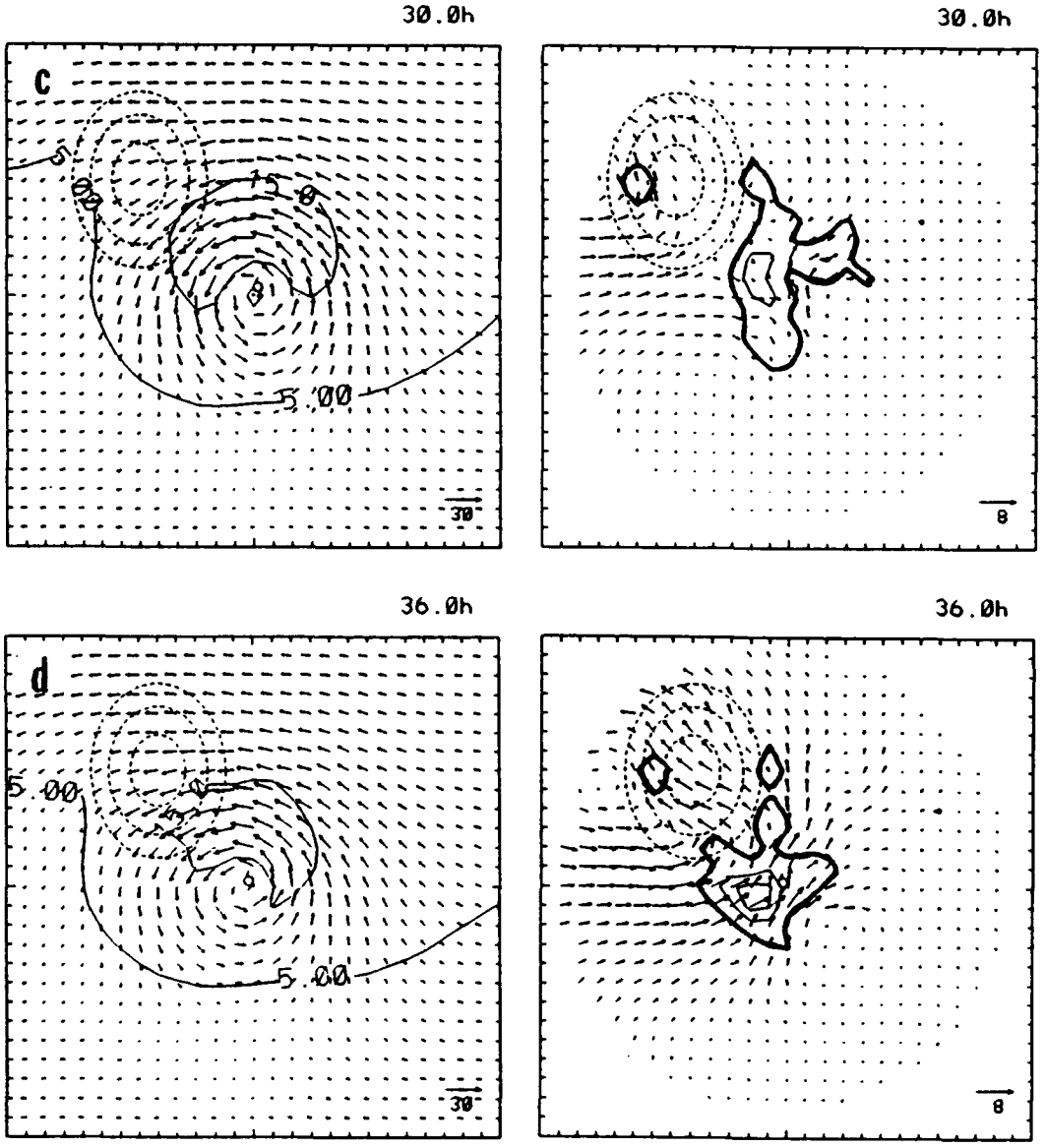

Fig. 4.22 (Continued)

At 24 h (Fig. 4.22b), the W6S center has just passed line AA' and entered Region-B (Fig. 4.14) and the outer boundary of the inner circulation has reached the coastline. At this time, a relatively small asymmetry has developed with stronger northerly winds about 180 km west of the center. This effect appears to be a channeling effect of the barrier on the low-level flow. The motion of the vortex is affected by both steering and the interaction of the outer edge vortex circulation with the mountain barrier. Six hours later (Fig. 4.22c), the size of the inner circulation has been slightly reduced as the southeastern barrier is covered with wind speeds greater than 15 m/s. However, the inner circulation structure does not have notable changes in this period. The larger terrain-induced asymmetric flow is located to the south and southwest of the island. Therefore, the vortex continues to be in the Region-B with similar motion characteristics as at 24 h.

When the vortex moves to Region-C at 36 h (Fig. 4.22d), significant changes in the inner circulation structure occur. Similar to Fig. 4.21 at 42 h, the wind on the west side of the vortex is blocked and deflected by the barrier. The unbalanced structure of the total wind circulation with stronger (weaker) cyclonic flow on east (west) side of the vortex is associated with the strong northward movement of the vortex (Fig. 4.12). Significant precipitation differences from the ocean-control occur when the vortex moves close to the barrier (e.g., 36 h), with a heavy precipitation cell southwest of the center. As mentioned above, the precipitation cell does not make a significant contribution to the formation of the asymmetric gyres.

A similar evolution of the asymmetric circulation induced by the mountain barrier exists in the other five simulations shown in Fig. 4.12, and these asymmetric circulations are similarly related to their vortex motions. Fig. 4.23 includes two examples, one (W2N) approaches the northern portion of the barrier and the other (W8S) approaches the southern portion of the barrier. When the vortex center is located in Region-C southeast (e.g., W1S, W4S and W8S) of the island, the asymmetric wind circulation evolves in a similar way as in simulation W6S described above due to the slowdown of the cyclonic flow in the area near and over the mountain. As the result, the vortex experiences an unbalanced cyclonic force to the northeast relative to the mountain center. The result of this extra forcing slows down the vortex and turns the vortex to the north.

The formation of the asymmetric circulation for the vortices approaching the northern portions of the island (e.g., W4N and W2N) is slightly different from those approaching the southern portion of the island. In the simulation W2N, the area with wind speeds greater than 15 m/s is located to the north of the island and does not directly encounter the barrier (Fig. 4.24). The induced asymmetric wind circulation is relatively weaker than for the southern island cases and occurs only when the center moves rather close to the island. For example, the terrain blocking effect at 36 h mainly changes the flow over and to the south and west of the barrier. The asymmetric flow vectors near the center are erratic and are very weak. This difference from the storms near the southern island may be the reason that line BB' is located closer to the island and the vector differences are relatively smaller (Fig. 4.14) for the two vortices approaching the

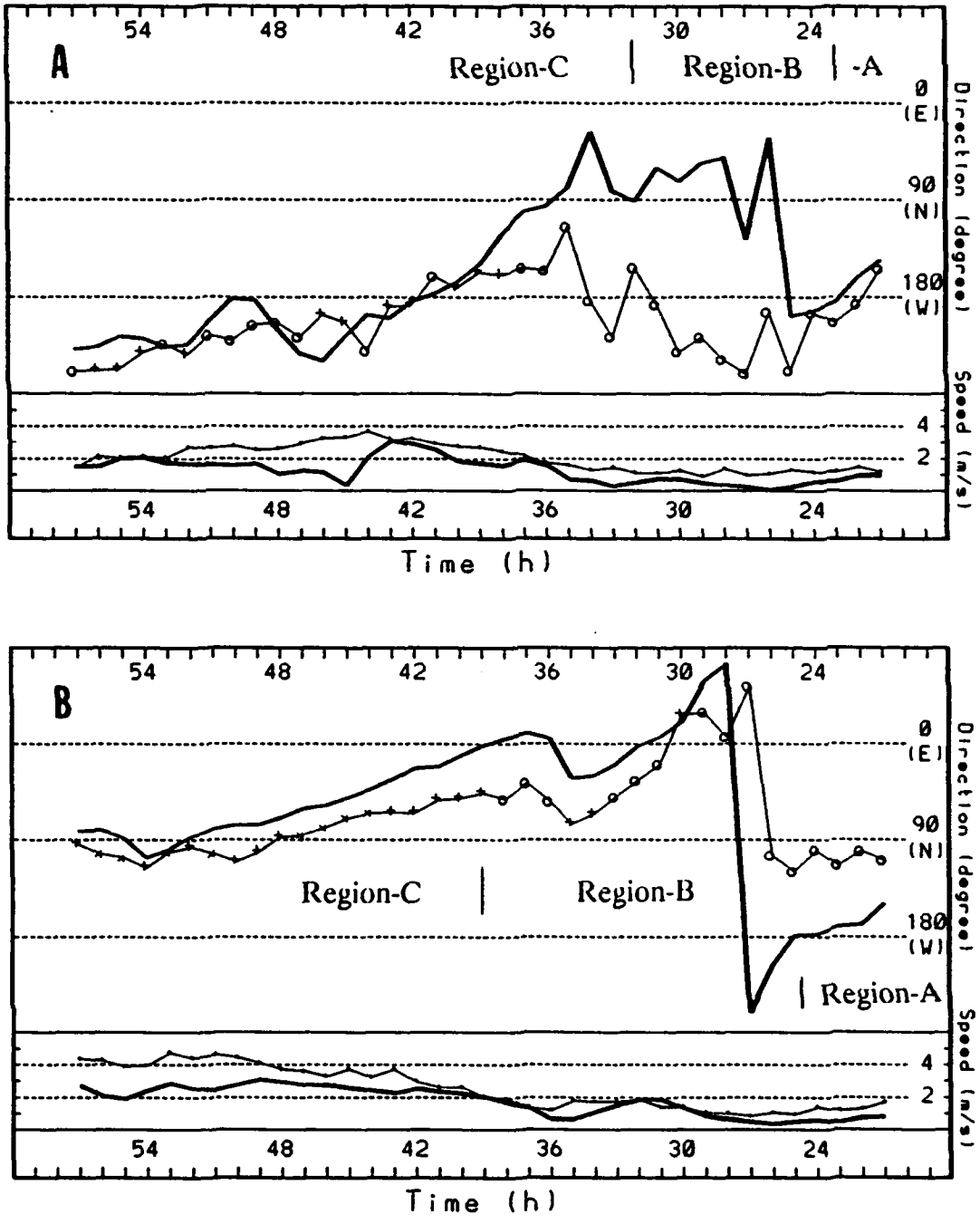

Fig. 4.23 As in Fig. 4.19, except for the relation between the ventilation flow and the vortex motion deviations (thick solid) of simulations (a) W2N and (b) W8S.

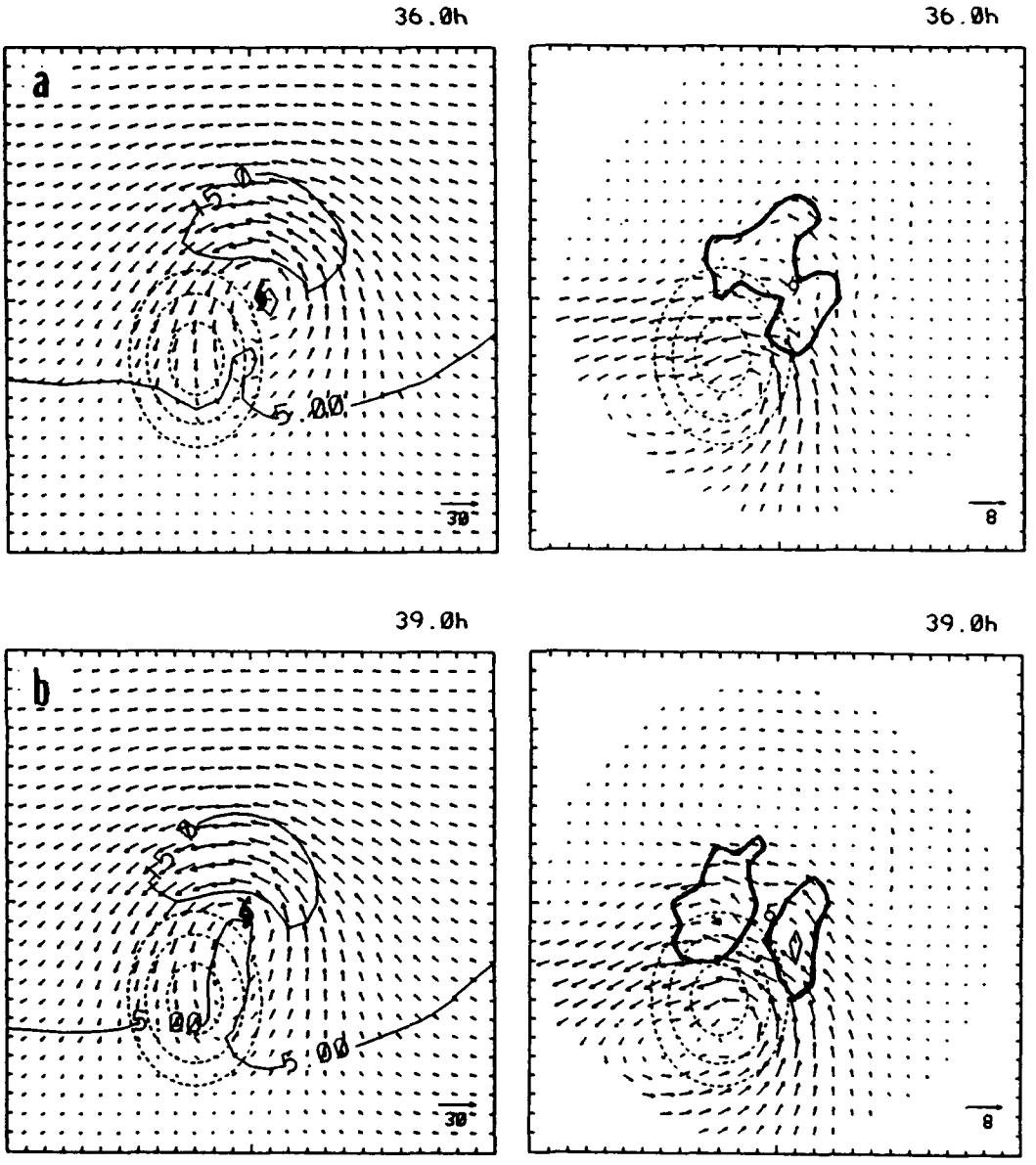

Fig. 4.24 As in Fig. 4.17, except for the deep-layer mean wind (left) and the asymmetric winds and the hourly accumulated precipitation (right) of W2N at (a) 36 h and (b) 39 h.

northern end of the island (W2N and W4N). After passing the long-axis of the barrier, the center of W2N is located to the northwest of the island. The slower cyclonic flow now is in the southeastern part of the center (not shown). This unbalanced structure results an cyclonic (relative to the mountain) ventilation flow that accelerates the vortex to the west and to the south (Fig. 4.14).

In summary, if a vortex is located within Region-C, asymmetries are generated as the mountain barrier significantly changes the inner structure of the vortex. The vortex stabilization mechanism of Carr and Williams (1989) will continually try to eliminate this asymmetry and thus restore the symmetric vortex. However, the asymmetries will continue to be generated as the strong wind region continuously encounters the barrier. The unbalanced structure results in an ventilation flow to direct the vortex motion that is anti-clockwise relative to the barrier, except when the center is southwest of the island. When the vortex center is southwest of the island (e.g., after 54 h of W8S), the asymmetric circulation and the vortex motion are still highly correlated (Fig. 4.23b), and the direction of the ventilation flow (clockwise relative to the barrier) is different from that for the other storm tracks (Fig. 4.14a). When the vortex center of simulation W8S is located to the east of the long-axis of the barrier (e.g., at 42 h in Fig. 4.25a), the deep-layer mean wind is similar to the situation of the other centers southeast of the island. The barrier slows down the cyclonic wind on the west side of the center, and the resulting unbalanced force moves the vortex to the north. When the center is to the southwest of the island (Fig. 4.25b) and the barrier now is northeast of the center, the cyclonic mean wind on the east side of the vortex is still

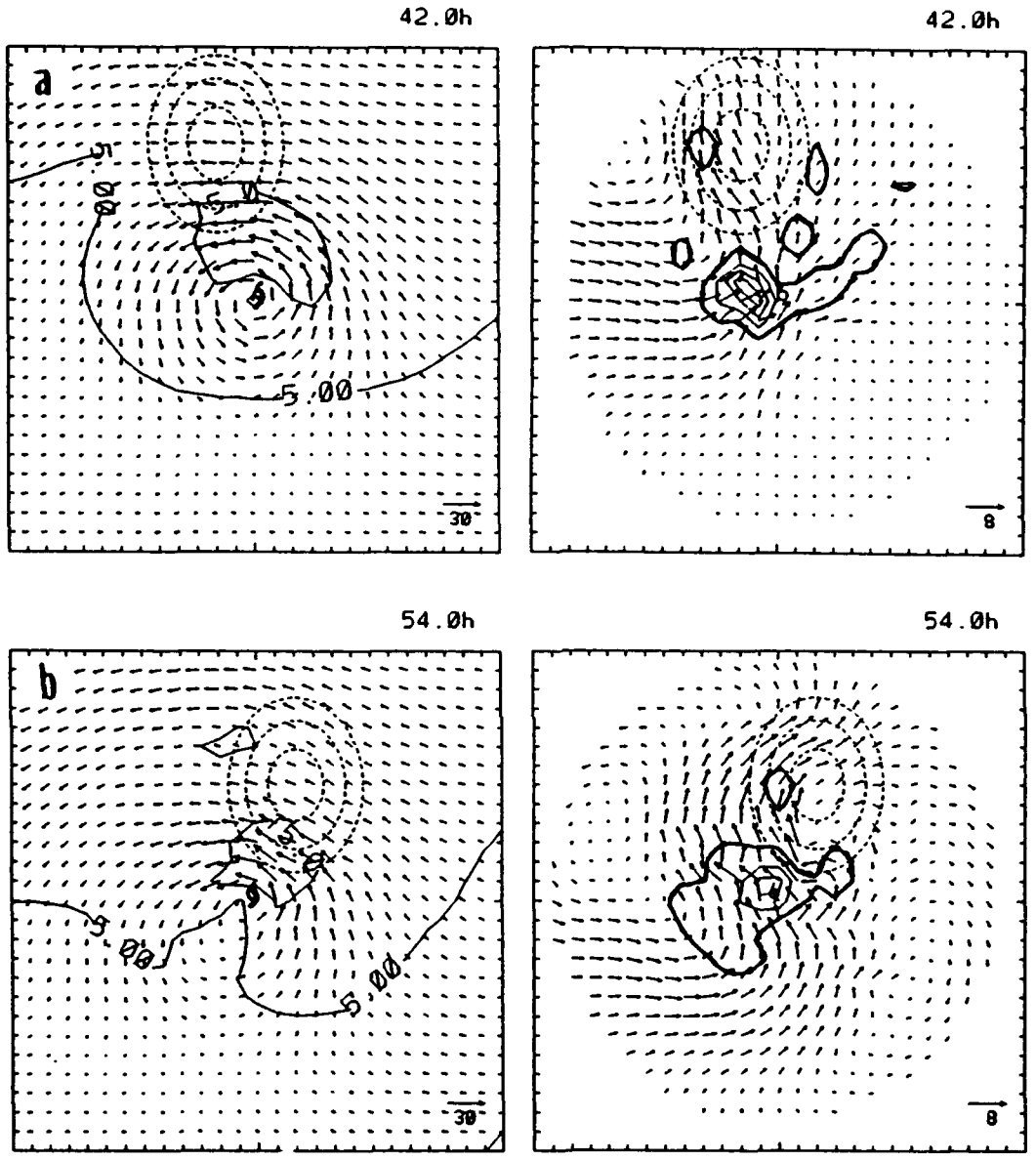

Fig. 4.25 As in Fig. 4.17, except for the deep-layer mean wind (left) and the asymmetric winds and the hourly accumulated precipitation (right) of W8S at (a) 42 h and (b) 54 h.

larger than on the west side of the center. This may be because a large area of flow to the north of the center has directly encountered the barrier, and therefore has slowed the downstream flow. The result of this asymmetric structure continuously forces the vortex toward the north (Fig. 4.23b) even after the center passes the long-axis of the island. As in the other examples, the diabatic heating effect is not the dominant factor to the vortex motion for this case in Region-C.

In the above discussion, the domain has been divided into three regions (Region-A, -B and -C). When the center is over or very close to the mountain barrier, significant center separations (vertically and/or between the pressure and wind fields) are found. The vortex motion in this case will not be easily explained by the asymmetric wind structure or ventilation flow, because of the difficulty of defining a center. Moreover, development of a secondary low on the other side of the barrier (as will be shown later) may result in the jumping of the lower level centers across the barrier. Thus, detailed discussion of these structure changes will be postponed until the next chapter.

D. DEPENDENCE ON THE VORTEX TRANSLATION SPEED

1. 10 m/s Basic Flow

Tracks (beginning from 9 h to 36 h) of three simulations with the weak vortex starting from 1,125 km upstream of the mountain barrier in a 10 m/s easterly flow are displayed in Fig. 4.26. Because the center movement of the corresponding ocean-control (WOCf) is so steady, that simulation is ended at 30 h. The track

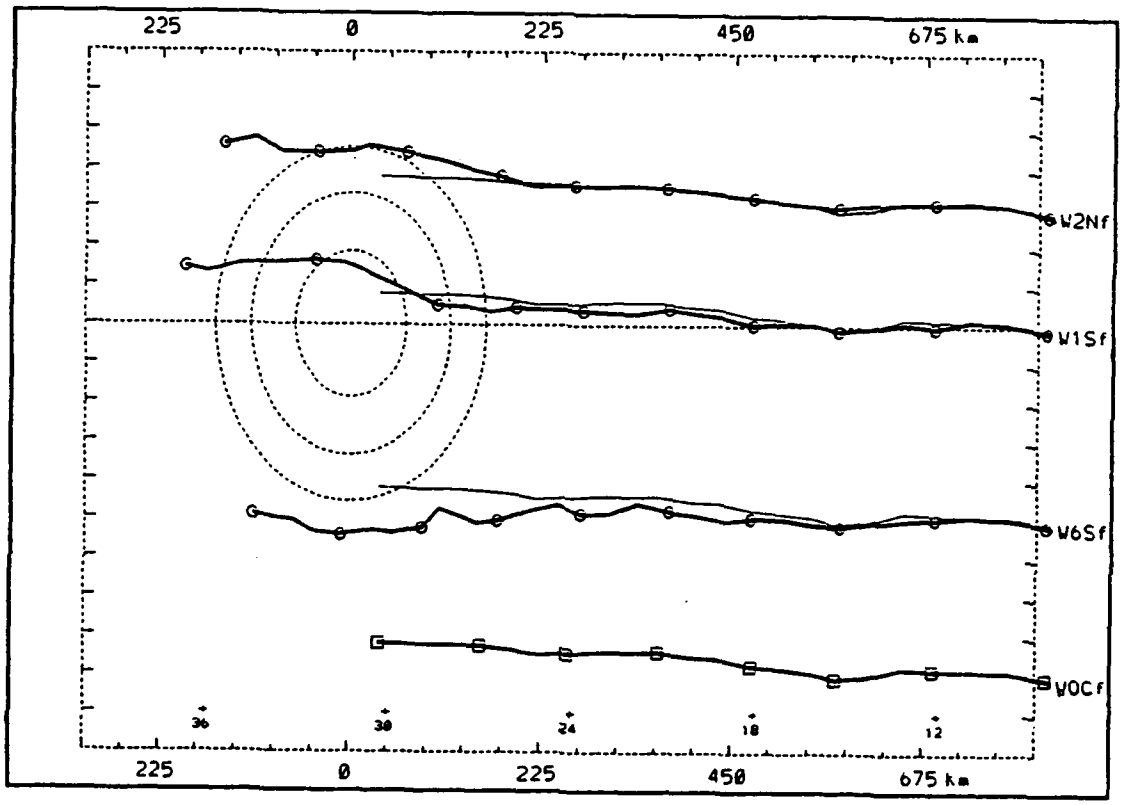

Fig. 4.26 As in Fig. 4.12, except for tracks of the weak vortex in a 10 m/s zonal flow. The tracks are from 9 h to 36 h for the three simulations with the mountain barrier included (W2Nf, W1Sf and W6Sf). For the ocean-control (WOCf), the track is from 9 h to 30 h.

fluctuations of the 10 m/s ocean-control (WOCf) are smaller than in the 5 m/s simulation. In the 10 m/s zonal flow, all three vortices (W2Nf, W1Sf and W6Sf) move much closer to the ocean-control than those vortices described above in 5 m/s zonal flow (Fig. 4.12). No significant track deflections are found upstream of the barrier for the two vortices approaching the northern portion of the island. Similar smaller track deflections are observed in Figs. 4.5 and 4.8, and are simulated by Bender et al.

The track deflections are larger (smaller) when the weak vortex approaches the southern (northern) portion of the barrier in a 5 m/s zonal flow (Fig. 4.12). Similar results are found when the basic flow is increased here to 10 m/s. For the weak vortex approaching the southern end of the island (W6Sf), a deflection of about 70 km to the south of the ocean-control is found.

Track deflections in these three simulations relative to the barrier-modified mean steering flow (Fig. 4.16a and 4.16b) are shown in Fig. 4.27. The vector differences (or vortex-barrier deflections) on the upstream are smaller than those when the weak vortex is in a 5 m/s zonal flow (Fig. 4.14a). The vortex-barrier deflections are very small in the region east of about 585 km from the mountain center. This region is similar to Region-A of Fig. 4.14 in which the steering is the main contributor to the vortex motion. Small southward deviations are found in the zone between about 585 km to 400 km upstream of the island, which is similar to the velocity differences in Region-B of Fig. 4.14. However, the magnitudes (<0.5 m/s) are smaller and the location is about 100 km to the east of Region-B in Fig. 4.14.

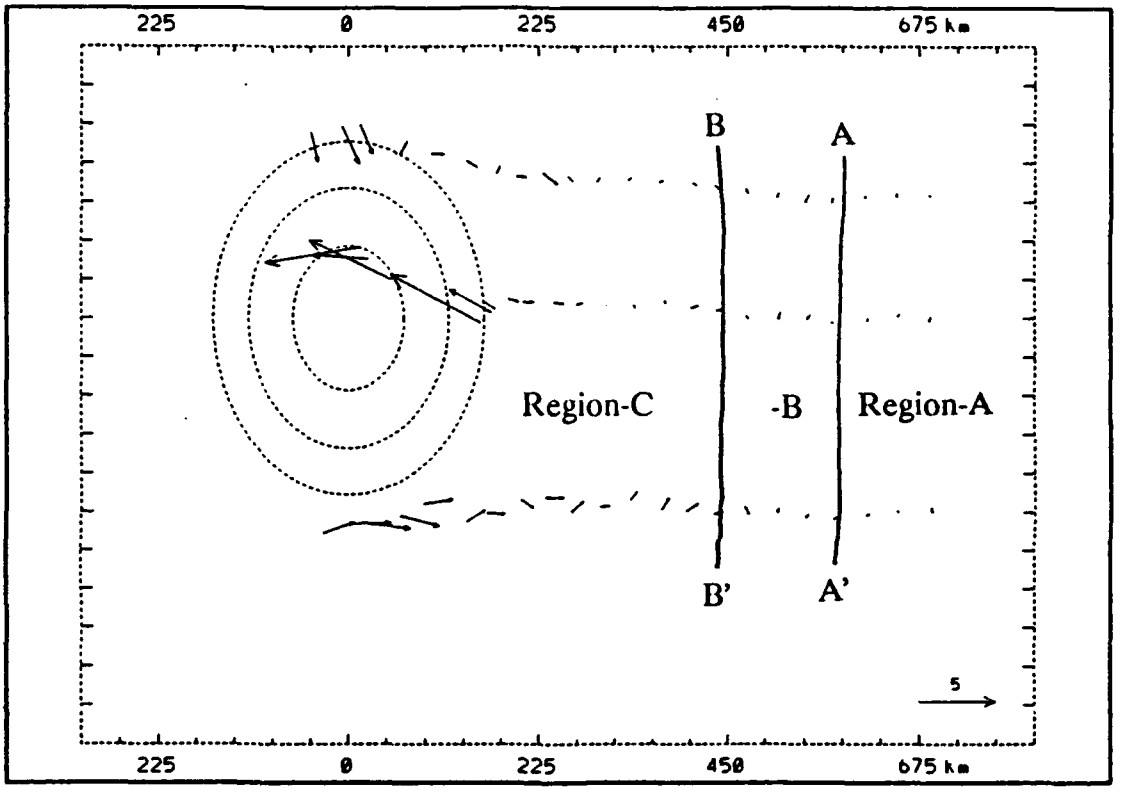

Fig. 4.27 Similar to Fig. 4.14a, except for hourly vectors of the vortex-barrier deflections for the three simulations in Fig. 4.26 from 12 h to 33 h.

Although the deep-layer mean wind of simulation W1Sf at 18 h (Fig. 4.28a) includes the same spun-up vortex, it appears to have a different size (the radial distance of the 15 m/s contour from the center) and intensity (maximum wind speed) when it is embedded in a stronger zonal flow. The vortex size in a 10 m/s zonal flow is about 150 km larger than in the 5 m/s zonal flow case. Therefore, the interactions between the vortex and the mountain barrier will begin farther upstream from the island.

When the center of W1Sf is located about 480 km east of the island at 18 h, the outer vortex circulation has reached the mountain barrier (Fig. 4.28a). The asymmetric flow pattern is similar to that of the ocean-control (not shown), and this is probably related to the asymmetric heating represented by the precipitation cell shown in Fig. 4.28a. As with the vortex motion in Region-B of Fig. 4.12, a southward deflection from the steering is created by the interaction of the outer vortex circulation and the mountain barrier. However, the magnitudes are smaller, which may be because the center is so far away from the island (similar to Fig. 4.13, the deflections caused by the mountain decrease away from the island). In the stronger easterly flow, the vortex has less time to react to the forces causing the deflections in Region-B. Another possible explanation is that the overall storm circulation is more intense and has a more effective vortex stabilization mechanism (such as in Carr and Williams 1989) to restore the symmetry by rapidly reducing asymmetric perturbations caused by the barrier. Thus, the deep-layer mean flow of the vortex in a 10 m/s zonal flow has significant changes only when the center is very close to or over the island.

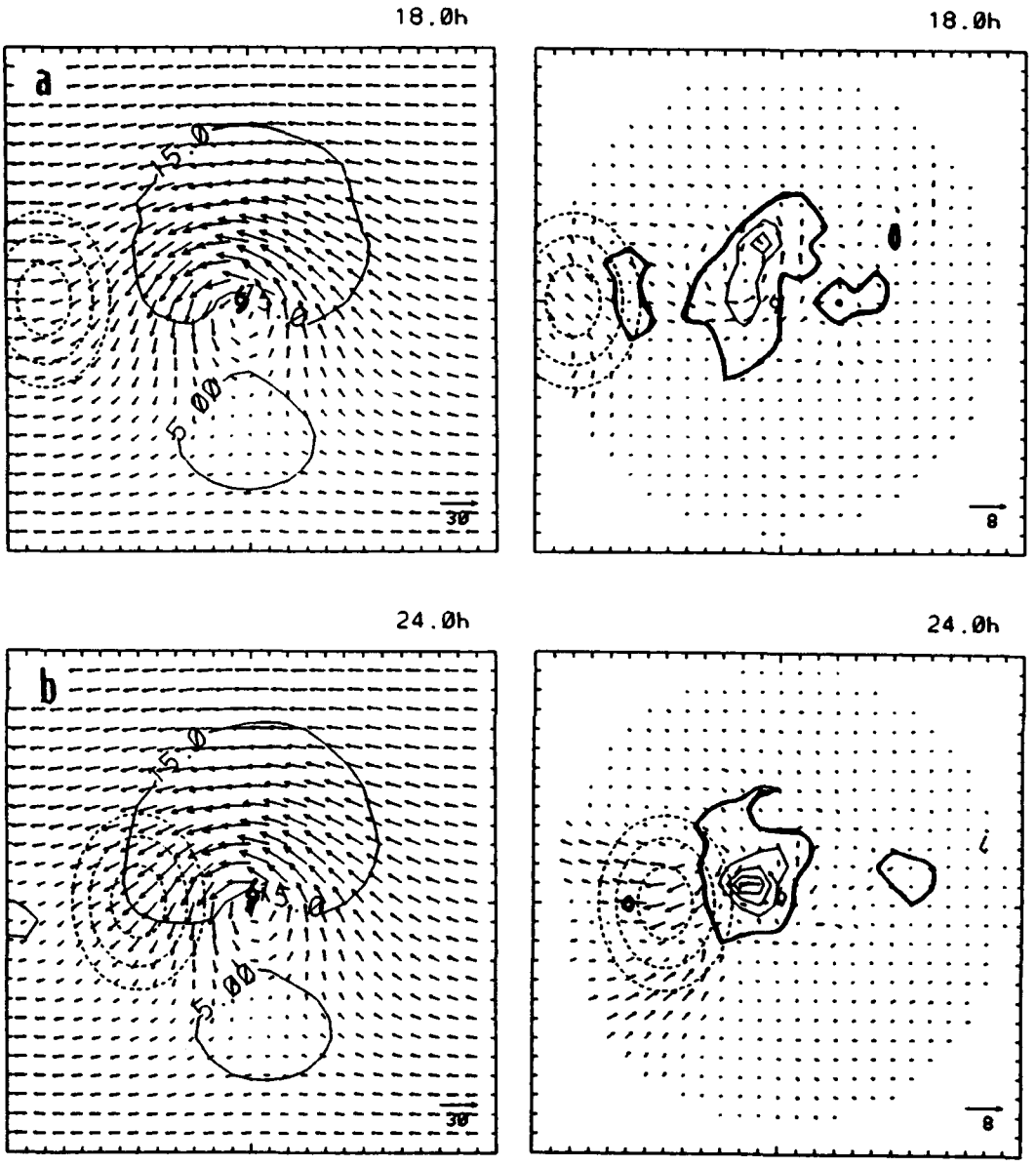

Fig. 4.28 As in Fig. 4.17, except for the deep-layer mean wind (left) and the asymmetric winds and the hourly accumulated precipitation (right) of simulation W1Sf at (a) 18 h, (b) 24 h, (c) 30 h and (d) 33 h.

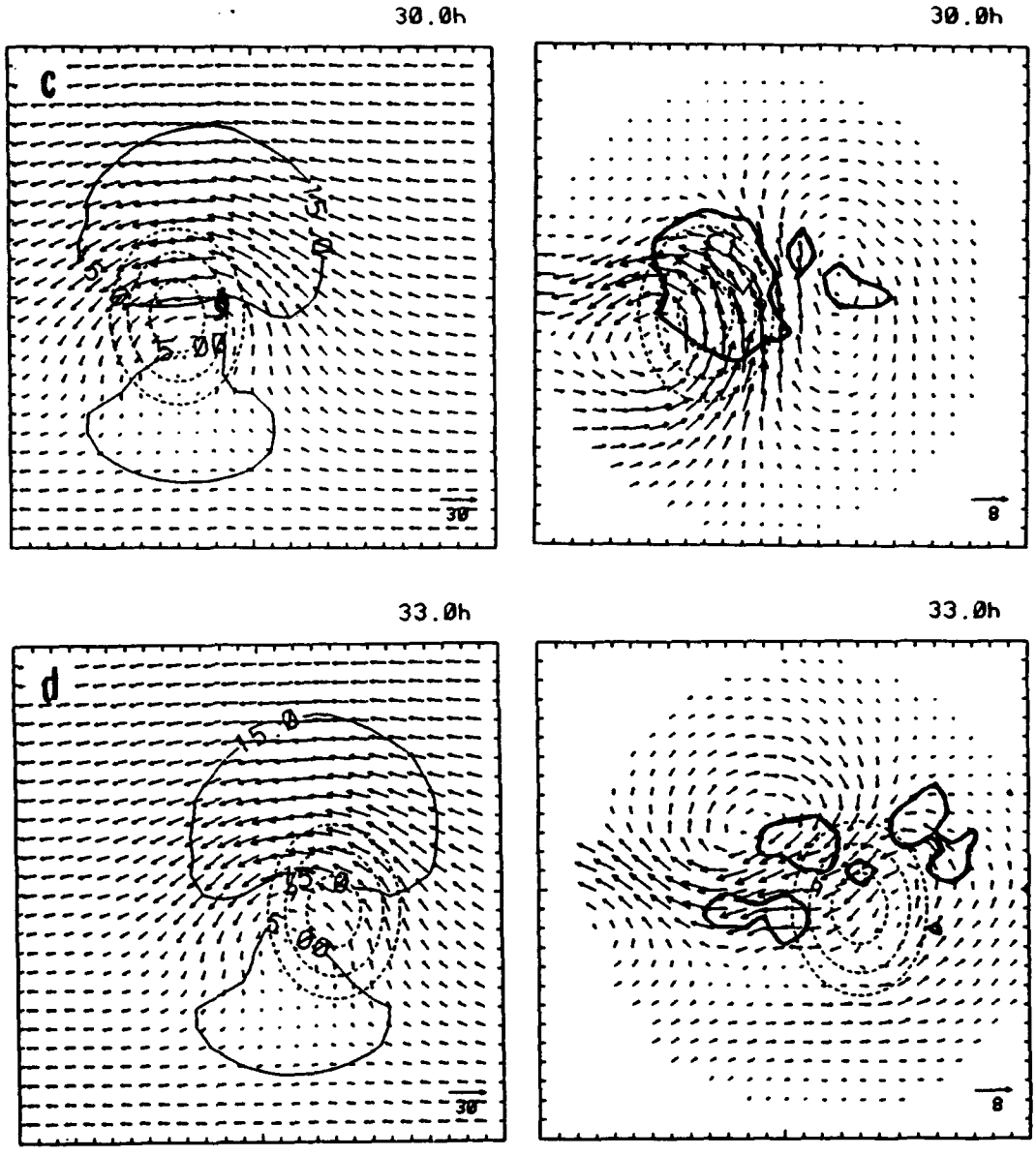

Fig. 4.28 (Continued)

At 24 h (Fig. 4.28b), the center of W1Sf is located about 270 km east of the island center. A large area of the island is already covered with strong wind (>15 m/s). However, the size of the vortex and the shape of the 15 m/s contour line have only minor changes from those at 18 h. The stronger asymmetric flows are located over and to the south of the barrier farther west of the center. Therefore, the motion change due to the interaction of the vortex with the mountain barrier is still very small.

When the W1Sf center has moved onto the terrain at an altitude of about 1,000 m at 30 h (Fig. 4.28c), the cyclonic vortex circulation has been slowed on the west side and the south side of the center. These modifications of the circulation are significant, especially to the south of the center. A strong cyclonic (anticyclonic) gyre is found to the west (east) of the center. Therefore, the vortex experiences a strong acceleration toward the northwest. After the vortex has moved to the west slope of the mountain barrier at 33 h (Fig. 4.28d), the larger cyclonic wind now is on the west side of the vortex. Thus, the ventilation flow associated with the asymmetry is correlated with the strong westward acceleration and slight southward motion of the vortex.

The other two vortices (W2Nf and W6Sf) in Fig. 4.26 also experienced similar mountain effects as they moved into Region-C. Because the mountain is at a different direction relative to these vortices, the interactions produce different vortex motions. In general, these cases with the vortex in a 10 m/s translation speed have the effect of the mountain reaching a larger distance upstream of the barrier, and the magnitude of the effects is smaller than those in a 5 m/s case.

2. 2.5 m/s Basic Flow

The general conclusion that the track deflections are larger for smaller translation speeds is further confirmed by the results in Fig. 4.29. The tracks of the two vortices encountering the mountain barrier in a 2.5 m/s zonal flow have very large northward deflections. The northward displacement of center W1Ss is about 160 km when it landfalls on the northern end of the island. The center of W6Ss also is about 130 km north of the ocean-control when the simulation is stopped.

Although some of the track deflections of centers W1Ss and W6Ss are due to the steering effect (not shown), significant vector deviations (vortex-barrier deflections) are found (Fig. 4.30). Because the vortices are started relatively close to the island, vectors corresponding to Region-A in Figs. 4.12a and 4.27 are not shown. In Region-B and Region-C, the vortices have similar track behaviors as the vortex in a 5 m/s zonal flow with southward deflections in Region-B and then a turn back to the north.

Two interesting issues are to be carefully examined. First, the storm interaction with the mountain will start earlier for a larger vortex as in the 10 m/s case. Although the size of the vortex in a 2.5 m/s flow (Fig. 4.31a) is slightly smaller than in the 5 m/s case, the northward track deflections start (location of line BB' in Fig. 4.30) farther to the east of the island than in the 5 m/s zonal flow (Fig. 4.14). Second, the slower moving vortex will have more time to interact with the mountain. The issue is why the vortex-barrier deflections (motion deviations due to the storm-barrier interactions) in Fig. 4.30 are smaller in the 2.5 m/s zonal flow than in the 5 m/s case.

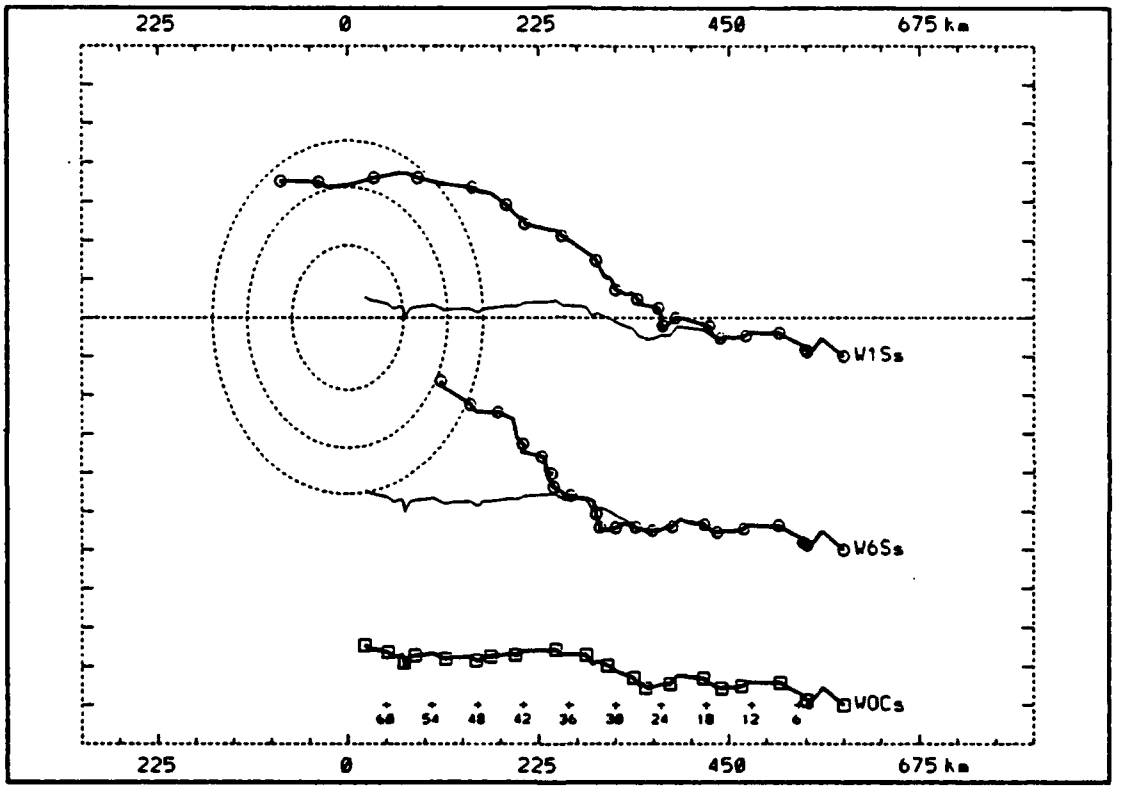

Fig. 4.29 As in Fig. 4.12, except for tracks of the weak vortex in a 2.5 m/s zonal flow starting from 585 km east of the island. The code of each simulation is given on the right side of the starting location.

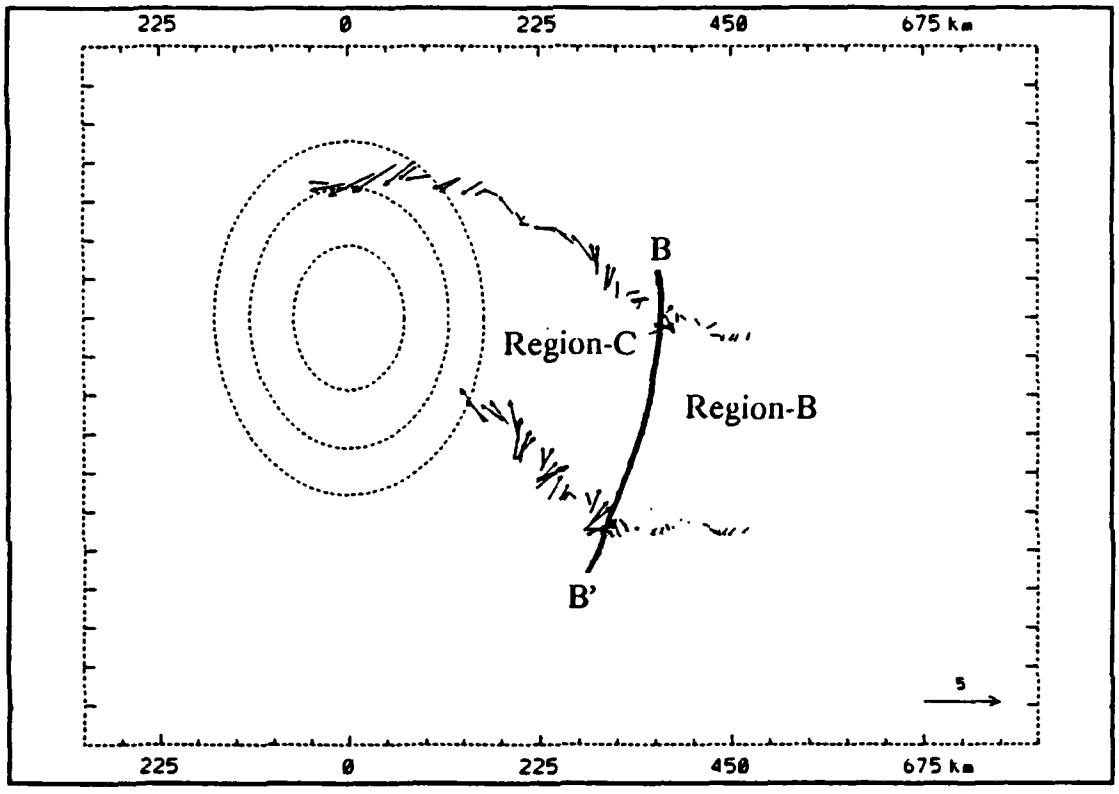

Fig. 4.30 Similar to Fig. 4.14a, except for hourly vectors of the vortex-barrier deflections for the two simulations in Fig. 4.29. Line BB' divides the domain into Region-B and Region-C.

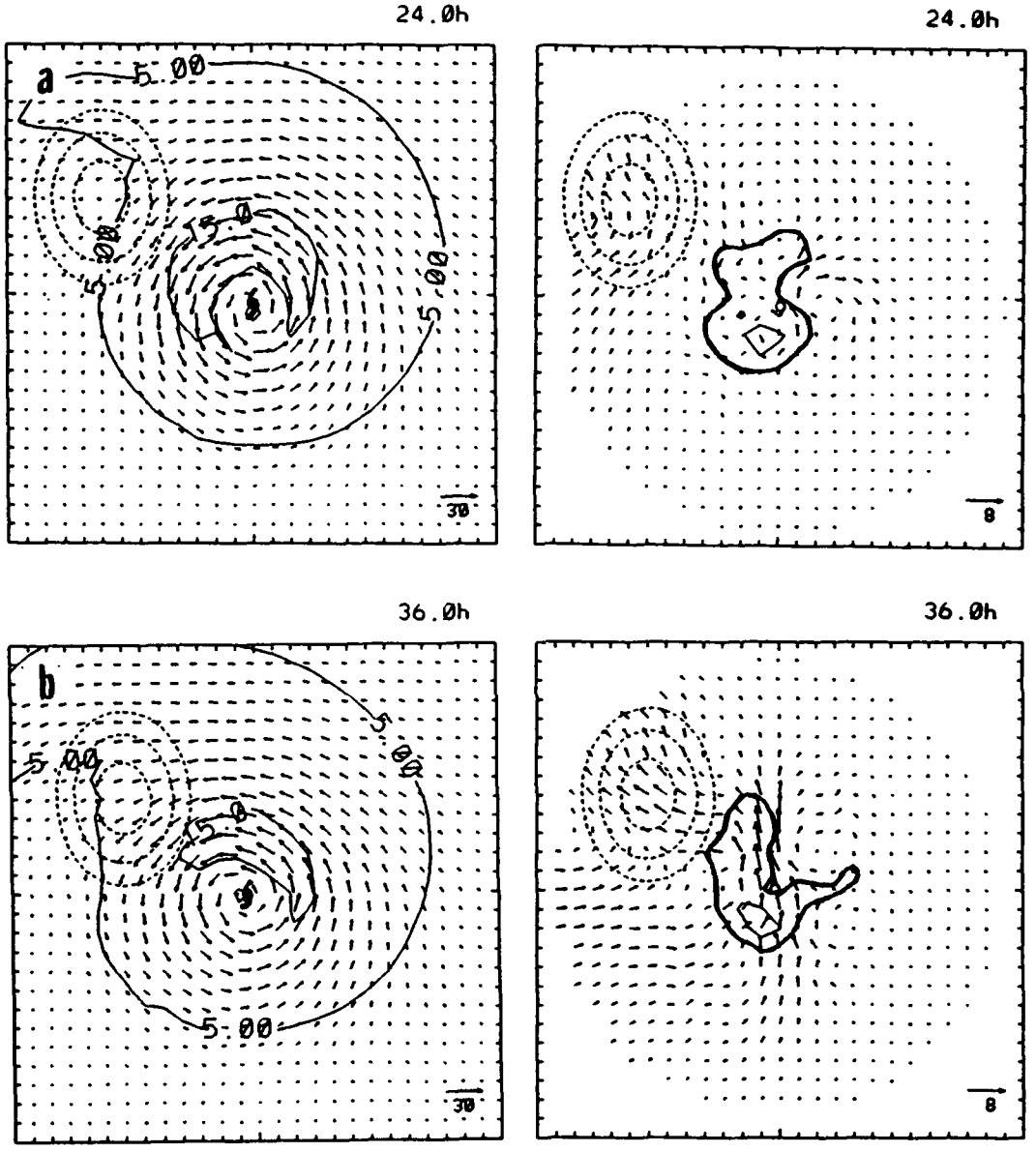

Fig. 4.31 As in Fig. 4.22, except for the deep-layer mean wind (left) and the asymmetric winds and the hourly accumulated precipitation (right) of simulation W6Ss at (a) 24 h, (b) 36 h, (c) 48 h and (d) 54 h.

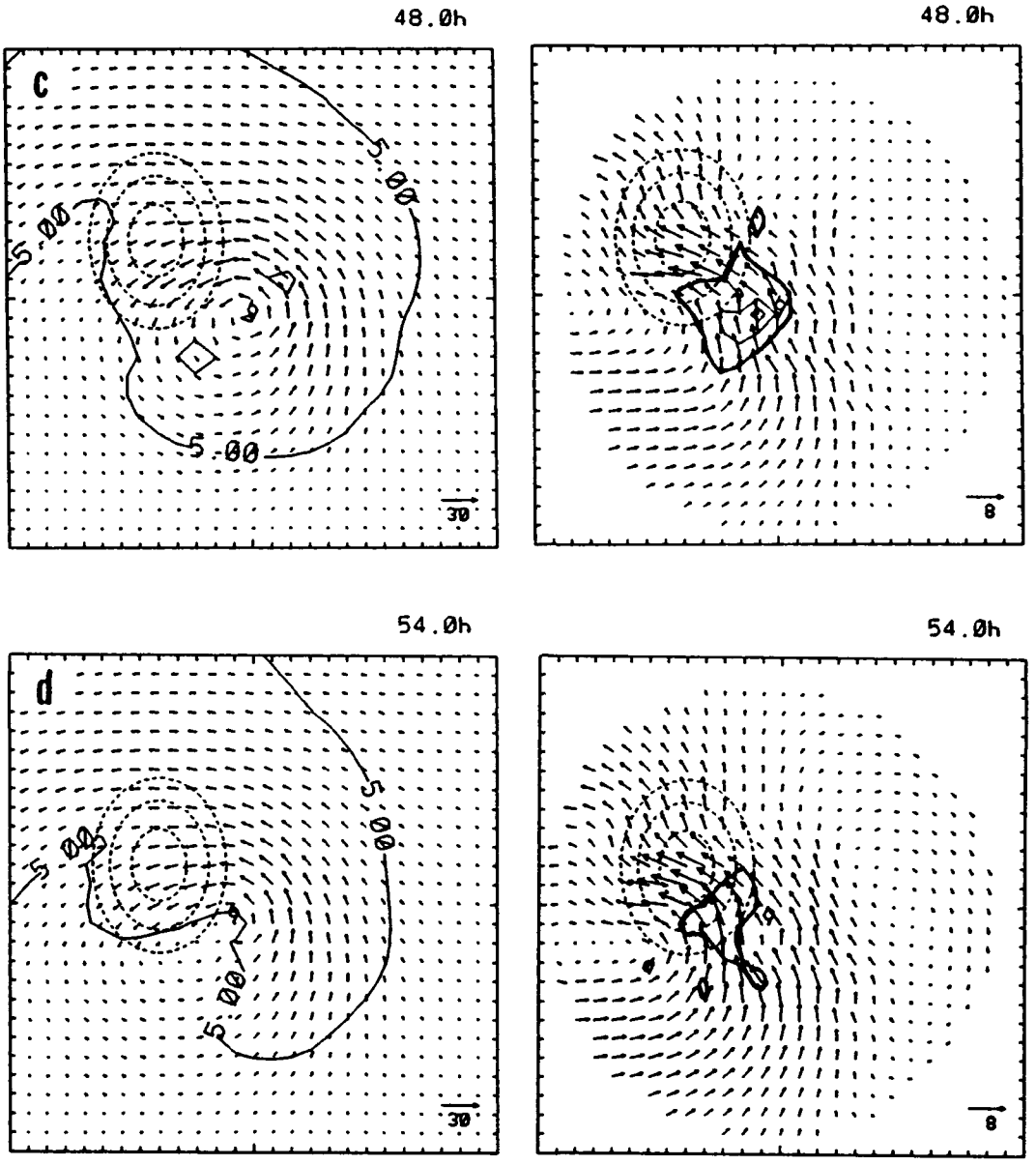

Fig. 4.31 (Continued)

Possible answers to these issues are provided in Fig. 4.31. Although the center is located about 220 km east of the coast at 36 h (Fig. 4.31b), and the 15 m/s contour line has not reached the island, the structure of the vortex has already been significantly modified. This may be because the outer edge circulation had encountered the mountain barrier more than 12 h earlier (Fig. 4.31a). The cyclonic circulation has been slowed on the west side of the center, which produces a southerly ventilation flow through the center and is correlated with the northward turn of the vortex. As the vortex moves only slowly toward the island, the vortex circulation will be more distorted by the mountain. After more than 24 h of terrain distortion, the 15 m/s wind at 48 h is limited to a very small area northeast of the center (Fig. 4.31c). Six hours later (Fig. 4.31d), none of the area has wind speeds greater than 15 m/s. The ventilation flow from the asymmetric circulation is toward the north-northwest. Perhaps because the vortex is so weakened, the vortex-barrier deflections produced by the interactions with the mountain are not as pronounced as that in the 5 m/s zonal flow. Consequently, the vector differences in Region-C due to the storm-barrier interactions (Fig. 4.30) are smaller in the 2.5 m/s zonal flow than in the 5 m/s case (Fig. 4.14). However, the total track deflections are larger than in the 5 m/s case due to longer period over which these deflections are experienced.

E. DEPENDENCE ON THE VORTEX INTENSITY

1. Ocean-control for the Intense Vortex

The track and time evolution of the central pressure for an intense vortex (Section B) that is superposed on a 5 m/s zonal flow in an ocean-control (IOC) simulation are shown in Fig. 4.32. Simulation IOC is similar to WOC (Fig. 4.10), except the weak vortex in WOC is replaced by the intense vortex. Because the intense vortex has not reached steady state during the 72-h spin-up process (Chapter III), the central pressure of the IOC case is still decreasing after the vortex has been introduced into the zonal flow. The central pressure is in a quasi-steady state after 36 h of simulation IOC with a minimum surface pressure of about 975 mb, which is about 25 mb lower than that of WOC.

Similar northward displacements and slightly faster translation speeds than the zonal flow are found in the IOC tracks as in the WOC simulation. The averaged speed from 18 h to 57 h is about 5.2 m/s westward and 0.4 m/s northward. However, the short-time oscillations of the center are more pronounced than in WOC. The standard deviations of the u- and v- components from 18 h to 57 h are about 1.2 m/s and 1.1 m/s, respectively, which are about 0.7 m/s and 0.4 m/s respectively larger than in WOC. The 45 km horizontal resolution in this model may introduce larger computational errors in the intense vortex simulations than in the weak vortex because of the larger pressure gradients, stronger wind shears and enhanced convection near the center of the intense vortex. However, the following discussion focuses on the

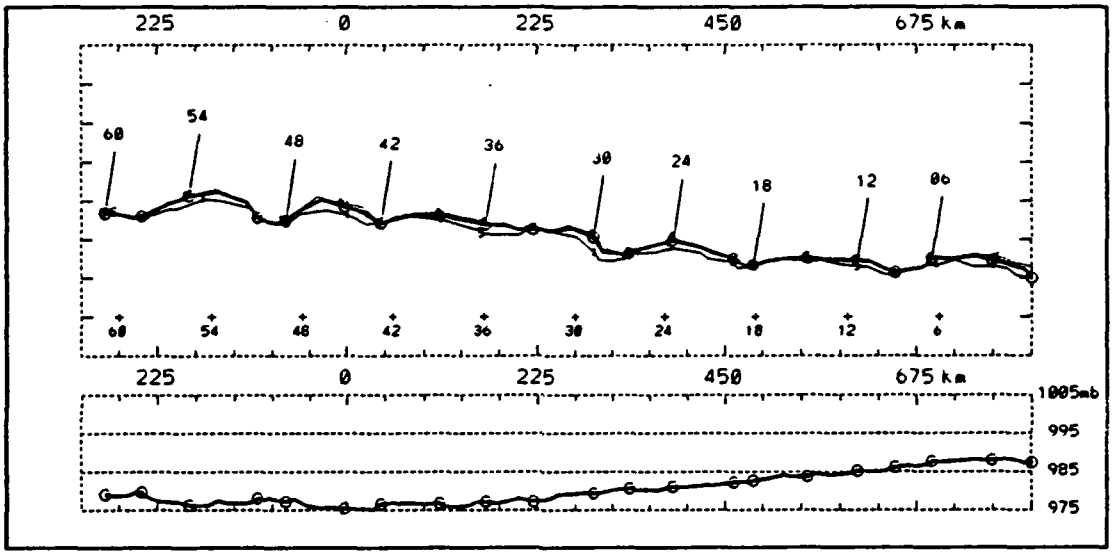

Fig. 4.32 As in Fig. 4.10, except for sea-level, 700 mb and 500 mb tracks (top panel) and the minimum sea-level pressure (bottom panel) of the intense vortex ocean-control simulation IOC.

systematic track changes after including a mountain barrier. Therefore, the sensitivity of the vortex track to the model resolution has not been examined.

Whereas the 500 mb center of the WOC departs from the two lower level centers after 15 h (Fig. 4.10), the centers at 500 mb and 700 mb of the IOC are vertically stacked. The intense storm has a stronger vertical circulation and a deeper layer of inflow that contributes to the vertical alignment of the centers in the IOC.

The ventilation flow between the asymmetric gyre circulations (Fig. 4.33) has a systematic speed bias of about 2 m/s greater than the vortex motion relative to the 5 m/s basic flow. Since the intense vortex has a larger size than the weak vortex, an increase from 180 km to 270 km in the outer boundary of the radial band within which the ventilation flow is calculated has been tested. For this larger domain, the ventilation flow speed is slowed by about 0.5 m/s (not shown), which is not a significant decrease of the difference in Fig. 4.33. Nevertheless, the ventilation flow from simulation IOC is highly correlated with the vortex motion relative to the basic flow, especially in the direction changes with time in Fig. 4.33. This shows the motion deviation follows the ventilation flow rotation, but the smaller magnitude of the deviations may indicate that the entire vortex is not affected by the inner cell convection. Comparing an averaged (2-h, 4-h and 6-h) vortex speed to an instantaneous ventilation flow may also contribute to the systematic speed difference in Fig. 4.33.

As in simulation WOC (Fig. 4.19), short time-scale center loops are occurring as the vortex is moving toward west. As in the WOC case (Fig. 4.17), the precipitation cells appear to be co-located with the asymmetric gyres (Fig. 4.34), and

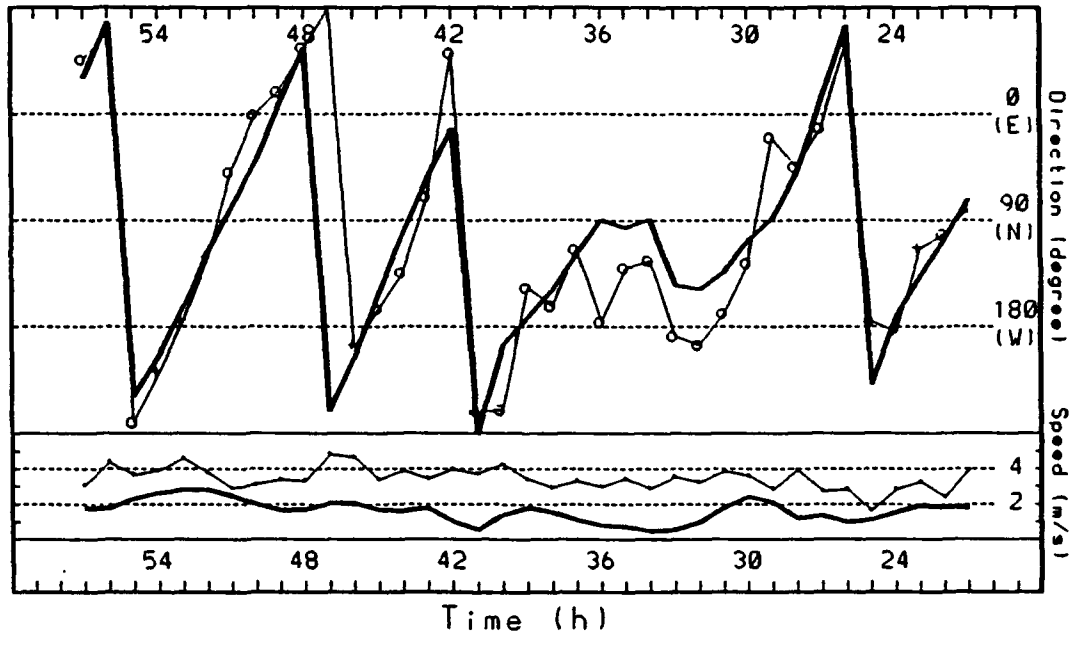

Fig. 4.33 As in Fig. 4.19, except for the ventilation flow and vortex motion deviations (thick solid) for simulation IOC.

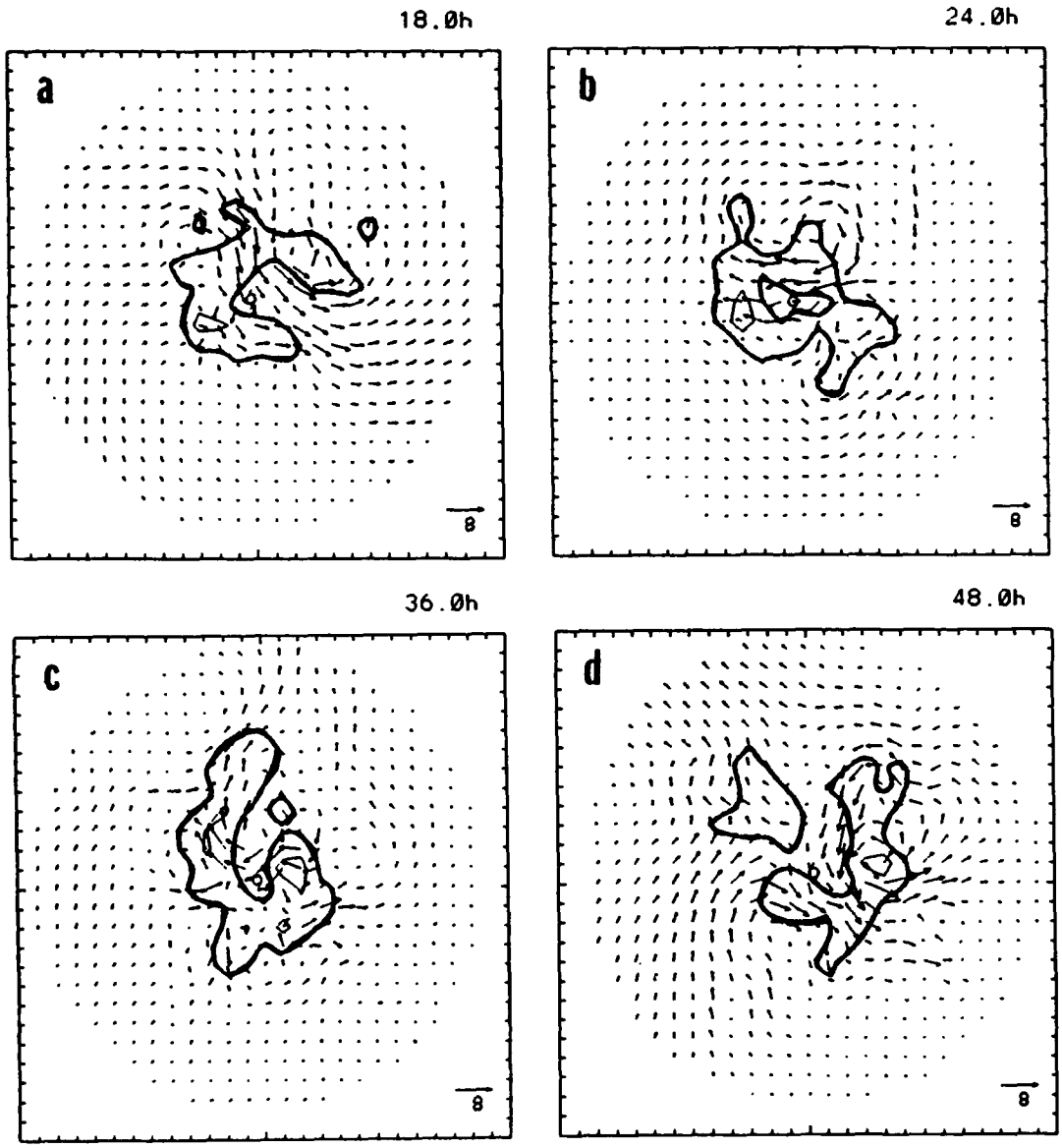

Fig. 4.34 As in right panel of Fig. 4.17, except for the asymmetric component of the deep-layer mean wind and the hourly accumulated precipitation of IOC at (a) 18 h, (b) 24 h, (c) 36 h and (d) 48 h. The precipitation contours are in 10 mm/h intervals beginning from 5 mm/h (thick).

thus the vortex motion. The precipitation cells in simulation IOC are stronger than in WOC, which results in stronger asymmetric circulations in the intense vortex simulation. Because the cyclonic circulation that advects these gyres is stronger, the period of the center loops (about 7 h) is smaller in simulation IOC than in simulation WOC. These effects will be discussed in Section F below.

2. Terrain Effects on the Motion of the Intense Vortex

a. 5 m/s basic flow

Five simulations with the intense vortex approaching different portions of the mountain barrier in a 5 m/s zonal flow have been studied (Fig. 4.35). The track of the corresponding ocean-control (IOC) has again been included in the figure and duplicated for the other five initial locations for ease of comparison. Instead of large track deflections upstream of the barrier as in the weak vortex simulations (Fig. 4.12), all of the tracks of the intense vortex approaching different portions of the mountain barrier are very close to the track of the ocean-control (IOC). The smaller terrain effect on the track of an intense vortex is consistent with the observations (Figs. 4.4 and 4.7). The largest track displacement of the intense vortex in 5 m/s zonal flow is about 30 km, which is similar in magnitude to the weak vortex in a 10 m/s zonal flow simulation (Fig. 4.26). Both simulations (weak vortex in 10 m/s zonal flow and intense vortex in 5 m/s zonal flow) have a larger size and stronger circulation than the simulations in Fig. 4.12.

Three regions in which different factors control the vortex track deflections have been demonstrated when the weak vortex encounters the mountain

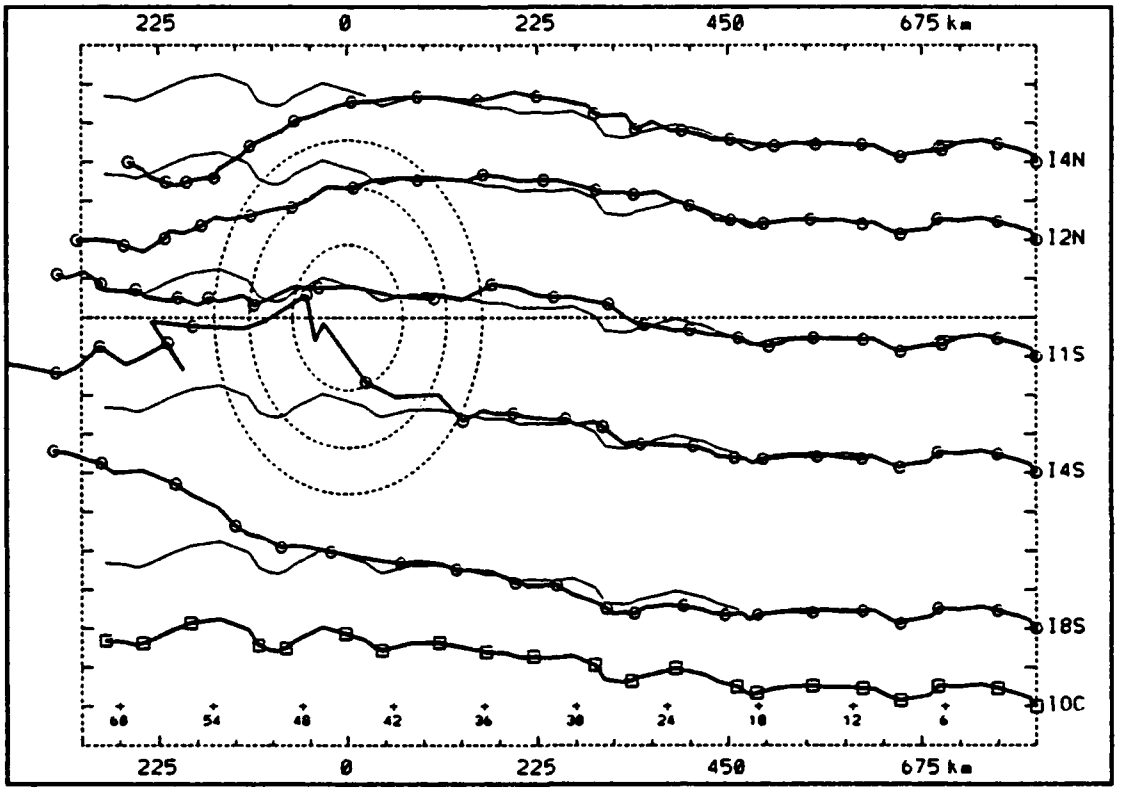

Fig. 4.35 As in Fig. 4.12, except for tracks of the intense vortices in 5 m/s zonal flow.

barrier (e.g., Fig. 4.14a). Similar characteristics also are found in the tracks of the five intense vortices in Fig. 4.35. The vectors (vortex-barrier deflections) in Fig. 4.36 are the departures of the vortex motion from the mean flow steering as in Fig. 4.14a. East of about 500 km upstream of the island, the vortex tracks are very similar to the mean flow steering, which is similar to Region-A of Fig. 4.14a. The Region-B in Fig. 4.36 is a zone of about 100 km in the east-west direction downstream of Region-A. In Region-B, southward deflections and decreases of the westward translation speed are similar to that of Fig. 4.14a. However, the region is narrower and is located farther to the east of the island. Within about 400 km of the island, differences between vortex motions from the steering become relatively large. As in Region-C of Fig. 4.14a, the effects of the vortex-barrier interaction have significant contributions to the storm motion in this case.

The time variations of the ventilation flow are highly correlated with the vortex motion relative to the mean flow of simulation I2N (Fig. 4.37a), as in the simulation of the weak vortex (e.g., Fig. 4.23). Therefore, the structures in the deep-layer mean wind will be used to study the vortex motion. Notice also in Fig. 4.37a that the ventilation flow of the intense vortex has relatively larger direction variations, particularly during the early hours of simulation. Although the trend of the ventilation flow before 36 h still agrees well with the storm motion, the consistency checks are relatively low, and the direction of the flow has larger amplitudes and shorter time scale variations. As in the ocean-control (IOC), the ventilation flow magnitude (Fig. 4.37) exceeds the relative vortex motion and is about 6 m/s at 42h. The strong precipitation

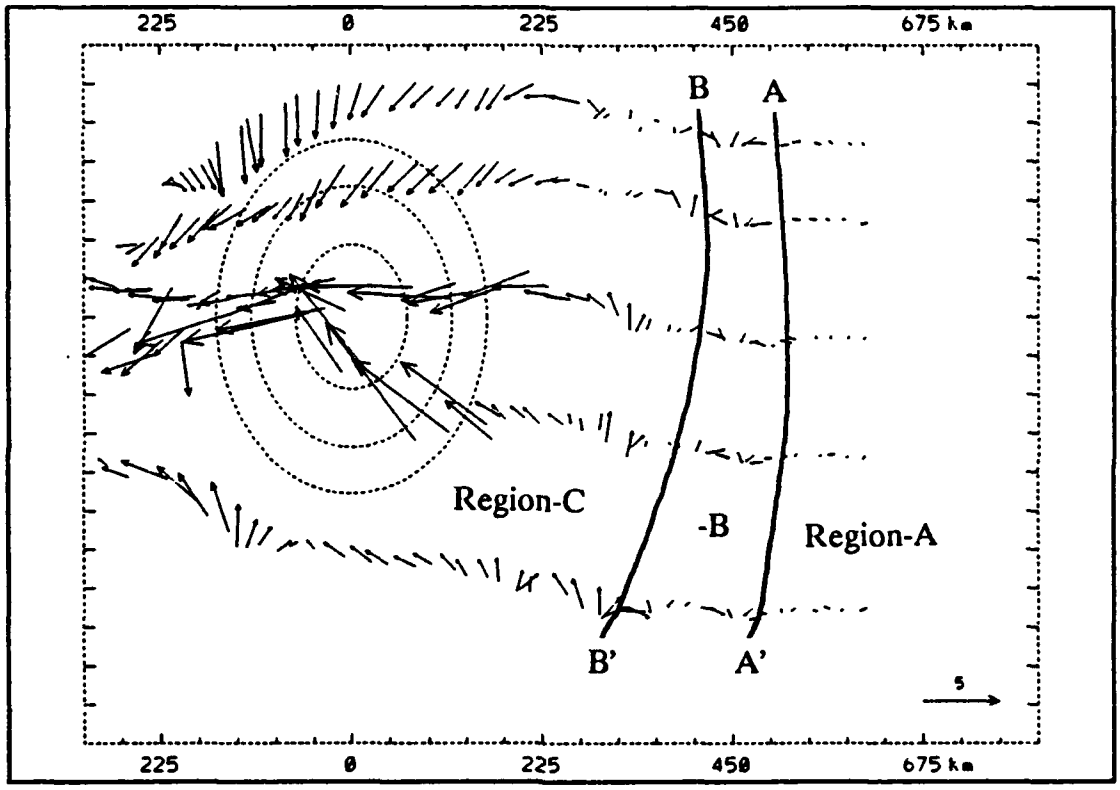

Fig. 4.36 Similar to Fig. 4.14a, except for the hourly vectors of the vortex-barrier deflections for the five intense vortex simulations in Fig. 4.35.

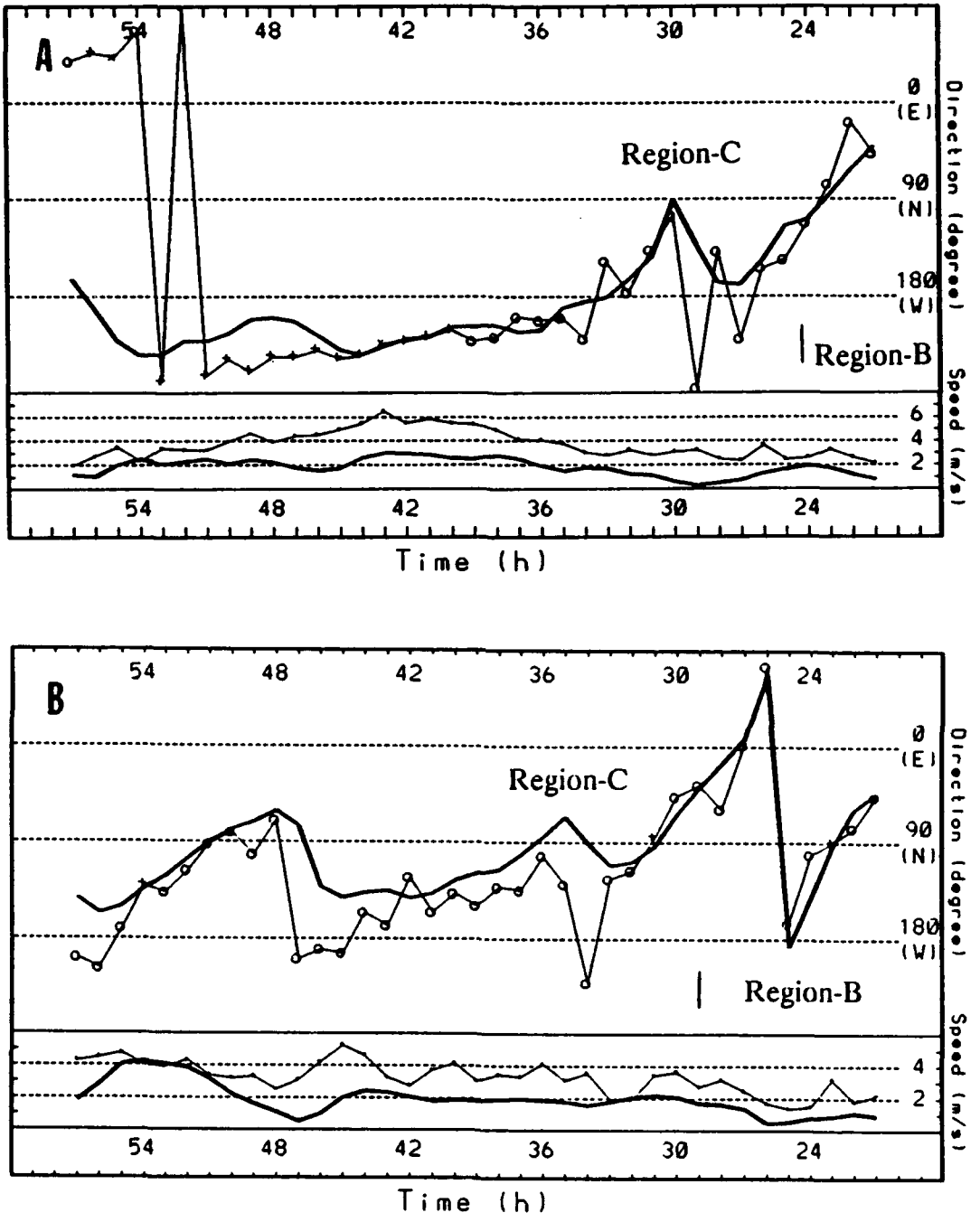

Fig. 4.37 As in Fig. 4.23 (or Fig. 4.19), except for the ventilation flow and the vortex motion deviations (thick solid) of (a) I2N and (b) I8S.

in the intense vortex case may be related to the rather noisy asymmetric flow distribution near the center.

Similar high correlations as in Fig. 4.37a between the ventilation flow and the vortex motion deviations are obtained for the vortices approaching other portions of the island. For the vortex approaching the southern end of the island (I8S), the motion (Fig. 4.37b) is very similar to the ocean-control (Fig. 4.33) in Region-A. Larger motion differences occur after the center moves into Region-C at about 29 h. The center no longer has a rather steady looping relative to the steering (Fig. 4.33), and the northwestward ventilation flow effectively accelerates the vortex northwestward. As the center passes just south of the island (about 48 h), the westward speed is slowed, which results in a more northward motion. When the center is southwest of the island (e.g., at 54 h), a similar northwestward ventilation flow as in the weak vortex case (Fig. 4.25b) is well correlated with the anticyclonic (relative to the island) vortex motion deviation.

Following the discussion of the motion of weak votices (i.e, Fig. 4.22), a sequence of deep-layer mean asymmetric and total wind fields from I2N is given in Fig. 4.38 to explain how the inner structure changes of the intense vortex are related to the vortex motion. At 18 h (Fig. 4.38a), the vortex is about 500 km east of the island center, which is inside Region-B. As the 15 m/s contour line is just over the east coast of the island, both the precipitation and the asymmetric wind distributions near the center are very similar to those of ocean-control (Fig. 4.34a). The inner structure of the vortex has not yet been significantly changed by the inclusion of the mountain barrier. However, the outer edge of the vortex circulation has altered the zonal and meridional

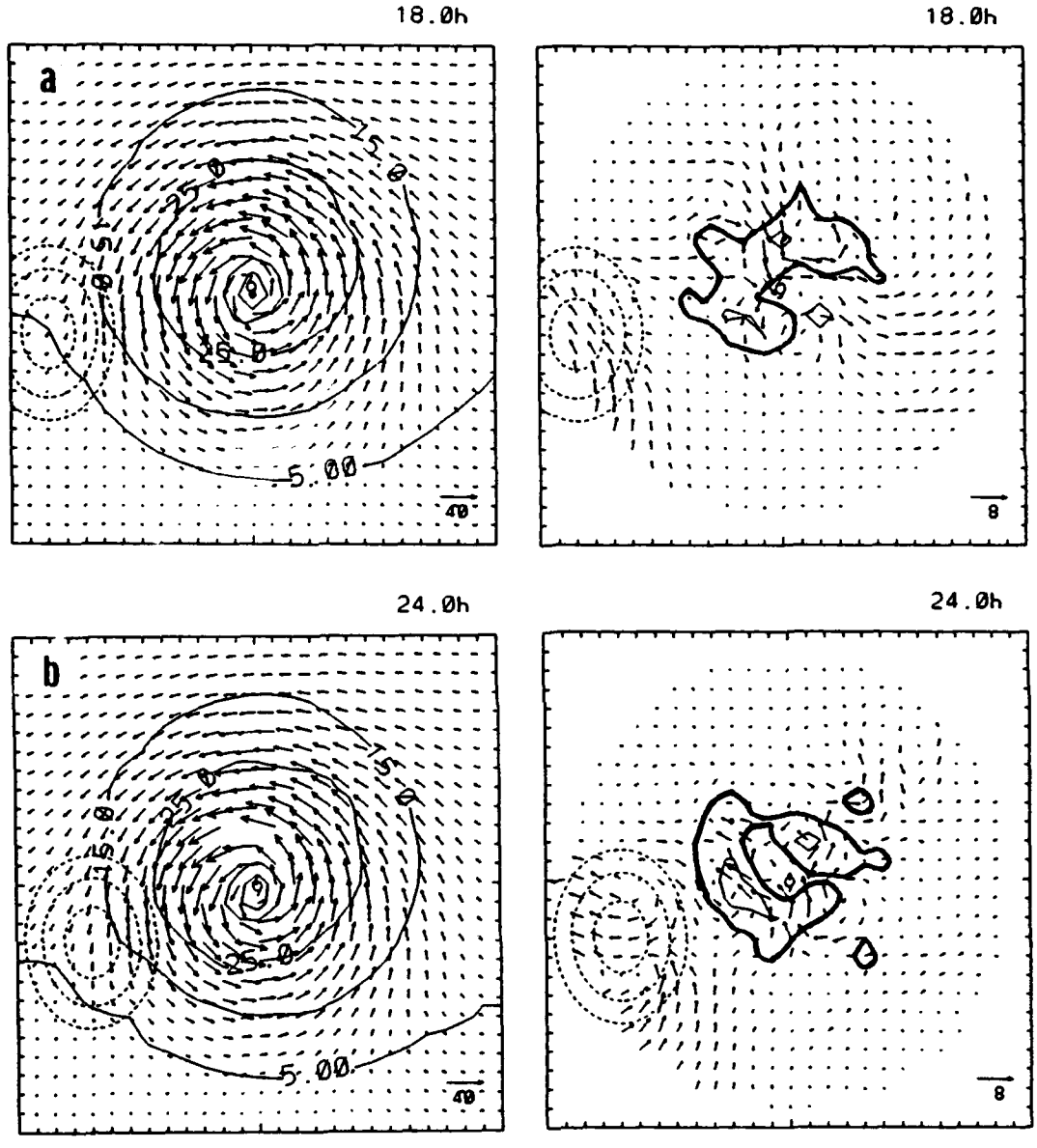

Fig. 4.38 As in Fig. 4.24, except for the deep-layer mean wind (left) and the asymmetric winds and the hourly accumulated precipitation (right) of I2N at (a) 18 h, (b) 24 h, (c) 30 h and (d) 36 h. Wind speeds greater than 40 m/s near the center are not plotted. The precipitation contours are in 10 mm/h intervals beginning from 5 mm/h (thick).

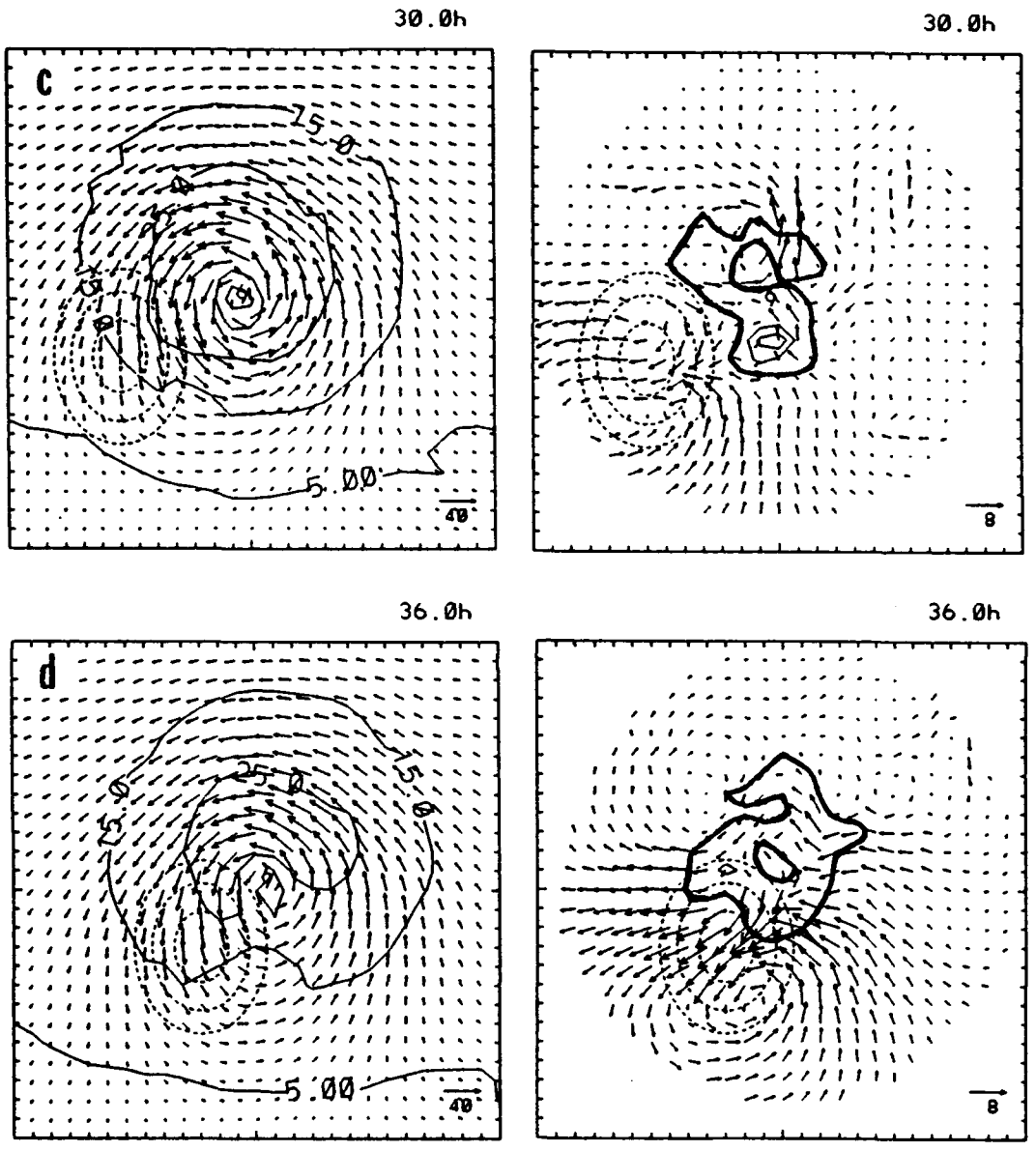

Fig. 4.38 (Continued)

flow near or over the island. As discussed before, the modification of the flow near the mountain by the outer vortex circulation contributes to the southward vortex motion in Region-B.

When the I2N center just enters the Region-C at 24 h (Fig. 4.38b), the maximum wind exceeds 40 m/s to the north of the center as a result of the general deepening of the system. As shown in Fig. 4.32, the vortex reaches maximum intensity at about 36 h. At 24 h, the northeastern portion of the island has been covered by strong winds of 15 m/s to 25 m/s. Although storm interaction with the mountain has begun, the modification of the vortex is still not significant, perhaps due to the stronger vortex stabilization mechanism (Carr and Williams 1989). The shape of the 15 m/s and 25 m/s contours has not changed much since 18 h. The inclusion of the barrier stabilizes the precipitation cells with a stronger cell on the mountain side of the vortex, so that the rotation of the precipitation cells is less important compared to the effect of the quasi-stationary cell on the barrier side of the vortex (compare to Fig. 4.34b). As a result, the asymmetric flow pattern over the barrier is modified with the ventilation flow changing from westward (Fig. 4.34b) to northwestward (Fig. 4.38b). The increase in the northward ventilation flow speed is correlated with the northward displacements relative to the control. As the I2N center moves closer to the island at 30 h (Fig. 4.38c), significant modifications of the flow structure are still limited to the southern portion of the barrier. The ventilation flow due to this asymmetric structure is still not effective in producing large motion deviations from the steering.

Significant modifications of the inner vortex structure only occur when the vortex is much closer to the island at 36 h (Fig. 4.38d). First, the winds in the southern part of the vortex are significantly slowed by the mountain barrier. Second, larger cyclonic flow exists between the vortex center and the island due to the mountain channeling effects. The combination of these blocking and channeling effects creates an intense anticyclonic gyre south of the center, and a southwestward ventilation flow that is consistent with the acceleration of the vortex toward the southwest (Fig. 4.37a). After the center crosses the mountain to the western coastal region at 48 h, slower cyclonic winds are found on the south and west sides of the center (not shown). This kind of wind distribution produces a ventilation flow that contributes to the cyclonic vortex motion relative to the island (Fig. 4.35).

Two interesting differences are noted between Fig. 4.35 and Fig. 4.14a. First, the vortex-barrier deflections upstream and near the island for an intense vortex significantly accelerate the vortex toward the island. By contrast, the vortex-barrier deflections of the weak vortex significantly slows the vortex westward speed. Second, the intense storm (i.e., I2N) does not continuously move toward the north to pass over the mountain at a lower altitude. The intense vortex turns toward the south early (e.g., I2N at about 33 h in Fig. 4.35) and landfalls on the northeastern coast before it passes the long-axis of the island.

Although this study has demonstrated that the vortex deflections in Region-C are correlated with the inner structure changes of the vortex, a prediction of how an arbitrary vortex structure will be changed by the mountain is evidently ..ther

complex. In the simulations of intense vortices encountering the mountain, a low-level trough forms over and near the island on the downwind side of the cyclonic vortex flow (Fig. 4.39a). Because the vortex flow is strong and produces large downslope motions, the trough is still identifiable at the 700 mb level (Fig. 4.39b). This pressure trough contributes to a stronger northerly wind on the west side of the vortex center (Fig. 4.38d) and favors the movement of the low center southward along the trough.

b. 2.5 m/s basic flow

Two simulations of an intense vortex in a 2.5 m/s zonal flow have been examined to study the mountain barrier effects on their tracks. The tracks of the two vortices (I1Ss and I4Ss) and the track of their corresponding ocean-control (IOCs) are given in Fig. 4.40. Both of the I1Ss and I4Ss centers are to the north of the IOCs case (Fig. 4.40) about 450 km upstream of the island. As in other vortices in Region-B, the vortices are slightly deflected to the south of the mean steering flow (Fig. 4.41). Perhaps because the intense vortex has a similar size in both the 5 m/s and the 2.5 m/s zonal flows, line BB' of Fig. 4.36 and Fig. 4.41 is located at about the same distance (400 km) upstream of the island. West of line BB', a zone with stronger northward departures (Fig. 4.41) is similar to the case with vortices in a 5 m/s zonal flow (Fig. 4.36). However, this region with the northward motion deviations is relatively narrow for the 2.5 m/s simulations. The vortices turn southward at about 270 km (I4Ss) and 310 km (I1Ss) upstream of the island center (Fig. 4.40).

The estimated ventilation flow speed (Fig. 4.42) for the intense vortex in a 2.5 m/s zonal flow has a systematic bias (about 2 m/s) relative to the vortex motion

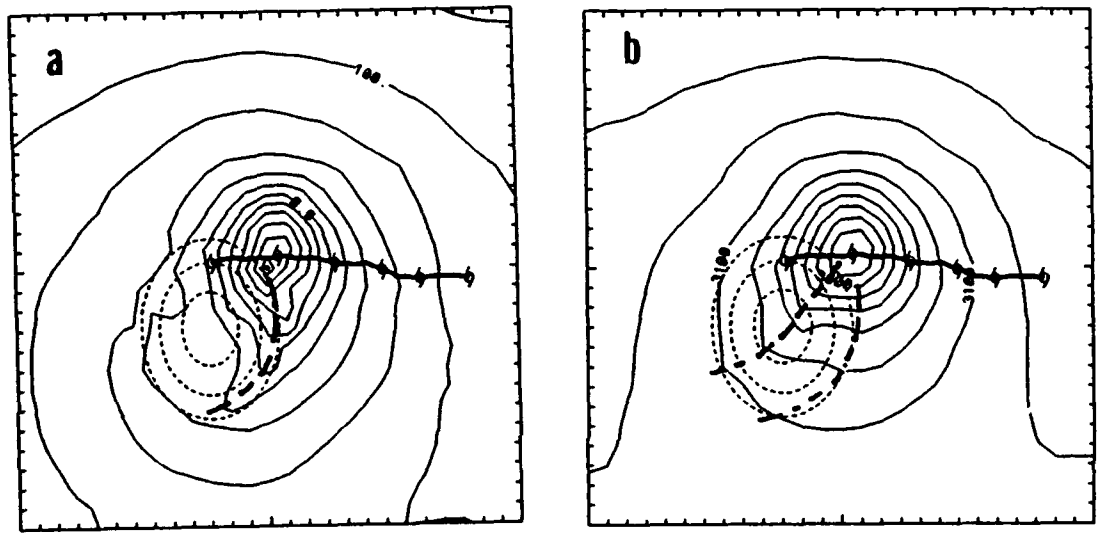

Fig. 4.39 Heights (m) of (a) 1000 mb and (b) 700 mb surfaces at 36 h from simulation I2N. Dashed lines highlight the pressure troughs. The domain is the same as in Fig. 4.38d. Six-hourly vortex positions from 12 h to 42 h are indicated with typhoon symbols.

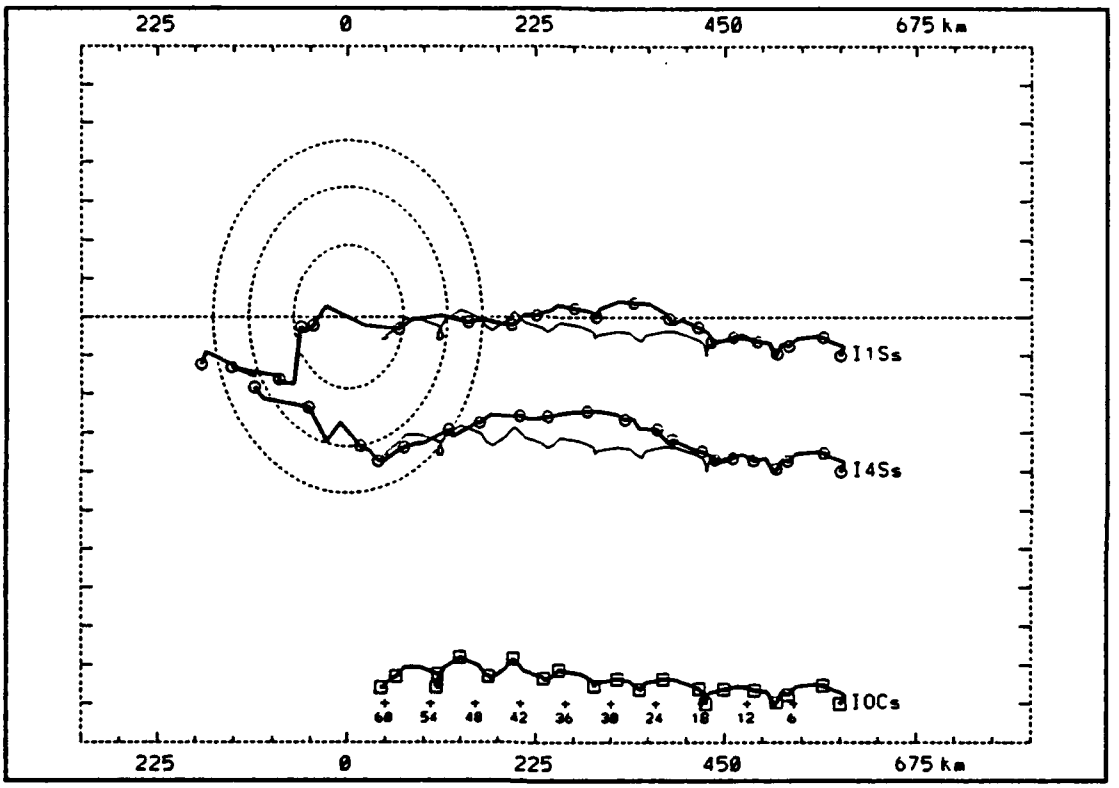

Fig. 4.40 As in Fig. 4.29, except for the tracks of the intense vortices in a 2.5 m/s zonal flow.

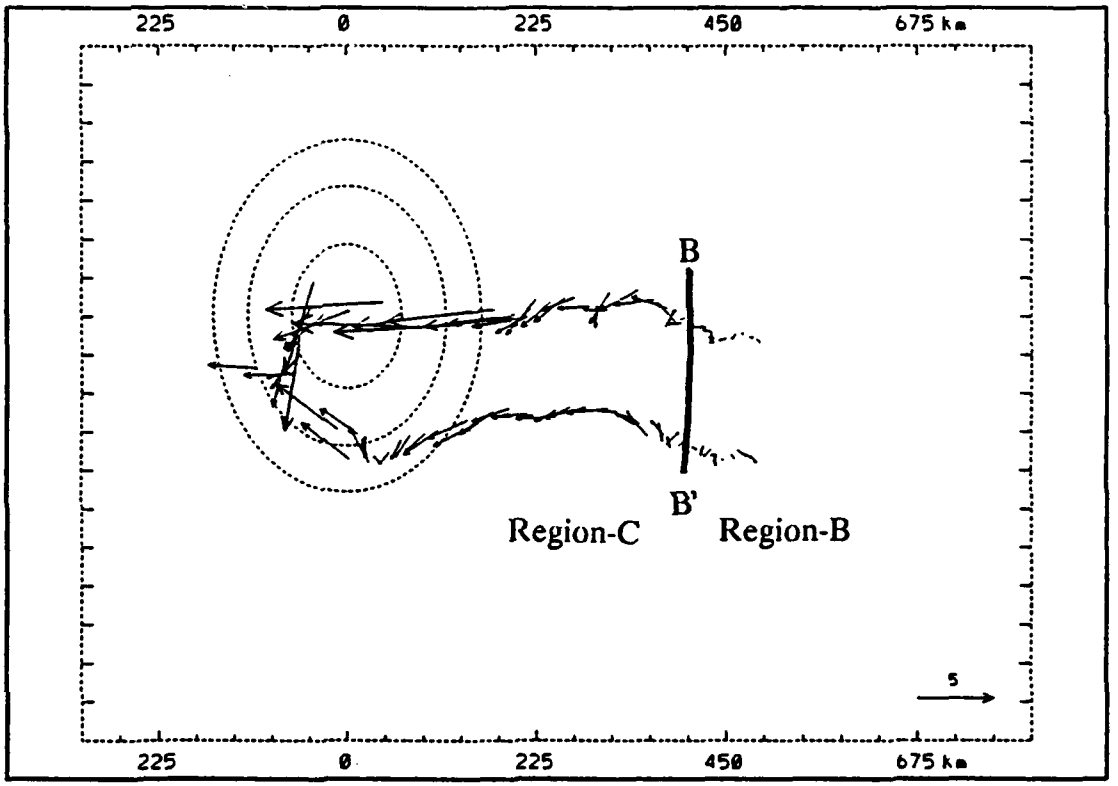

Fig. 4.41 As in Fig. 4.30, except for the hourly vectors of the vortex-barrier deflections for the two intense vortices in a 2.5 m/s zonal flow.

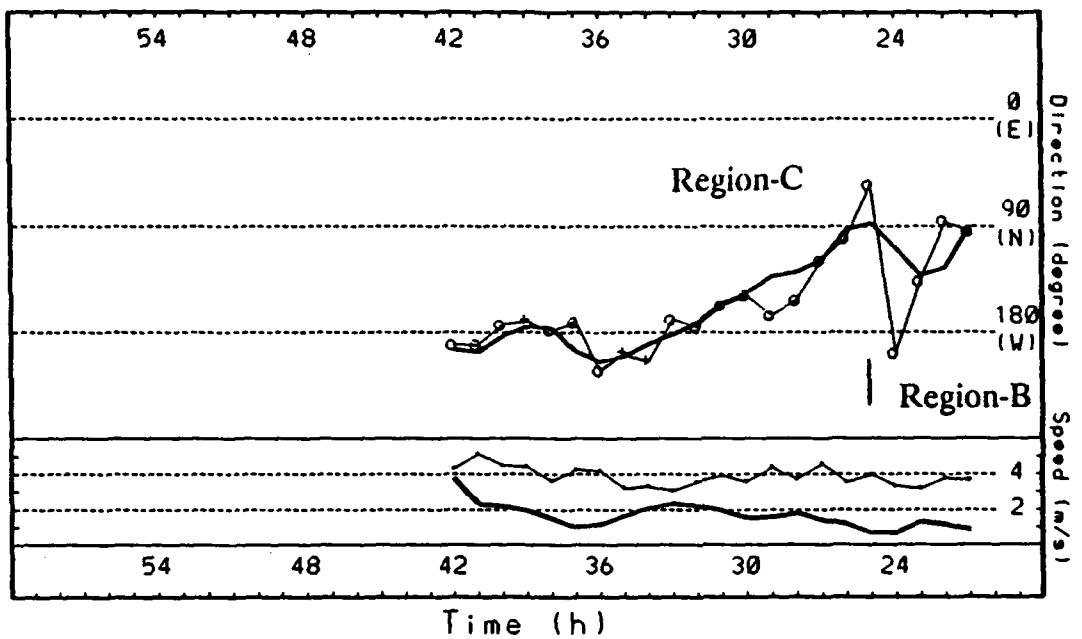

Fig. 4.42 As in Fig. 4.37a, except for the ventilation flow and the motion deviations (thick solid) of I4Ss. Because of the significant vertical separation of the centers, the ventilation flow and vortex motion are not shown after 42 h.

deviation as in the 5 m/s zonal flow cases (e.g., Fig. 4.37). Nevertheless, the correlation between the ventilation flow and the vortex motion direction change is still very high especially when the center is within Region-C. Shortly after the vortex enters Region-C, the intense vortex in a 2.5 m/s zonal flow accelerates toward the island.

When the intense I4Ss vortex is located about 180 km from the east coast at 30 h (Fig. 4.43a), the deep-layer mean flow has an outward (westward) flow deflection on the west side of the center. This asymmetric wind distribution induces a ventilation flow across the center, and contributes to the small northward and large westward vortex accelerations (Fig. 4.42). When the center is located closer to the island at 42 h (Fig. 4.43b), the deep-layer mean flow is significantly modified by the barrier with slower wind speeds south of the center. Furthermore, the size (radius to the outer 15 m/s wind speed) is reduced on the west side. Moreover, the northerly wind between the vortex center and the mountain is increased. This wind speed increase due to the channeling effect is similar to Fig. 4.28b (weak vortex in 10 m/s zonal flow) and Fig. 4.38d (intense vortex in 5 m/s zonal flow), and produces a southward asymmetric circulation across the vortex center that contributes to the southward vortex motion. Because the vortices in Fig. 4.41 move slower than those in Fig. 4.36, the southward turn and the increase of the westward motion upstream of the barrier are more pronounced in the 2.5 m/s simulations.

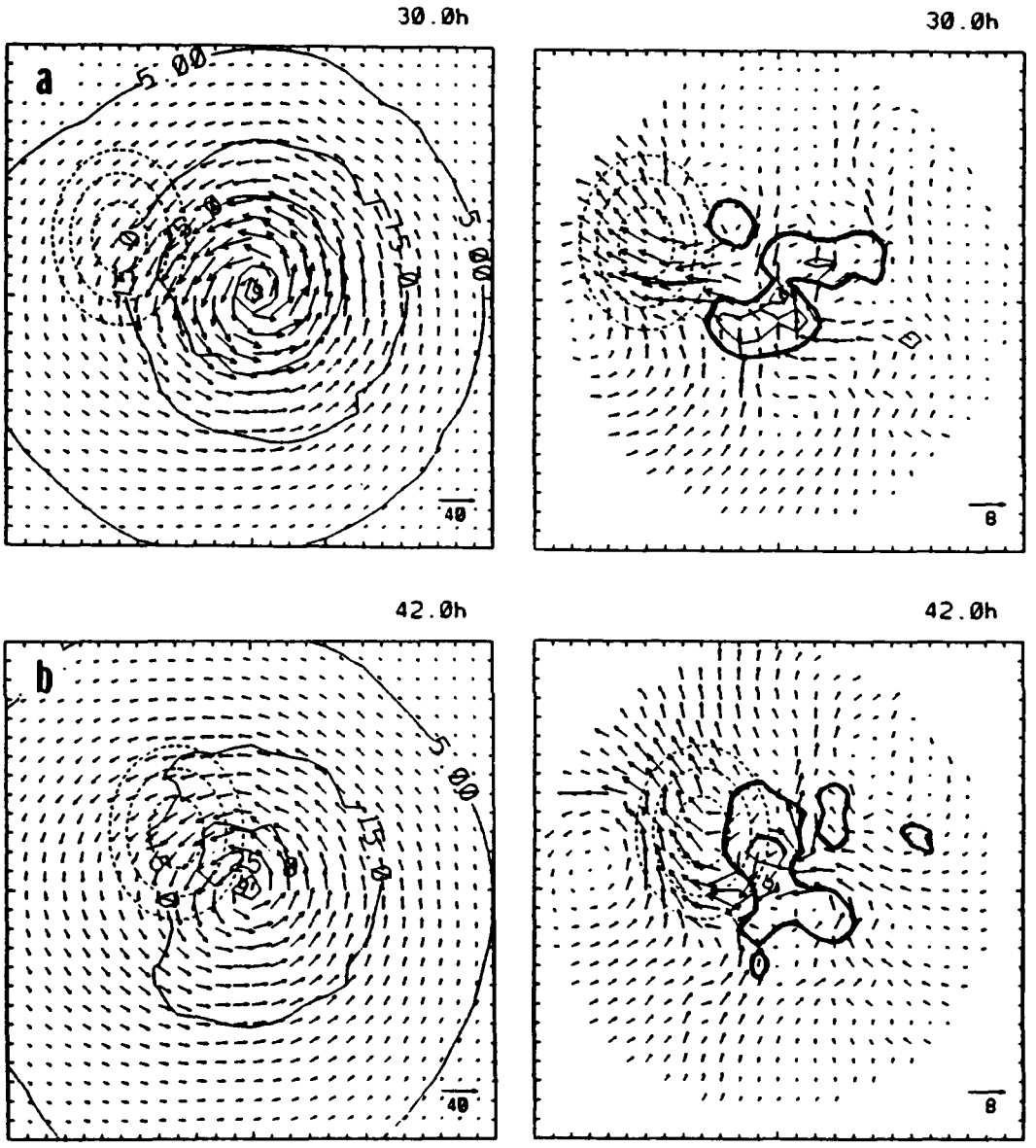

Fig. 4.43 As in Fig. 4.38, except for the deep-layer mean wind (left) and the asymmetric winds and the hourly accumulated precipitation (right) of I4Ss at (a) 30 h and (b) 42 h.

F. VORTEX MOTION ASSOCIATED WITH DISTRIBUTION OF LATENT HEATING

Short-time scale (6 h to 12 h) center position oscillations have appeared in many of the above simulations. For example, recall the tracks of WOC (Fig. 4.10), WOCs (Fig. 4.29), IOC (Fig. 4.32), IOCs (Fig. 4.40) and others. As was indicated, the asymmetric distribution of latent heating is related to these oscillations. The ocean-control simulation with the intense vortex in a 2.5 m/s current (IOCs) will be used to demonstrate how the latent heating distribution is related to the vortex motion via the asymmetric circulation (ventilation flow).

As in other simulations (e.g., Figs. 4.18, 4.20, 4.23, 4.33, 4.37 and 4.42), a high correlation is found between the ventilation flow and the vortex motion deviations in the IOCs simulation (Fig. 4.44). Although the vortex is generally moving toward the west with an average speed of about 2.5 to 3.0 m/s, short-time scale cyclonic looping relative to the steering with a period of about 6-7 h is very pronounced.

Willoughby (1992) included a rotating mass sink-source in a shallow water model to represent convective clusters rotating about the tropical cyclone. His test demonstrated that vortex looping may be due to the asymmetric heating. To examine whether the looping in the IOCs simulation (Fig. 4.44) is related to the asymmetric heating, the time variations of the phases and amplitudes of the wavenumber one hourly accumulated precipitation are shown in Fig. 4.45. In the figure, the spectrum analysis is calculated for the radially-averaged (45 km to 225 km band from the center) hourly accumulated precipitation (PRCP). The phase of the wavenumber one component of PRCP indicates

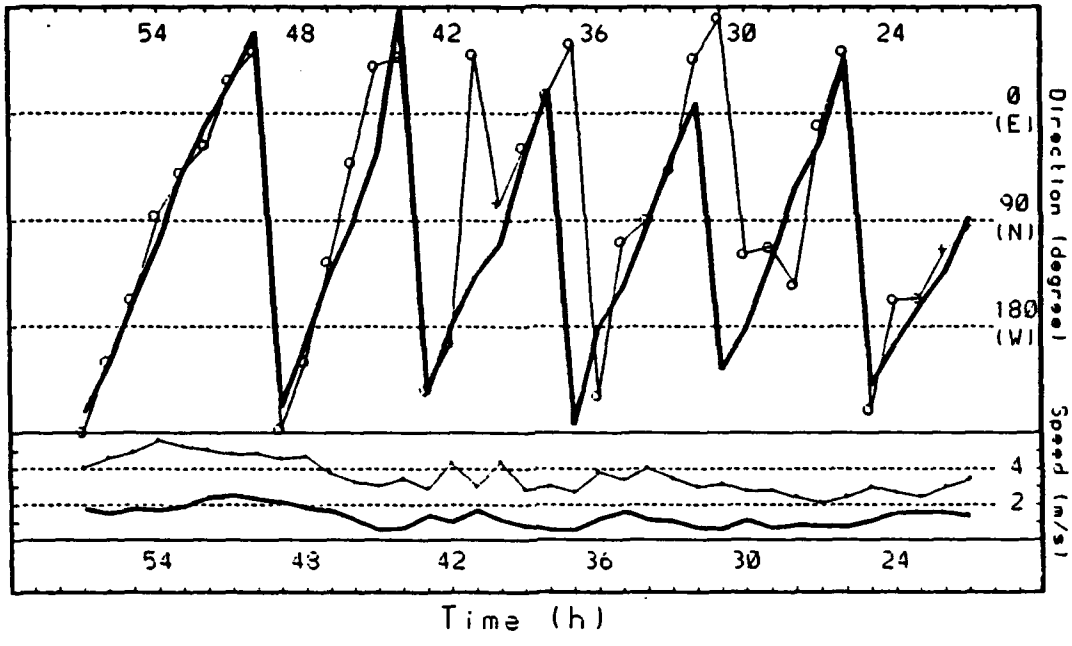

Fig. 4.44 As in Fig. 4.37a, except for the ventilation flow and the vortex motion deviations (thick solid) in the IOCs simulation.

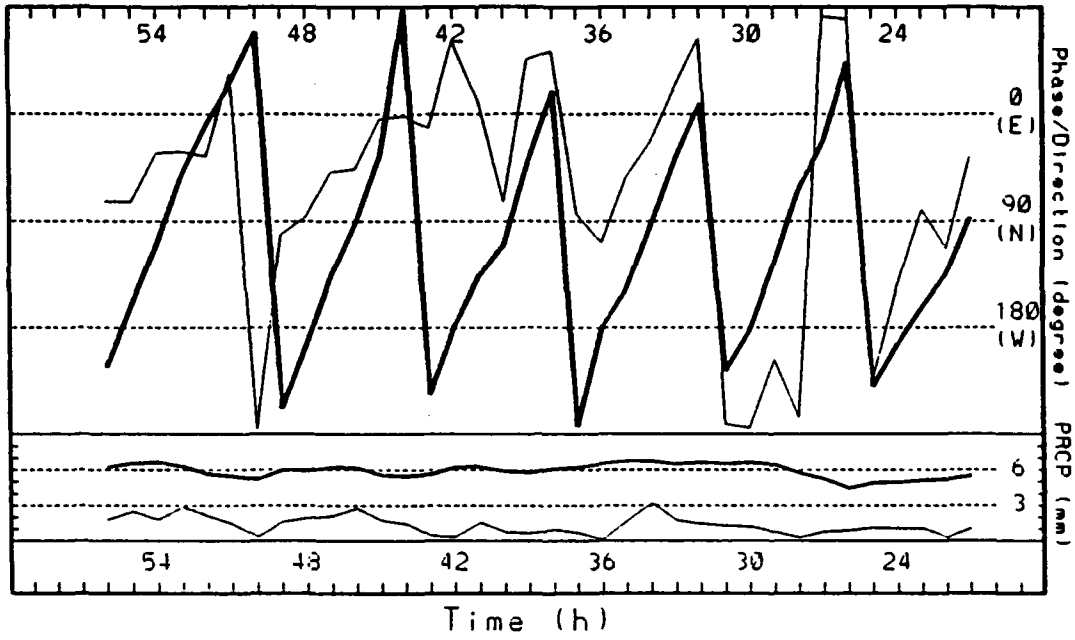

Fig. 4.45 Similar to Fig. 4.18, except for the time variations of the phase (top panel, thin line in units of degrees) and the amplitude (bottom panel, thin line in units of mm/h) of the wavenumber one radially-averaged hourly accumulated precipitation (see text) for the IOCs simulation. The vortex motion direction relative to the mean flow (top panel, thick line) and the mean precipitation rate (bottom panel) are also shown.

the direction of the precipitation maximum relative to the vortex center. For example, a phase of 90 (180) degrees indicates the wavenumber one maximum precipitation is north (west) of the center. As shown in the bottom panel of Fig. 4.45, the mean PRCP is about 6 mm and the wavenumber one amplitude of the PRCP is about 1-2 mm, with a maximum value of about 3.5 mm at 34 h. Similar to the vortex motion, the wavenumber one PRCP also has short-time variations with a period of about 6 to 8 h. The phase of the wavenumber one PRCP generally shifts cyclonically in a somewhat erratic manner.

Notice that the difference between the motion direction and the phase of wavenumber one of PRCP does not maintain a constant relationship. Therefore, the effect of precipitation heating is not represented simply by mass sink-source and the short-time oscillation of the vortex motion also not be related to the wavenumber one heating in a simple way as demonstrated by Willoughby (1992) or heating is not represented simply by mass sink-source.

Detailed distributions of the hourly accumulated precipitation around the center of IOCs are shown in Fig. 4.46 from 33 h to 44 h. At 34 h, the wavenumber one of PRCP would be associated with the heavy precipitation on the east side of the center and the dry region on the opposite side. However, a pattern of three precipitation cells is also clearly present at a radial distance of about three gridpoints from the center, and these cells move cyclonically around the center with a period of about 9 to 10 h.

The asymmetric wind components and the hourly accumulated precipitation are overlaid in Fig. 4.47 to explain the relation of the 9-10 h rotating precipitation cells to

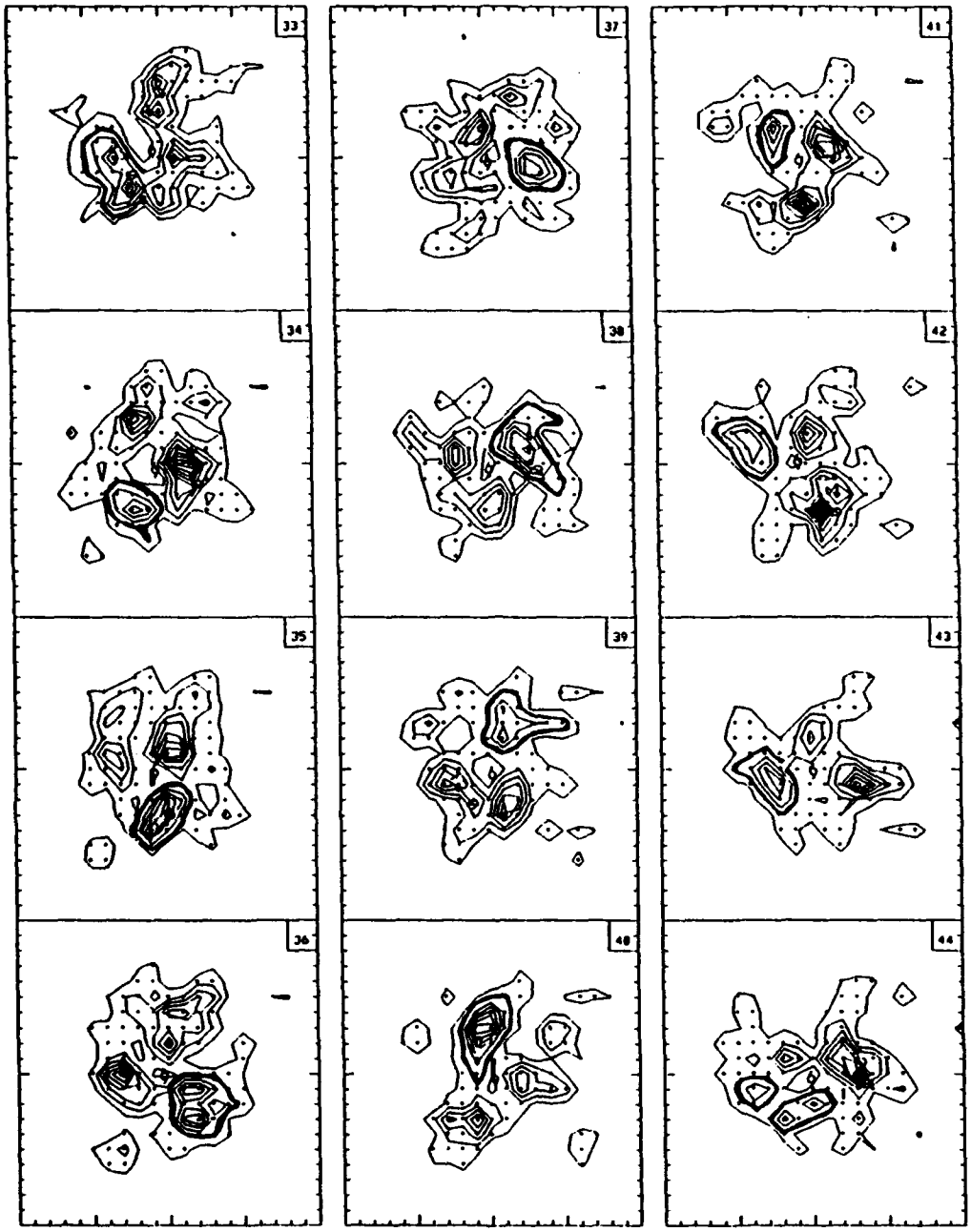

Fig. 4.46 Distribution of the hourly accumulated precipitation near the vortex center (typhoon symbol, near the center of each diagram) for the IOCs simulation from 33 h (top-left, time indicated at the top-right corner of each diagram) to 44 h. The hourly accumulated precipitation contours starts from 3 mm and the contour interval is 3 mm. The area with an hourly accumulated precipitation greater than 3 mm is shaded, and the 6 mm contour surrounding one of the precipitation cells is highlighted. The domain of each diagram covers 21 X 21 grid points (900 km X 900 km).

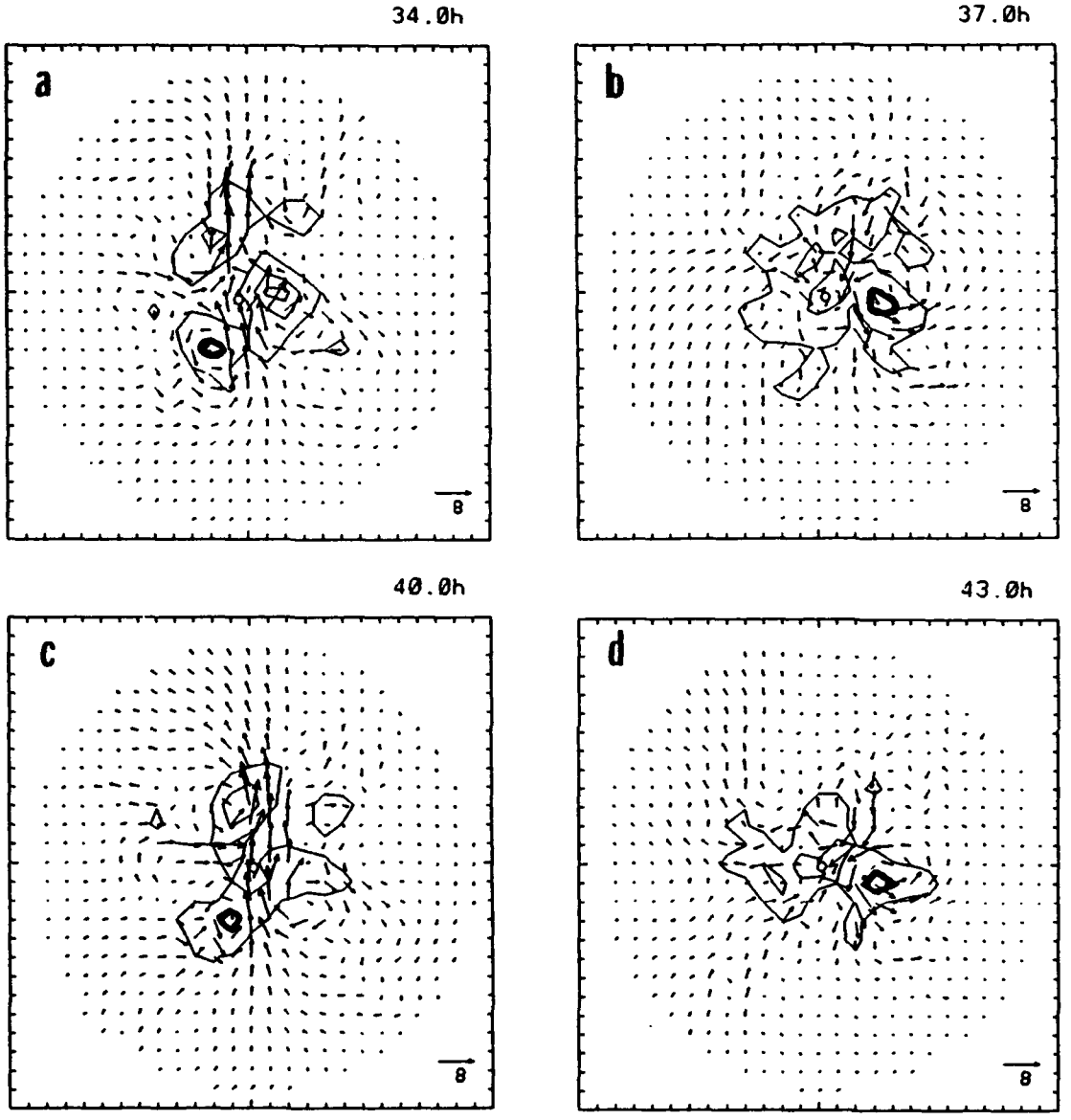

Fig. 4.47 As Fig. 4.34, except for the asymmetric component of the deep-layer mean wind and the hourly accumulated precipitation of IOCs at (a)34 h, (b) 37 h, (c) 40 h and (d) 43 h. The 15 mm precipitation contours associated with the α-cell (see text) at 34 h and 37 h and with α2-cell (see text) at 40 h and 43 h are highlighted.

the faster (6-7 h) track oscillations (Fig. 4.44). Although the asymmetric wind components are very noisy near the center, one of the three precipitation cells (α-cell) has a cyclonic asymmetric circulation associated with it. The other two precipitation cells may or may not be associated with such a cyclonic asymmetric circulation. The ventilation flow near the center is dominated by the asymmetric flow associated with the α-cell. Because the α-cell is located to the southwest of the center at 34 h (Fig. 4.47a), and the southerly wind associated with the α-cell penetrates the center, this ventilation flow is correlated with the northward vortex motion deviation. As the α-cell rotates around the center, the cyclonic asymmetric circulation cell also rotates for a certain period of time. Perhaps due to the change of the precipitation pattern, the cyclonic asymmetric circulation and the associated ventilation flow are also changed. At 37 h (Fig. 4.47b), the cyclonic circulation associated with the α-cell moves to the east of the center, and the size of the circulation is larger than at 34 h. However, the asymmetric flow does not directly penetrate the center. The α-cell continues to move around the center cyclonically. Although the cyclonic circulation at 40 h (Fig. 4.47c) is still associated with the cell to the north-northwest of the center, the center of the α-cell and the center of the circulation are not co-located as well as before. Meanwhile, a second cell (α2-cell) is found at about the same location relative to the center as the α-cell at 34 h. The α2-cell is becoming organized with an associated cyclonic circulation. Although the cells only complete two-thirds of a cycle from 34 h to 40 h, the ventilation flow at 40 h is very similar to that at 34 h, so that a cycle of the ventilation flow change (Fig. 4.44) is complete. The intensity of the α-cell becomes weaker after 40 h (i.e., 41 h and

42 h in Fig. 4.46), and the cyclonic circulation is no longer associated with the α-cell (not shown). At 43 h (Fig. 4.47d), the dominant asymmetric cyclonic circulation associated with the $\alpha 2$-cell are located at about the same location as the α-cell at 37 h. Both ventilation flows associated with the asymmetric circulation at 37 h and 43 h are related to the southward vortex motion deviations (Fig. 4.44).

When a mountain barrier is included in the simulation, the regular cyclonic rotation of the precipitation cells is restricted. Using the simulation I4Ss as an example, the most important feature is the development of a heavy precipitation cell (T-cell) on the east slope of the mountain (Fig. 4.48). The T-cell does not move over the barrier to circle around the center as do the cells in the simulation IOCs. Such enhanced precipitation regions have been observed on the east slope of the CMR and will be discussed in the next chapter. Although cyclonic shifting cells are found in other parts of the domain (Fig. 4.48), the cell motions are not as regular as in simulation IOCs. When a cell moves close to the T-cell, it may change the intensity of the T-cell (e.g., 37 h of Fig. 4.48) and later join with the T-cell (e.g., 38 h of Fig. 4.48).

Because the precipitation cells of I4Ss no longer have a regular rotation around the center, a looping motion such as in simulation IOCs (Fig. 4.44) is not found (Fig. 4.42). As was indicated in Section E, the heavy precipitation cell on the east slope of the mountain lasts for several hours (Fig. 4.48), but the dominant feature of the asymmetric circulation of I4Ss (Fig. 4.43) is the flow created by the dynamical effect of the terrain. A clear and simple relation between the T-cell and the vortex motion of I4Ss is not revealed.

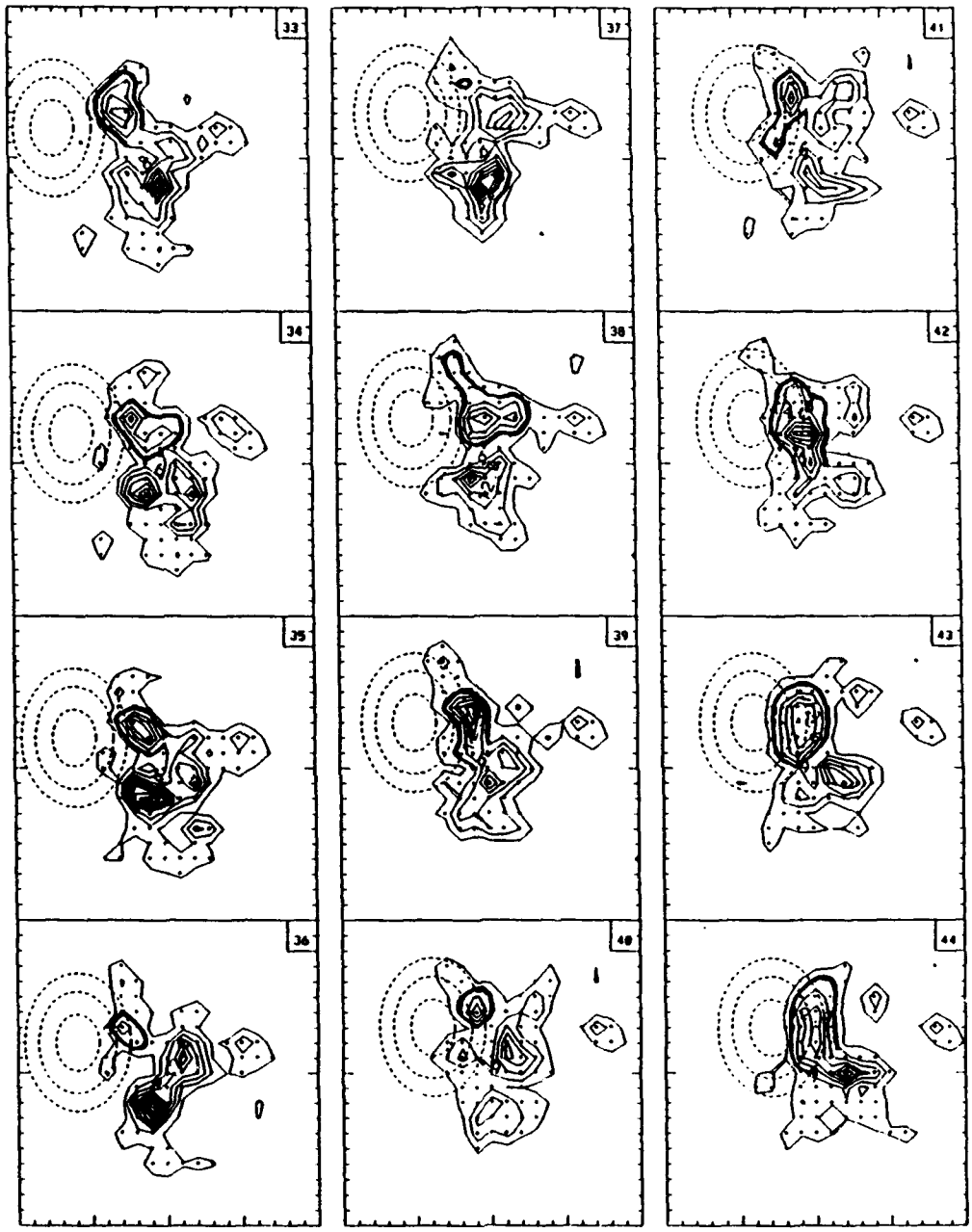

Fig. 4.48 As in Fig. 4.46, except for the hourly accumulated precipitation near the vortex center of I4Ss. 1,000 m and 2,000 m contours of the idealized mountain barrier are indicated by dashed lines.

Similar modifications of the precipitation field have been found in the other simulations with the intense vortex (i.e., Fig. 4.38). In all of these simulations, the inclusion of the barrier stabilizes the precipitation cells from rotating around the center. However, the track change due to the latent heating effect is smaller than the track changes associated with the dynamical effects of the terrain interaction with the vortex flow. In the simulation with a weak vortex encountering the mountain (i.e., Figs. 4.22, 4.24, 4.25, 4.28 and 4.31), the intensity of the precipitation is weaker. Therefore, the contribution of the latent heating effect to the motion of the weak vortex is even smaller.

The small flow modification via the precipitation heating effect may be because the small-scale disturbance on the mass field is likely to adjust to the wind field from the geostrophic adjustment theory (e.g., Chapter 2.8 of Haltiner and Williams 1980). Moreover, the heavy precipitation area is generally associated with strong low-level convergence and upward motion in the model. Thus, expansion cooling will reduce the precipitation warming effect. Future research should test the sensitivity to the latent heating scheme and reduce the grid size to study their impact on the vortex motion, which may advance the understanding of how the precipitation heating contributes to the vortex motion.

G. SUMMARY

The observational study of Brand and Blelloch (1974) on typhoon track deflections upstream of Taiwan has been extended by including more cases and defining a reference track via a second-order polynomial curve fitted to the JTWC 6-h best track positions.

For all 53 westward-moving typhoons that landfalled on Taiwan from 1947 to 1990, a downstream acceleration is noted with along-track speed increases from about 4.5 m/s at 72 h prior to landfall to about 6 m/s at landfall. However, this rather steady downstream along-track acceleration is likely to be due to environmental flow changes rather than to interaction with the topography of Taiwan.

The along-track acceleration does depend on the typhoon intensity. For 18 weaker typhoons, the averaged along-track speed is not increased from about 48 h prior to landfall. This suggests the CMR may slow the weaker storm upstream, but the CMR has relatively small effect on more intense storms. Changes in the along-track component depend on the typhoon translation speed. The CMR apparently decelerates the slower-moving storms upstream, but has a relatively small effect on the faster-moving typhoons.

The cross-track deflections are calculated as the displacement of the center locations from the second-order polynomial curve fitted to the two ends of the track positions from -72 h to -54 h prior to landfall and from 6 h to 18 h after leaving Taiwan. The upstream cross-track deflections are at first consistent with the blockage of the low-level steering flow around the island. However, another deflecting force turns the track back toward the island prior to landfall. Larger cross-track deflections are found for the weaker or slower-moving typhoons.

A version of the Limited-Area Weather Prediction Model of the Naval Research Laboratory with a 45 km horizontal resolution has been employed to simulate the Taiwan terrain effect on the westward-moving typhoon motion. In the simulation, a weak

typhoon is represented by a 'spun-up' vortex that has a maximum azimuthally averaged wind at 900 mb of about 19 m/s and a size of about 200 km. The vortex is embedded in a 5 m/s basic flow. The Taiwan topography, which is simplified to be an isolated, elliptical-shaped barrier with a horizontal scale slightly larger and a height (2500 m) lower than the CMR, is then included.

The simulations have similar results to the observational study. As the basic flow is more clearly defined in the simulation, the terrain effect is relatively easier to isolate. Three-dimensional structures from the simulations allow an investigation of the physics causing such track changes.

Four regions are depicted along the tracks. Only small track deviations from the ocean-only control simulation occur in Region-A, which is more than about 400 km upstream of the barrier for a weak, small vortex. Thus, this first region has an insignificant barrier effect on the vortex motion.

Significant track deflections occur as the vortex moves closer to the barrier. A second region (B) between about 250 to 400 km upstream has track deflections in the same sense, but larger in magnitude, than those expected from a basic flow approaching the barrier. The larger track deflections in Region-B are due to the superposition of the outer edge of the vortex circulation onto the basic flow that acts to accentuate the blocking effect of the barrier.

In Region-C, which extends from about 250 km upstream to the barrier, the track deflections are opposite to those expected from barrier blocking effects. The imbalance in the inner vortex structure as it approaches the barrier induces an asymmetric flow

across the vortex center. This asymmetric circulation leads to both a deceleration of the zonal component and a northward deflection of the storms approaching the southern and central portion of the barrier. For storms passing the northern end, the highest wind region on the right side of the path does not interact with the barrier, so the effect is much smaller and is toward the south.

A fourth region is defined when the storm center is over the barrier. Erratic tracks include discontinuous jumps from the east side of the barrier to the west side of the barrier. These unusual tracks depend on detailed terrain-induced structure changes that will be discussed in Chapter VI.

Similar regions (e.g., Region-B and Region-C) can be identified in simulations in which the basic flow is increased to 10 m/s or decreased to 2.5 m/s. Even though the same initial vortex is superposed, the apparent size of the wind structure is increased (decreased) as the basic current speed is increased (decreased). For example, the radii at which critical wind speeds such as 15 m/s begin to interact with the topography are changed. In particular, the eastern boundaries of Region-B and Region-C are increased to 585 km and 400 km respectively for the 10 m/s case. Another important effect is that the time during which the impact of the barrier forcing is experienced by the storm circulation is reduced (lengthened) when the basic current speed is increased (decreased). Thus, the slowly (rapidly) moving storm has much larger (smaller) track deflections than the 5 m/s case. These trends are similar to the observations.

Simulations with a more intense (33 m/s versus 19 m/s) vortex also contained track deflections with similar regions. However, the storm track deflections upstream of the

barrier are smaller than in the weak vortex, which is consistent with the observations. Thus, the intense storm circulation appears to resist the development of asymmetric circulations more so than in the weak vortex case, perhaps due to the vortex stabilization mechanism of Carr and Williams (1989).

V. OBSERVATIONAL STUDY OF TERRAIN EFFECTS ON THE SURFACE STRUCTURE OF TYPHOONS

A. DATA AND METHODS

The area of study and the outline of Taiwan terrain are shown in Fig. 5.1. The 22 surface stations over the area are identified with a letter-number code that is related to the relative geographical locations on the island and are explained in TABLE IV. The latitude, longitude and altitude of the stations are also included in the table.

The analysis uses observations from the 20-year period (1971-1990). A list of the 82 typhoons that resulted in a total of 1446 cases (synoptic observation times at 3 h intervals) is given in TABLE V. A typhoon is selected for inclusion in this study if at any time the surface center is located inside the domain of 19°-27°N, 117°-125°E, as delineated in Fig. 5.2. The typhoon center locations are also taken from the JTWC best tracks. For each typhoon, the time starts 14 h prior to the first occasion the typhoon enters the domain, and ends 2 h after the typhoon leaves the domain. Thus, the number of cases from each typhoon depends on its duration inside the domain. The occurrences of typhoon (Fig. 5.2) have a maximum southeast of Taiwan, which defines the main track of the typhoons approaching Taiwan from the southeast. Another maximum is located to the southwest of Taiwan near Dongshadao (20.5°N, 118°E), which includes both westward-moving typhoons passing south of Taiwan and those active in the northern South China Sea. A relative minimum is found over western Taiwan and the adjacent

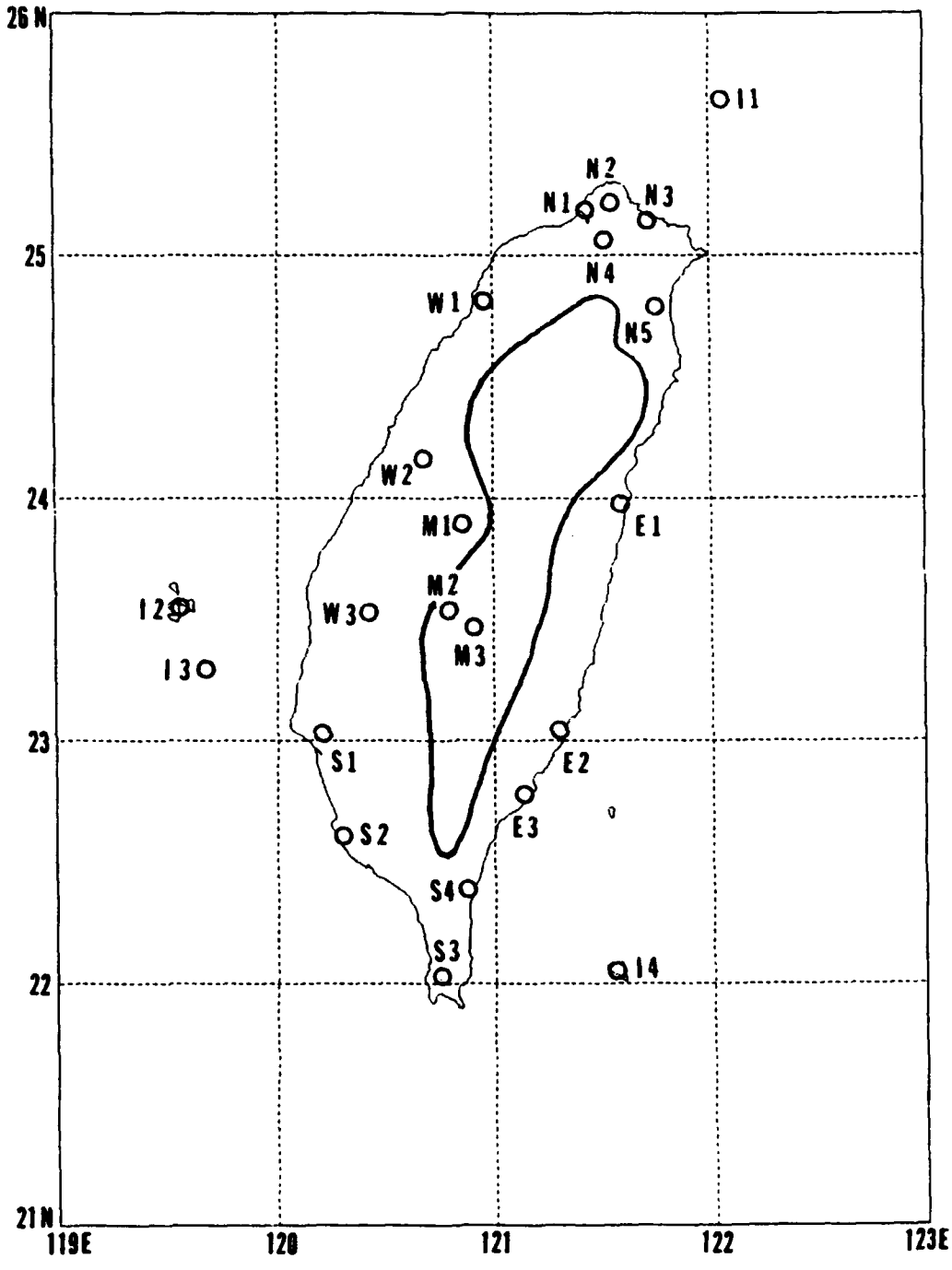

Fig. 5.1 Area of study with the CMR topography indicated by the 1000 m contour line. The two-letter codes identify surface stations (see Table 5.1 for details).

TABLE IV LIST OF SURFACE STATIONS. The convention for the station identifier codes is: I for islands off Taiwan, M for mountain stations, N for northern stations, S for southern stations, E for eastern stations, and W for western stations.

Identifier Code	Station Name	Lat. °N	Long. °E	Height (m)
I1	Peng-Chia-Yu	25.63	122.07	99
I2	Peng-Hu	23.53	119.55	9
I3	Tung-Chi-Tao	23.27	119.67	46
I4	Lan-Yu	22.04	121.55	324
M1	Jih-Yuen-Tan	23.88	120.85	1015
M2	A-Li-Shan	23.52	120.80	2406
M3	Yu-Shan	23.49	120.95	3850
N1	Tan-Shui	25.17	121.43	23
N2	Chu-Tze-Hu	25.17	121.53	600
N3	Kee-Lung	25.14	121.73	27
N4	Tai-Pei	25.03	121.52	8
N5	I-Lan	24.77	121.75	7
S1	Tai-Nan	23.00	120.20	13
S2	Kao-Hsiung	22.58	120.30	2
S3	Heng-Chun	22.00	120.75	22
S4	Ta-Wu	22.35	120.90	8
E1	Hua-Lien	23.97	121.62	18
E2	Hsin-Kang	23.00	121.36	33
E3	Tai-Tung	22.75	121.15	9
W1	Hsin-Chu	24.80	120.97	33
W2	Tai-Chung	24.15	120.68	84
W3	Gai-Yu	23.50	120.42	27

TABLE V THE TYPHOONS AND PERIODS OF STUDY. The ID numbers and typhoon names are those given by the Joint Typhoon Warning Center at Guam. The last two digits of an ID indicate the year.

ID	Name	Period mmddhh-mmddhh	ID	Name	Period mmddhh-mmddhh
1671	LUCY	071912-072109	1382	DOT	081312-081509
1871	NADINE	072412-072609	1582	FAYE	082500-082621
2671	AGNES	091618-091915	2082	KEN	091900-092121
2771	BESS	092112-092303	0483	WAYNE	072312-072509
0972	SUSAN	070800-070909	0683	CARMEN	081312-081415
0873	GEORGIA	080812-080903	1083	ELLEN	090612-090721
1773	NORA	100718-101015	0284	WYNNE	062218-062403
3174	GLORIA	110706-110821	0384	ALEX	070200-070321
0475	NINA	080200-080321	0884	FREDA	080606-080715
0675	ORA	081000-081103	1084	GERALD	081518-081609
1475	BETTY	092106-092309	1484	JUNE	082906-083009
1775	ELSIE	101106-101315	2884	BILL	111700-111903
0576	OLGA	052506-052603	0585	HAL	062112-062303
0776	RUBY	062606-063021	0785	JEFF	072812-073003
1376	BILLIE	080812-081009	1185	NELSON	082112-082403
0677	THELMA	072212-072603	1785	VAL	091512-091721
0777	VERA	073000-080103	2085	BRENDA	100218-100409
1277	DINAH	091800-092115	2485	FAYE	102612-102915
1977	KIM	111512-111621	0486	MAC	052512-052721
0278	OLIVE	042406-042515	0586	NANCY	062206-062403
1878	IRMA	091112-091215	0786	PEGGY	070906-071021
2478	ORA	101112-101403	1386	WAYNE	082018-082509
1079	GORDON	072700-072821	1386	WAYNE	082700-090321
0979	HOPE	073106-080109	1586	ABBY	091712-092003
1279	IRVING	081312-081503	2486	JOE	112100-112309
1379	JUDY	082218-082309	0587	THELMA	071312-071409
1779	MAC	092106-092121	0687	VERNON	071912-072115
0380	DOM	051512-051621	0887	ALEX	072506-072703
0880	IDA	070812-071021	1487	GERALD	090706-091021
1180	KIM	072512-072615	2187	LYNN	102306-102621
1580	NORRIS	082612-082809	0288	SUSAN	053100-060315
1980	PERCY	091612-091821	0688	WARREN	071718-071821
2580	BETTY	110518-110621	1788	KIT	092000-092115
0481	IKE	061200-061321	2088	NELSON	100318-100515
0581	JUNE	061806-062103	2289	SARAH	091018-091215
0881	MAURY	071812-071921	0390	MARIAN	051712-051903
1381	ROY	080606-080703	0690	OFELIA	062018-062315
2081	CLARA	091918-092021	0790	PERCY	062600-062821
2681	IRMA	112500-112621	1390	YANCY	081512-082003
1082	ANDY	072712-072921	1590	ABE	082912-083009
1282	CECIL	080812-081209	1790	DOT	090612-090803

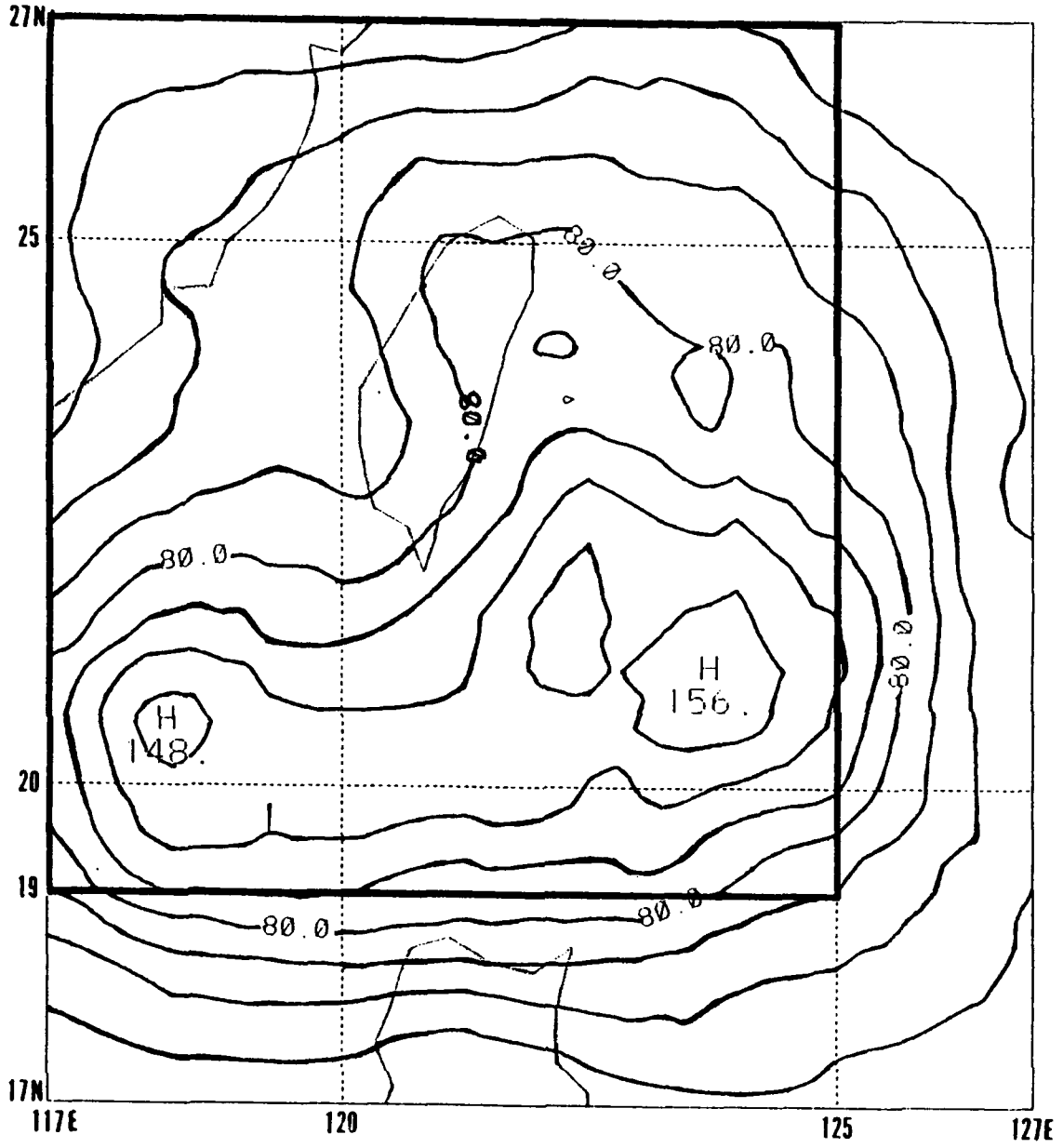

Fig. 5.2 Occurrences of typhoon centers at each of the 2°x2° grid points. The thick black line defines the domain of typhoon selection. See text for details.

region of the Taiwan Strait, which may be a manifestation of the blocking effect of the typhoon tracks by the CMR.

The surface reports include surface pressure, wind direction and speed, temperature, relative humidity and hourly rainfall. Sea-level pressure is not used to avoid the uncertainty involved with the hydrostatic reduction. The effect of the different station altitudes is minimized because all pressure patterns (other than the mean) are calculated as departures from the time mean (over all cases) at that station. The wind data are decomposed into components that are parallel and normal to the main axis of the CMR, respectively.

The principal method of identifying the structure patterns is the empirical orthogonal function (EOF) analysis of the surface pressure. The EOF method is the same as that by Chang and Chen (1992). In most meteorological studies, EOF analysis is applied to gridpoint values. In this study, the analysis will be applied to station data directly, which avoids any effect due to another layer of objective analysis. One may simply view the station network as the equivalent of a non-uniform grid, and that the resulting EOF modes are represented on the same non-uniform grid.

The pressure EOF modes are considered the basic modes of the terrain-affected circulations. The corresponding structures of winds, temperature, relative humidity and rainfall rate are determined by a regression method. Prior to the regression calculations, these fields are first subjected to an EOF analysis for the purpose of data smoothing and reduction. For each variable, the regressions between the amplitude time series of each of the first 10 EOF modes and those of each pressure EOF mode are then computed.

The structures of these variables associated with each pressure mode are produced by summing up the pertinent regression coefficients multiplied by their respective EOF patterns.

Since the 1446 cases consist of only a portion of the data during the typhoon season, the individual EOF modes from a direct EOF analysis represent anomalous patterns from the mean state of all cases rather than from the seasonal climatology. It is possible to produce the EOF modes that represent the anomalies from the climatology by using the latter in the calculation (Chang and Chen 1992). We have experimented with this method in the present study but found that the two calculations produced no discernible differences. In all the results shown below, the climatological mean is not used.

B. DISTRIBUTION OF COMPOSITE PRESSURE AND RAINFALL

The mean field (Fig. 5.3a) depicts the lower pressures due to higher altitudes at the mountain stations that are centered at station W3, which is located near the highest peak of the CMR. The mean pressure at W3 is 637 mb, compared to the mean of about 1000 mb at the plains stations. The standard deviations (Fig. 5.3b) at the high altitude stations are proportionally smaller, with a minimum of 4.1 mb at W3, compared to 6.2-6.7 mb in the southwestern plain region and 7.0-7.8 mb in northern Taiwan and the eastern coast. A local minimum exists at the northern station N2, where the mean is 935 mb and the standard deviation is 6.5 mb. Station N2 is the only mountain station used in northern Taiwan and has an altitude of 600 m.

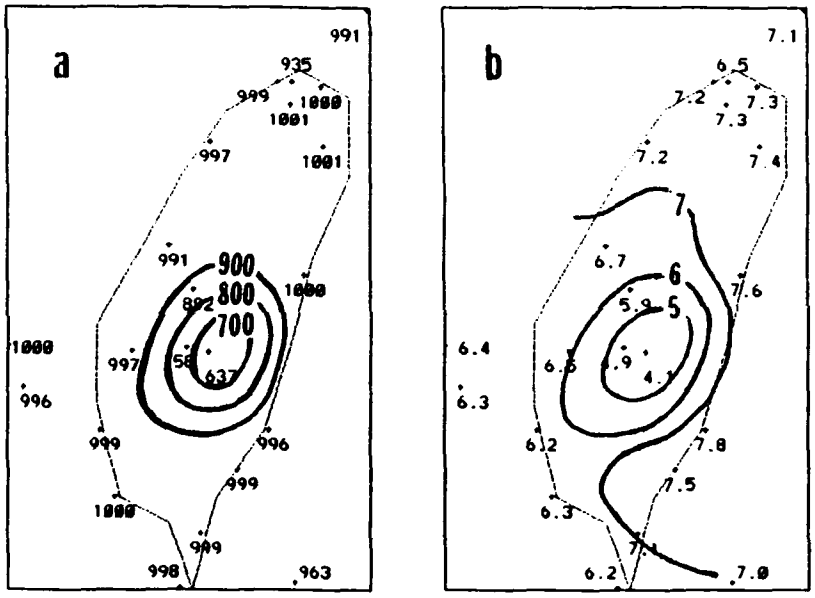

Fig. 5.3 (a) Mean, and (b) standard deviation of surface pressure (mb) of the 1446 cases at each station.

The pressure distribution over the entire Taiwan island is displayed as a function of typhoon center location after the removal of two means as follows:

$$p'' = p - p^t - p^a ,$$

where p is the pressure at a given station and p^t is the time mean (average of all cases) of p as shown in Fig. 5.3a. The purpose of removing the time mean is to minimize the differences due to the altitude of the stations. The quantity p^a is the instantaneous area mean of $(p-p^t)$. The purpose of removing this area mean is to highlight the spatial gradient of the pressure distribution when the entire domain may be subject to a simultaneous pressure decrease (increase) as a typhoon is approaching (departing).

Distributions of p'' as a function of typhoon center location within 2° squares are shown in Fig. 5.4 as 25 panels aligned in five latitudes (rows) and five longitudes (columns). A general feature in many panels of Fig. 5.4 is that most of the isobars are parallel to the long axis of CMR rather than having a circular distribution with respect to the typhoon center. This is apparently the result of the terrain effect. Furthermore, the gradient normal to the long axis of CMR is stronger when the typhoon center moves closer to Taiwan. The pressure difference can reach about 10 mb between the east and the west coast. A leeside low center or trough can be found in several panels. The most conspicuous closed center is in the central panel of Fig. 5.4. When the typhoon center is just southeast of the island between 21°-23°N, 121°-123°E, a low center is on the west coast between stations W2 and W3. The pressure difference between the low center and the northeast coast is a modest 3 mb, which reflects the results of averaging the 107 cases within the 2° square. A leeside effect can also be found when the typhoon center

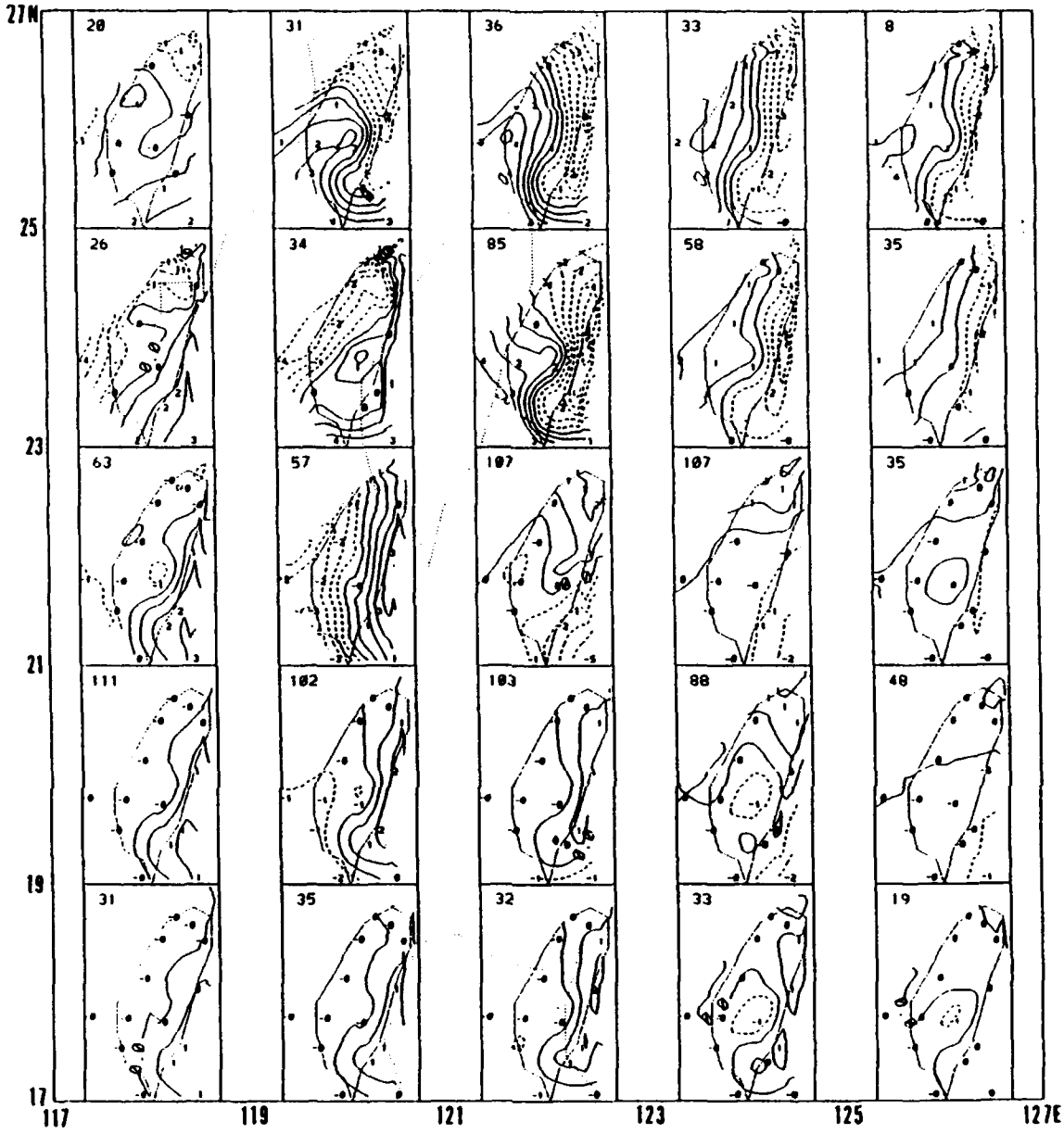

Fig. 5.4 The distribution of p'' as a function of typhoon center location. Each of the 25 panels covers a 2°x2° grid square and shows a composite of p'' over the entire Taiwan island for those cases where the typhoon center is located inside the particular grid square. Solid lines are positive (above area mean) and dashed lines are negative values. The interval unit is 1 mb. For each grid square, the number of cases is given in the upper left corner. The outlines of the coastlines of Taiwan, southeastern China, and northern Luzon are also plotted in the background to assist the identification of the geographic locations of the 25 grid squares relative to Taiwan.

is located to the north, northwest or northeast of Taiwan, which are in the panels 23°-27°N, 119°-127°E. Although no closed center is present in these cases, a local trough separated from the typhoon center is found over the southeastern coast.

Significant terrain modification of the precipitation pattern is shown in the hourly rainfall distributions (Fig. 5.5). When the typhoon center is north of 23°N, the maximum rainfall occurs near the station M2 on windward side of the CMR. When the typhoon center is south of 23°N, the maximum rainfall occurs along the southeastern coast near stations E3 and S4. A prominent maximum with averaged hourly rainfall greater than 9 mm occurs near station E3 when the typhoon centers are in the panel of 21°-23°N, 119°-121°E. To assure that this concentrated rainfall maximum is not due to the presence of a few cases of very high rainfall over station E3, all cases associated with this panel are partitioned into four sub-periods, each with one quarter of the cases. The rainfall composites for each of the sub-periods (not shown) resemble closely that in Fig. 5.5.

C. EMPIRICAL ORTHOGONAL FUNCTION PRESSURE MODES

Two sets of EOF calculations are carried out. The first is done on the original data and the second is done with the area mean removed. The resultant EOF modes of the second set resemble very closely the respective patterns of the first set, except for a change of the relative magnitudes of the percentage variance among the first three modes. Excellent correlations (around 0.9) also exist between the amplitude fluctuations of each

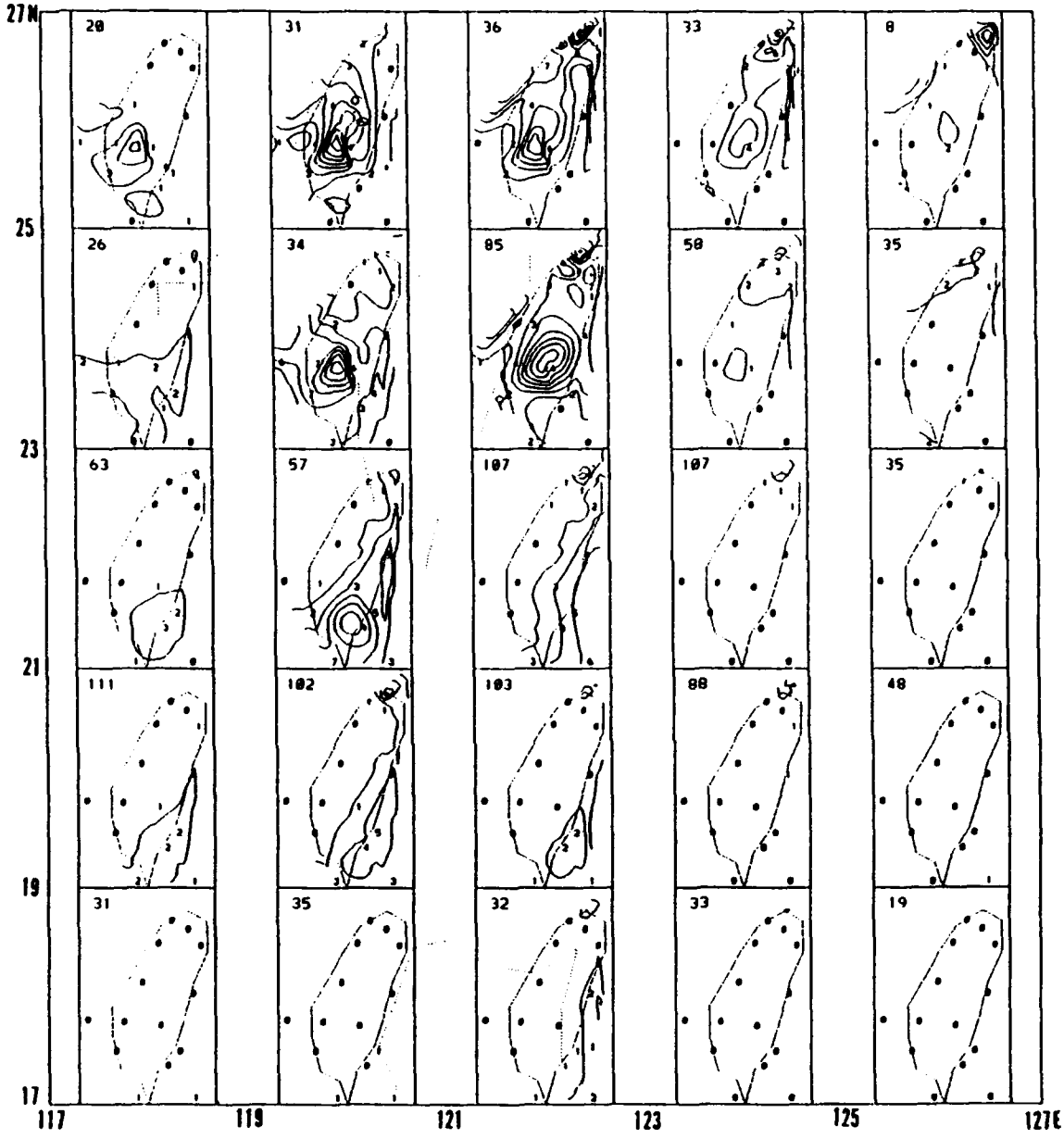

Fig. 5.5 As in Fig. 5.4, except for the distribution of the hourly rainfall (interval of 2 mm/h) as a function of typhoon center location.

pair of corresponding modes. For both sets, the percentage variances of the first eight EOF modes of the surface pressure are given in TABLE VI.

TABLE VI THE PERCENTAGE CONTRIBUTION OF EACH MODE. The percentage of total variance represented by each of the first eight EOF modes of the surface pressure.

Mode	without removing area mean	area mean removed
1	86.39	8.80
2	7.25	50.24
3	2.68	18.58
4	0.82	5.40
5	0.54	3.48
6	0.39	2.48
7	0.35	2.33
8	0.30	1.96

Without removing the area mean, Mode 1 dominates the total variance with 86.39%. This mode (Fig. 5.6a), in which the amplitude equals one standard deviation, has no sign variation within the entire region. The large percentage variation is apparently a reflection of the area-wide (mean value of 6.1 mb) pressure decrease (increase) during the approach (departure) of a typhoon. The minimum value at the peak

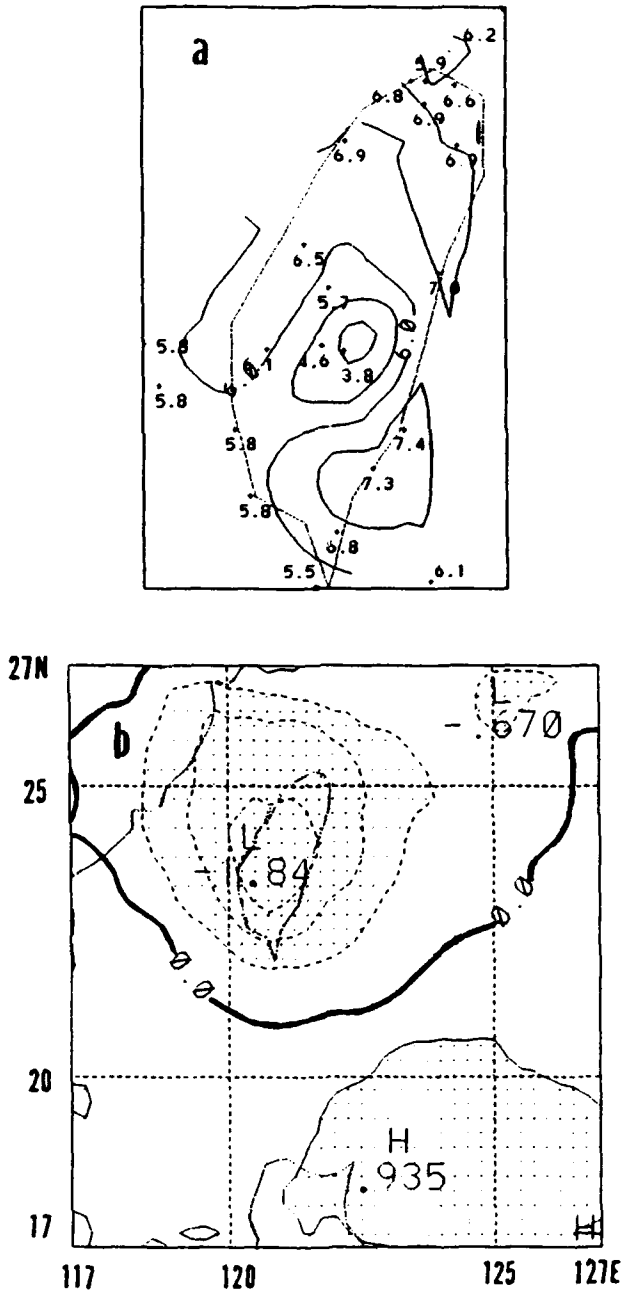

Fig. 5.6 (a) The pattern of the EOF surface pressure (mb) Mode 1 at one standard deviation, and (b) the distribution of the normalized amplitude according to the typhoon center location for Mode 1. The product of values in (a) and (b) defines the sign and magnitude of the pressure anomaly.

station M3 is 3.8 mb, and a maximum of 7.4 mb at station E2 on the southeastern coast. A local elongated maximum of about 6.0-6.5 mb is along the central-western coast. As a typhoon is approaching or departing, the pressure values are above average along the coastal areas and below average on the high mountains. Because this "trend" of pressure change overwhelms all other patterns, it presents a somewhat misleading impression of the relative importance of each mode. The percentage variance of the second set of EOF (calculated after the removal of the area means) allows a more suitable representation of the terrain effects.

The amplitude of Mode 1, normalized by its standard deviation, is plotted according to the location of a typhoon center (Fig. 5.6b). The amplitude of this mode is negative when the typhoon center is over Taiwan (maximum magnitude -1.84 standard deviation). It is slightly positive (less than one standard deviation) when the typhoon is to the south of and away from the island.

To alleviate the concern that the results may have arisen from the average of opposite-sign cases, the percentage of cases for a given location that have the same sign as indicated in Fig. 5.6b is calculated. The resultant pattern (not shown) resembles Fig. 5.6b and verifies that the latter is representative of the majority of cases. This sign consistency check is performed and verified for all the leading modes. In all areas in which the amplitude of a mode exceeds 0.5 standard deviation, the consistency is found to be higher than 70%.

Patterns and the normalized amplitude distributions for Modes 2-4 are shown in Figs. 5.7-5.9. Higher modes are not included because the percentage variances are

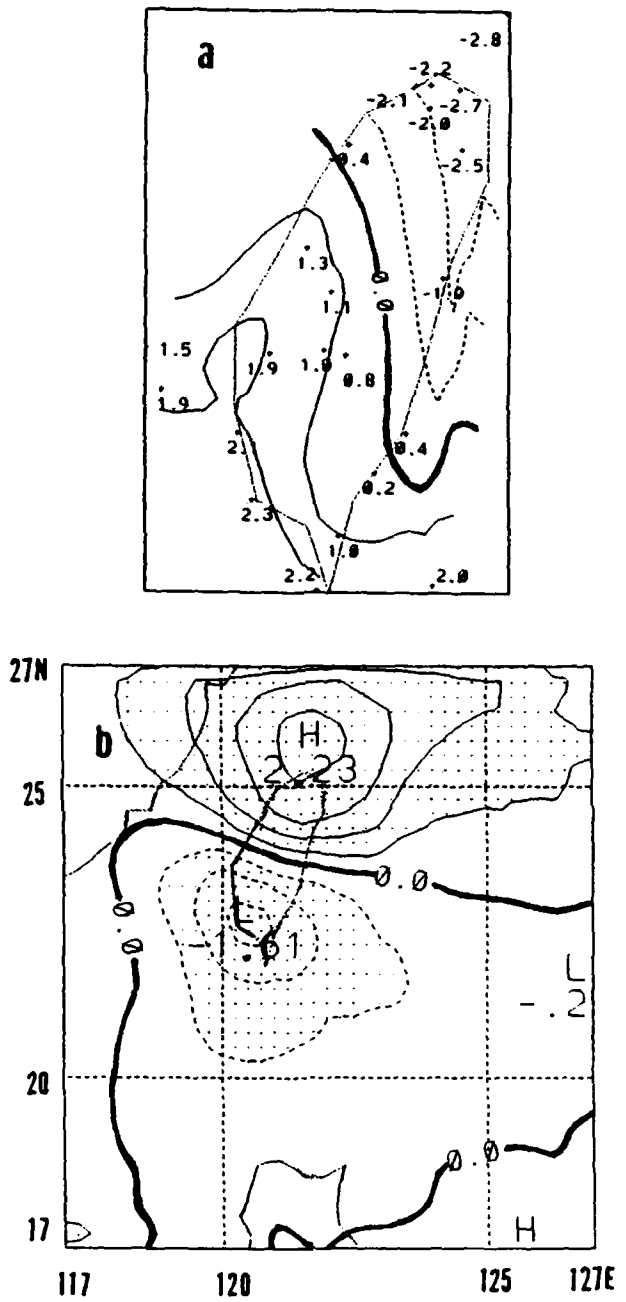

Fig. 5.7 As in Fig. 5.6, except for Mode 2.

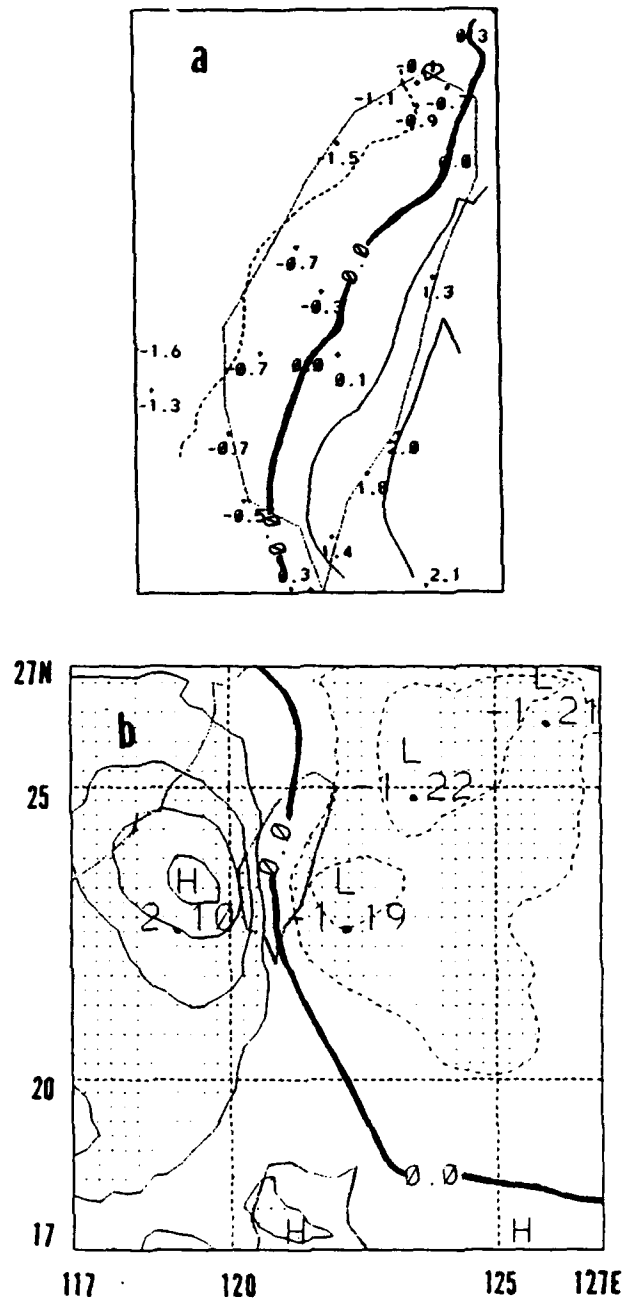

Fig. 5.8 As in Fig. 5.6, except for Mode 3.

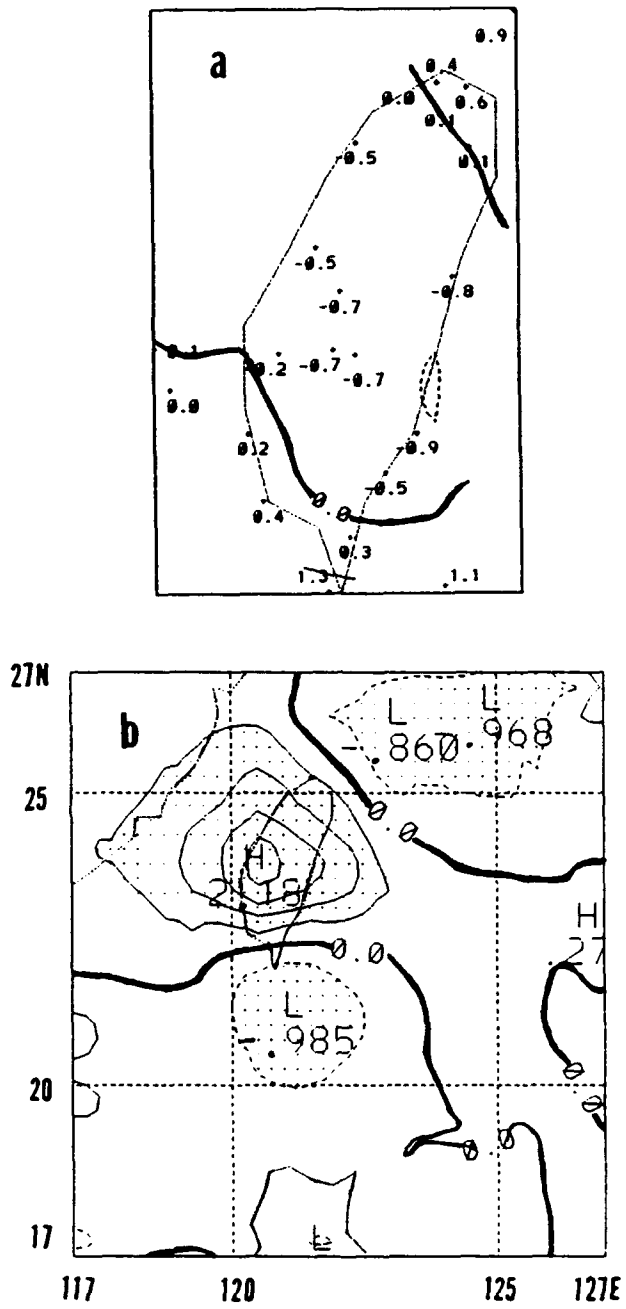

Fig. 5.9 As in Fig. 5.6, except for Mode 4.

smaller (TABLE VI). Mode 2 has a "node line" extending north-northwest to south-southeast with an out-of-phase pattern distribution between the northeast and the southwest parts of Taiwan. The amplitude distribution (Fig. 5.7b) has an anti-symmetric dipole with respect to central Taiwan. When a typhoon center is over the southern part of the island, a trough is found along the southwestern coast and a ridge along the eastern and northern coast. The opposite phase occurs when the center is over the northern part of the island. The isobars are mostly oriented north-northwest to south-southeast. From the distribution shown in Fig. 5.7b, one would expect a north-south (N-S) pressure gradient. However, the pressure gradient is significantly stronger in the east-west (E-W) direction, which is apparently a CMR terrain effect.

The pattern of Mode 3 (Fig. 5.8a) has isobars oriented in the south-southwest to north-northeast direction with the zero node line nearly parallel to the CMR along the long axis of the island. The amplitude distribution (Fig. 5.8b) has a zero line crossing Taiwan in north-south direction, with a stronger and concentrated maximum for a typhoon center to the southwest, and a weaker and broader minimum for typhoons to the east. Whereas Fig. 5.8b would suggest a E-W pressure gradient, Fig. 5.8a clearly contains a N-S gradient component. Therefore, the N-S gradient in Mode 3 is likely a result of the CMR terrain effect. This mountain-induced N-S pressure gradient is weaker than the mountain-induced E-W gradient in Mode 2. The difference is due to the aspect ratio of the CMR. The long (N-S) axis of CMR is about 4.7 times the short (E-W) axis.

The two northwest-southeast node lines in Mode 4 separate the two narrow belts in the northeastern and southwestern coasts from the large central area of the opposite

sign (Fig. 5.9a). This mode has a significant contribution when the typhoon center is situated over Taiwan (Fig. 5.9b). Whereas most of the stations have negative pressure anomalies, the stations in the two narrow coastal belts have positive anomalies. The opposite phase occurs when the typhoon center is either to the south or to the north of the island.

The direction and speed of typhoon motion for all cases with a substantial contribution to the positive phase of a particular mode is shown in Fig. 5.10 for Modes 1-4. It is clear that for each mode the scattering of both direction and speed is so large that no dependence is discernible. Similar results are found for the negative phase of each mode. Therefore, the basic structures are mainly a function of the typhoon center location rather than typhoon motion. It will be demonstrated in Section E that, a difference in the typhoon structure can be found, at least to the extent that different steering flows can be inferred from different smooth tracks.

D. WIND, TEMPERATURE, RAINFALL AND RELATIVE HUMIDITY

The horizontal wind (V), temperature (T), hourly rainfall (rf) and relative humidity (RH) that correspond to each of the leading pressure EOF modes are identified by a regression method. Prior to the regression calculations, the data of these variables are first subjected to an EOF truncation to eliminate the small-scale noise. Only the first 10 EOF modes for each variable are retained, and then the regressions between their amplitude time series and that of each pressure mode are computed. The amount of total variance represented by the first 10 EOF modes is 90% for V, 95% for T, 82% for rf,

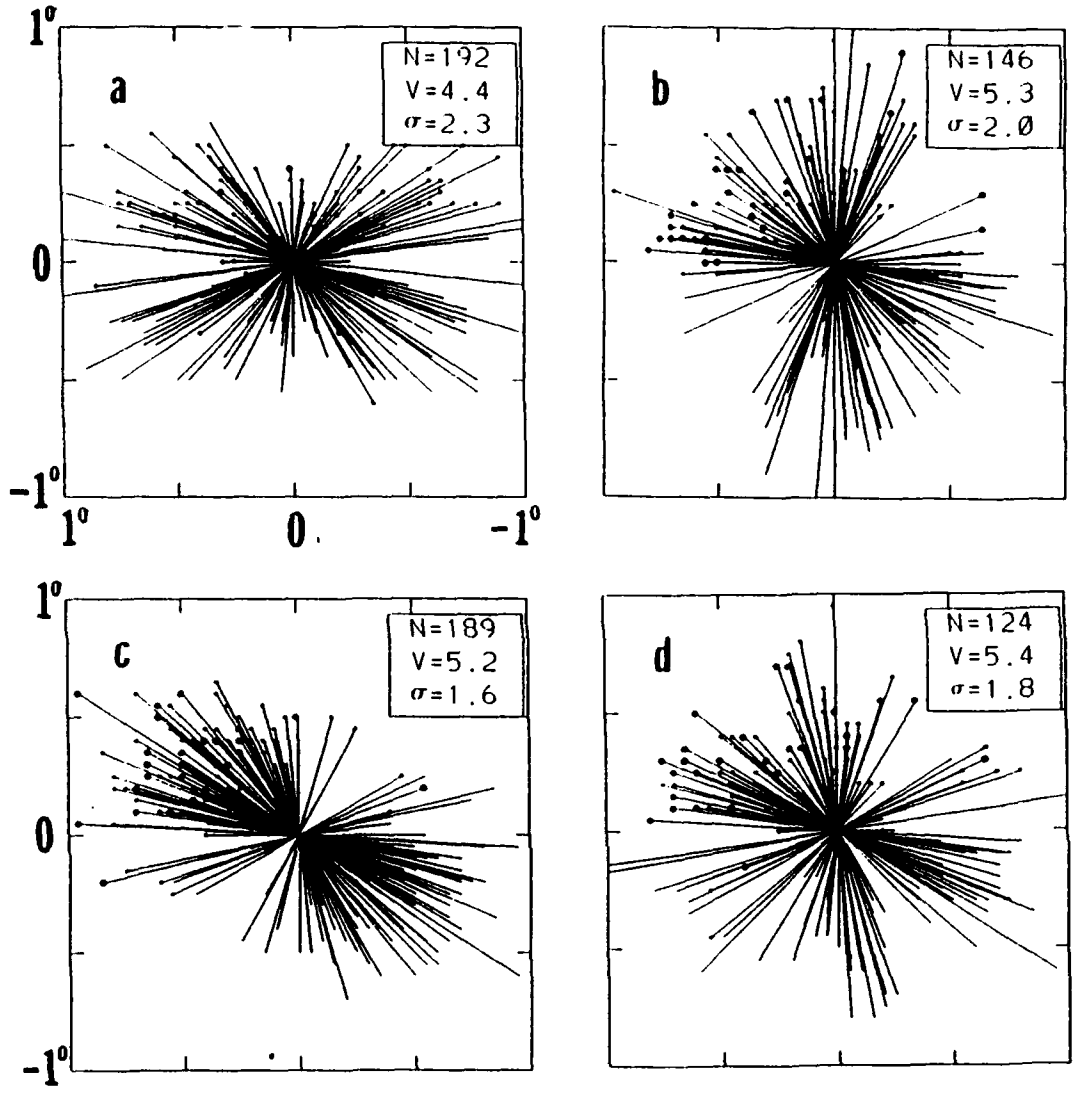

Fig. 5.10 The direction and speed of three-hourly typhoon motion for each case that has a contribution of at least one standard deviation to the positive phase of (a) Mode 1, (b) Mode 2, (c) Mode 3, and (d) Mode 4. Each vector is ended with a dot (a larger dot indicates that the amplitude is greater than 2 standard deviations). Therefore a line connecting the center with a dot indicates the departure motion of a typhoon. The arriving motion is indicated by a line connecting the center up-track to a point without a dot. The interval indicated in the abscissa and ordinate of each panel is 0.5° long. and lat., respectively. Within each panel the number of cases (N), the average speed (V, m/s) and its standard deviation (σ) are given in the upper right corner.

and 87% for *RH*. The *V*, *T*, *rf* and *RH* fields associated with each pressure mode are produced by summing the pertinent regression coefficients multiplied by their respective EOF patterns.

The *V*, *T*, *rf* and *RH* structures associated with the negative phase of Mode 1 of the surface pressure (Fig. 5.6) are shown in Fig. 5.11. The wind vectors (Fig. 5.11a) at most stations indicate a cyclonically converging onshore flow, with the exception of the strong winds at the peak station M3 and the offshore wind at the small island I4. This convergence toward the low pressure center is consistent with rising motion against the terrain and the maximum rainfall centered at station M2 on the western slope of the CMR (Fig. 5.11c). The northwest coast area has relatively calm winds compared to the southwest coast, where the onshore flow is towards the mountain and appears to be responsible for the production of the local ridge (Fig. 5.6a). This local ridge is important to the formation of a secondary low that will be discussed in Section F.

The minimum temperature at M1 is to the north of the warm region over south-central Taiwan (Fig. 5.11b). Even though the maximum temperature is near the peak of the CMR, the warm region is basically consistent with the significant northwesterly wind at the peak station M3, which produces subsidence on the southeastern side of the range. The southeastern coastal area, which is downwind from the peak and outside of the highest rainfall region, has lower *RH* values (Fig. 5.11d). This is an area where dry and warm subsiding foehn winds typically occur (e.g., Wang 1980). Other drier regions are found in the western and northeastern sections where rainfall is low.

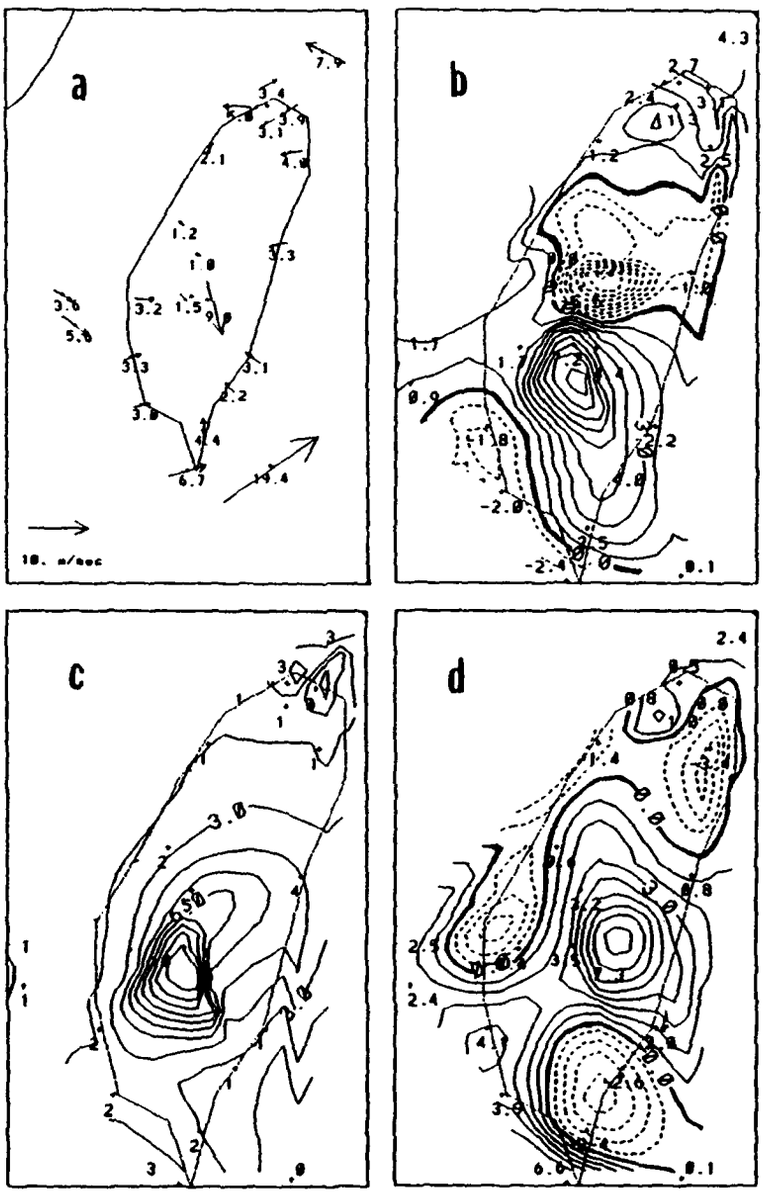

Fig. 5.11 The structure of (a) wind (V, vector scale in lower left), (b) temperature (T, °K), (c) rainfall rate (rf, mm/h), and (d) relative humidity (RH, %) associated with Mode 1 of the surface pressure at negative phase. Panel (a) has a smaller geographical scale to allow the plotting of wind vectors within the figure.

The structures corresponding to the negative phase of Mode 2, which is most prominent when the typhoon center is over southern Taiwan (Fig. 5.7b), are shown in Fig. 5.12. The generally cyclonic winds (Fig. 5.12a) have an onshore flow on the east coast and offshore flow on the west coast. As a result, a ridge develops on the windward side of the CMR and a trough develops on the lee side. The onshore flow impinging the steep eastern slope of the CMR produces strong rising motion along the central and northern east coast, and thus the heavy rainfall (Fig. 5.12c) and high *RH* values (Fig. 5.12d). The onshore flow tends to follow the isobars (Fig. 5.7a) in the sense of a gradient wind, with a turning from easterly to southeasterly as the air moves downstream over the CMR. The warm and dry center at the central station M1 (Figs. 5.12b and 5.12d) may be a result of the downslope flow after the air passes the highest peak. The cold center at the southeastern coast has a sign that is consistent with other fields, which is probably related to the opposite phase of Mode 2 when the typhoon center is over northern Taiwan. In that case, all fields in Fig. 5.12 will have the opposite signs. Onshore flows on the west coast induces rising motion and higher rainfall on the west slope of the CMR. The flow over the mountain again follows the isobars such that northwesterly components result in a maximum temperature and dry region on the southeast coast. Thus, Mode 2 also will contribute to the development of the foehn wind there.

The structures corresponding to the negative phase of Mode 3 (Fig. 5.7), which is most prominent when the typhoon center is located to the east of Taiwan, are given in Fig. 5.13. The cyclonic flow surrounding the center has northerly flows ascending the

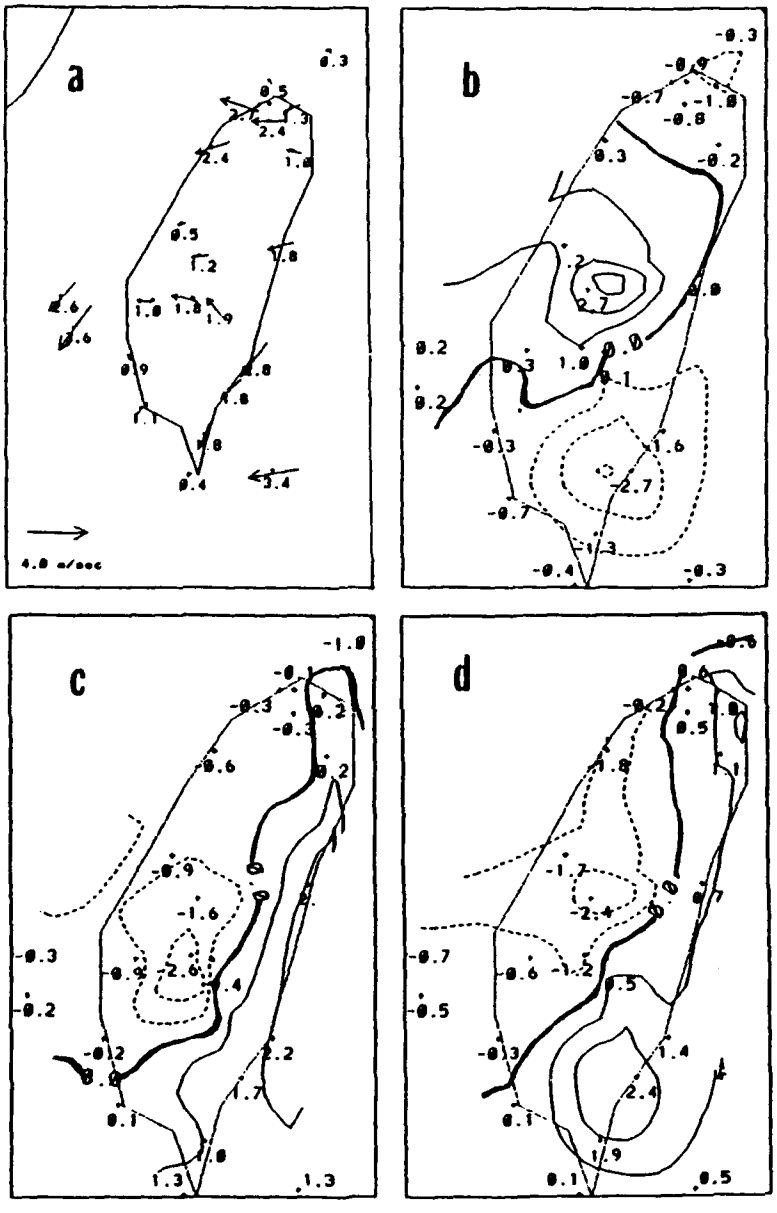

Fig. 5.12 As in Fig. 5.11, except for Mode 2 at negative phase.

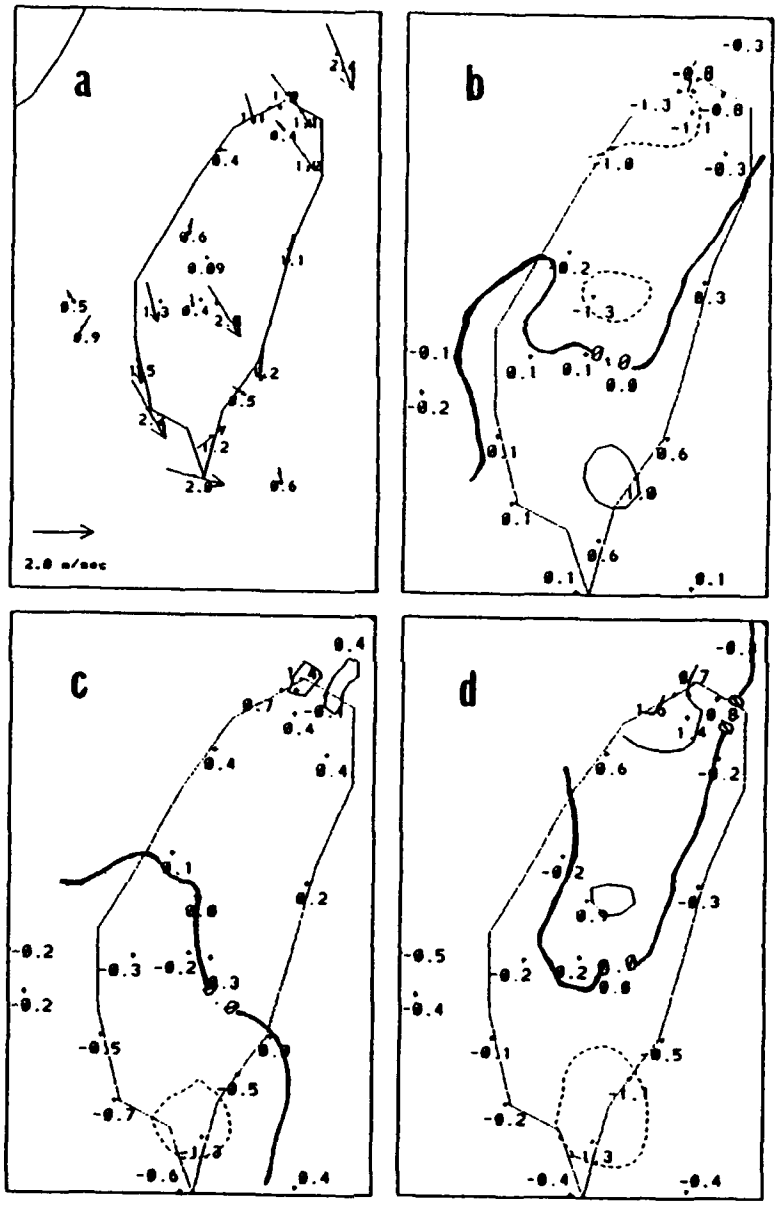

Fig. 5.13 As in Fig. 5.11, except for Mode 3 at negative phase.

mountains from the north and subsiding on the south side. This leads to somewhat higher rainfalls (Fig. 5.13c) in northern Taiwan and lower rainfalls in southern Taiwan, where the temperature (Fig. 5.13b) is higher and the relative humidity (Fig. 5.13d) is lower. The opposite phase of this mode is important when the typhoon center is located to the west of the island. In that case, the predominant southerlies rise against the southern mountains. All of the other fields are reversed.

Because the percentage variance associated with Mode 4 (Fig. 5.9) is relatively small (TABLE VI), the winds in Fig. 5.14a are plotted with a scale that is considerably larger than in the previous figures. When the typhoon center is over western Taiwan (Fig. 5.9b), the onshore winds impinging on the southwestern slope of the CMR result in a tendency for positive pressure anomalies on the southwest coast, and those impinging on the northeastern mountains cause positive pressure anomalies in the northeastern corner (Fig. 5.9a). The patterns of temperature, rainfall and relative humidity are consistent with the vertical motions forced by the mountains, but the anomalies are relatively small. Because the variance of higher modes is even smaller, the associated *V*, *T*, *rf* and *RH* patterns will not be discussed.

E. STRUCTURE AS A FUNCTION OF TYPHOON CENTER LOCATION

The consistent wind, temperature, rainfall and relative humidity structures corresponding to each of the leading pressure EOF modes verify the validity of the decomposition of the surface typhoon structure into these modes. We may therefore consider the typhoon structure over Taiwan as a linear combination of these basic modes.

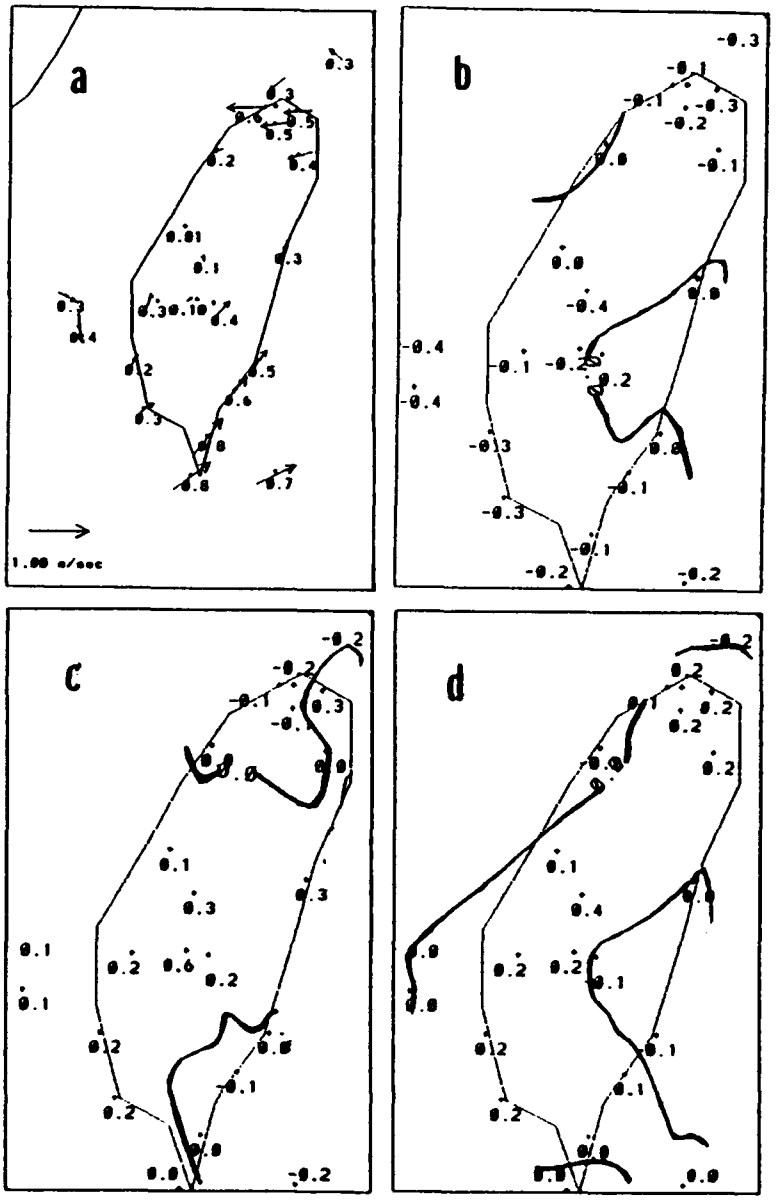

Fig. 5.14 As in Fig. 5.11, except for Mode 4 at positive phase.

The relative importance of these basic structure modes as a function of the typhoon center location is presented in Fig. 5.15. For each of the first four modes, an area(s) is found within which a typhoon center produces a significant 'response' of that mode. This is done by defining each area in such a way that the pressure difference over Taiwan between the highest and lowest value that can be produced by the corresponding mode is larger than 2 mb. A mode may have two areas that correspond to the two phases of its pattern. The areal distributions for each mode resemble the corresponding panel b of Figs. 5.6-5.9. For example, negative-phase Mode 1 and positive-phase Mode 4 are centered over Taiwan, and Modes 2 and 3 are antisymmetric with respect to the short (E-W) and long (N-S) axes of Taiwan, respectively. However, the use of the standard deviation-normalized typhoon center distributions is unsuitable for this purpose, because the pressure gradients arising from each mode vary greatly.

A basis for partitioning the domain into different center location regimes that define the different characteristics of the surface structure is provided in Fig. 5.15. Within each regime, the surface structure of all the variables can be approximated by a composite of the relevant modes with the proper phase sign. For example, the main contributors to the structure over the area 21°-23°N, 119°-121°E are negative-phase Mode 2 and positive-phase Mode 3 (Fig. 5.15). Referring to Fig. 5.12c, the single most prominent feature in the negative-phase Mode 2 is an elongated belt of maximum rainfall along the east coast line. Since the negative-phase Mode 3 rainfall in Fig. 5.13c has a minimum over the southeastern tip of Taiwan, the positive Mode 3 will have a maximum rainfall there. The combination of these two features is shown prominently in the corresponding

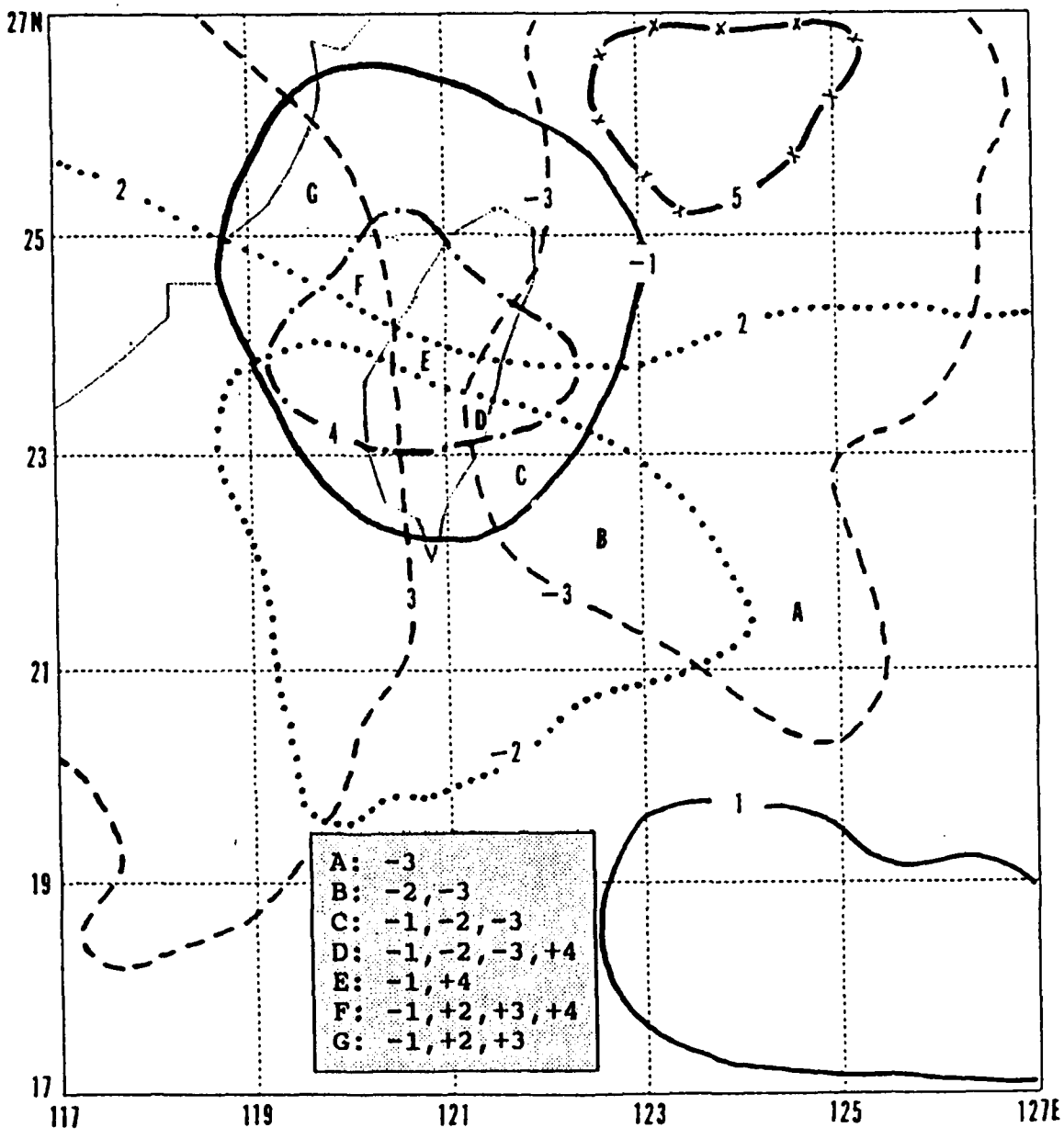

Fig. 5.15 Relative importance of the EOF modes as a function of the typhoon center location. The isopleths define the areas that a given mode can produce a maximum pressure difference over Taiwan that is greater than 2mb. The sign of each of the two phases of a mode is indicated in front of the mode number marking each isopleth. A track example is shown by capital letters from A to G, each letter representing a sub-region along the track. The shaded rectangular box lists the modes (with sign) that are important within each subregion.

panel of Fig. 5.5. Since the rainfall distribution for each mode has been explained by the terrain effects on the surface typhoon winds in the preceding section, this description of the rainfall pattern allows an easy understanding of the pertinent mechanism that produces the pattern.

The change of the surface structure as a typhoon center moves from one location to another may also be studied from Fig. 5.15. This is possible because the consistency check performed for each mode shows only limited variations of the structure dependence on center location for each EOF mode. A track example is shown by capital letters from A to G, with each letter representing a sub-region along the track. The shaded rectangular box in the lower part of the figure lists the modes (with sign) that are important within each subregion.

Although Fig. 5.10 indicates that no dependence on the direction and speed of the typhoon motion is discernible, two typhoons located at the same position may have dissimilar structures if the associated large-scale flow is significantly different. Assuming that different track characteristics represent different large-scale steering flows, we separate the tracks into several categories that each represent a mean steering flow. Each category is required to have a sufficient number of typhoons with persistently smooth and similar tracks within the domain, so that the composite of each category can have some significance in describing the effect of the particular steering flow.

In the present data set, it is difficult to find adequate samples of cases to further differentiate those centers in a given location into two or more categories of mean flows. Nevertheless, it is possible to identify two persistently-smooth tracks that approach

Taiwan from the southeast (Fig. 5.16), each with a modest number of typhoons lasting at least 36 h, to examine this problem. The first type with seven typhoons has a more westward direction and crosses southern Taiwan and will be called the S(south)-track. The other type with four typhoons has a more northward direction and is confined to a much more concentrated path that crosses northeastern Taiwan. This will be called the E(east)-track. The two tracks intersect in an area between 20°-23°N, 122°-123°E, which is a regime of multiple mode importance.

Distributions of the pressure pattern p'' when the typhoon center is along the S-track (Fig. 5.17a) and E-track (Fig. 5.17b) are constructed separately using the same method as in Fig. 5.4, except that only the S-track cases and E-track cases, respectively, are used. The results of the temperature, hourly rainfall and relative humidity when the typhoon center is in the grid square of 21°-23°N, 121°-123°E (where the two tracks overlap) are shown in Fig. 5.18. In general, the S-track has a larger contribution from Mode 2 than the E-track, as the former is characterized by stronger west-east pressure gradients in its p'' diagrams and a secondary low near W3. Since the east to west S-track will be associated with an easterly steering flow, the stronger west-east pressure gradient may be explained by the lee-side effect of the mean flow. For the same grid square, the E-track indicates a weak, low pressure region in the northwestern corner. This low region is consistent with the leeside effect expected from the southeasterly mean flow associated with the steering direction of the E-track. Moreover, for the S-track the western coast is under warm and dry conditions (Fig. 5.18) and the maximum rainfall is over the eastern coast. For the E-track, the warm and dry sector is over the northwest

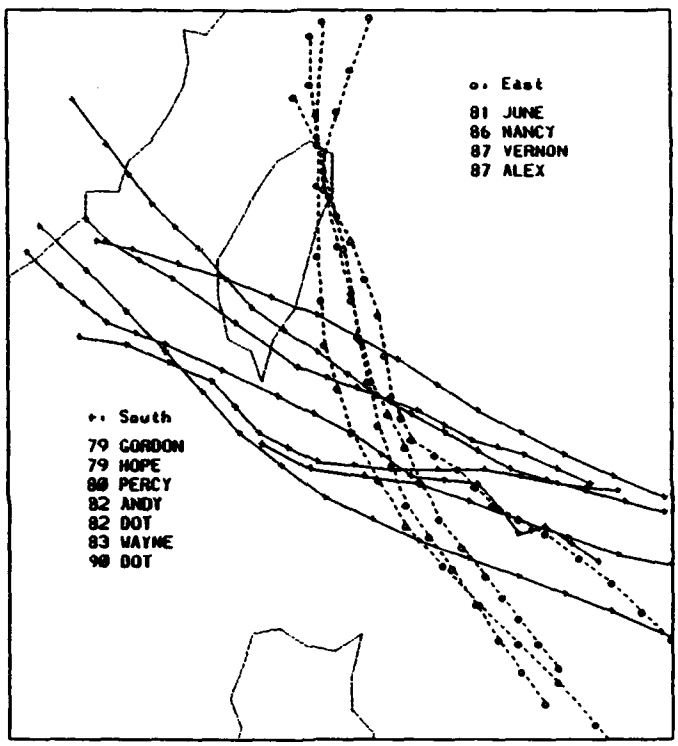

Fig. 5.16 Two primary types of typhoon tracks that approach Taiwan from the southeast. The year and name of each typhoon are listed.

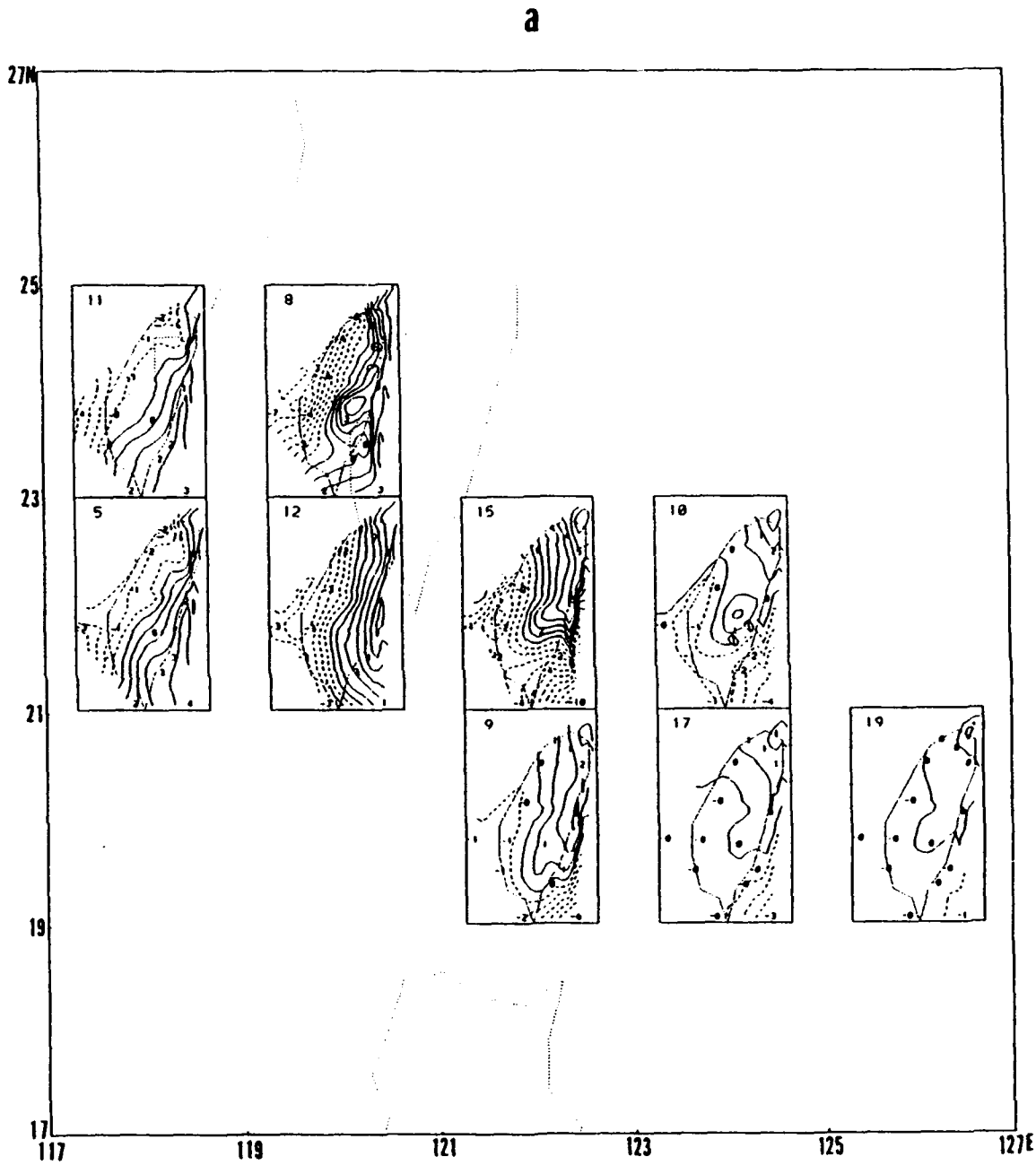

Fig. 5.17 As in Fig. 5.4, except (a) for the S-track; and (b) for the E-track.

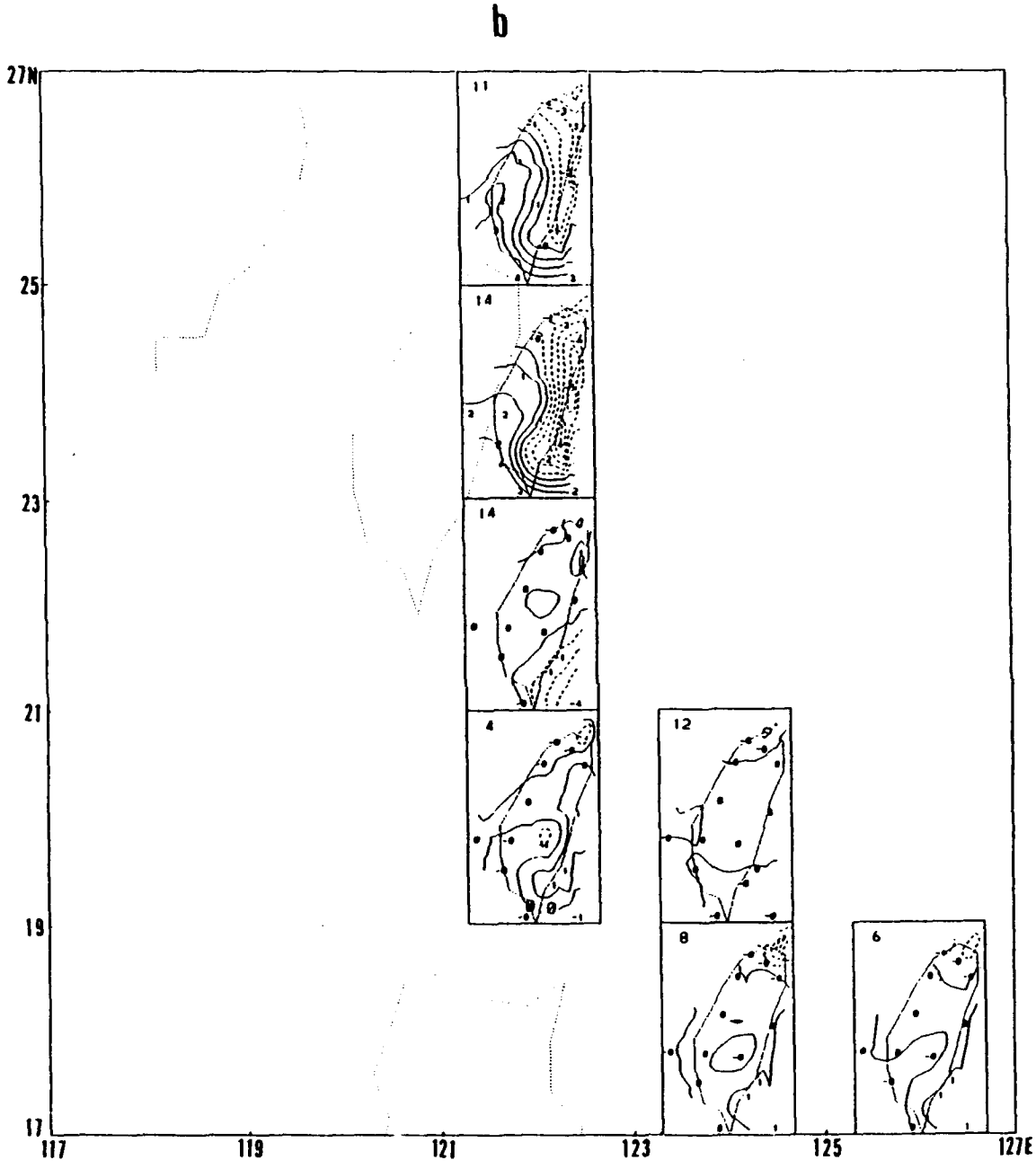

Fig. 5.17 (Continued)

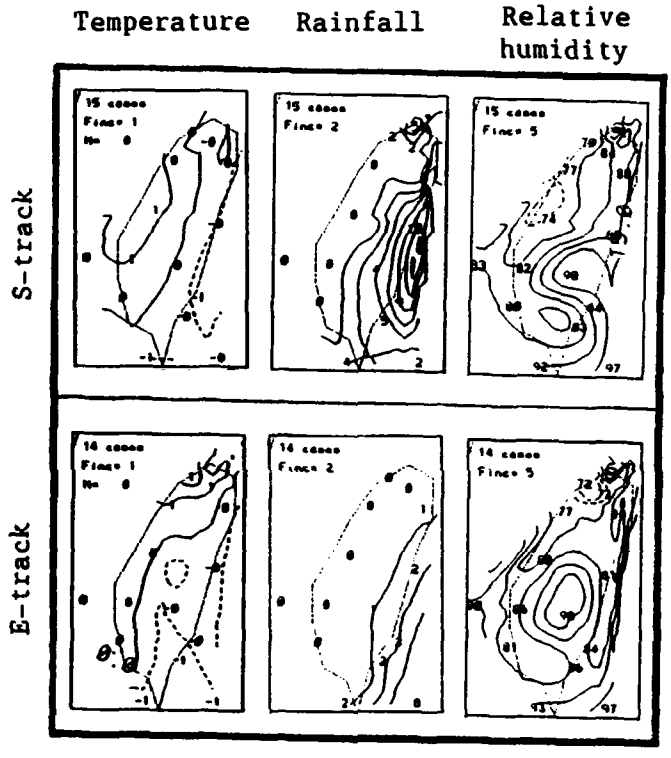

Fig. 5.18 The temperature, rainfall and relative humidity distributions for the S- and E-tracks in the panel 21°-23°N, 121°-123°E.

of the island, and the maximum rainfall occurs over the southeastern coast. These differences are consistent with the vertical motion produced by a mean flow over the CMR in the respective steering directions.

The differences between the two tracks do not appear to be due to typhoon translation speed or intensity differences. The average translation speeds for the S-track (5.8 m/s) and E-track (5.7 m/s) are nearly identical. The S-track typhoons have an average intensity (maximum wind) of 43 m/s while the E-track typhoons have an average intensity of 34 m/s. However, only including the three weakest S-track typhoons (containing eight cases within the most-overlapped grid square of 21°-23°N, 121°-123°E) with an average intensity of 32 m/s does not change the results.

Another smooth track type includes six typhoons moving from east to west across northern Taiwan (N-track) (not shown). The N-track intersects with the E-track over northeastern Taiwan. Perhaps because of the steering flow and the vortex circulation over Taiwan area are generally of opposite sign, the lee-side effect when the typhoon in the intersection area (northeastern Taiwan) is relatively insignificant. The two track types do not give appreciably different structures (not shown). No other smooth track type with more than three typhoons can be found in the data set.

F. THE SECONDARY LOW CENTER

A secondary low pressure center on the western coast near the station W3 can be seen in a number of the structure diagrams (e.g., Fig. 5.4). This center is believed to be a result of significant topographical effects and presents considerable local wind,

precipitation and motion forecast difficulties near or after a typhoon makes landfall (Wang 1980). A measure of the presence and intensity of the secondary low center is calculated from the pressure differences between station W3 and surrounding stations: $\delta p = p_{(W3)} - p^s$. Here, p^s represents the surrounding pressure that is measured in four different directions (Fig. 5.19): S1; the average of I2 and I3; N1; and the average of M1 and M2. In the north direction, the choice of N1 instead of a station closer to W3 is to include the possibility that a secondary center may exist to the north of station W3 along the western coast. When the pressure at station W3 is lower than all the surrounding values, i.e., δp less than zero in all directions (and the typhoon center is away from station W3), a closed secondary center exists.

TABLE VII shows the contributions of the leading eight EOF modes to the pressure differences in the four directions from station W3. For a given direction and mode number, a larger value means a larger contribution by this mode to the pressure difference. Whether this difference will help or hurt the formation of a secondary low center depends on the product of the sign and the phase of a particular mode. Since none of the modes have the same sign for all four directions, it is not possible for a single mode to produce a closed low center (or a high center).

The maximum δp (of the four directions) as a function of typhoon center location when all modes are added together is shown in Fig. 5.20. A closed secondary center will exist along the western coast (near or to the north of station W3) when the typhoon is within the negative area and east of the CMR. This area will be called the development regime of the secondary low center. A typhoon that enters this area from

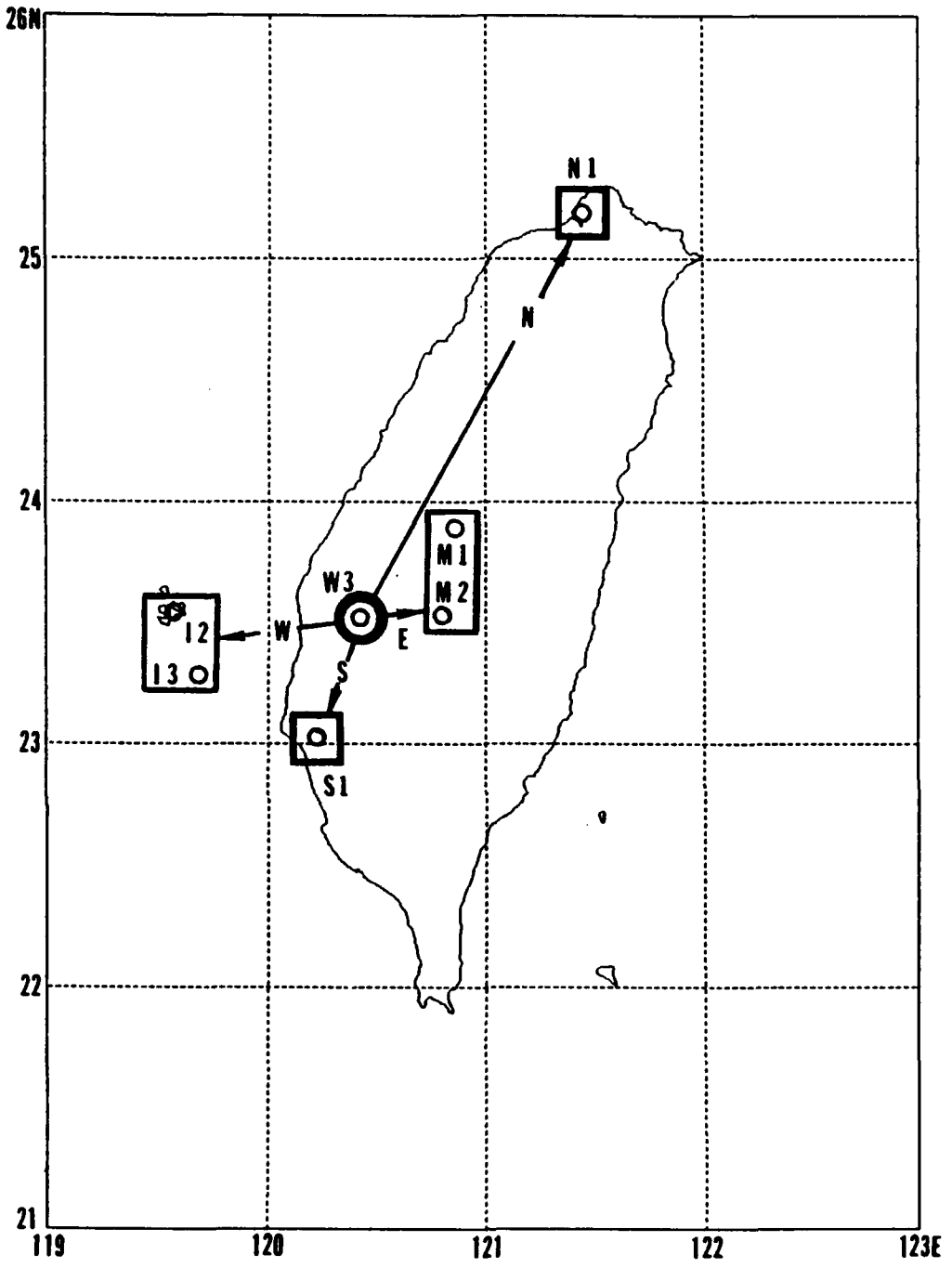

Fig. 5.19 The definition of the secondary low center parameter, $\delta p = p_{(W3)} - p^s$. Here p^s represents the surrounding pressure and is measured in four different directions: S1, the average of I2 and I3, N1, and the average of M1 and M2. These give the pressure differences from station W3 in the south, west, north and east directions, respectively.

TABLE VII THE CONTRIBUTION OF EACH MODE TO THE FORMATION OF SECONDARY LOW. The contribution (mb) of the individual EOF modes at one standard deviation to the pressure difference of each of the four directions from station W3.

Mode	#1	#2	#3	#4	#5	#6	#7	#8
South	.3	-.2	.0	-.3	.2	-.1	.0	.0
West	.3	.1	.8	-.1	.3	.5	-.2	.4
North	-.7	3.8	.3	-.1	-.6	.3	.1	-.4
East	.9	.8	-.6	.5	-.1	-.2	.1	-.3

the southeast and moves toward the south-central part of the CMR would have a prominent and systematic development of a secondary low center on the western coast. If we assume that the typhoon moves at an average speed of 5 m/s along this track, then the secondary center will gradually develop to its maximum intensity over a period of about 12 h. This time scale is more than sufficient for the secondary low being observed. On the other hand, the development of a secondary center may not be possible for the surface data to detect if a typhoon enters the area and then exits in less than a few hours.

The maximum δp as a function of typhoon center location when the EOF modes are successively added to Mode 1 is shown in Fig. 5.21. Modes 1 and 2 would produce a secondary center when the typhoon center is within an extensive west-east zone from

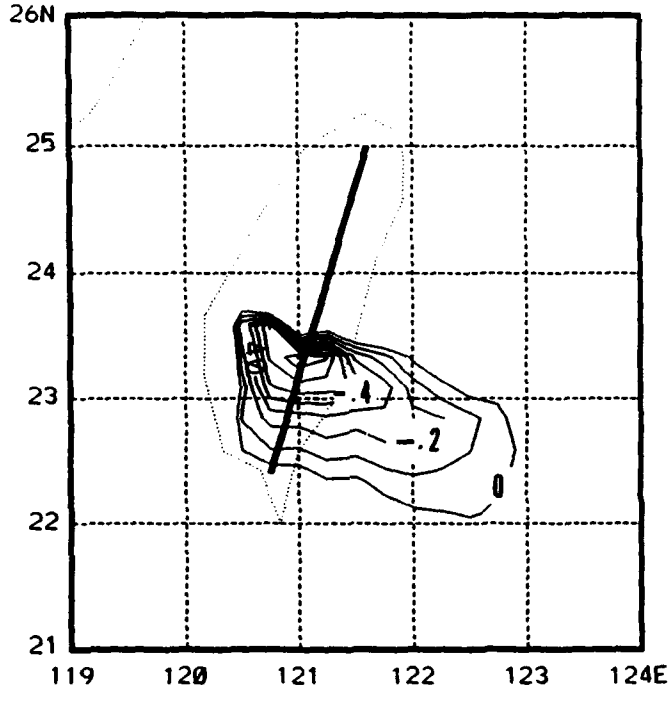

Fig. 5.20 The maximum δp (of the four directions, in mb) as a function of the typhoon center location when all modes are included. Only the negative area is shown. The thick line indicates the long axis of the CMR. If a typhoon center is located within this area and to the east of the CMR axis a secondary low center is produced.

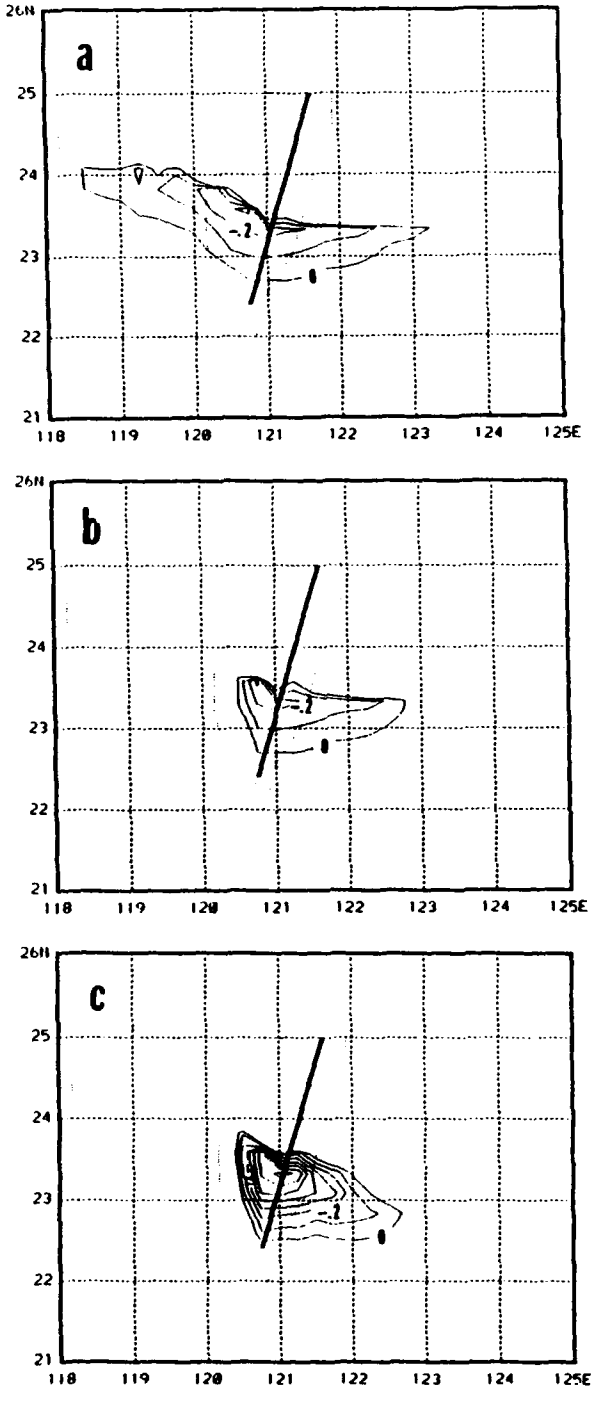

Fig. 5.21 As in Fig. 5.20, except for the sum of (a) Modes 1 and 2; (b) Modes 1, 2 and 3; and (c) Modes 1, 2, 3 and 4.

119°-123°E (Fig. 5.21a). Mode 2, which is primarily due to easterly winds crossing over the CMR, produces a trough along the western coast (Fig. 5.7). The onshore flow associated with Mode 1 (Fig. 5.6) impinging the western slope of the mountains in the southwestern Taiwan also contributes to the pressure difference because a local pressure ridge is built up there. Thus, the combinations of the two modes results in a closed low. However, the intensity of the secondary low as measured by the maximum δp is substantially lower than that shown in the total field (Fig. 5.20).

The effect of Mode 3 (Fig. 5.8) is to limit the area of typhoon centers that can lead to secondary low center development. As discussed in Section C, this mode is primarily due to a typhoon located to the east or west of Taiwan, which produces a zonal pressure gradient, plus the secondary effect of a meridional pressure gradient that is produced by meridional flow over the CMR. When the typhoon is to the east of Taiwan, the general zonal pressure gradient does not contribute to a secondary low on the west coast. If the typhoon center is too far to the east, the lee trough induced by Mode 2 (Fig. 5.7) will be too weak to overcome the unfavorable pressure gradient of Mode 3, which results in a restriction of the development regime on the east side to an area closer to the island. If the typhoon center is situated to the west, the strong pressure gradient produced by Mode 3 will again preclude the formation of a secondary low center immediately to the east of the primary center. Therefore, the secondary low development regime also is restricted when the typhoon center is located to the west of the CMR.

Addition of Mode 4 (Fig. 5.9) enhances the intensity of the secondary low center. When a typhoon approaches Taiwan, the effect of the terrain-induced local circulation

(Mode 4) on the southwestern coast is similar to that of the primary circulation (Mode 1). That is, an onshore flow produces a higher pressure against the southwestern slope of the CMR and the ridging immediately south of the station W3 contributes to the pressure difference (intensity) of the secondary low. Addition of higher modes produces only minor modifications of the development regime (Fig. 5.20), and primarily expands the area to the southeast.

G. SUMMARY

EOF and regression analyses have been applied to study the CMR effects on the surface structure of typhoons that approached Taiwan during 1971-1990. A total of 82 typhoons covering 1446 three-hourly cases is included. The basic terrain-induced modifications to the structure of a typhoon can be represented by a few EOF modes.

The first basic mode represents the trend of pressure reductions due to the approaching typhoon. It has a corresponding cyclonic inflow around the entire island. This flow structure results in rising motion and heavy precipitation over the south-central CMR. The corresponding temperature and relative humidity fields contain more structure. For example, the warm and dry downslope region on the southeastern coast, which is an area well-known for such foehn winds, is depicted clearly.

The second mode has a strong east-west pressure gradient normal to the CMR that is consistent with the terrain effect. This mode contributes approximately half of the total variance when the area mean is removed (detrending), and is most prominent when the typhoon center is located at the northern or southern tip of Taiwan. It has a strong

east-west gradient of rainfall anomalies, due to the narrow zone along the entire east coast and a region of opposite sign near the central peak region. Combined with a north-south relative humidity distribution, this mode also contributes to a distinct foehn wind pattern on the southeast coast when the typhoon center is to the north of Taiwan.

The third mode also gives rise to a strong east-west pressure gradient but it is probably due to the axisymmetric part of the typhoon circulation, as the preferred typhoon center location is to the east or west of Taiwan. In addition, this mode contains a relatively weak north-south pressure gradient that is attributed to the effect of the terrain. As with the first mode, the fourth mode has largest contributions as the typhoon center moves over Taiwan, but this mode has a higher order structure with a lower pressure region over most of the island and higher pressure in the northeastern and southwestern coast sectors. These high pressure zones are due to the effects of the flow against the mountains in the northeastern and southwestern coastal regions. Modes 3 and 4 contribute slightly less than 20% and slightly more than 5%, respectively, of the total variance of the detrended data. The rainfall, temperature and humidity patterns of both modes are again consistent with the up- and down-slope vertical motions.

In general, no significant surface structure dependence on the direction or speed of typhoon motion is found when all cases are included. However, differences in the structure are identified for two clearly different, persistently-smooth track types. The first type is south-to-north along the eastern coast of Taiwan and the other is southeast-to-northwest over southern Taiwan. Discernible differences in surface fields are observed when storms are in the region where the two tracks intersect. The most

prominent structure difference is on the western coast where a secondary leeside low center appears as a salient feature for the southern track. In the case of the east-coast track, only an open leeside trough is observed. The differences are attributable to the different mean steering flows that are assumed to be responsible for the different tracks.

The leeside secondary low develops only when a typhoon center is located within a special region, which covers southeastern Taiwan and extends east-southeastward to include an ocean area of approximately 2° long. x 1° lat. offshore. Modes 1, 2 and 4 are important components of the secondary low. The development does not seem to have a high dependency on the translation speed of the typhoon, as reported by some numerical modeling studies (e.g., Bender et al. 1987).

The development of the secondary low cannot be explained simply as a leeside effect of the mean steering flow crossing the CMR. Numerical simulations by Smolarkiewicz and Rotunno (1989) and Sun et al. (1991) show that the scale of the leeside vortex is comparable to that of the barrier. The interaction of mean steering flow and the CMR would give a vortex scale much too large compared with the observed scale. Our results show that the secondary low has a smaller scale because the return flow of the cyclonic circulation on the lee side is against the mountain. This causes a local build-up of the surface pressure south of the lee vortex, and thus a smaller-scale low center.

The secondary low center identified in this study is based on pressure data. In model simulation studies of terrain effects such as Smolarkiewicz and Rotunno (1989) and Sun et al. (1991), the induced pressure and circulation centers are typically at

different locations. Although the current data set is not adequate to reliably locate the circulation center, the indications are that the circulation center is more offshore. The lack of upper-level data is a serious shortcoming. Numerical model simulations will be utilized in the next chapter to investigate the terrain effects on typhoon structures.

VI. SIMULATION STUDY OF TERRAIN EFFECTS ON VORTEX STRUCTURE

The synoptic observation network near the Taiwan area is not adequate to observe in detail the vertical structure of the typhoon. Even though many more surface stations are available, definition of such features as the multiple secondary lows over western Taiwan or the structure over the adjacent ocean area have to be based on subjective interpretations (e.g., Wang 1980). Therefore, the discussion of terrain effects on vortex structure in the previous chapter has been based on a climatological method and restricted to the island surface station network. In this chapter, numerical simulations of the barrier effect on the vortex structure change are studied. As all these simulations have been introduced in Chapter IV, the focus here is the structure changes as the vortex passes over the barrier.

A. STRUCTURE OF THE WEAK VORTEX WITHOUT TERRAIN EFFECT

The central pressure of the weak vortex is nearly constant at about 1,003 mb (Fig. 4.10) after being superposed in a ocean-only 5 m/s zonal flow (WOC). The surface pressure and wind fields are also in a quasi-steady state as the vortex is translated westward (Fig. 6.1). The isobars are nearly circular and the cyclonic circulation converges into the center. The strongest low-level wind is located north of the center, and the maximum wind speeds decrease slightly as the simulation continues. The heavy

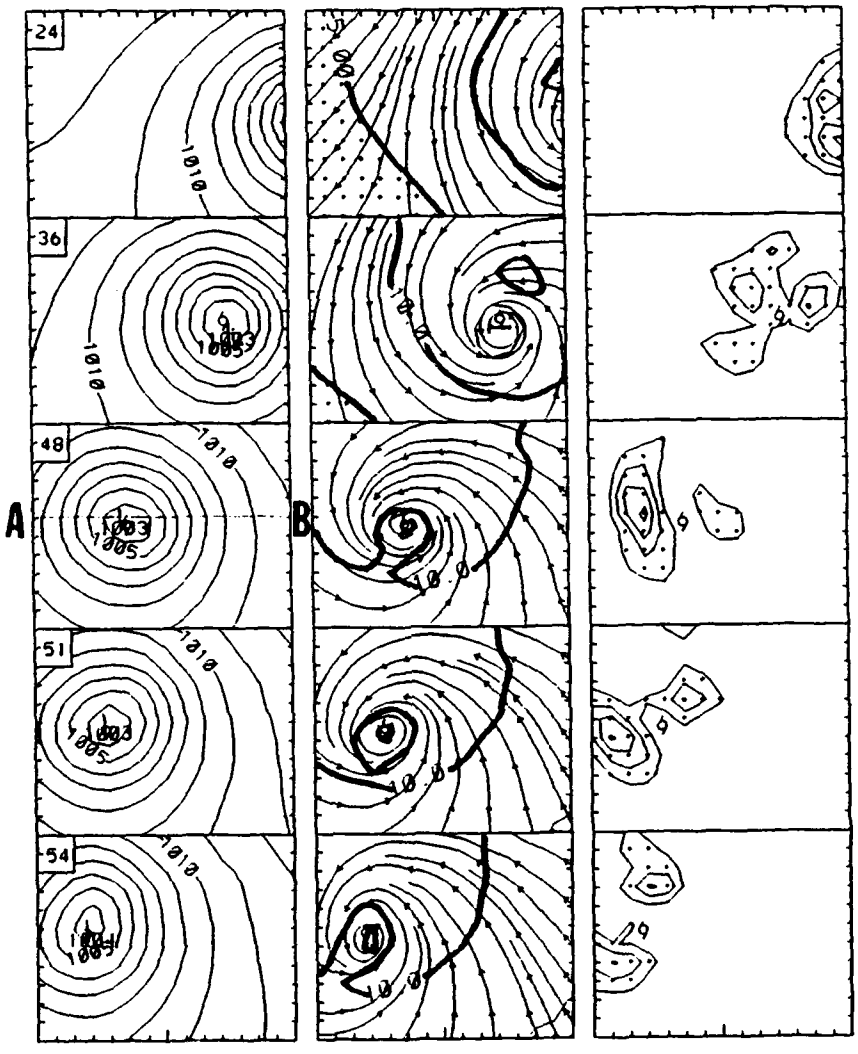

Fig. 6.1 A sequence (time at upper-left of each row, not in same interval) of sea-level pressure (left, in 1 mb intervals), streamlines and isotachs (5, 10 and 15 m/s) at the lowest model level (center column), and the hourly accumulated precipitation (right, in 2 mm/h intervals) from simulation WOC. Area of wind speed smaller than 5 m/s and hourly precipitation greater than 2 mm are shaded. Each panel covers same east-west (630 km) and north-south (495 km) subarea of the model domain. Cross-section diagrams in Fig. 6.3 are taken along line AB at 48 h.

precipitation cells associated with the low-level convergence regions do not reach a steady state. The precipitation pattern is continually changing as the cells are rotated around the center. Two major precipitation cells are found at 48 h. One heavy precipitation cell with an hourly accumulated rainfall greater than 8 mm is located west of the center, and another weaker precipitation cell is east of the center.

Whereas a large area of wind speeds greater than 15 m/s is found at higher levels (Fig. 6.2), the winds (Fig. 6.1) on the surface are all less than 15 m/s at 48 h. The low centers can be easily identified at the four levels in Fig. 6.2 within nearly circular height contours. As expected for cyclonic warm-core vortices, the intensity is weaker at the 500 mb level as the pressure gradients and the wind speeds are both weaker than at the lower levels. The center positions are not vertically co-located in this weak vortex, as the centers below 700 mb are north of the 500 mb center. The convergence is concentrated near the surface for the weak vortex, with no significant inward motion found above the 850 mb level.

Both of the precipitation cells at 48 h (Fig. 6.1) are associated with humid regions with strong and deep upward flows (Fig. 6.3), especially west of the center where the maximum upward motion is larger than 30 cm/s in the middle troposphere. Near the center, dry and downward motions with higher temperature are simulated (Fig. 6.3). The wind direction changes in the vertical from westerly to easterly west of the center (Fig. 6.3), which is the result of the upper-level anticyclonic outflow plus an effect due to the center tilt. The upper-level center is located south of the cross-section. A shallow humid layer near the surface is due to the continuous moisture supply from the warm

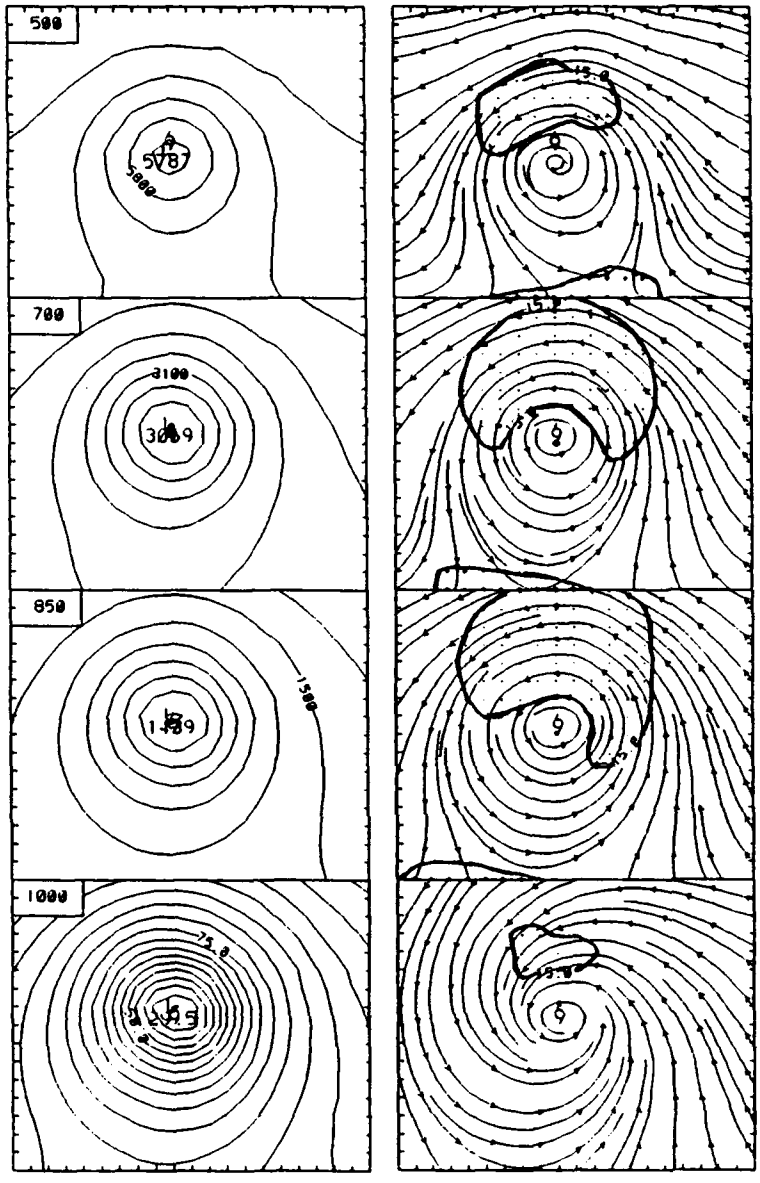

Fig. 6.2 Geopotential heights (left), and streamlines and isotachs (2.5 and 15 m/s on right) for simulation WOC on four levels at 48 h. The height contour intervals are 10 m at 500 mb, 700 mb and 850 mb, and 5 m at 1000 mb. Wind speeds less than 2.5 m/s and greater than 15 m/s are shaded. This area is only a portion (900 km X 720 km) of the model domain that is centered on the 700 mb vortex position (typhoon symbol).

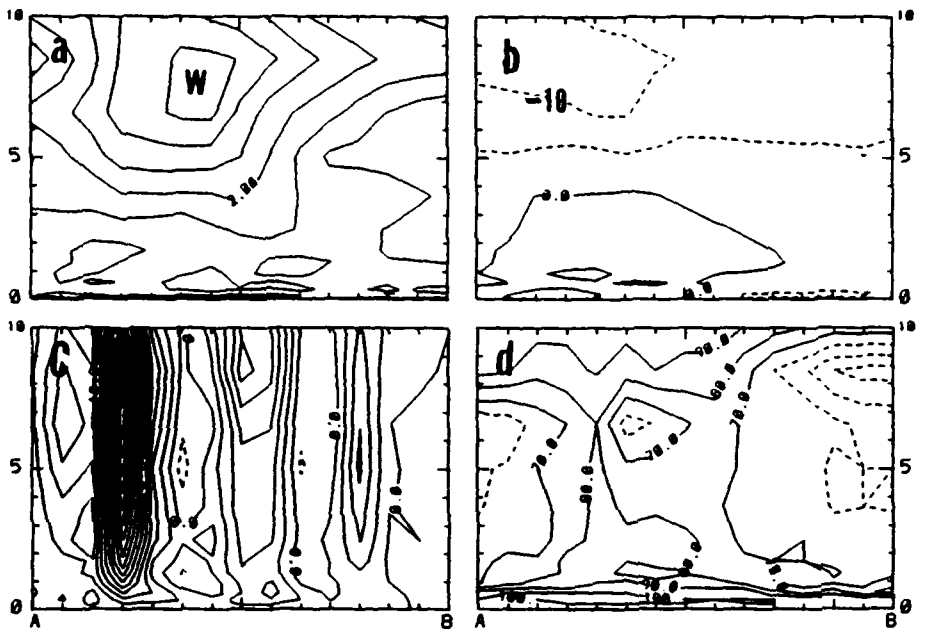

Fig. 6.3 Vertical cross-section from ground to 10 km of (a) temperature (°C) deviation from the initial profile (TABLE II), (b) *u*-component of wind speed (m/s), (c) vertical velocity (10 cm/s) and (d) relative humidity (%) taken along line AB of Fig. 6.1 for the WOC simulation at 48 h. The temperature lower than the initial profile, easterly wind, downward motion and relative humidity below 70 % are in dashed lines. The intervals are (a) 0.5°C, (b) 5 m/s, (c) 2 cm/s and (d) 10 %.

ocean. Evaporation from the sea-surface, combined with boundary layer convergence and cumulus parameterization process produces a deep column of moist air near the center region. The high relative humidity area at 8 km above the center indicates the moisture is advected outward by the upper-level flow.

The budget of vorticity is useful to understand the vortex movement. The total vorticity tendency on an f-plane may be separated into components (e.g., Holton 1979)

$$\frac{\partial \xi}{\partial t} = - V\cdot\nabla\xi - (\xi+f)\nabla\cdot V - \omega\frac{\partial \xi}{\partial p} + \left(\frac{\partial u}{\partial p}\frac{\partial \omega}{\partial y} - \frac{\partial v}{\partial p}\frac{\partial \omega}{\partial x}\right) + Residual \qquad (6.1)$$

where the terms on the right are due to the horizontal advection of absolute vorticity, the vorticity produced by convergence (stretching term), the vertical advection, twisting of horizontal vorticity into the vertical (tilting term), and a residual term that includes friction, diffusion and other computational effects.

Based on an observational study, Chan (1984) reported typhoons tend to move toward the maximum positive vorticity tendency, and the horizontal advection of the total vorticity has a very high correlation with the total vorticity change at the middle levels. Similar results are shown in Fig. 6.4a at the 700 mb level for the ocean-only simulation WOC at 48 h. For example, the vortex center (typhoon symbol) of WOC is co-located with the vorticity center. Only small divergence or convergence is found at 700 mb. The vorticity tendency has a maximum (minimum) to the west (east) of the center, which is in agreement with the westward vortex track (Fig. 4.10). The vorticity tendency due

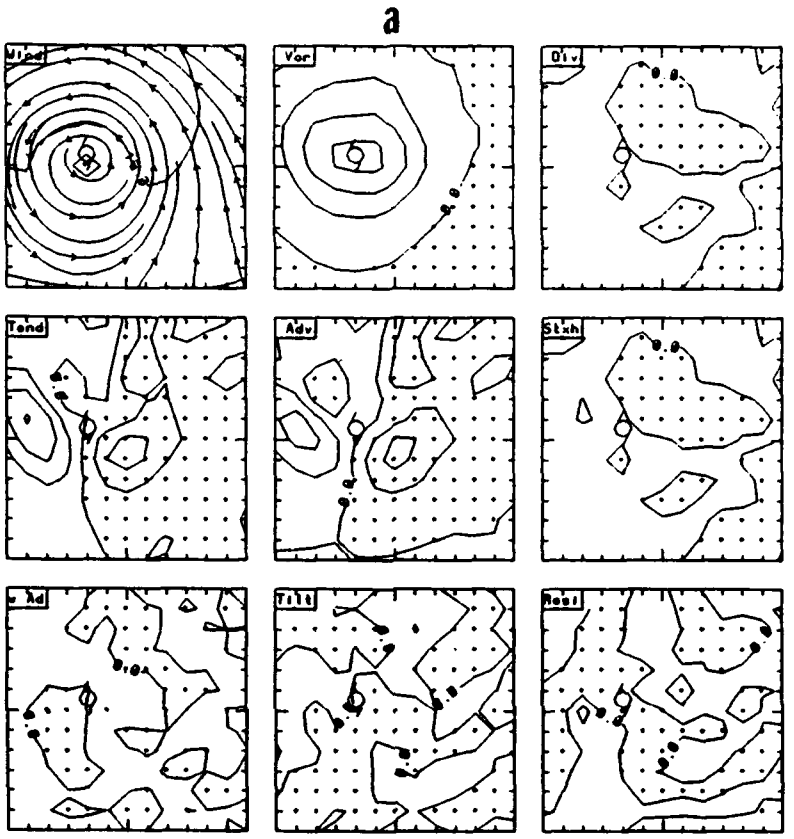

Fig. 6.4 (a) 700 mb fields from the WOC simulation at 48 h. From left to right and top to bottom, the panels are wind streamlines and isotachs (Wind), relative vorticity (Vor), divergence (Div), vorticity tendency (Tend), and the vorticity tendency from horizontal advection (Adv), stretching effect (Stxh), vertical advection (w ad), tilting (Tilt) and residual (Resi). The intervals are $1x10^{-4}$ s^{-1} for vorticity, $5x10^{-5}$ s^{-1} in divergence, and $5x10^{-9}$ s^{-1} in all of the vorticity tendency fields. The shaded areas indicate wind speeds less than 5 m/s, negative relative vorticity, positive divergence areas, and negative vorticity tendencies. The domain covers only a portion (540 km square) of the model domain with the 700 mb vortex center indicated by the typhoon symbol. (b) As in (a), except for 1000 mb fields.

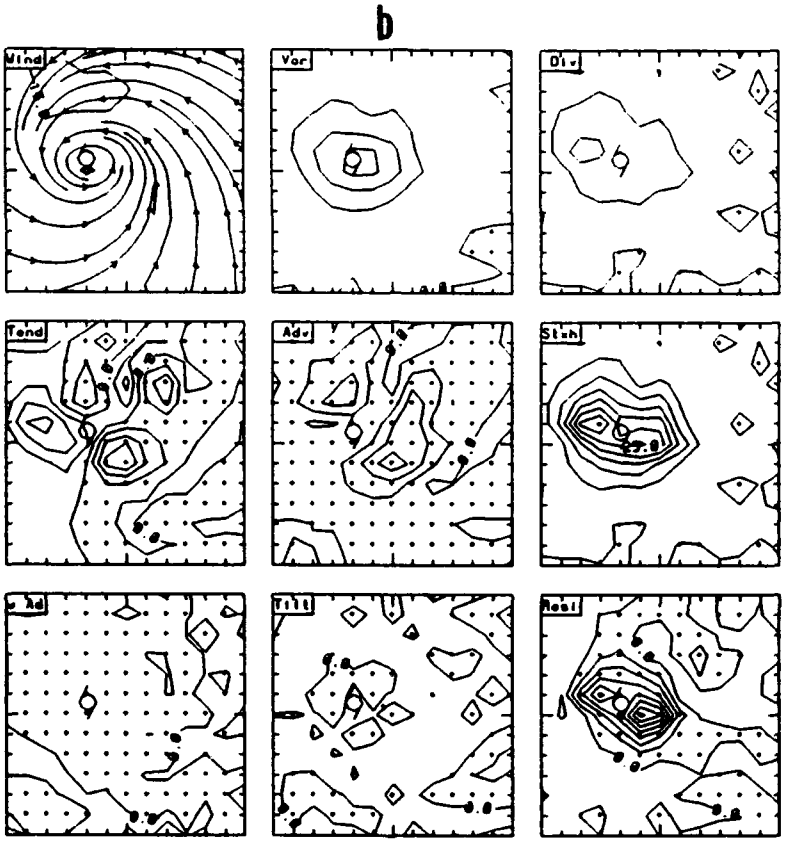

Fig. 6.4 (Continued)

to the horizontal advection term is very close to the total vorticity tendency near vortex center. The other terms such as vertical advection and tilting terms are both one order magnitude smaller than the advection term, and the stretching term (the residual term) produces a maximum vorticity increase of about 5 x 10^{-9} sec^{-2} 90 km to the northwest (west) of the vortex center where the advection effect is about twice as large as the vorticity increase.

Different terms in the vorticity budget are expected to contribute at low levels (e.g., 1000 mb in Fig. 6.4b) because the divergence/convergence and friction effects are all significant in the lower levels near the vortex center. The cyclonic flow tends to maintain the circular flow as it re-distributes the vorticity so that the vorticity contours are nearly concentric around the center at the 1000 mb level. Maximum convergence is found to the west of the center under the location of maximum precipitation (Fig. 6.1). The inflow from lower vorticity areas away from the center toward the high vorticity area near the center produces strong negative vorticity advection, especially northwest and east of the center where the inflow is strong. The vortex stretching production from the strong low-level convergence near the center is the major vorticity source to maintain the system against low-level frictional dissipation (residual term). Notice that the excess of this vorticity production over dissipation is the prime contribution to the net positive tendency region in advance of the center. Because the vertical motions are smaller near the surface than at middle level (Fig. 6.3c), the vorticity tendencies due to vertical advection or tilting effects are even smaller. As the advection and convergence terms are all very important contributions to the low-level vorticity tendency, modifications of

these fields when the barrier is included are expected to contribute to the vortex structure change over the barrier. Discussion of these changes is in Section B below.

B. STRUCTURE OF THE WEAK VORTEX UNDER THE TERRAIN EFFECT

1. Surface Structure

a. Sea-level Pressure

Surface pressure anomalies near and over the island area are shown in Fig. 6.5 for three different stages as the weak vortex approaches the barrier along three latitudes (simulations W2N, W1S and W6S). The pressure anomaly is relative to the mean pressure over 225 gridpoints near and over the barrier in the small panel of Fig. 6.5. The isobars over the terrain area illustrate the significant deviations from the circular distribution of the ocean-control vortex (Fig. 6.1) when the mountain barrier is included. Generally, high pressure anomalies are over the highest region of terrain and negative anomalies are on the coasts. Most of the contours are oriented along the long-axis of the barrier, which is similar to the observations (Fig. 5.4). The pressure gradients normal to the long-axis of the barrier are also increased as the vortices move close to the barrier. However, the pressure difference between the east and west coast is smaller in Fig. 6.5 than in the observations because the simulation is only for a weak vortex.

The pressure low (secondary low) or trough over the terrain area away from the vortex center in Fig. 5.4 is also found in the simulation (Fig. 6.5). For example, low centers are formed over the west coast of the barrier when the vortex in

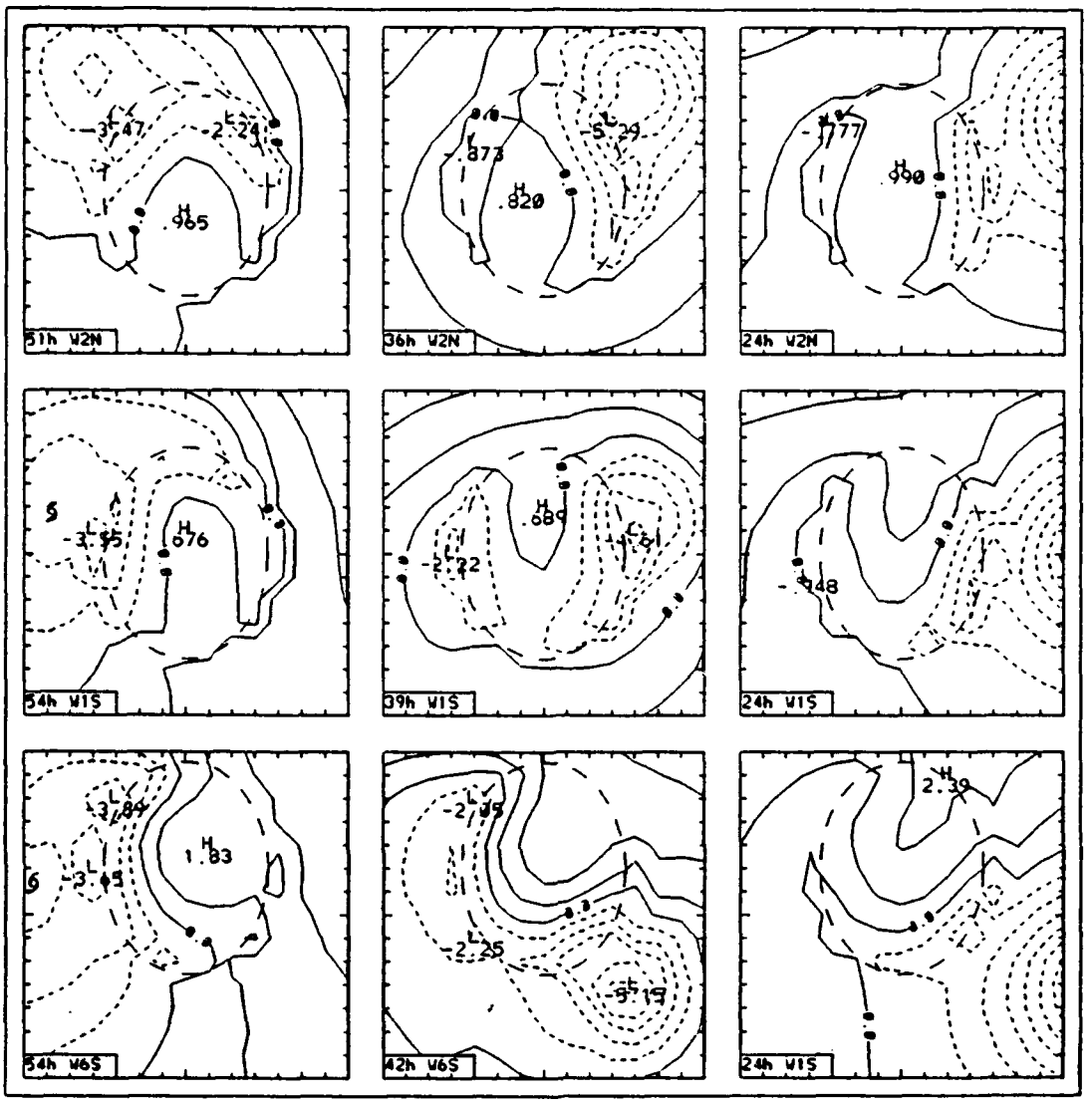

Fig. 6.5 Sea-level pressure anomalies relative to the area mean near the mountain barrier (long dashed line). The panels in the three rows are for simulations W2N, W1S and W6S, which are for vortices with different initial positions in the N-S direction. The three columns (right to left) show the terrain effect as a function of vortex center location. These simulation codes and the times are indicated in the lower-left corner of each panel. Each panel covers 630 km square, and the panels in the bottom row are displaced 90 km to the south of the others to better show the vortex structure. The pressure intervals are 1 mb, and anomalies less than the area mean are dashed. The weak third low described in the text is indicated by typhoon symbol at 54 h of the W1S and W6S simulations.

simulation W6S is southeast of the barrier at 42h (lower-central panel in Fig. 6.5). This pressure distribution is very similar to the observations in the central panel of Fig. 5.4. When the vortex is northeast (simulation W2N in Fig. 6.5) or east (simulation W1S) of the barrier, the pressure anomalies are also similar to the observations (Fig. 5.4). Although a trough is formed over the east coast as in the observations, the simulation also includes a low center over the west coast that is not present in the observations. The idealized mountain barrier included in the simulation is larger than the actual scale of the CMR in Taiwan, especially in the west-east direction. The larger mountain may enhance the blocking effect on the northerly flow. The small number of observation sites in the northern central region of Taiwan may also contribute to the uncertainty of establishing the pressure distribution between northwestern and northeastern Taiwan, especially if the pressure signal is weak. Notice that the low over the west side of the barrier does not intensify as the simulated vortex moves closer to the barrier. This result agrees with the observations (Fig. 5.20) that the secondary low over western Taiwan becomes significant only when the typhoon center is over southern Taiwan and the nearby ocean.

After the formation and intensification of the secondary low and the weakening and dissipation of the vortex over the terrain, discontinuous surface center tracks are found for simulations W1S and W6S. When the W1S vortex center is blocked and deflected northward on the east slope (Fig. 6.6a), the surface pressure center is filled and is dissipated after 47 h. Meanwhile, the secondary low over the western coast is slightly intensified to become the minimum pressure center at 45 h (not shown).

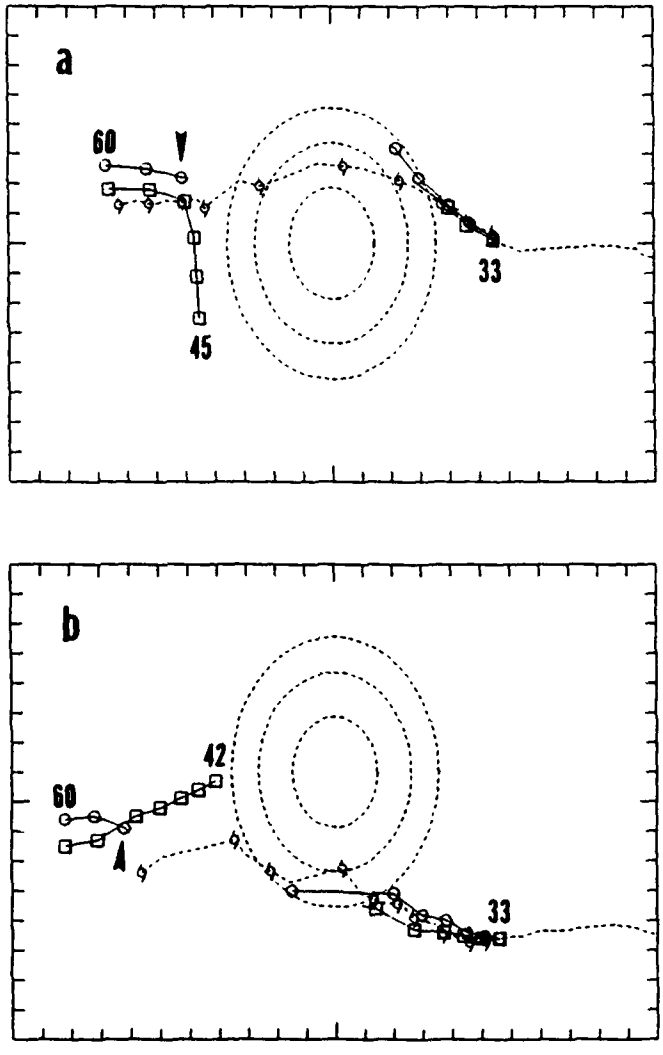

Fig. 6.6 Tracks of 700 mb pressure center (dashed line connecting typhoon symbols), sea-level pressure center (solid line connecting circles) and surface wind circulation center (solid line connecting boxes) for simulation (a) W1S and (b) W6S. Three hourly center positions are indicated by symbols. The grid interval is equal to 45 km, and the elliptical-shaped barrier is in dashed lines. Arrows point to the third low center (see text).

However, the secondary low, which seems to have been locked over the terrain area, does not move westward as the new vortex. A third pressure center is found northwest of the 700 mb center at 54 h (Fig. 6.6a). This newly formed center moves westward and later becomes the minimum pressure center. The terrain-locked secondary low and the formation of a third center are similar to the Bender et al. simulation, except the location of the secondary low in their Fig. 15 is located closer to the mountain center and it is produced only for a fast-moving typhoon. However, the secondary low in the W1S simulation is located near the west coast and it can be formed in a slower-moving vortex, which is similar to the observations (e.g., Wang 1980).

The upstream weakening of the vortex and slight intensification of the terrain-locked secondary low is also found in simulation W6S. However, the original vortex in the W6S simulation is not deflected northward, but moves westward along the southern slope (Fig. 6.6b) before it is dissipated at 51 h. A third low pressure center is found about 150 km west of the barrier. This newly formed center also moves westward and becomes the minimum pressure center later as in the W1S simulation.

The vortex intensities become much weaker (smaller pressure gradients) after the vortices have passed over the barrier (left column in Fig. 6.5). Significant barrier modifications of the vortex structure are still occurring. Lee troughs are produced over the northeastern coast for the W2N and W1S simulations. Over the western barrier, the isobars do not circle around the vortex center as in the ocean-control (Fig. 6.1), but are oriented more along the terrain with lows or troughs induced over the western coast. These terrain-modified features are similar to the observations (Fig. 5.4).

b. Surface Wind

The surface wind distributions corresponding to Fig. 6.5 are shown in Fig. 6.7. The inclusion of the mountain barrier significantly distorts the surface flow structure from the ocean-control simulation (Fig. 6.1). Near and over the barrier, the streamlines no longer are circles around the center. Notice also that the wind and the pressure (Fig. 6.5) fields do not have a simple balance relation, and the two centers do not necessarily coincide over the barrier. The surface wind speeds over the barrier are generally smaller than over the adjacent water, as the friction slows the flow over the barrier and blocking effect deflects and accelerates the flow around the barrier.

When the vortex of simulation W2N (upper row in Fig. 6.7) is far to the east of the barrier at 24 h, a light wind area with speeds of less than 5 m/s is co-located with the pressure ridge (Fig. 6.5) on the upwind side of the barrier. The flow moving upslope onto the barrier is slowed. However, most of flow is deflected to pass around the barrier. The flow deflection increases the wind speeds between the vortex center and the barrier, and thus the horizontal wind shear on the east slope. The wind speed northwest of the barrier also is increased. Although upslope cyclonic and convergent motions are found over the west barrier, the wind speeds are generally very weak (less than 2.5 m/s). Most of the blocked flow moves along the west coast to pass around the southern end of the barrier, and then it accelerates to converge with the northerly flow along the east side of the barrier.

A similar upwind flow speed decrease, deflection of the streamlines around the barrier to the southern end of Taiwan, and then a convergent zone south of

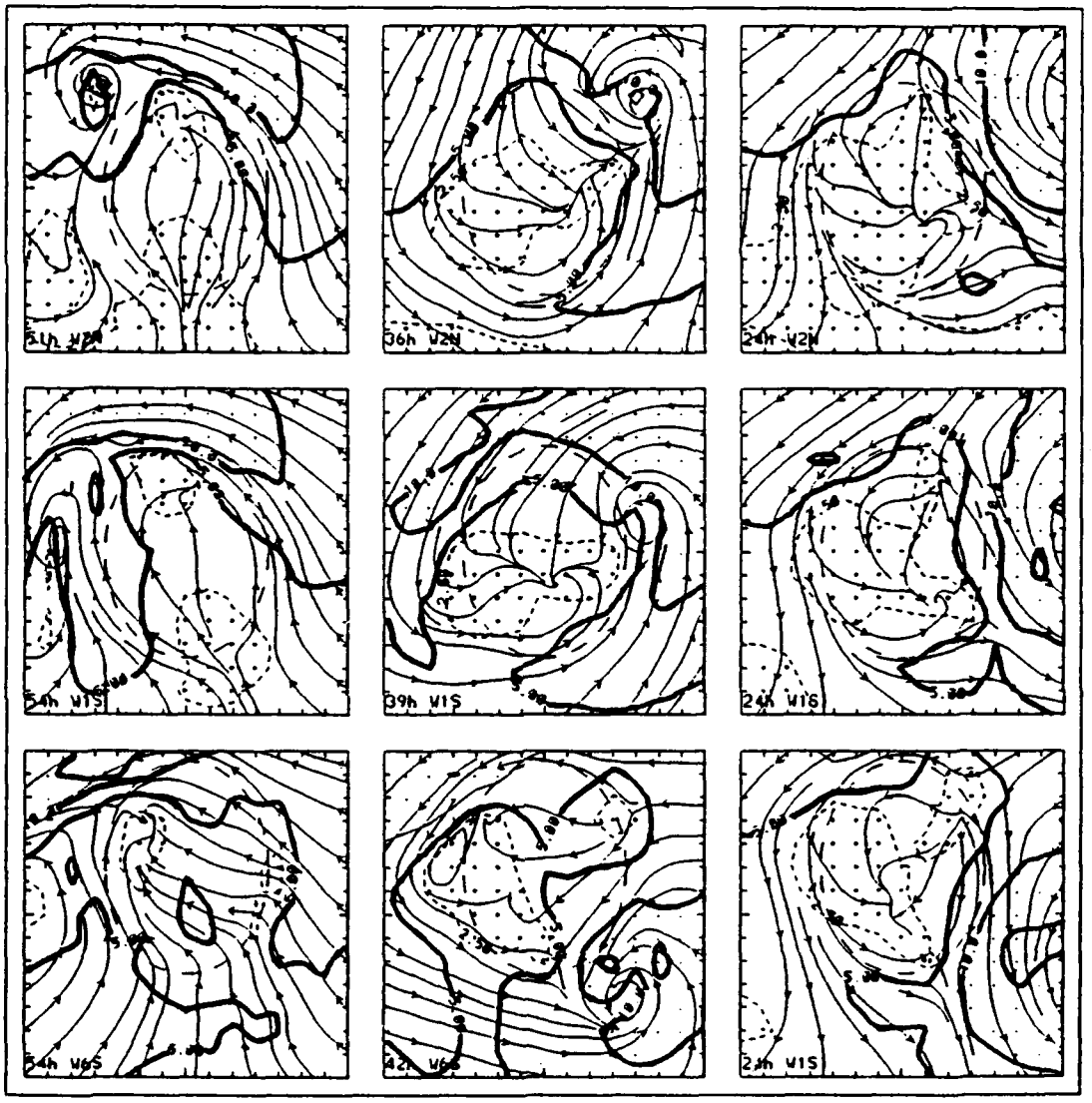

Fig. 6.7 As in Fig. 6.5, except for the surface streamlines and isotachs from the different simulations. The isotachs are thick solid lines from 5 m/s to 15 m/s. Areas with wind speeds less than 2.5 m/s (thin dashed line) and greater than 10 m/s are shaded.

the typhoon center have been observed. For example, Wang et al. (1992) showed the surface streamlines were divided on the northeast end of Taiwan when Typhoon Opal (1962) was east of Taiwan (Fig. 6.8a). The northerly wind speeds over northern Taiwan were decreased strongly from the nearby ocean toward the land. The flow to the west of Taiwan did not pass over the CMR, but was deflected around the southern end of Taiwan before it accelerated to converge with the northerly flow.

The streamlines are deflected less as the stronger winds near the vortex center in simulation W2N move over the northern barrier at 36 h (Fig. 6.7). The 5 m/s isotach is pushed inland, and more of the flow is able to move upslope over of the barrier as a result of the increased Froude number. However, most of the flow is still not strong enough to pass over the barrier. The streamlines along the west coast pass around the southern end of the barrier and create the convergent zone south of the center. Notice that the position of the convergent zone is rotated from the eastern side to the northeastern quadrant of the barrier between 24 h and 36 h.

When the W2N vortex moves to the northwest of the barrier at 51 h (Fig. 6.7), a southerly wind covers most of the barrier. Speed minima are found on both the southern and northern ends of the island. Stronger winds are located over the eastern side and to the northwest of the barrier. A similar wind distribution (Fig. 6.8b) was reported by Wang et al. (1992) in which the southerly streamlines were divided at the south end of Taiwan when Typhoon Opal (1965) had moved into mainland China northwest of Taiwan. A calm wind area was located over the northern tip of Taiwan, and a convergent zone extended from the calm wind area northwestward to east of the

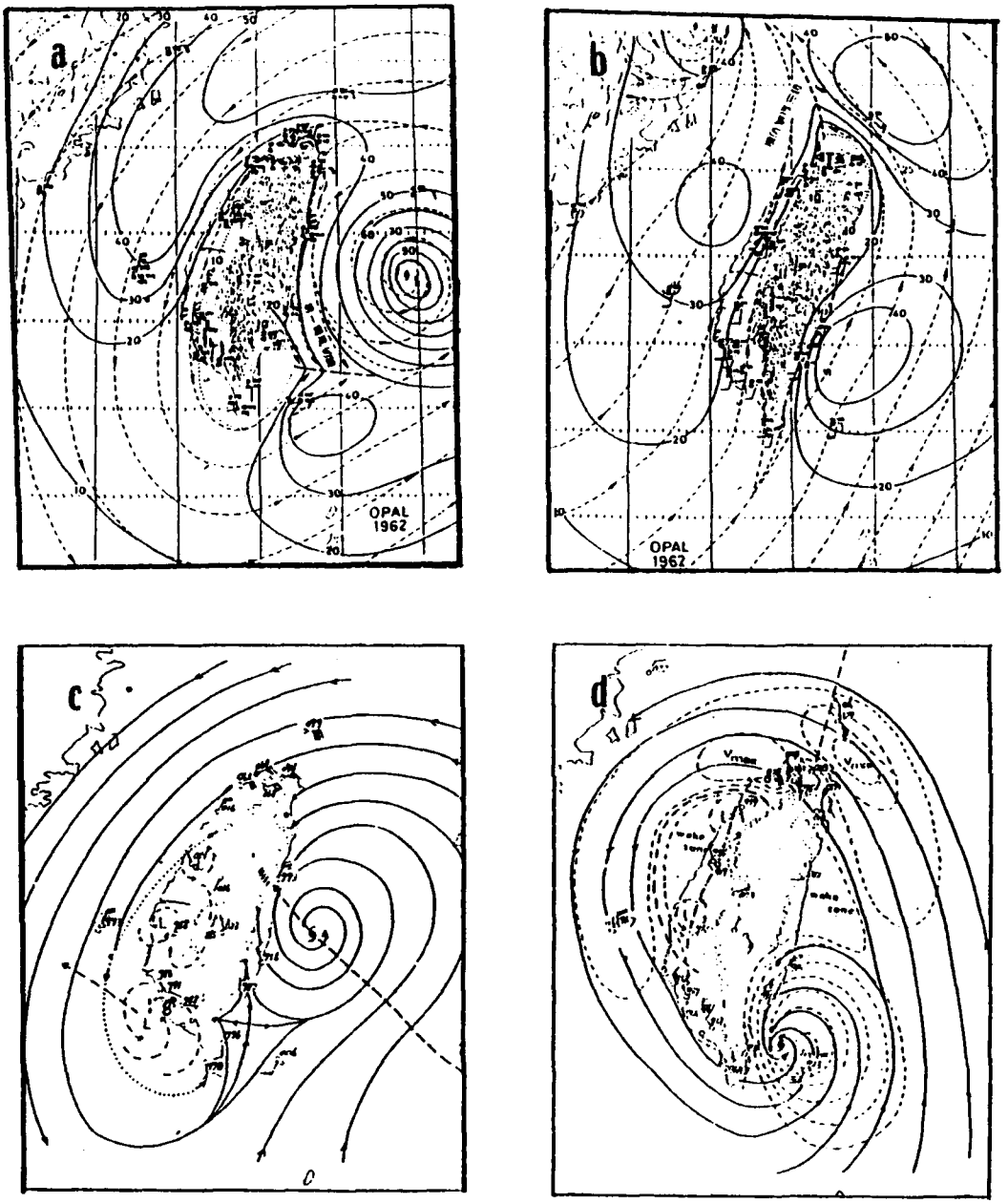

Fig. 6.8 (a) Surface streamlines (dashed) and isotachs (solid) of Typhoon Opal at 10 UTC 5 August 1962 (Fig. 3b, Wang et al. 1992). (b) As in (a), except for streamlines and isotachs at 4 UTC 6 August (Fig. 3d, Wang et al. 1992). (c) Surface streamlines (solid) of Typhoon Gilda at 00 UTC 18 November 1967 (Fig. 3.7a, Wang 1980). (d) Surface streamlines (solid) and isotachs (dashed) of Typhoon Iris at 13 UTC 23 August 1955 (Fig. 3.3b, Wang 1980).

typhoon center. Strong winds also were analyzed over the Taiwan Strait and the ocean area east and northeast of Taiwan.

The vortex in simulation W1S (central row in Fig. 6.7) approaches the central portion of the barrier. When the center of vortex W1S is far to the east of the island at 24 h, the general features of the surface wind distribution are very similar to those in simulation W2N at 24 h. The barrier induces a split in the streamlines, the wind speed is slowed on the upwind and lee sides, and the convergent zone is southeast of the barrier. When the center of W2N moves close to the barrier at 39 h (Fig. 6.7), the streamlines over the northern end of the barrier are deflected less and the 5 m/s isotach is pushed inland because more of the air is able to ascend the slope as a result of the increased Froude number.

A major difference between the wind field of W1S at 39 h and the wind field of W2N at 36 h is the greater cyclonic curvature in the flow to the southwest of the barrier. A similar structure was observed by Wang (1980) when Typhoon Gilda (1967) was near the east-central coast (Fig. 6.8c). Although Wang emphasized the formation of multiple secondary lows over the west coast, the cyclonic curvature in the streamlines southwest of Taiwan in Fig. 6.8c is very similar to the central panel of Fig. 6.7.

A cyclonic circulation center (secondary vortex) is later found southwest of the barrier at 45 h in the W1S simulation (Fig. 6.6a). This secondary vortex shifts north-northwestward and is located near the 700 mb center at 54 h (Fig. 6.6a). Meanwhile, the wind center associated with the vortex has dissipated on the east side of

the barrier at 41 h, which results in a track discontinuity from the surface wind circulation center. The circulation center is difficult to define between 41 h and 45 h.

After the secondary vortex in the W1S simulation moves to the west of the barrier at 54 h (Fig. 6.7), the major characteristics of the surface wind structure are similar to the simulation W2N at 51 h. Strong winds are found along the north and west coasts. Calm wind areas are again over the southern and northern ends of the barrier. A convergent zone extends from the northern calm wind area to the north of the vortex center. Notice that the streamlines associated with the secondary vortex are quasi-balanced with the pressure field near the third pressure low (Fig. 6.5). The surface wind center and the surface pressure center become closer to the 700 mb center and move in parallel after 54 h (Fig. 6.6a).

The vortex in simulation W6S (lower row in Fig. 6.7) approaches the southern portion of the barrier. The flow blocking effect becomes more evident because the impinging flow of the outer vortex circulation is perpendicular to the long-axis of the barrier. The upwind calm area over the northeast quadrant barrier in simulation W6S extends over a larger domain than in the other two simulations in Fig. 6.7 at 24 h. Wind speeds less than 2.5 m/s extend from the northeastern barrier to the ocean area. The wind speeds between the vortex center and the eastern edge of the barrier also are stronger than in the other two simulations, because the long-axis of the mountain barrier effectively blocks the flow from passing over the mountain.

Formation of a secondary vortex and a track (wind center) discontinuity are also found in the W6S simulation (Fig. 6.6b). When the vortex is southeast of

barrier at 42 h (lower-central panel in Fig. 6.7), a weak cyclonic vortex (secondary vortex) is found near the west-central coast. The formation of the secondary vortex in the W6S simulation may be similar to the formation of a pair of lee-side vortices when a zonal flow with small Froude number is forced around a barrier. However, the anticyclonic vortex in the pair is not produced here due to the large curvature in the flow.

A similar structure of a secondary vortex over the western coast was observed by Wang (1980) prior to the landfall of Typhoon Iris (Fig. 6.8d). Because Wang has not carefully distinguished between the secondary low (pressure) and the secondary vortex (wind), two lows were analyzed inside the calm area (wake zone) west of CMR. The simulated pressure field (Fig. 6.5) and the wind field (Fig 6.7) near the surface are not necessarily in balance, and the centers may not be co-located (e.g., Fig. 6.6). Therefore, a clear distinction is required for these two features induced by the vortex-barrier interaction.

Unlike the secondary vortex in the W1S simulation, the secondary vortex in the W6S simulation is shed southwestward before the dissipation of the original circulation center over the southern barrier (Fig. 6.6b). At 54 h, the wind center is more than 135 km to the west of the barrier. Calm areas are found on the upwind and lee sides. The strongest wind is over the northern coast, which is similar to the other two simulations in Fig. 6.7. Notice that a low pressure center is found near the secondary vortex (Fig. 6.6b), and the whole system moves westward more than 100 km ahead of the 700 mb center.

2. Lower Tropospheric Structure

Due to observational limitations, the terrain effects on the typhoon structure changes above the surface are not well-known. These model simulations suggest the modifications of the vortex structure due to the barrier are not limited to the surface, but extend over a deep layer. Height and wind fields from the W1S simulation are shown in Fig. 6.9 for three times. The vortex is elongated in the southwest-northeast direction up to at least the 700 mb level when the vortex center of W1S is about to make landfall at 39 h (Fig. 6.9a). Below 850 mb, the flow is unable to pass over the barrier to complete a cyclonic circulation around the vortex center because of the blocking effect of the barrier. Flow deflections are found over the mountain area even at the 700 mb level, which is more than 500 m above the top of the barrier. The strongly curved circulation southwest of the barrier extends more than 150 mb above the surface. Although the vortex motion below 700 mb is retarded upstream, the vortex at the 500 mb level is able to move westward relatively unaffected. This introduces a tilt of the centers with height, which may further weaken the system. The 500 mb height center at 39 h has filled about 15 m compared to the ocean-control (Fig. 6.2) and is not well-defined by concentric contours.

The pressure and wind centers are no longer co-located as the vortex-barrier interaction continues. The height center at 500 mb moves faster than the wind center from 39 h to 45 h (Fig. 6.9b), and the height center is now to the northwest of the wind center. By contrast, the 700 mb wind center moves faster than the height center during the same period. Whereas the minimum 700 mb height is located to the north of the

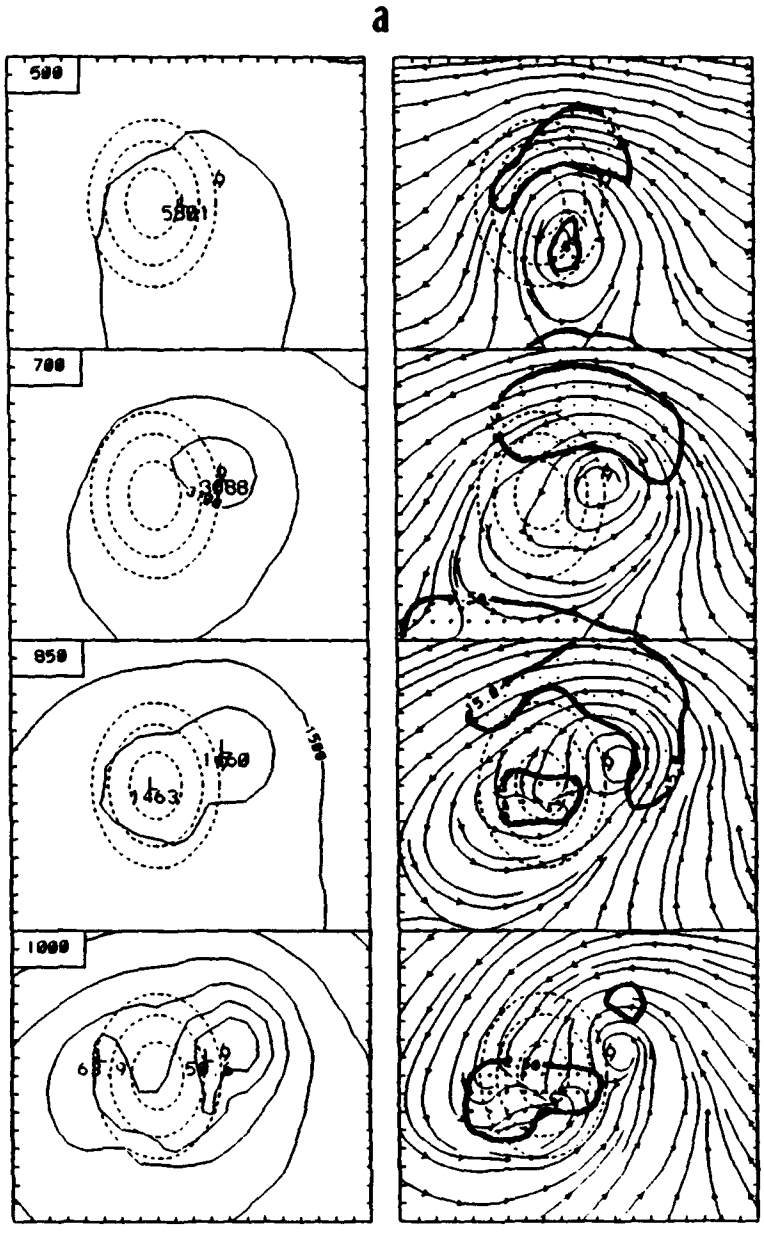

Fig. 6.9 As in Fig. 6.2, except for the height (left), and streamlines and isotachs (2.5 and 15 m/s on right) for simulation W1S for four levels at (a) 39 h (b) 45 h and (c) 60 h. Different areas are covered in (a), (b) and (c) to keep the vortex and barrier (dashed lines) near the domain center.

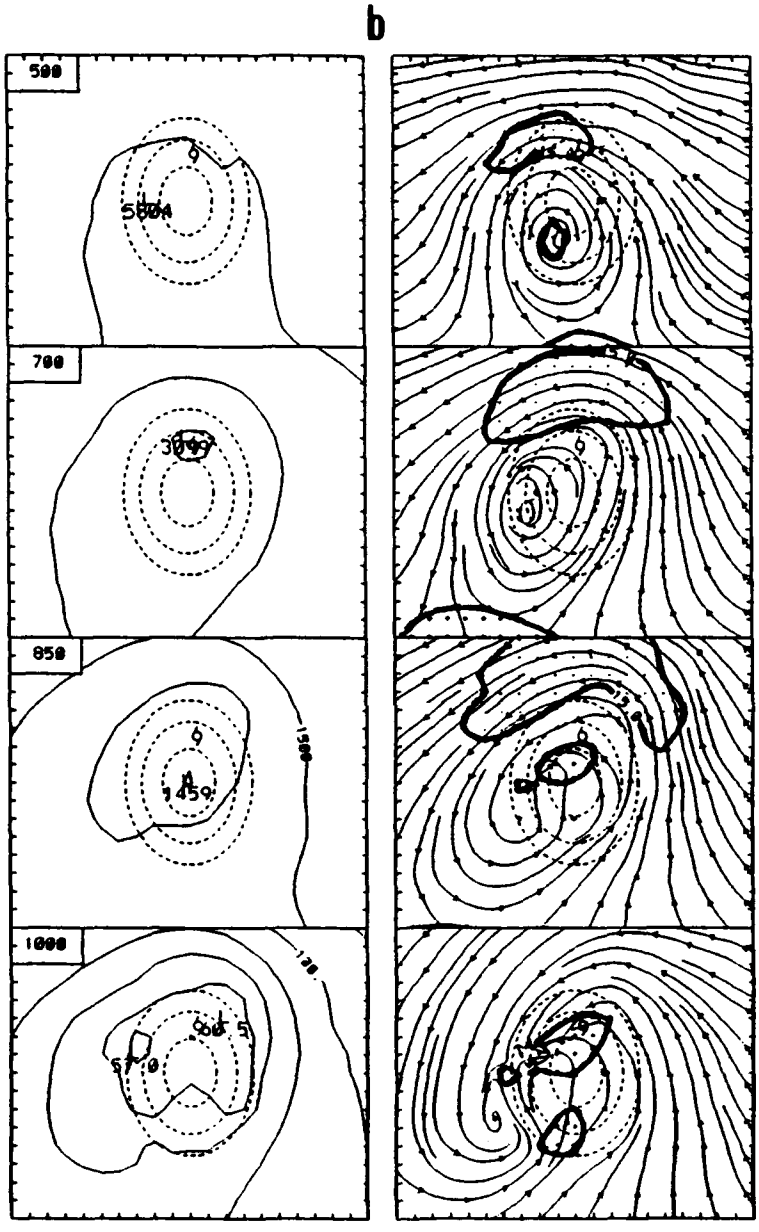

Fig. 6.9 (Continued)

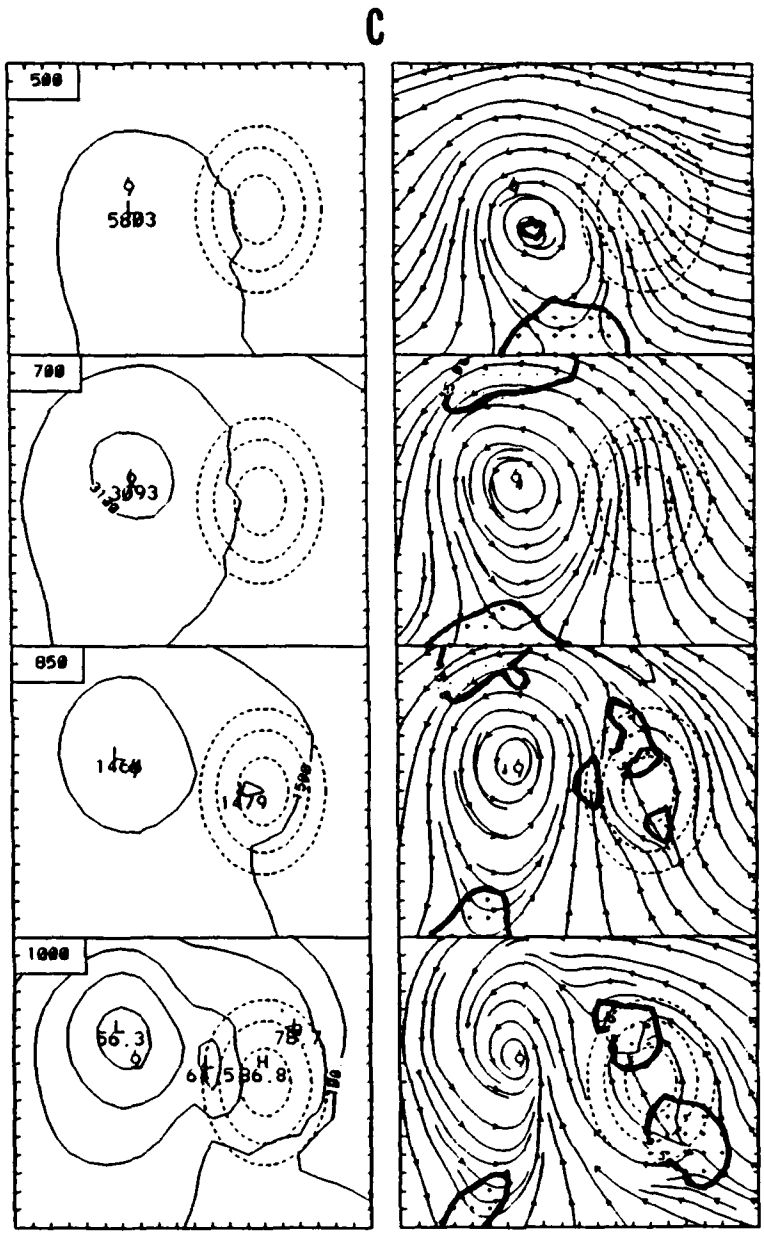

Fig. 6.9 (Continued)

mountain center, the wind circulation center is found over the southwestern coast. The minimum 850 mb height is near the mountain peak (actually this would be underground) from 39 h to 45 h. Thus, this low center may be a result of the surface pressure extrapolation scheme. However, the cyclonic circulation and height field over the southwestern coast are clearly intensified as the 850 mb wind and height center associated with the original vortex are dissipated on the east slope. Similarly, the upstream 1000 mb center dissipates and a secondary center is formed on the lee side. This suggests that the observed discontinuous track when a typhoon appears to jump across the CMR is not limited to the surface, but extends to a deeper layer. Distinguishing the wind center from the height center is also required at levels above the surface since these centers are not co-located. The secondary low at 1000 mb is north of the secondary vortex and the upper-level streamline centers are east of the secondary vortex at 1000 mb at 45 h.

Later, the low-level secondary vortex shifts north-northwestward slowly similar to the movement of the secondary vortex at the surface (Fig. 6.6a) as the upper-level streamline centers move westward. At the end of the simulation (Fig. 6.9c), the centers are much closer to being vertically aligned, and the system is undergoing weak intensification. Notice the 1000 mb low center over the western coast associated with the surface secondary low (Fig. 6.5) has persisted throughout 45 h to 60 h. Although this low center may have shifted in location, it has been locked over the west coast. As mentioned above, a similar terrain-locked low is shown in the Bender et al. simulation (their Fig. 15). In fact, they included the changes in the terrain-locked low center as part of the vortex track. This simulation suggests the low center (e.g., north

of the secondary vortex in Fig. 6.9b) is due to the local barrier modification of the height field. It is perhaps better to focus attention on the secondary vortex that has a quasi-balanced height field, e.g., the curved contour heights tend to follow the streamlines southwest of the barrier in Figs. 6.9a and 6.9b. A track-determination algorithm that simply searches for the lowest pressure center may not accurately represent the motion of the reforming vortex on the lee side.

For the W2N vortex that approaches the northern portion of the barrier, the highest winds are north of the barrier and do not interact with the barrier directly. Therefore, the structure modifications are mainly in the lower levels below the mountain top (not shown). The centers at various pressure levels are relatively close together and the passage around the barrier forms a continuous track.

For the W6S vortex that approaches the southern portion of the barrier, the highest cyclonic winds associated with the vortex directly impinge on the long-axis of the barrier, which results in more severe structure modifications. Very marked westward tilts of the wind and height centers with increasing height are found at 39 h (Fig. 6.10a) due to the deceleration of the low-level vortex (see Section IV.C). Significant flow structure modifications have already been produced at lower levels, with the development of a closed streamline secondary vortex and a deep trough at 1000 mb on the lee side of the barrier. However, the height centers and the wind centers at 1000 mb to 700 mb are relatively close together at 39 h.

As in the W1S case, the modification of the W6S vortex structure becomes more severe as the vortex-barrier interaction continues. Even the 500 mb streamline

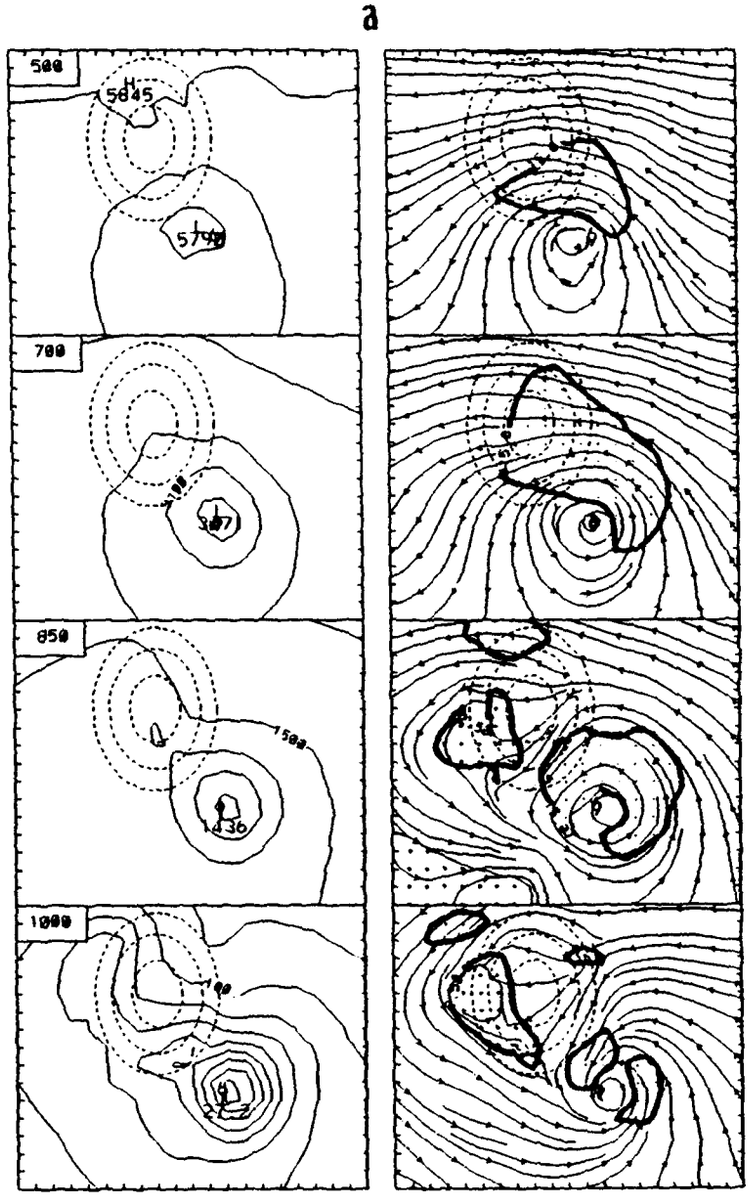

Fig. 6.10 As in Fig. 6.9, except for the height (left), and streamlines and isotachs (2.5 and 15 m/s, right) for simulation W6S for four levels at (a) 39 h, (b) 48 h and (c) 51 h.

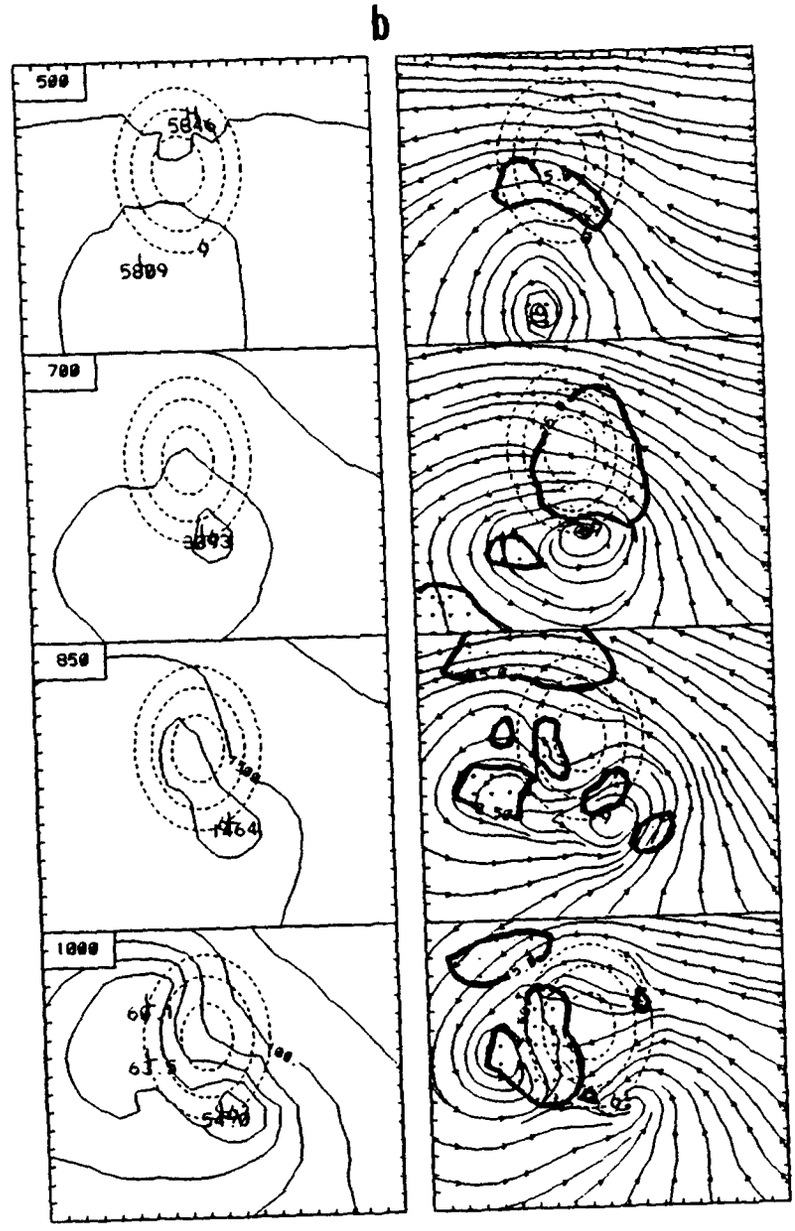

Fig. 6.10 (Continued)

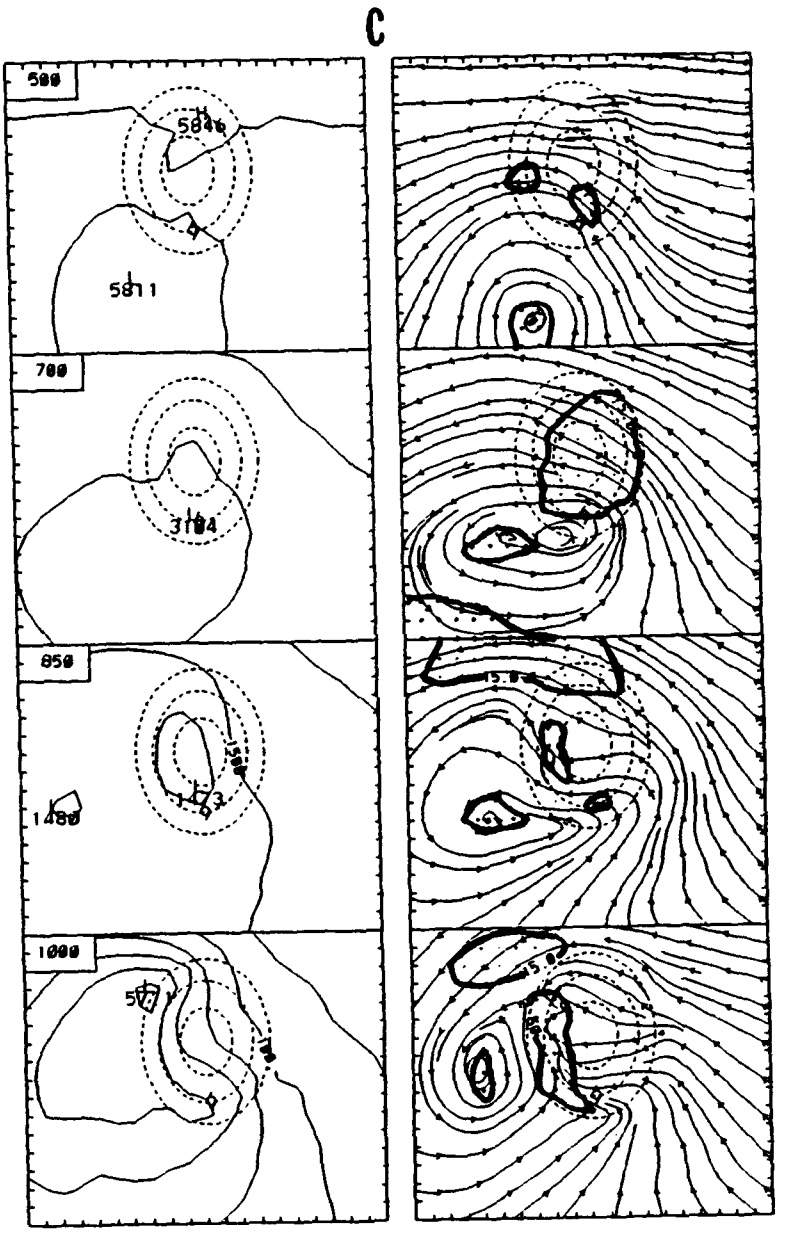

Fig. 6.10 (Continued)

center is deflected southwestward and is more than 200 km south-southwest of the weak height center at 48 h (Fig. 6.10b). The streamlines at 700 mb and 850 mb are elongated in the east-west direction when the low-level secondary vortex intensifies and shifts southwestward. The low-level lee trough along the west coast also becomes stronger with increased pressure gradients along the western slope of the barrier. Although the pressure minima are locked on the western coast area as in Fig. 6.9, contours in the height field are shifted westward over the ocean as well.

The 500 mb flow is practically unmodified during the next 3 h (Fig. 6.10c). However, the height center is weaker than at 48 h and is shifted southward closer to the wind field. Continued weakening of the vortex occurs in the lower levels. The 700 mb low center is filled 11 m, and the circulation is severely elongated in the west-east direction. Both the 1000 mb and 850 mb wind centers associated with the original vortex have been dissipated over the southern barrier at 51 h. Meanwhile, the wind circulation on the west side of barrier has intensified. A 850 mb low center is found near the wind circulation center west of the barrier. The track discontinuity in this simulation occurs in a deep layer up to at least 850 mb. However, the wind centers on the west side are not co-located, as the 850 mb center is to the east of the 1000 mb center. The minimum 1000 mb height also is not associated with the secondary vortex, because of the local modifications of the height field. The wind and height field centers at different levels are still not co-located by the end of the simulation at 60 h (not shown) because a longer adjustment period is required after the more severe structure modifications of the W6S vortex.

C. FORMATION AND DEVELOPMENT OF SECONDARY CENTERS

The model simulations described in Section B apparently reproduce observed surface structure characteristics such as the secondary low, secondary vortex, calm wind areas, wind channeling effects, convergent zones, etc. detected when typhoons pass nearby Taiwan. Increased model resolution to include the detailed topography and more of the storm structure may be necessary to compare with the local observations. Therefore, discussion of temperature, precipitation and other meteorological variables will not be further pursued here. The focus will be the formation of the secondary centers that appear to be adequately simulated with the present model. Although these are less well-observed features in the typhoon-CMR interactions, they are important for forecasting the track downstream of the CMR.

1. Physical Mechanisms

a. Secondary Low

The height tendency equation has been used successfully to diagnose the physical processes in midlatitude weather systems (e.g., Hirschberg and Fritsch 1991). No simplifying assumption between wind and pressure fields such as the quasi- or semi-geostrophic relation is required, and all the variables such as vertical motion and diabatic heating can be obtained from the model output. Therefore, the height tendency equation is applied here to examine the formation of a secondary low when the vortex approaches the barrier.

Under the hydrostatic assumption, the height tendency at a bottom pressure level (p_b) is equal to the height tendency at the top pressure level (p_t) plus a term from the vertical logarithmic integral of the temperature change between p_b and p_t (Holton 1979). The temperature change can be separated into terms due to different processes. Therefore, the height tendency on a lower level (Z_b) can be written as:

$$\frac{\partial Z_b}{\partial t} = -\frac{R}{g}\int_{p_b}^{p_t} V\cdot\nabla T \, d\ln p - \frac{R}{g}\int_{p_b}^{p_t} \omega\left(\frac{\partial T}{\partial p}-\frac{RT}{pc_p}\right) d\ln p + \frac{R}{g}\int_{p_b}^{p_t} \frac{\dot{Q}}{c_p} d\ln p + \frac{\partial Z_t}{\partial t} + Residual \qquad (6.2)$$

where the terms on the right side are due to horizontal advection, vertical motion, diabatic (precipitation) heating, the height change above the top boundary (Z_t) and a residual term that includes contributions from diffusion, planetary boundary effects, dry convection and calculation errors.

Formation of the secondary low near the surface is studied with the height tendency on the 1000 mb surface. The temperature profile below the ground is assumed to be unchanged. The top boundary (p_t) is set to 100 mb, because the 1000 mb height changes from the height changes above 100 mb are generally very small (the maximum value is less than 2 m/h). Moreover, no obvious relation between the height change above 100 mb and the formation of the secondary low is found. Therefore, the height change contributed from above 100 mb will not be included.

The sea-level pressure at a location three grid intervals to the north and six grid intervals to the east of the mountain center (location N3E6) for simulation W2N

(Fig. 6.11a) reaches a minimum value at 30 h when the vortex center is nearby. The precipitation heating is the largest contribution to the 1000 mb height change at N3E6 during the period from 18 h to 36 h. Two maxima in the precipitation heating term indicate heavy precipitation on the eastern and western sides of the vortex as shown in the ocean-control simulation (Fig. 6.1). However, the precipitation heating term is mostly offset by the associated upward motion expansion cooling effect. Furthermore, the sum of these terms is merely offset by the residual term. Consequently, the 1000 mb height tendency closely follows the advection component at location N3E6 where the terrain effect is relatively small. Similarly, the advection term determines the height change for other locations away from the barrier. The calculations in the ocean-control simulation (not shown) also support the conclusion that the advection is the dominant term for the 1000 mb height change when the barrier effect is not important.

A second location chosen for the height tendency study (Fig. 6.11b) is three grid intervals north and three grid intervals west of the mountain center (location N3W3) near the center of the secondary low (before 36 h, Fig. 6.5) in the W2N simulation. The sea-level pressure at N3W3 decreases gradually from about 1010 mb at 18 h to a minimum value of about 1006 at 50 h when the vortex center is nearby (see Fig. 6.5 at 51 h). The 1000 mb height tendency at N3W3 is about -1 m/h in the period from 18 h to 34 h, and the height decrease becomes larger (about -2 m/h) from 35 h to 40 h. The largest decrease (about -3 m/h) occurs near 43 h.

Two different mechanisms contribute to the two periods of pressure change at location N3W3 for simulation W2N. Before 36 h, the precipitation heating has

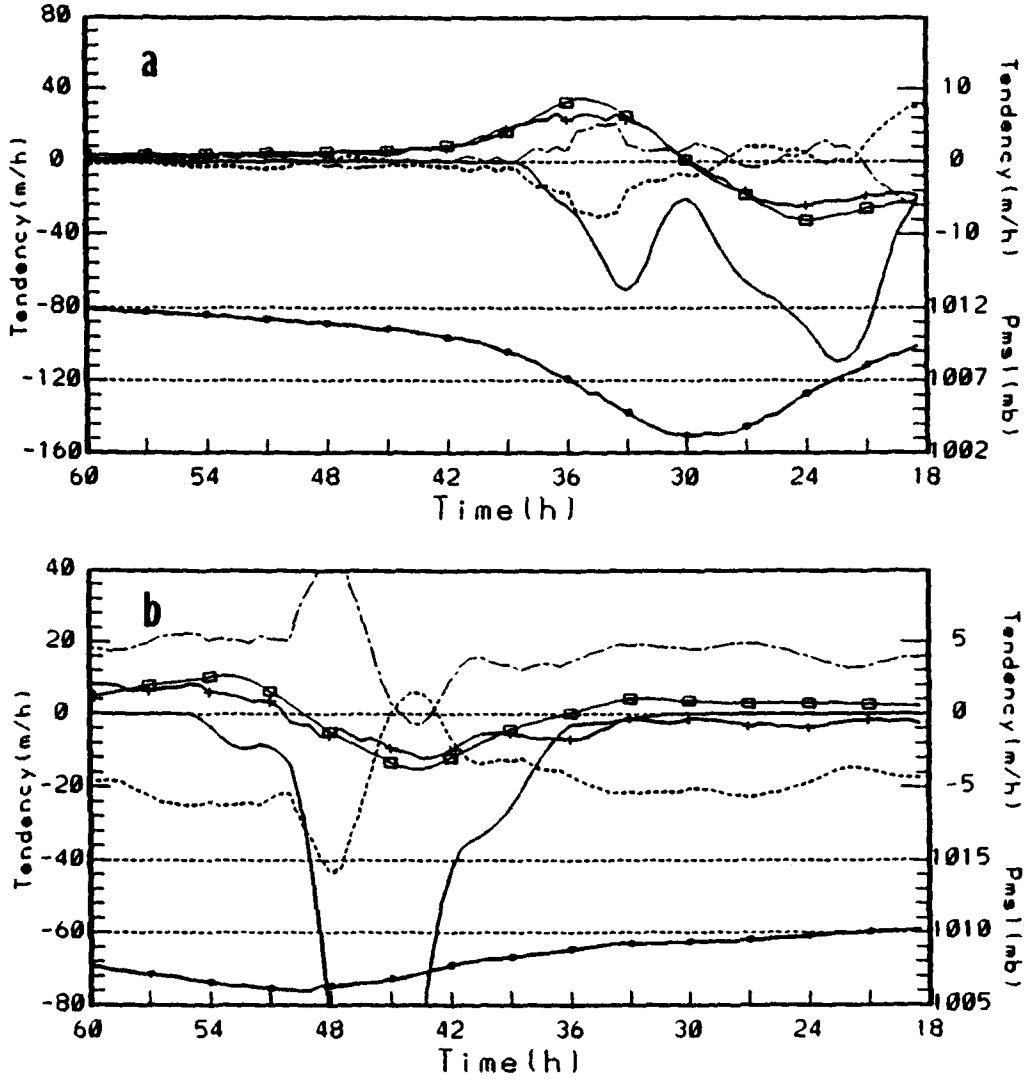

Fig. 6.11 Time variations (from right to left) of the 1000 mb height tendency (thin line connecting plus signs) at (a) N3E6 (three grid intervals or 135 km north and six grid intervals east of the barrier center) and (b) N3W3 from simulation W2N. The contribution from the horizontal advection (thin line connecting boxes), the precipitation heating (thin line), combination of the vertical motion and the precipitation heating (dashed), and the residual (dot-dashed) are also shown. The scale for the total height tendency and the horizontal advection term is 1/4 (on right) of the scale for the other terms (on left). The sea-level pressure (thick line connecting dots) is shown in the lower portion of the figure.

a very small contribution to the height change at N3W3. The strong warming from downward motion would be expected to produce a height decrease of about 20 m/h. However, most of the subsidence warming does not enhance the low pressure at N3W3 directly. Perhaps because the secondary low is a small-scale feature, strong diffusion and frictional effects and perhaps also the adjustment processes (all are included in the residual term) effectively offset most of the warming effect from the downward motion. The horizontal advection also produces a height increase of about 1 m/h. These result in a net height decrease of only about 0.5 m/h to 1 m/h. After 36 h, the advection term has a positive contribution to the height decrease when the vortex moves close to location N3W3. The contribution from the horizontal advection is even more important after 39 h when this term is nearly equal to the total height tendency. Although the precipitation has the largest contribution to the height change at N3W3 from 39 h to 48 h, nearly all of the precipitation heating is offset by the associated vertical motion expansion cooling. The net effect of these two terms is offset by the residual term that includes diffusion, friction, dry convection, etc. Therefore, the secondary low at N3W3 in simulation W2N appears to be formed and maintained (before 36 h) by the subsidence warming effect. However, the subsequent decrease in pressure at N3W3 between 36 h and 51 h is due to the approaching vortex center. After the vortex has passed the barrier (i.e., 51 h), subsidence warming (Fig. 6.11b) continues to contribute to the formation of a lee trough over the northwestern coast (e.g., 51 h in Fig. 6.5). However, the horizontal advection is the deciding factor in the vortex movement and the net effect becomes a pressure rise at N3W3.

The time variations of the height tendency distribution at two other selected locations from simulation W1S are given in Fig. 6.12. As in simulation W2N, one location (N0E6) is 270 km upstream from the barrier center, and the other (N0W3) is near the center of the secondary low (three grid intervals west of the mountain center). The height changes from different contributions at location N0E6 (Fig. 6.12a) are almost identical to N3E6 in simulation W2N (Fig. 6.11a). A strong deepening tendency from the heavy precipitation cells on the east and west sides of the vortex is mostly offset by the associated upward motion expansion cooling. Then the combination of these two terms is nearly offset by the residual term that contains the diffusion and friction effects. The horizontal advection component is very nearly equal to the total height tendency with a positive contribution to the height decrease (increase) before (after) the passage of the center.

The sea-level pressure at N0W3 (Fig. 6.12b) in simulation W1S decreases slightly to reach a minimum value near 1007 mb at 42 h, and this value is maintained until 54 h. During the earlier period (18 h to 36 h), the height decrease at N0W3 (Fig. 6.12b) is mainly due to the subsidence warming effect similar to location N3W3 in the W2N simulation (Fig. 6.11b). The horizontal advection term has a filling contribution to the height tendency because N0W3 is near the secondary low center. The main difference from Fig. 6.11b after 36 h is that the advection effect at N0W3 in the W1S simulation does not have a deciding contribution to the height change. This is because the vortex center in the W1S simulation is not well defined after it moves over the barrier (see Section B). Although precipitation warming at N0W3 increases from 33

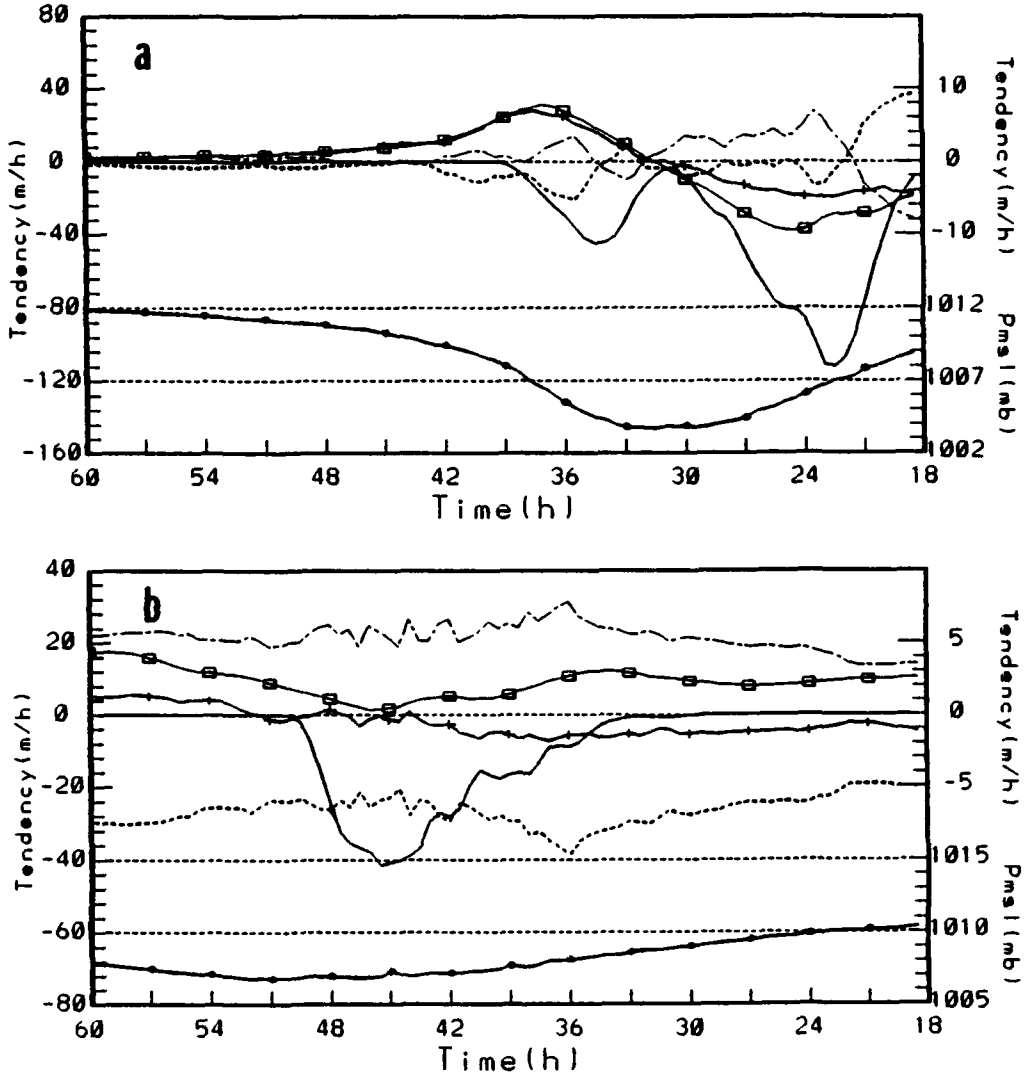

Fig. 6.12 As in Fig. 6.11, except for the time variations of the 1000 mb height tendency and the sea-level pressure at (a) N0E6 (six grid intervals east of the barrier center) and (b) N0W3 for the simulation W1S.

h to a maximum value near 45 h, the latent heating is again offset to a large degree by the associated upward motion expansion cooling. The net contribution from the vertical motion and the precipitation effects at N0W3 is nearly constant throughout the period from 18 h to 60 h. After the precipitation stops near 48 h, subsidence effects are nearly as strong as in the earlier period from 18 h to 33 h. Because the remnants of the vortex aloft are translated to the west, the advection term now contributes to the height increase at N0W3.

Similar results, that the horizontal advection term determines the height tendency at a location away from the barrier, and that subsidence warming continues to produce low pressures on west coast, are found in other simulations. For example, the time variation of the 1000 mb height tendency at a location six grid intervals south and six grid intervals east from the barrier in simulation W6S (Fig. 6.13a) is primarily determined by the horizontal advection. For a location (N0W3) near the secondary low center (three grid intervals west of the mountain peak) in simulation W6S (Fig. 6.13b), precipitation has almost no contribution to the height change in W6S. The horizontal advection only has a small opposing contribution to the height decrease at N0W3. As a result, the dominant factor to maintain or increase the intensity of the secondary low is the subsidence warming.

In summary, a secondary low may just be a relative minimum in the lee trough formed by subsidence warming. The special case is when the pressure minimum of the secondary low is due to the horizontal advection associated with the remnants of the vortex aloft that are superposed on the lee trough. In this special case, the secondary

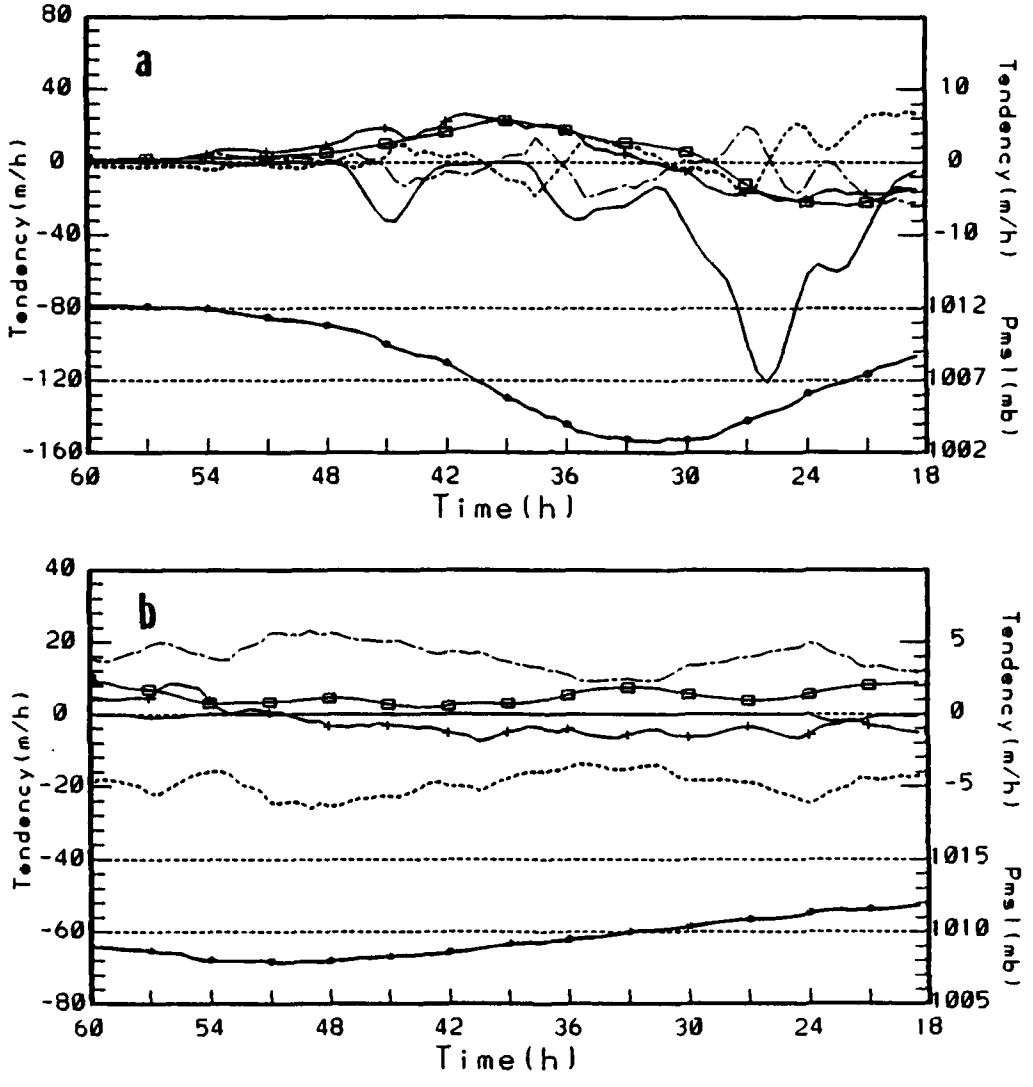

Fig. 6.13 As in Fig. 6.11, except for the time variations of the 1000 mb height tendency and the sea-level pressure at points (a) S6E6 (six grid intervals south and six grid intervals east of the barrier center) and (b) N0W3 for the simulation W6S.

low becomes part of the (discontinuous) track of the vortex across the barrier, and the downstream positions will be connected to the secondary low. Even in this case, the subsequent track will be determined by the horizontal advection of the upper-level remnants, as the subsidence warming near the secondary low position is tied to the barrier.

b. Secondary Vortex

It was demonstrated in Section A above that both horizontal advection and convergence are the leading factors in the low-level vorticity change for the ocean control simulation WOC (Fig. 6.4b). Similar vorticity budget studies (Equation 6.1) at 1000 mb are applied in this section to examine the modifications of the vorticity field when the barrier is included, and especially to explore the physical mechanism for the formation and development of the secondary vortex.

Significant changes in the vortex vorticity distribution and vorticity budgets relative to the ocean control simulation (Fig. 6.4b) occur when the vortex in the W1S simulation moves close to the barrier. At 36 h (Fig. 6.14), the circulation and vorticity centers at 1000 mb are slowed and are to the east of the 700 mb height center. An asymmetric (relative to the center) distribution of vorticity is found with larger vorticity to the northeast of the barrier where enhanced convergence is produced by circulations impinging on the barrier. This convergence (stretching term) has a positive contribution to the vorticity tendency. The horizontal advection has a positive contribution to the vorticity tendency increase along the northeast coast, and a strong negative contribution to the southeast of the center. The residual, which includes the

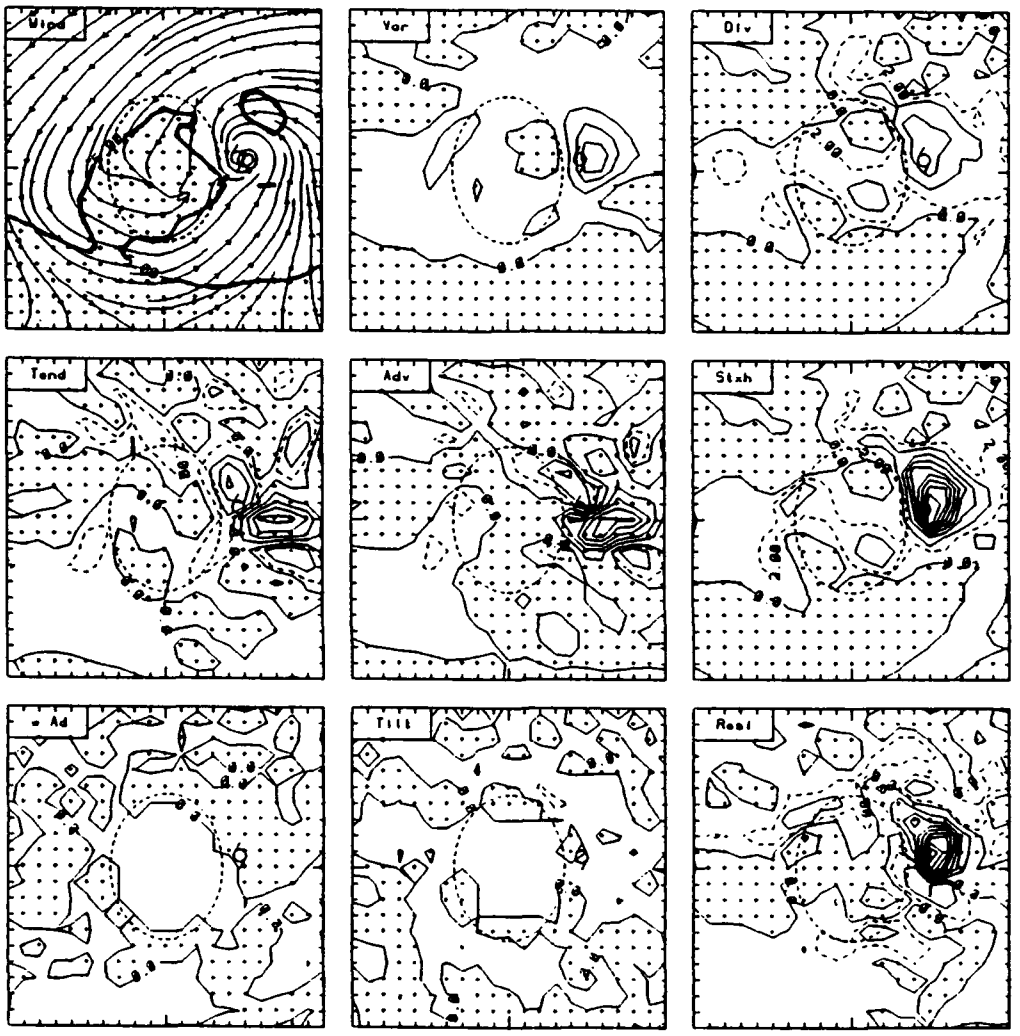

Fig. 6.14 As in Fig. 6.4b, except for W1S simulation at 36 h in a larger domain (900 km square). The barrier is indicated by dashed line.

effects from friction and diffusion effects and the calculation errors, has a magnitude similar to the vortex stretching and horizontal advection effects. However, it is passive in general and reduces the vorticity tendency increases/decreases from the stretching and advection contributions. Both the vertical advection and the tilting contributions to the vorticity tendency are one order of magnitude smaller than the leading terms. The net vorticity tendency has a positive area along the northeast coast and a negative area south and southeast of the center. Thus, the vortex is translating northwestward along the northeast coast.

A positive vorticity center is also found associated with the large curvature flow on the northwest coast. Both the horizontal advection and stretching effects have a positive contribution to the vorticity tendency increase near the west and southwest coast. The stretching production is due to the vortex circulation on the west side of the barrier being blocked (slowed) before it moves eastward over the barrier. The persistent flow blocking on the southwest slope forms a cyclonic circulation center at 42 h (Fig. 6.15a). Therefore, the formation of the secondary vortex in the W1S simulation is due to the flow blocking of the vortex circulation on the southwestern slope, which is different from the formation of leeside vortices for a zonal flow over a barrier (e.g., Smolarkiewicz and Rotunno 1989).

The circulation center associated with the vortex has dissipated near the northeast coast at 42 h (Fig. 6.15a). However, the vorticity maximum is still well defined. Similar to the result at 36 h, the horizontal advection contributes to the vorticity tendency increase (decrease) to the northwest (southeast) of the vorticity maximum, and

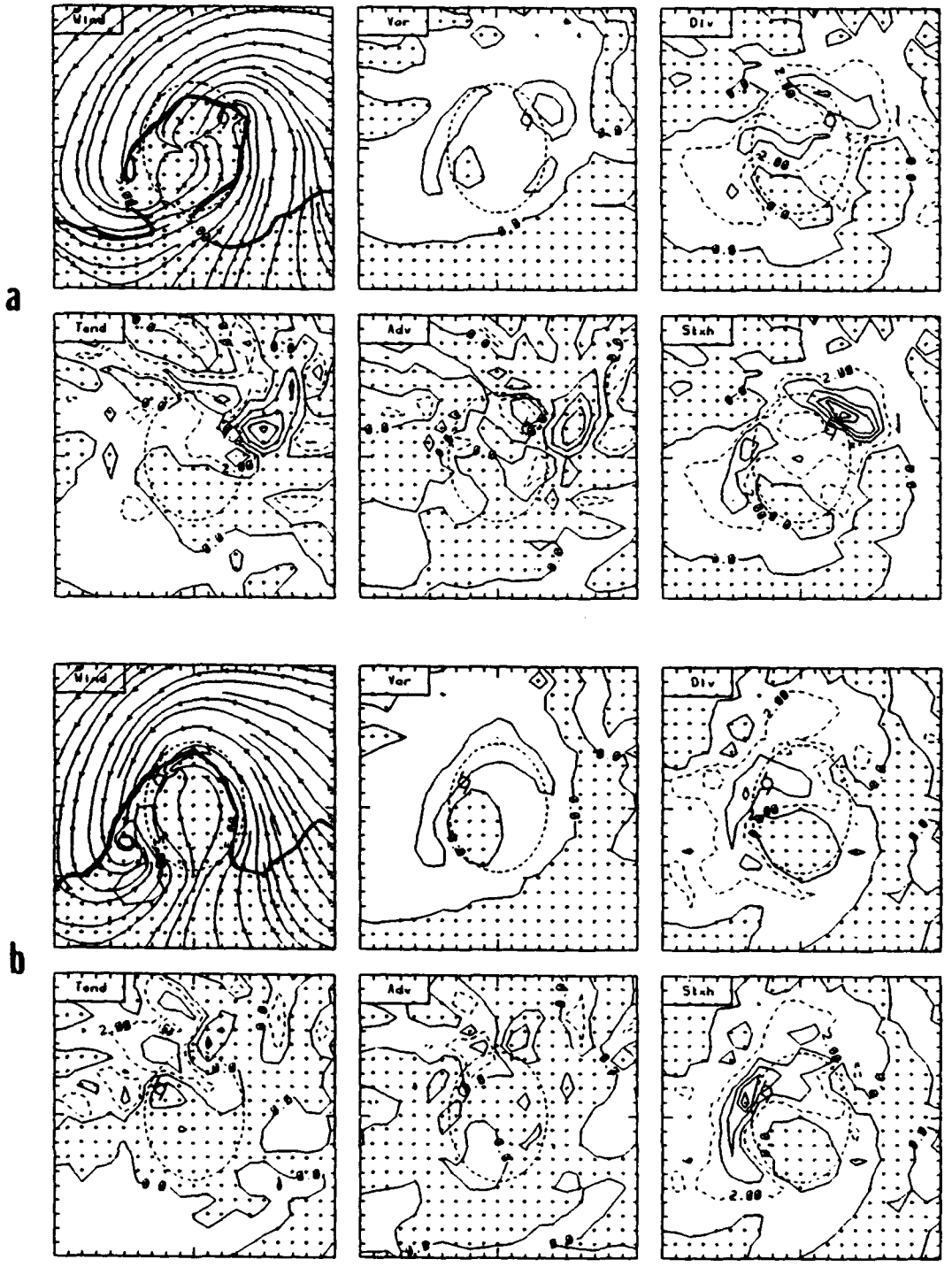

Fig. 6.15 As in Fig. 6.14, except at (a) 42 h and (b) 48 h, and the vorticity tendencies from the vertical advection, tilting and residual terms are not shown.

convergence associated with the stretching effect contributes to the vorticity tendency increase along the northeast coast. The net vorticity tendency has a vorticity increase (decrease) area northwest (southeast) of the vorticity center, which tends to shift the vorticity field northwestward continuously along the coast. Because the vertical advection and tilting effects have relatively smaller contributions and the residual term has a compensating effect on the vorticity tendency similar to those at 36 h, these three terms are not included in Fig. 6.15.

Advection of the vorticity field westward along the northern coast occurs continuously as the 700 mb center passes over the barrier along the northern slope. At 48 h (Fig. 6.15b), the vorticity field associated with the vortex has become weaker and has merged with the positive vorticity maximum area northwest of the barrier, which results in a positive vorticity region along the coast from northeast to southwest. The maximum vorticity center is barely noticeable near the northern tip of the barrier. Positive (negative) vorticity tendency on the west (east) side of the center displaces the vorticity westward. On the west side of the barrier, strong convergence near the coast produces a positive vorticity tendency north of the secondary vortex. This strong positive vorticity production north of the secondary vortex and the advection of the vorticity along the north coast results in a positive vorticity tendency offshore northwest of the barrier at 51 h (not shown). The secondary vortex is shifted toward the positive vorticity tendency area in the north. At 54 h (Fig. 6.7), the secondary vortex is slightly intensified and is located northwest of the barrier, and then is moved westward after the vorticity and convergence field associated with the original vortex has passed the barrier.

Although weakening and modification of the vorticity field are found in the W2N simulation (not shown) when the vortex is near the barrier, both the circulation center and the vorticity center follow a continuous track westward along the north coast. A secondary vortex is found southwest of the barrier between 45 h to 48 h, but the circulation is very weak. When the vortex passes the barrier, the weak secondary vortex is merged into the strong circulation associated with the original vortex.

Similar to the W1S simulation, the circulation and the vorticity centers are slowed when the vortex in simulation W6S approaches the southern portion of the barrier. At 42 h (Fig. 6.16a), the vorticity center is more than 50 km behind the 700 mb height center. The total vorticity tendency has a positive (negative) value on the west (east) side of the barrier, which suggests the vorticity center will be shifted westward. However, the positive vorticity tendency on west side of the vorticity center is due to flow convergence. The horizontal advection results in a negative contribution west of the center. On the west side of the barrier, the flow decelerates and turns from easterly toward the barrier, which also produces convergence. A weak secondary vortex is found on the west-central coast. Unlike the secondary circulation in the W1S simulation (Fig. 6.15a), the secondary circulation on the leeside of the barrier does not have a direct connection with the flow associated with the vortex in the W6S simulation. Persistent easterly flow also is found at the upper levels (i.e., Fig. 6.10a). This may suggest the secondary vortex in the W6S simulation is formed similar to the vortices produced on the leeside of the barrier from impinging zonal flows as shown by Smolarkiewicz and

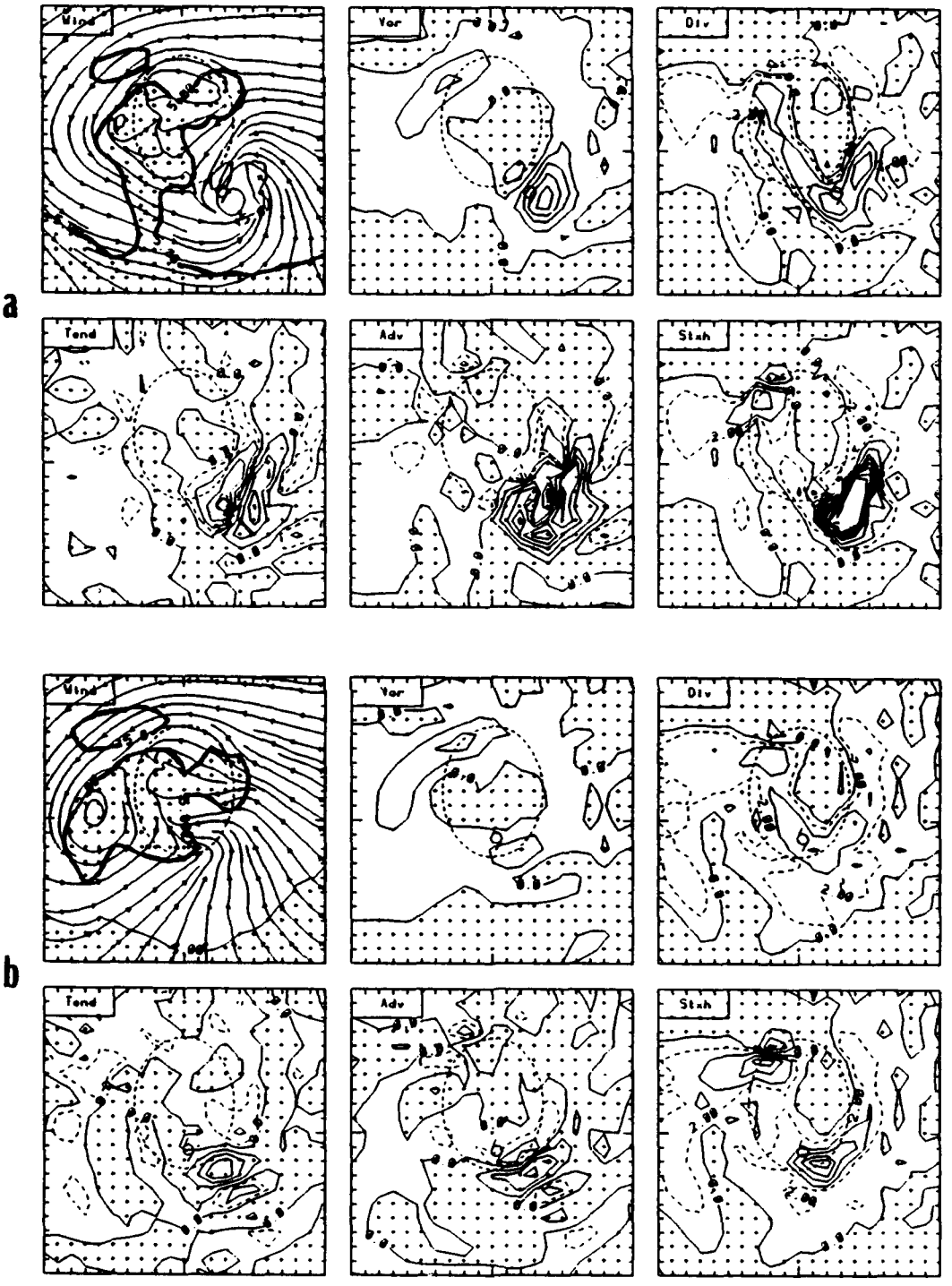

Fig. 6.16 As in Fig. 6.15, except for simulation W6S at (a) 42 h and (b) 51 h.

Rotunno (1989). However, significant modifications occur due to the large curvature of the flow at low levels on the west side of the barrier.

The secondary vortex in the W6S simulation is shed southwestward. At 51 h (Fig. 6.16b), the secondary vortex is slightly intensified and is located more than 250 km west of the 700 mb vortex center. As the circulation center associated with the vortex is destroyed on the southern coast, the vorticity is also weakened. Moreover, the total vorticity tendency has a negative value near and west of the vorticity center in spite of strong convergence along the southern coast. Therefore, the development of the secondary circulation is not due to the vortex circulation passing the barrier around the southern slope. The blocked circulation passing around the northern tip of the barrier, which induces vorticity to the northwest of the barrier through convergence/stretching, and the advection of the vorticity downstream, contributes to the increase of the vorticity near the secondary vortex.

In summary, these vorticity budgets suggest that two types of secondary vortices may be formed. One type of secondary vortex, such as in the W6S simulation, is formed similar to the vortices produced when a zonal flow encounters a barrier. The secondary vortex is shed and intensified when the low-level structure of the upstream vortex is blocked and destroyed by the barrier. Only a small contribution to the development of this type of secondary vortex is directly advected or produced from circulations associated with the original vortex.

The other type of secondary vortex, such as in the W2N and W1S simulations, is formed due to the vortex circulation near the southwestern coast being

blocked and deflected northwestward. This type of secondary vortex does not shed away from the barrier. Since the secondary vortex is rather weak, it will be merged into the vortex circulation if the low-level circulation is not destroyed by the barrier, such as in W2N simulation. If the low-level wind center is disrupted on the east side of the barrier as in simulation W1S, the secondary vortex will be reorganized as the circulation associated with the original vortex persists and passes around or over the barrier.

2. Structure

The discussion above suggests two types of secondary centers are possible as the vortex encounters a barrier. The structure changes in the W6S and W1S simulations are examined below to compare and further clarify the differences.

a. W6S Simulation: Secondary Center Developing From Low Levels Upward

Subsidence warming is the major factor related to the formation of the secondary low center in the simulation W6S. Vertical cross-sections (Fig. 6.17) passing east-west through the center-plane of the barrier from simulation W6S at 39 h show the temperature deviation from the initial profile (Fig. 6.17a), zonal wind speed (Fig. 6.17b), vertical motion (Fig. 6.17c) and relative humidity (Fig. 6.17d). These distributions are significantly different from the ocean-control simulation (Fig. 6.3) due to the barrier modifications. Easterly winds are expected over the barrier because the vortex is located southeast of the mountain. The low-level easterlies are effectively slowed by the barrier (Fig. 6.17b). Nevertheless, the easterly components impinging on the east slope cause

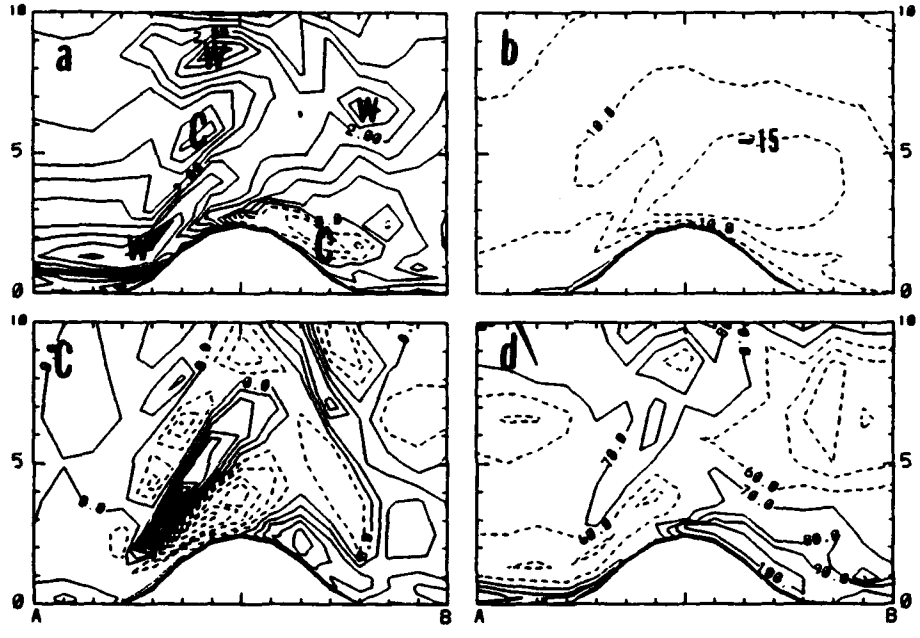

Fig. 6.17 As in Fig. 6.3, except for the vertical cross-section east-west through the center plane of the barrier of (a) temperature (°C) deviation from the initial profile (TABLE II), (b) u-component of wind speed (m/s), (c) vertical velocity (cm/s) and (d) relative humidity (%) at 39 h for the simulation W6S. The temperature lower than the initial profile, easterly wind components, downward motion and relative humidity below 70 % are in dashed lines. The intervals are (a) 0.5°C, (b) 5 m/s, (c) 2 cm/s and (d) 10 %.

strong upward motions near the surface (Fig. 6.17c). Stronger easterlies are found over the top of the barrier, which also produce strong downslope motions on the west side. However, the downward motion does not extend to the western coast. A thin layer of upslope westerly winds is found near the west coast, which may be similar to the upslope leeside return flow for a small Froude number current over a barrier (e.g., Smolarkiewicz and Rotunno 1989). However, the upslope return flow in Fig. 6.17b is limited to a shallower and smaller area close to the barrier. No anticyclonic gyre is found, perhaps due to the low-level cyclonic northerly circulation west of the barrier (Fig. 6.10).

Wave structures are found in the temperature (Fig. 6.17a) and vertical velocity field (Fig. 6.17c). The eastward-tilted waves over the west slope of the barrier are similar to the waves generated in the zonal flow in the barrier-control simulation (not shown). Similar wave structures tilted against the impinging flow on the lee side of a 2-dimensional barrier are also reported by Williams et al. (1992). At N0W3 (three grid intervals west of the mountain center) in Fig. 6.17, the major subsiding motions are found about 1.5 km above the thin upslope flow near the surface and in another layer from 3.5 km to 6 km.

The vertical motions also modify the relative humidity (Fig. 6.17d) and temperature (Fig. 6.17a) distributions. Saturated air is found over the east slope due to the upslope motion. On the west slope, downward (upward) motions are associated with dry (moist) and warm (cool) air. When the downslope motion reaches the surface, then the warm and dry wind will be similar to the often-observed foehn phenomenon (e.g.,

west of the mountain peak in Fig. 6.17). This foehn wind is also observed on the lower slope later (e.g., 54 h not shown) and in the other simulations (e.g., W1S) at various locations.

The vertical motion structure in Fig. 6.17c is persistent and only slightly intensified over a long period of time at N0W3 (Fig. 6.18a). The downslope motion near the surface is below 2 km and reaches the maximum intensity near 42 h. The depths of the alternating layers of vertical motion increase with time. A relatively dry layer (Fig. 6.18b) is above the thin return flow on the west slope.

Early in the simulation, the flow at N0W3 is blocked significantly beneath the mountain top (2.5 km), as the wind speeds are less than 5 m/s in a 2 km layer above the ground (Fig. 6.18c). The wind speeds are increased in the middle layer (i.e., 3 to 6 km) from 30 h to 48 h as the vortex approaches. The easterlies in the middle layer are part of the vortex cyclonic circulation. The wind directions also change significantly between the layers above and beneath the mountain elevation (close to 5 m/s isotach). The direction near 2.5 km varies from northeasterly at 33 h to southeasterly at 42 h. This wind change is not due to the passage of the vortex center, but is the result of the westward shedding of the secondary vortex. After 48 h, the wind in the lower layers becomes stronger when the southerly circulation associated with the secondary low is channeled over the west slope.

The closed secondary centers indicated in Fig. 6.10 extend up to 950 mb (Fig. 6.19a) at 39 h. An eastward-tilted pressure trough, and weak but large curvature flow, is found at the 900 mb and 850 mb levels. Both the secondary low and the

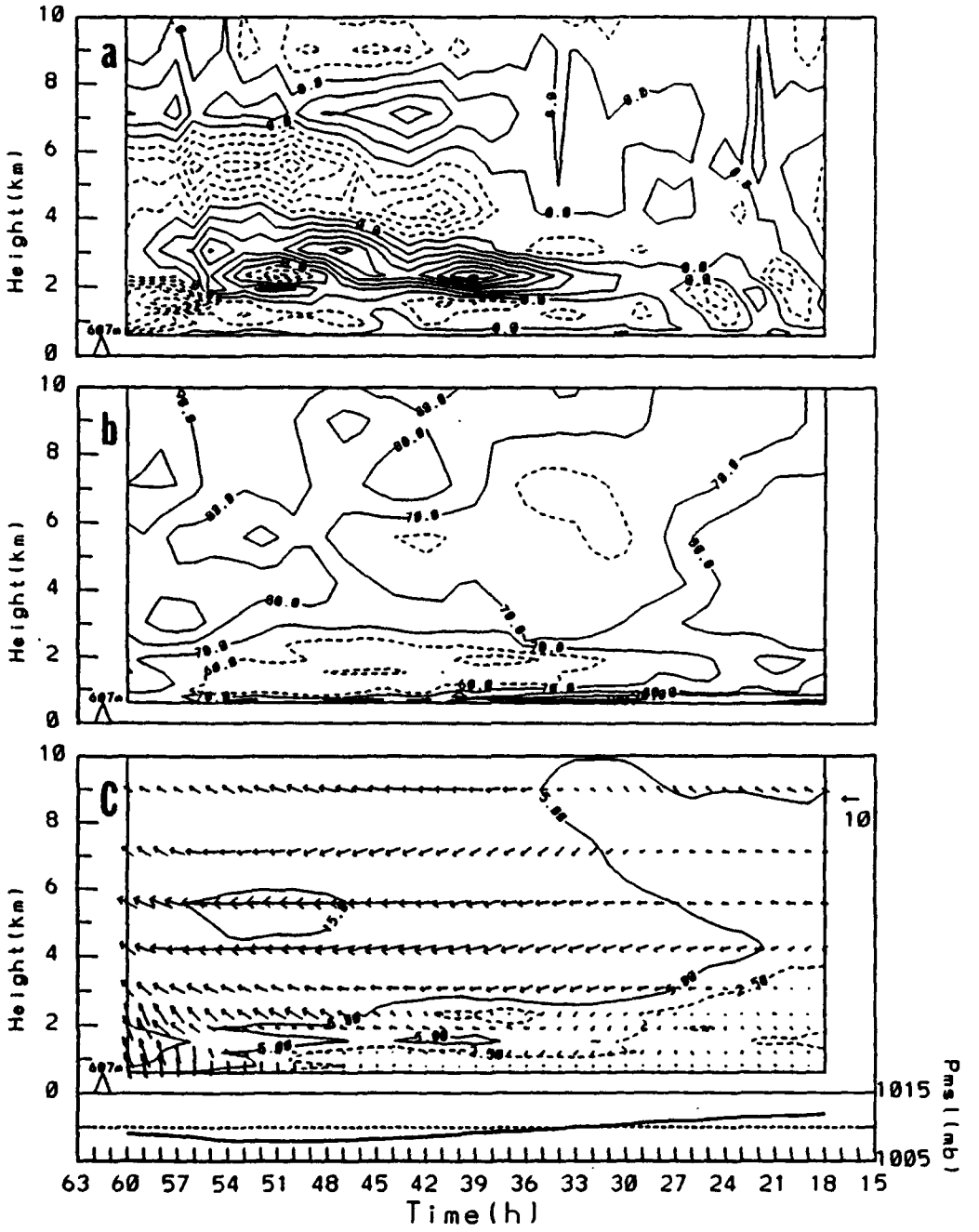

Fig. 6.18 Time (from right to left) sections of (a) vertical motion (in 2 cm/s intervals), (b) relative humidity (%) and (c) wind vectors (scale at upper right) and isotachs (2.5 m/s, 5 m/s and 15 m/s) at location N0W3 (three grid intervals west of barrier center) from simulation W6S. Downward motion, relative humidity less than 70 % and wind speeds equal to 2.5 m/s are in dashed lines. The terrain height at N0W3 (607 m) is indicated at lower left. The sea-level pressure (thick solid) is also shown.

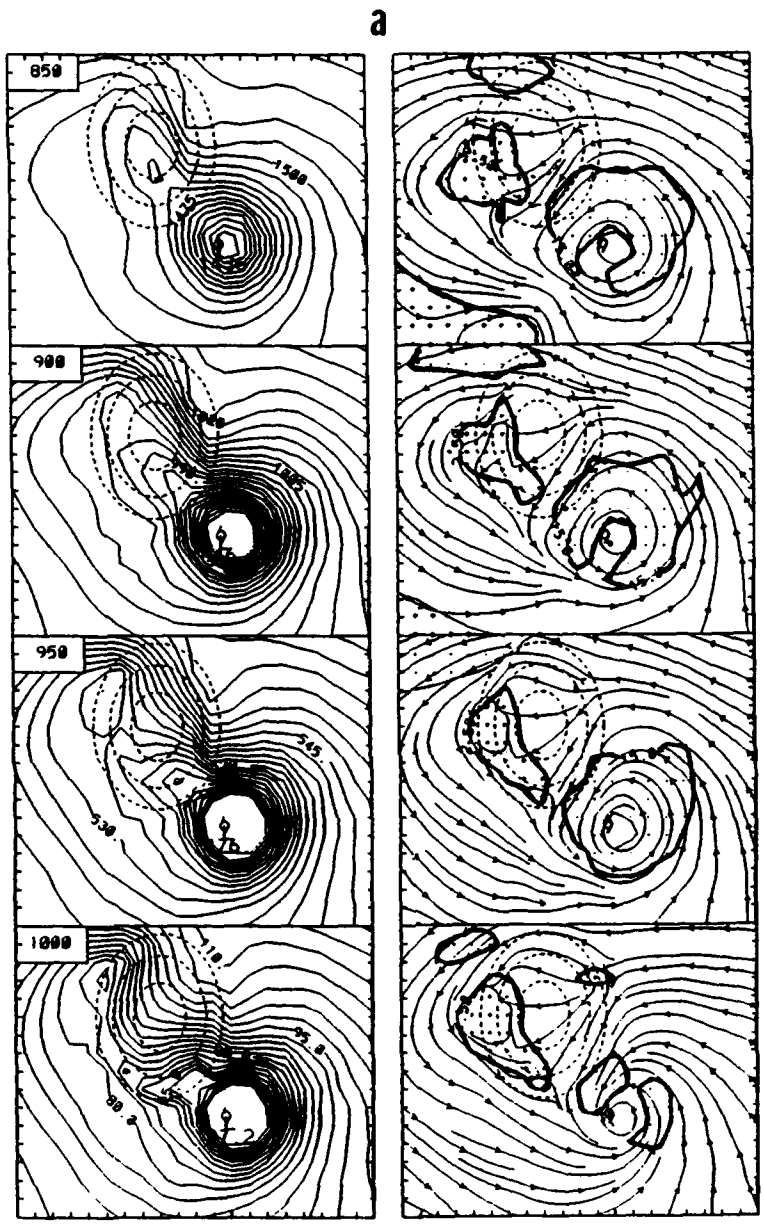

Fig. 6.19 As in Fig. 6.9, except for the height (left), and streamlines and isotachs (2.5 and 15 m/s, right) of simulation W6S at four pressure levels (850 mb, 900 mb, 950 mb and 1,000 mb) at (a) 39 h and (b) 45 h. The interval of the height contours is 5 m at the 850 mb level and 3 m at the other levels.

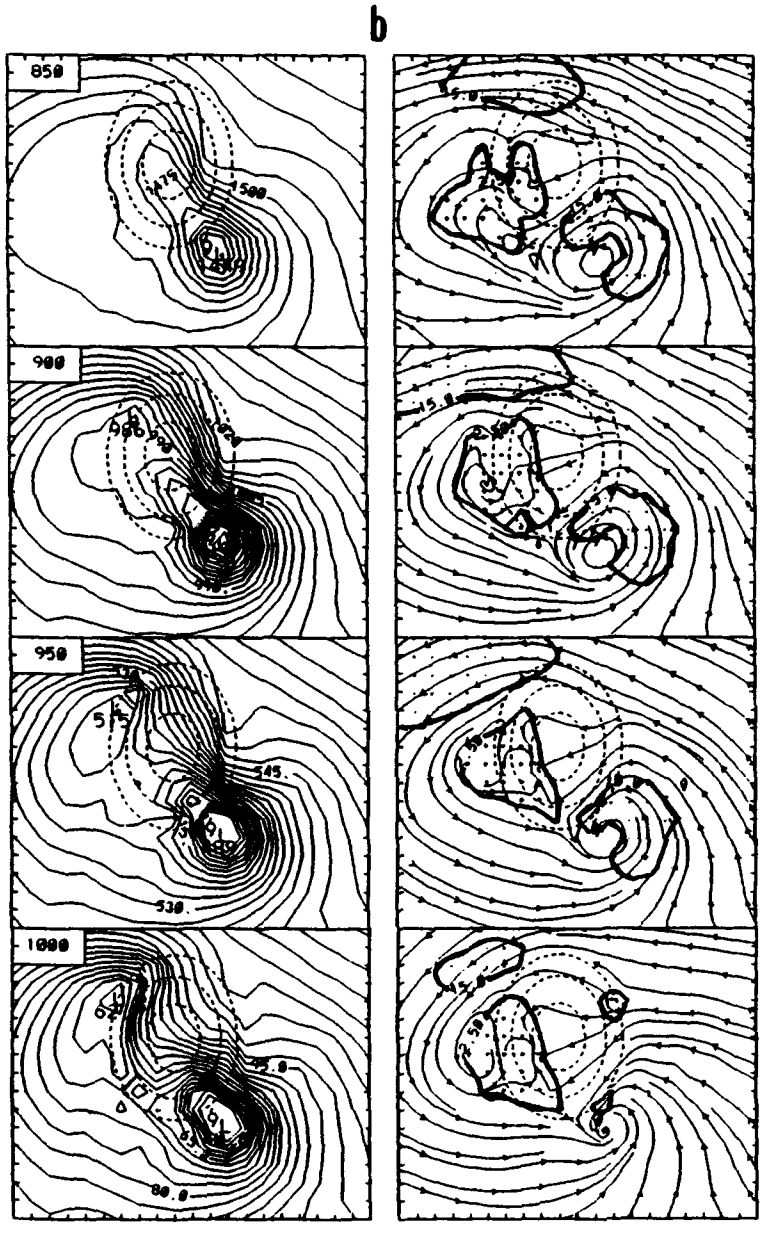

Fig. 6.19 (Continued)

secondary vortex intensify and extend vertically later. For example, the secondary vortex center at 45 h (Fig. 6.19b) is shifted westward and extends up to 900 mb, and the streamline curvature at the 850 mb level is increased. Although the secondary low center (minimum height) is still located close to the barrier, the contours near the barrier center-plane suggest the height field is shifting westward with the secondary vortex. At 51 h (Fig. 6.10c), the secondary vortex and the associated low are found up to 850 mb.

b. W1S Simulation: Secondary Center Reorganized From Upper Levels Downward

Subsidence warming is the major factor in initiating the height decrease during the earlier period of this type of secondary low. The height decrease at N0W3 in simulation W1S (Fig. 6.11b) is different from the W6S simulation, as the subsidence warming is not the dominant factor later. The vertical motion over the region of the secondary low (Fig. 6.20a) also has a different vertical structure. Subsidence motions similar to the wave structure generated by small Froude number zonal flow over a barrier (i.e., Fig. 6.17c from W6S) are found at N0W3 before 36 h. This vertical motion is weaker than in the W6S simulation. Significant differences between Fig. 6.20a and Fig. 6.18a are from 36 h to 48 h, when the wave structure of vertical motion at N0W3 in the W1S simulation is gradually replaced by alternating deep vertical motions. The deep upward motion is accompanied by high relative humidity (Fig. 6.20b), which is similar to the structure near the vortex center from the ocean-control simulation (Figs. 6.3c and 6.3d). The winds (Fig. 6.20c) also change direction from northeasterly to southeasterly

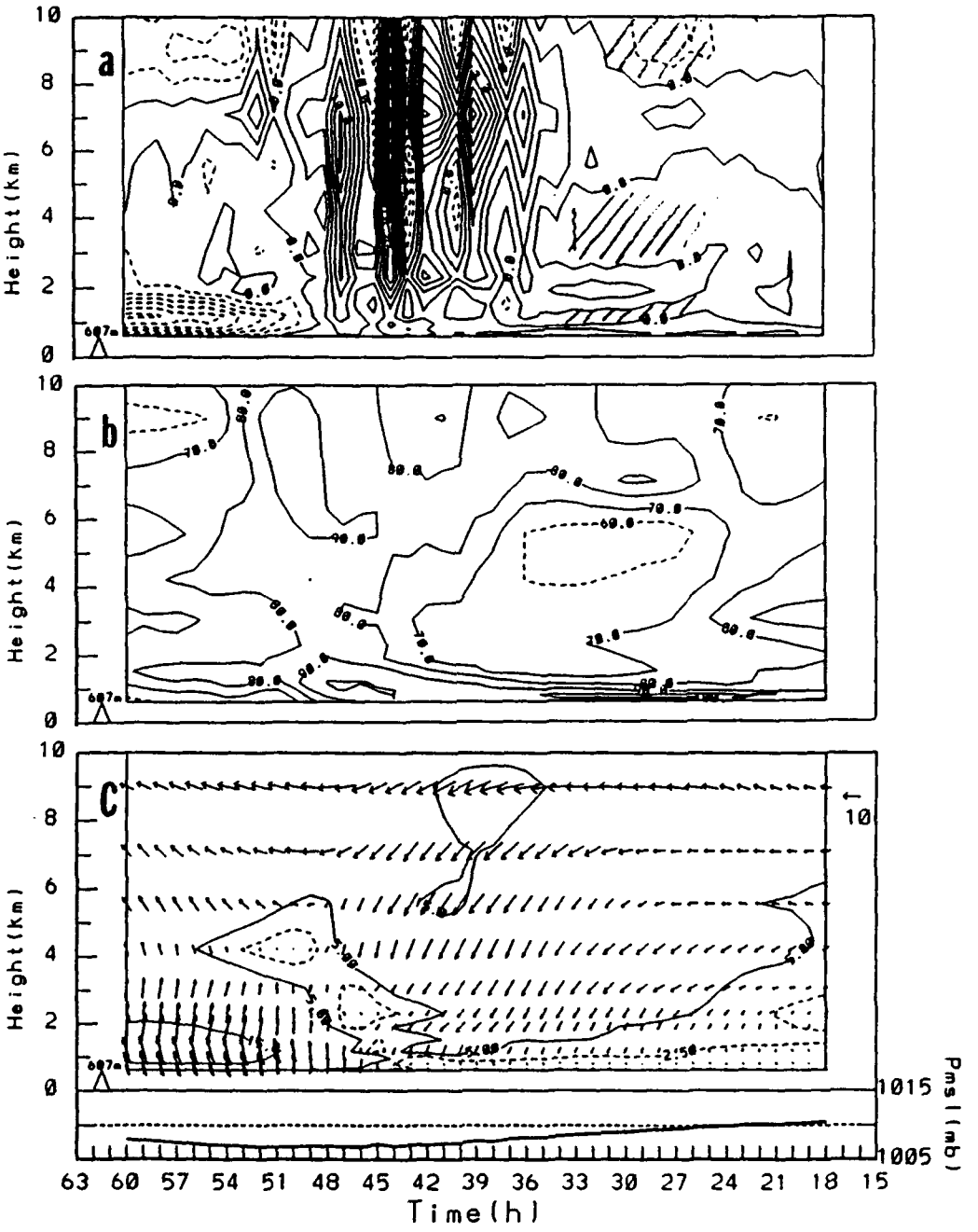

Fig. 6.20 As in Fig. 6.18, except for the time section at N0W3 (3 grid intervals west of barrier center) of (a) vertical motion (cm/s), (b) relative humidity (%) and (c) wind vectors (scale at upper right) and isotachs (2.5 m/s, 5 m/s and 15 m/s) from simulation W1S.

at 7 km around 48 h. This wind shift indicates the passage of the upper-level vortex occurs before the sea-level pressure at N0W3 reaches the minimum value.

The wind blockage by the barrier at N0W3 in simulation W1S is not as persistent as in simulation W6S because the low-level flow in W1S (Fig. 6.20c) is not directly impinging on the long-axis of barrier. The wind speeds less than 5 m/s are limited to the lower 1 km from 33 h to 42 h, which is about 1 km shallower than in the W6S simulation. Another area of winds smaller than 5 m/s in Fig. 6.20c extends from the lower level to about 5 km height after 42 h as the vortex moves close to location N0W3. The outward increase in wind speed to the radius of maximum wind (Fig. 6.9b) is consistent with such a small wind near the center. Although the tilt of the 5 m/s isotach indicates the low-level vortex occurs prior to the middle-level center, the wind centers are vertically aligned below 3 km. A similar center tilt is shown in Fig. 6.9b at 45 h.

The secondary low on the western coast is limited to below 950 mb at 39 h in simulation W1S (Fig. 6.21a). However, the strong curvature of the flow southwest of the barrier is not limited to the lower layer, but extends to at least the 850 mb level when the western portion of the vortex circulation is deflected.

The secondary low on the west coast in the W1S simulation does not extend upward as in the W6S simulation. The secondary low is only shown at 1000 mb in Fig. 6.21b, while the 1000 mb vortex center is blocked and shifted northward at 42 h. The flow curvature southwest of the barrier is increased at all four levels while the cyclonic circulation center associated with the original vortex is deflected northward and

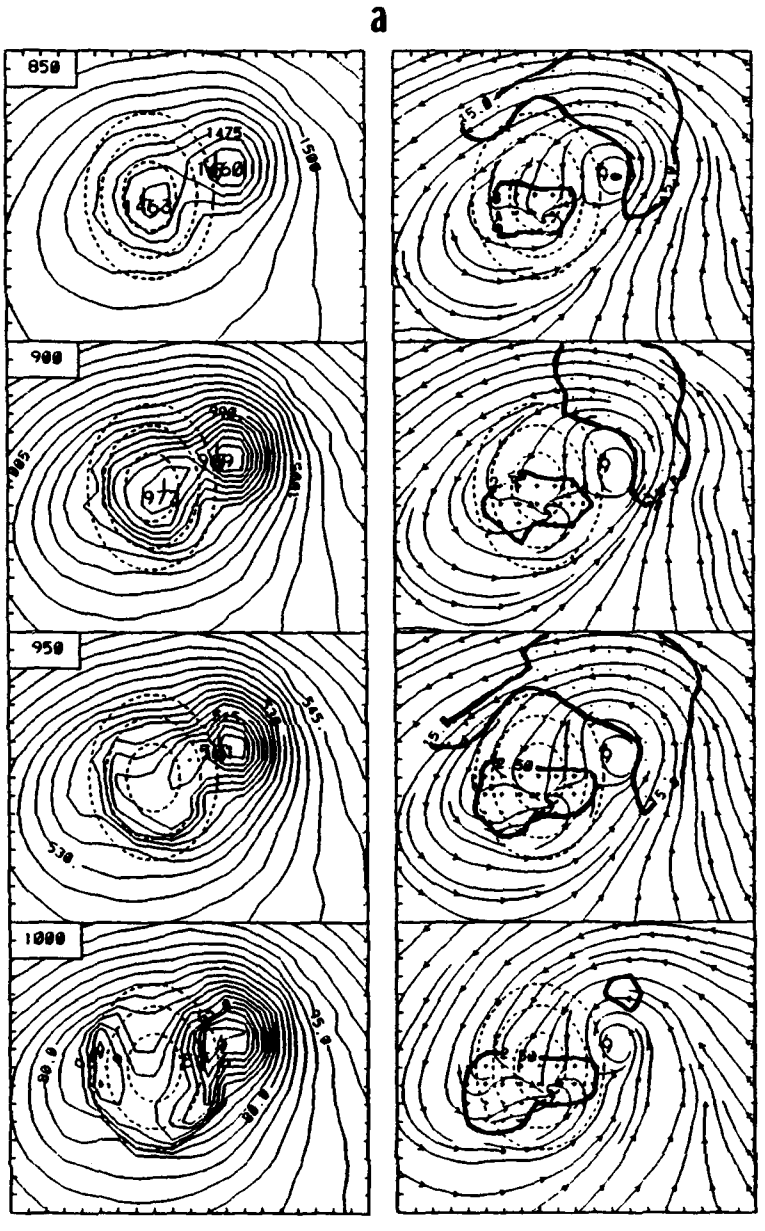

Fig. 6.21 As in Fig. 6.19, except for the height (left), and streamlines and isotachs (2.5 and 15 m/s, right) at (a) 39 h, (b) 42 h, (c) 45 h and (d) 51 h for the W1S simulation.

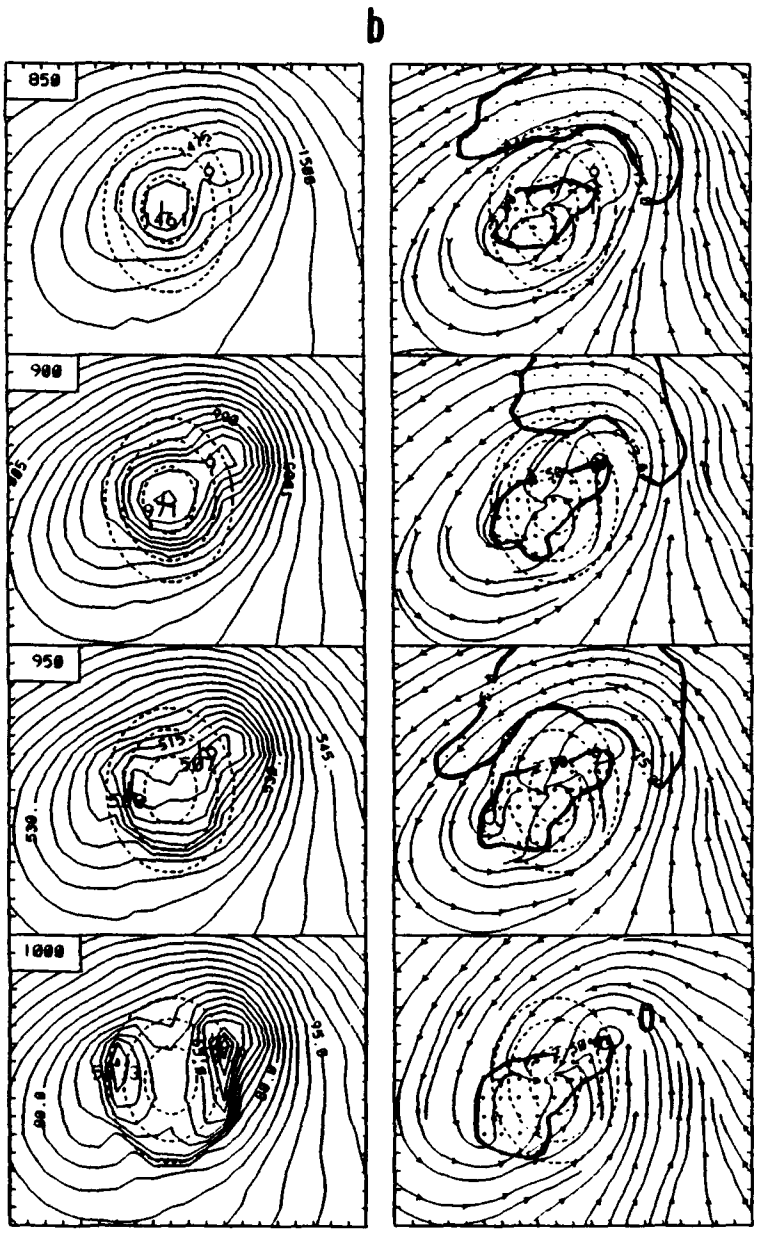

Fig. 6.21 (Continued)

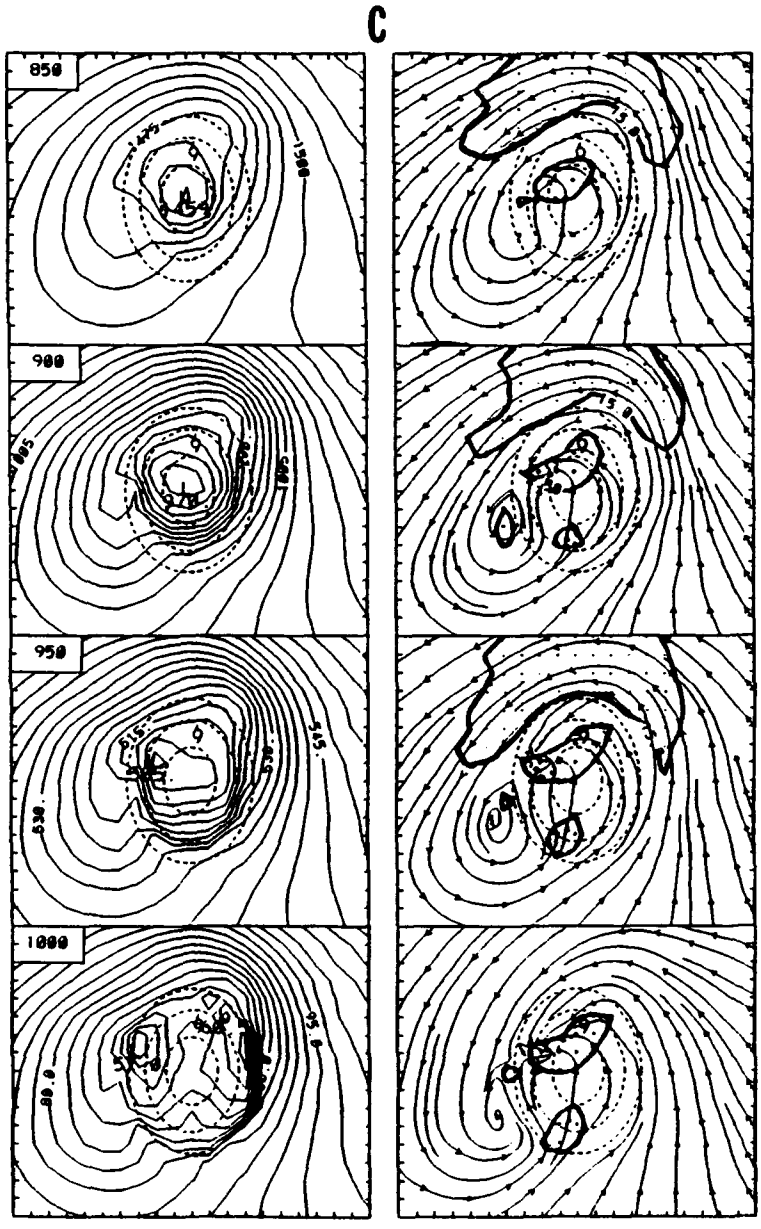

Fig. 6.21 (Continued)

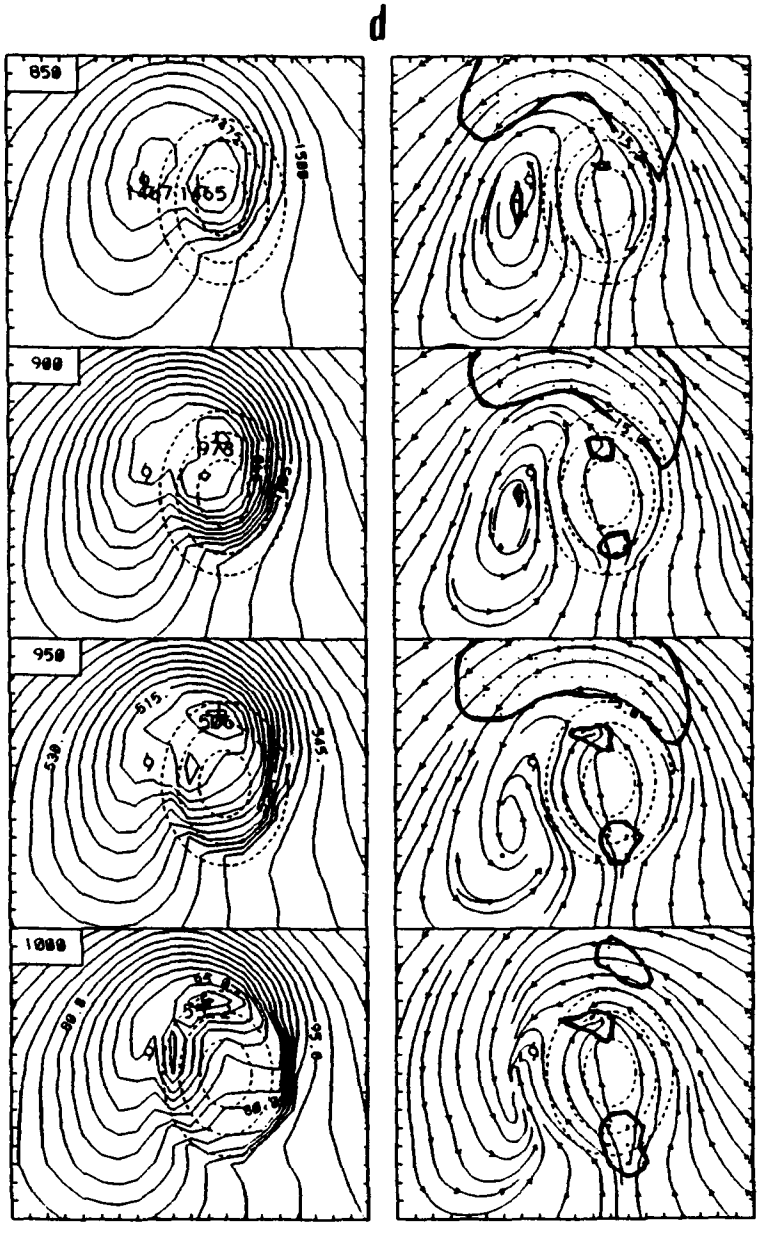

Fig. 6.21 (Continued)

weakened east of the barrier. The secondary vortex center on the west side of the barrier is unclear at this time.

Three hours later (Fig. 6.21c), the cyclonic circulation center to the southwest of the barrier is found at all three lower levels, with very large curvature of the flow at 850 mb. Meanwhile, the original wind center has dissipated on the northern slope. The geopotential height fields show the low centers above 950 mb level are not blocked by the barrier. Although a closed secondary low is not present in the three upper levels of Fig. 6.21c, a trough is developed along the west coast associated with the wind distributions.

At 51 h (Fig. 6.21d), the wind circulation at 850 mb has a clear cyclonic center west of the barrier near the 700 mb center. At the lower levels, the flow is still deflected and the center is located slightly to the south of 850 mb center. A closed low is associated with the wind circulation at 850 mb above the lower-level trough. This structure suggests the upper-level vortex system moves continuously westward, and the vortex-barrier interaction produces the low-level center(s) over the terrain area. At 60 h (Fig. 6.9c), the low extends downward to the surface and the 1000 mb circulation center also shifts northward to an area close to the 850 mb center.

In summary, the secondary vortex that develops in simulation W6S (labelled as Type-A) is generally similar to a small Froude number zonal flow over the barrier. The secondary vortex is deeper than in the W1S simulation and later is shed from the barrier when the vortex is slowed and weakened on the east side of barrier. The circulation intensification of the secondary vortex is not directly from the original

vortex, but through the production and advection from the northwestern slope. Thus, the development of the secondary center is from lower levels and extends upward.

The initial development of the secondary low in simulation W1S (labelled as Type-B) is similar to Type-A in that it is due to the subsidence warming. However, the secondary low is shallower. In addition, the secondary vortex is produced only when the original center moves closer to the barrier and the circulation is not directly impinging on the long-axis of the barrier. At the middle level, the vortex system is not greatly disrupted in the W1S simulation because the vortex-barrier interaction is relatively short-lived. Even at levels much below the mountain peak (e.g., 900 mb), the vortex system is able to pass around the barrier along the northern slope. Therefore, the low-level secondary vortex intensifies and the low center develops when the upper-level system moves over. A similar downward extension of the low center is reported by Lee (1992) when Typhoon Yancy encountered northern Taiwan during August 1990.

D. EFFECT OF VORTEX TRANSLATION SPEED

1. Zonal Flow of 10 m/s

The observational study in Chapter V shows the terrain-induced surface pressure structure when a typhoon is nearby Taiwan depends mainly on the typhoon location. A similar result may be shown by increasing the vortex translation speed from 5 m/s to 10 m/s. The surface pressure anomalies of the weak vortex in a 10 m/s zonal flow (Fig. 6.22a) are similar to those in the 5 m/s simulations (Fig. 6.5). For example, the low center in the W2Nf simulation passes around the barrier similar to the W2N

a

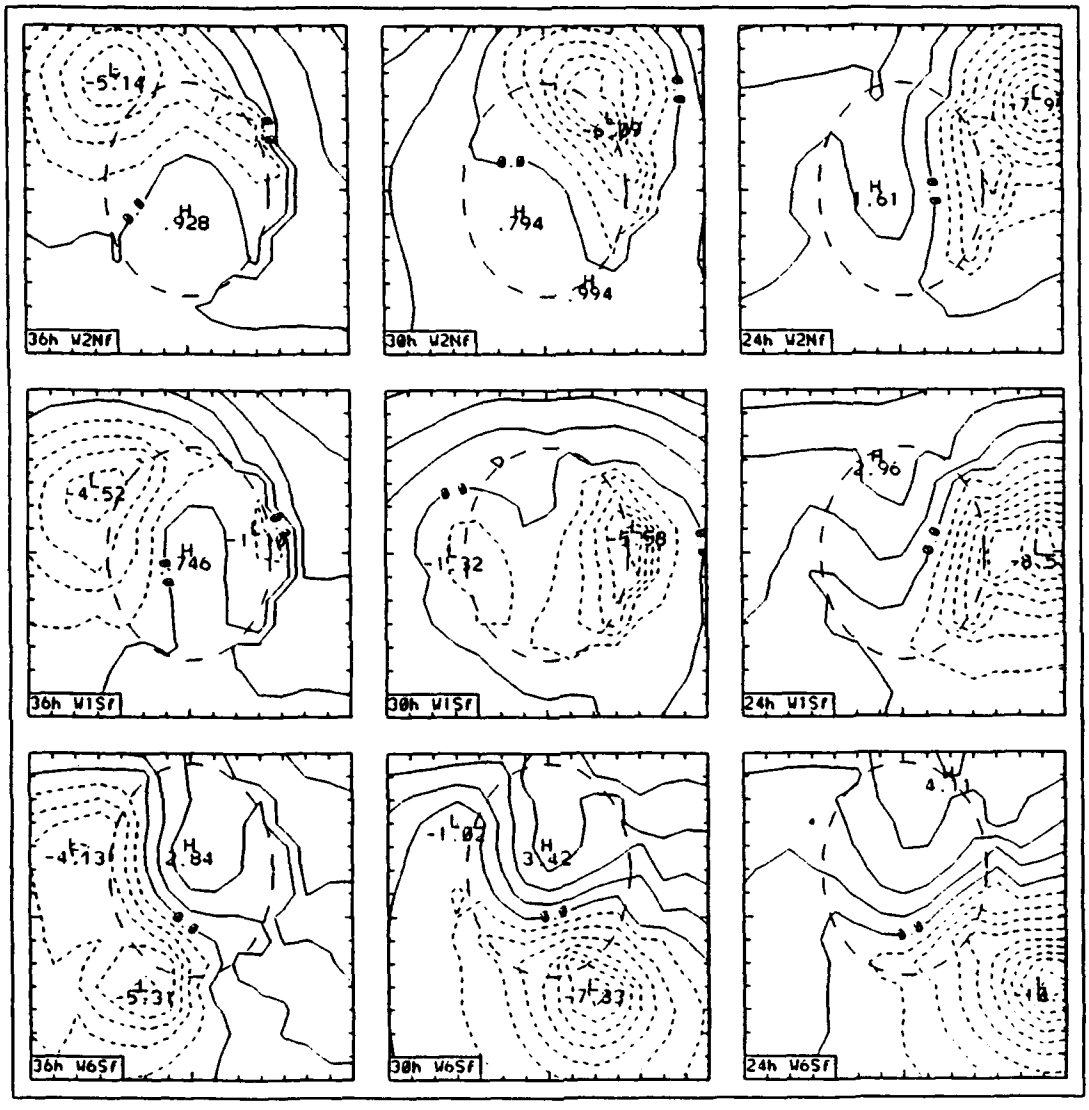

Fig. 6.22 (a) As in Figure 6.5, except for the sea-level pressure anomalies of the vortex in the 10 m/s zonal flow simulations (W2Nf, W1Sf and W6Sf). (b) As in Fig. 6.7, except for the surface streamlines and isotachs corresponding to (a).

b

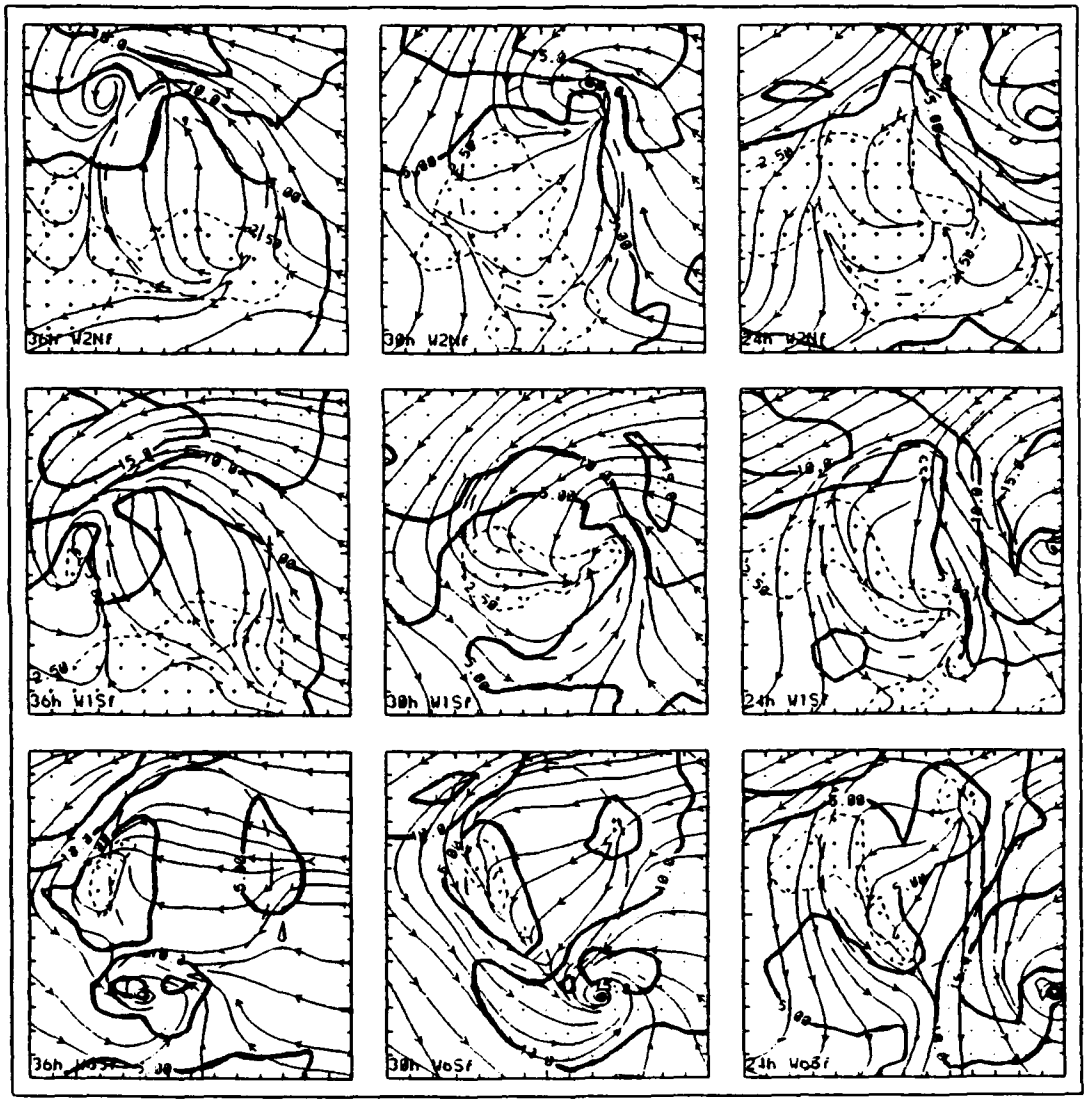

Fig. 6.22 (Continued)

simulation (Fig. 6.5), even though the trough is formed on the east coast when the center approaches the northern portion of the barrier. The dissipation of the vortex center and the formation of a secondary low on the western coast in the W1Sf simulation are also similar to the W1S simulation. One difference between Fig. 6.22a and Fig. 6.5 is that the vortex in the 10 m/s flow is stronger (pressure gradient near the center is larger) due to the shorter period of barrier distortion. As a result, the center in the W6Sf simulation passes over the southern end of the barrier without being destroyed. Notice that dual centers are simulated with a secondary low near the northwest coast at 36 h of simulation W6Sf.

The barrier modifications of the surface wind circulation for the weak vortex in a 10 m/s zonal flow (Fig. 6.22b) are also similar to those in the 5 m/s flow (Fig. 6.7). For example, the impinging outer vortex circulation to the northeast of the barrier is slowed and is also deflected to pass around the barrier. The calm wind area is also located leeside of the impinging flow. For W2Nf, which approaches the northern portion of the barrier, the circulation center passes the barrier with a continuous track similar to the vortex in W2N (Fig. 6.7). A secondary vortex is not found.

The circulation center in the W1Sf simulation is destroyed after making landfall near the central east coast (central panel in Fig. 6.22b) similar to the W1S simulation. The curvature of the flow to the southwest of the barrier is smaller in the W1Sf simulation at 30 h than at 39 h in the W1S simulation (Fig. 6.7). However, the flow curvature increases later. A weak secondary vortex is formed near the central west coast at 34 h (not shown). This secondary vortex quickly reorganizes after the

circulation associated with the original vortex passes the barrier. At 36 h (Fig. 6.22b), the circulation structure near the barrier is very similar to the W1S simulation at 54 h (Fig. 6.7). Notice the strong wind shear near the northern coast, and the confluence zones near the southwestern coast and to the north of the vortex center.

The formation of the secondary vortex in the W6Sf simulation (e.g., 36 h in Fig. 6.22b) is also similar to that in the W6S simulation. In both cases, the secondary centers are formed in the leeside calm wind area similar to the barrier-induced leeside vortex when a zonal flow encounters a barrier. However, the vortex center in the W6Sf simulation is not destroyed, and the secondary vortex is formed after the original vortex has passed around the southern end of the barrier. Thus, dual centers are shown on the west side of the barrier.

Similar dual centers on west side of Taiwan have been reported by Wang (1980) when Typhoon Sally passed over the southern tip of Taiwan and also induced a secondary center near the central west coast. Wang showed (his Fig. 2.12) the typhoon center and the secondary center moved westward in parallel. The center pressure, maximum wind, size and translation speed of Typhoon Sally before landfall were about 975 mb, 35 m/s, 200 km and 8 m/s, respectively. Thus, Typhoon Sally was a small, weak and fast-moving typhoon similar to the vortex in the W6Sf simulation.

Notice that the strong cyclonic wind shear near the northwestern coast increases as the vortex in the W6Sf simulation moves westward. At 36 h (Fig. 6.22b), the cyclonic wind shear reaches about 2×10^{-4} s^{-1} to the northwest of the secondary vortex. Another interesting feature is the strong anticyclonic shear near the southwestern

coast. As the vortex center passes the barrier, the cyclonic circulation associated with the center is channeled on the southwestern slope and results in strong easterly winds. The strong easterlies not only produce convergence north of the vortex center, but an anticyclonic shear of more than 1 x 10^{-4} s^{-1} is produced between the westerlies to the south of the secondary vortex center and these strong easterlies. The importance of the strong anticyclonic wind shear to the local weather systems is an interesting subject for future study.

2. Zonal Flow of 2.5 m/s

Structure modifications also occur when the vortex approaches the barrier in a 2.5 m/s zonal flow. Both the secondary low and secondary vortex are induced when the vortex approaches either the central (W1Ss, Fig. 6.23) or the southern (W6Ss, Fig. 6.24) portion of the barrier. Although the vortex in the W1Ss simulation approaches the central portion of the barrier (Fig. 4.29), the 700 mb center is located northeast of the barrier at 48 h (Fig. 6.23a). The lower-level center has been deflected northward even more than in the 5 m/s flow to avoid crossing the high terrain area. Therefore, all of the centers are well defined even though the system is weakening and the 500 mb center has moved over the barrier.

The 1000 mb secondary low is found near the west coast (Fig. 6.23a) similar to the W1S simulation (Fig. 6.5). The secondary low is not co-located with the secondary vortex, which is southwest of the barrier. Since the secondary vortex is formed before the dissipation of the original vortex center, the presence of two wind centers at 1000 mb is different from the wind distributions in the W1S simulation. Later,

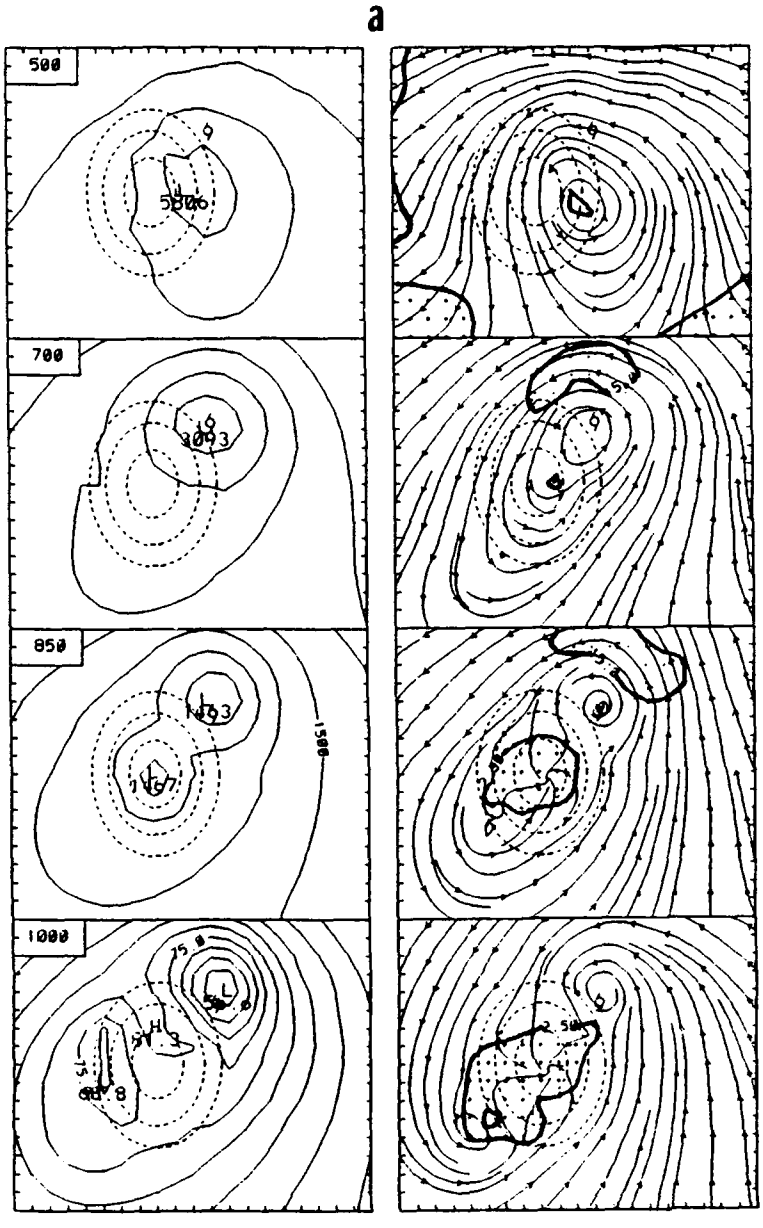

Fig. 6.23 As in Fig. 6.9, except for the height (left), and streamlines and isotachs (2.5 and 15 m/s, right) at (a) 48 h and (b) 60 h for the W1Ss simulation.

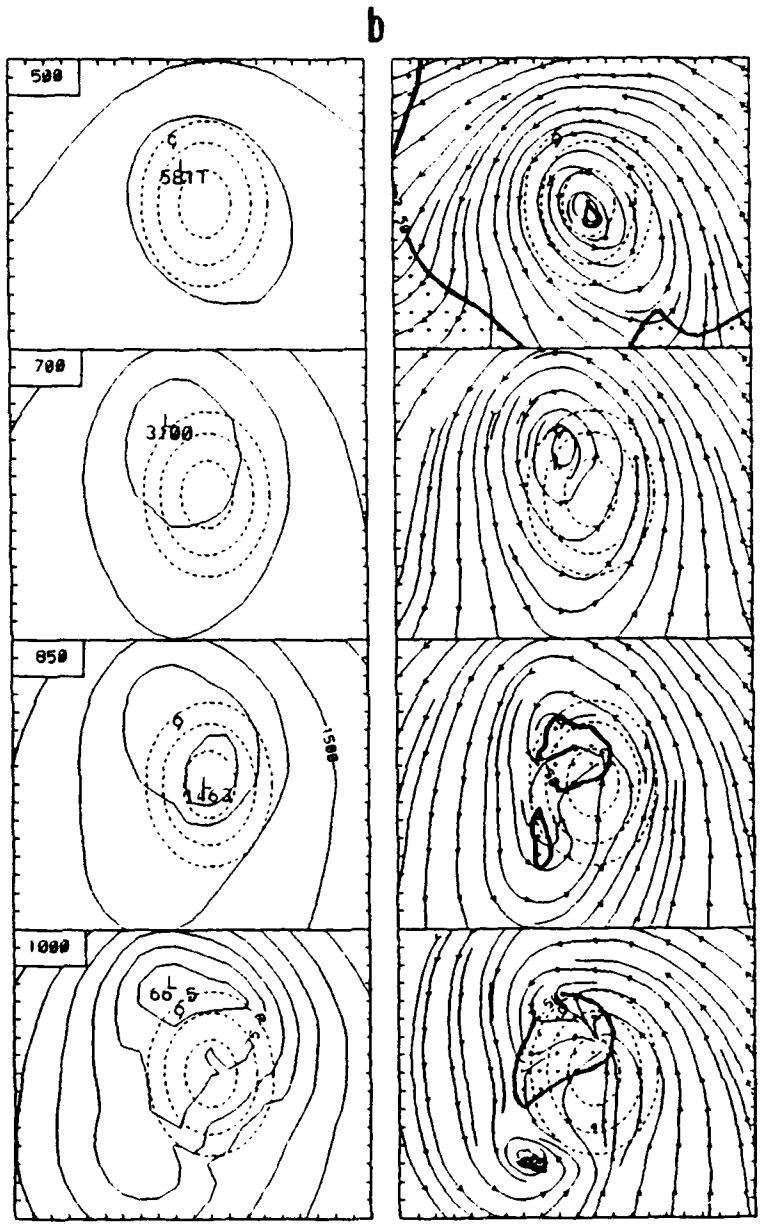

Fig. 6.23 (Continued)

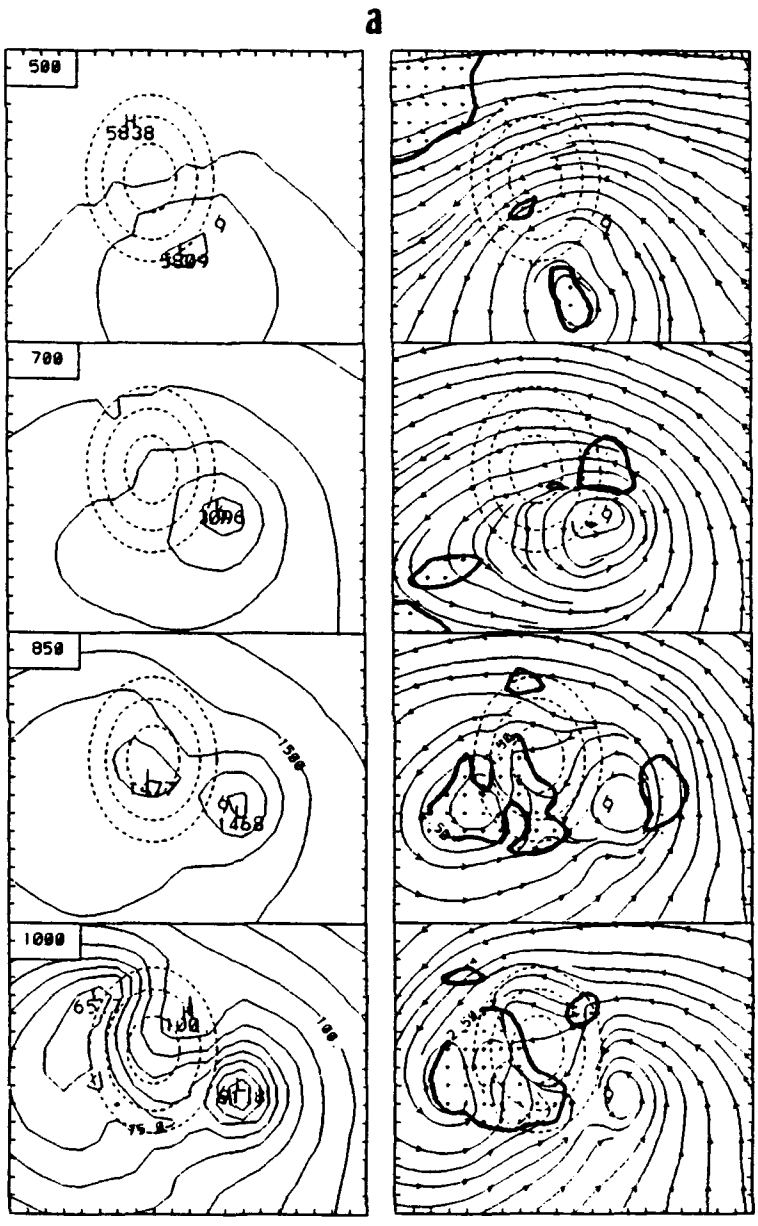

Fig. 6.24 As in Fig. 6.9, except for the height (left), and streamlines and isotachs (2.5 and 15 m/s, right) at (a) 54 h and (b) 60 h for the W6Ss simulation.

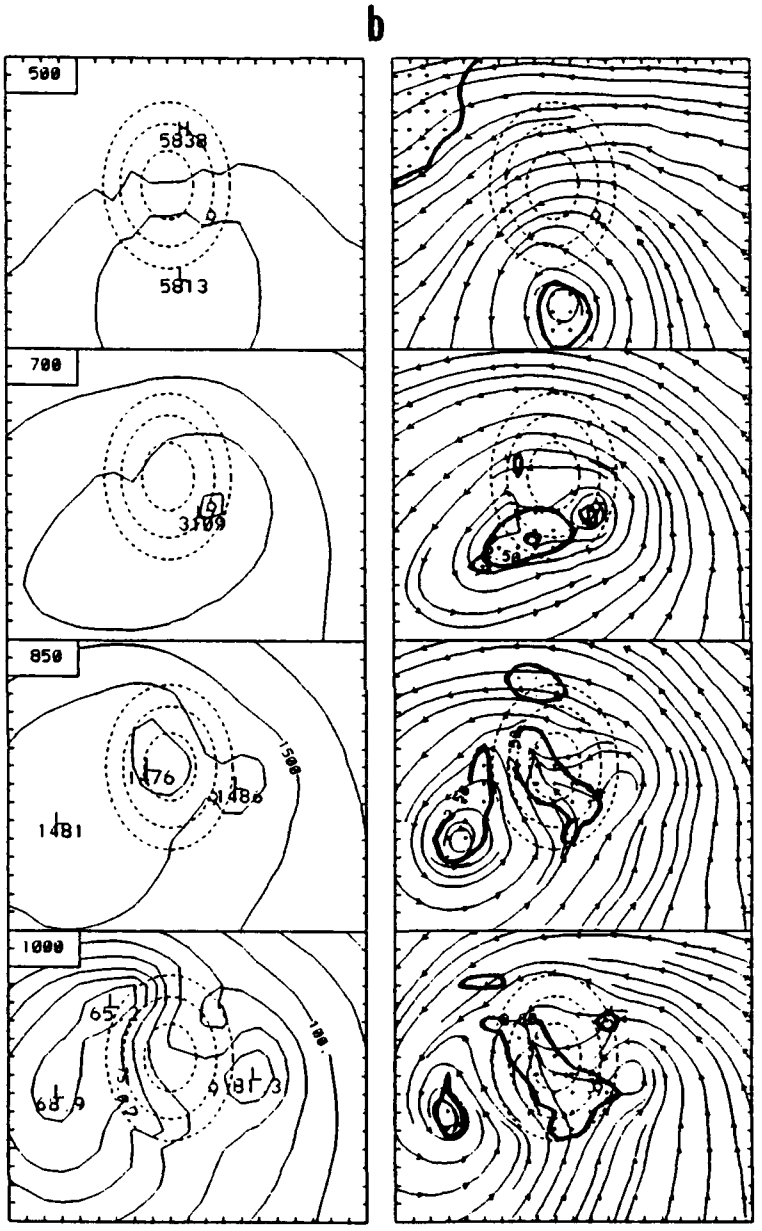

Fig. 6.24 (Continued)

the vortex circulation center is destroyed at 51 h (not shown) even though the low center continuously passes around the barrier (Fig. 6.23b). As the vortex moves cyclonically to pass the barrier, the secondary vortex also shifts cyclonically to a position farther to the south at 60 h (Fig. 6.23b). This southeastward shifting of the secondary vortex is different from the northward shifting of the secondary vortex in simulation W1S (Fig. 6.6a), and from the westward shedding of the secondary vortex in the W6S simulation (Fig. 6.6b).

Notice that the secondary low on the western coast in the W1Ss simulation is not intensified, which is similar to the W2N simulation (Fig. 6.5). Curved isobars are developed southwest of the barrier in association with the secondary vortex at 60 h (Fig. 6.23b). Large curvature of the flow southwest of the barrier is also found at 850 mb. However, the maximum 1000 mb vorticity center and convergence center are advected westward to pass around the northern end of the barrier at 60 h (not shown). The upper-level (i.e., 700 mb and 500 mb) height and wind fields also show the upper-level center has passed the barrier to the northwestern coast. Although the simulation is stopped at 60 h, reorganization of the low-level wind circulation center around the location of the low center may be expected later.

The formation of the secondary center in the W6Ss simulation is very similar to that in simulation W6S. The secondary lows are located near the western coast, and the secondary vortices are formed on the west side of the barrier and then are shed westward (Fig. 6.24). The development of the secondary center in the W6Ss simulation is from the low levels upward, which is also similar to simulation W6S. At 54 h (Fig.

6.24a), the low center associated with the secondary vortex is not shown at 850 mb. However, a 850 mb low begins to develop 6 h later west of the southern end of the barrier (Fig. 6.24b). Meanwhile, the secondary circulation has extended upward to 700 mb. Notice that the secondary center below 850 mb is more than 400 km west of the original center at the end of the simulation (60 h, Fig. 6.24b).

In summary, the simulations with different vortex translation speeds show the terrain modifications such as the formation of secondary centers are mainly dependent on the vortex location. One difference is that the faster-moving (10 m/s) vortex may be able to pass the barrier without being destroyed due to the shorter period of vortex-terrain interaction. Therefore, the secondary center may be quickly merged into the original circulation if it is not shed away from the barrier. When the secondary center is shed westward after the formation, then dual centers exist to the west of the barrier, which will be similar to that observed when Typhoon Sally passed Taiwan (Wang 1980).

The slower moving (2.5 m/s) vortex may also be able to avoid crossing onto the high terrain area by a gradual northward deflection of the low-level center such as in W1Ss simulation. Because the upstream vortex is slowed, the secondary vortex is formed before the upstream vortex moves close to the barrier. In this situation, the secondary vortex shifts cyclonically relative to the barrier as the upstream vortex passes cyclonically around the northern barrier. For a vortex that approaches farther south along the barrier such as in the W6Ss simulation, the barrier effectively blocks the low-level center from passing westward. However, the formation and shedding of the

secondary vortex results in a discontinuous track. The new center is developed from the low levels upward and is separated more than 200 km from the 500 mb center.

E. EFFECT OF VORTEX INTENSITY

The intense vortex (Chapter III) reaches a quasi-steady state after 36 h of integration after being superposed on an ocean-only 5 m/s zonal flow (Fig. 4.32). The minimum sea-level pressure of the intense vortex (IOC) is about 25 mb lower than in the WOC simulation (Fig. 4.10). Whereas the 500 mb center of the weak vortex is tilted toward the south (Fig. 6.2), the intense vortex has vertically stacked centers below 500 mb (Fig. 6.25). The strong wind and pressure gradients of the intense vortex are not limited to the surface, but are extended to a deep layer and expanded to a wider region. The 500 mb wind speeds are greater than 15 m/s inside a radius of about 300 km from the center compared to inside 220 km north of the center in the WOC simulation (Fig. 6.2). Notice the large convergence is still limited to the boundary layer as no significant inflow is found above 850 mb of the intense vortex.

When the barrier is included, the central pressure begins to depart from the ocean-control simulation about 300 km upstream of the barrier center. The pressure is about 15 mb higher than the ocean-control just prior to when the center makes landfall (not shown). The existence of the barrier not only weakens the vortex, but significant surface structure modifications are also found (Fig. 6.26). Surprising similarities between the sea-level pressure patterns in Fig. 6.5, Fig. 6.22a and Fig. 6.26a further confirm that the terrain-induced sea-level pressure modifications depend mainly on the

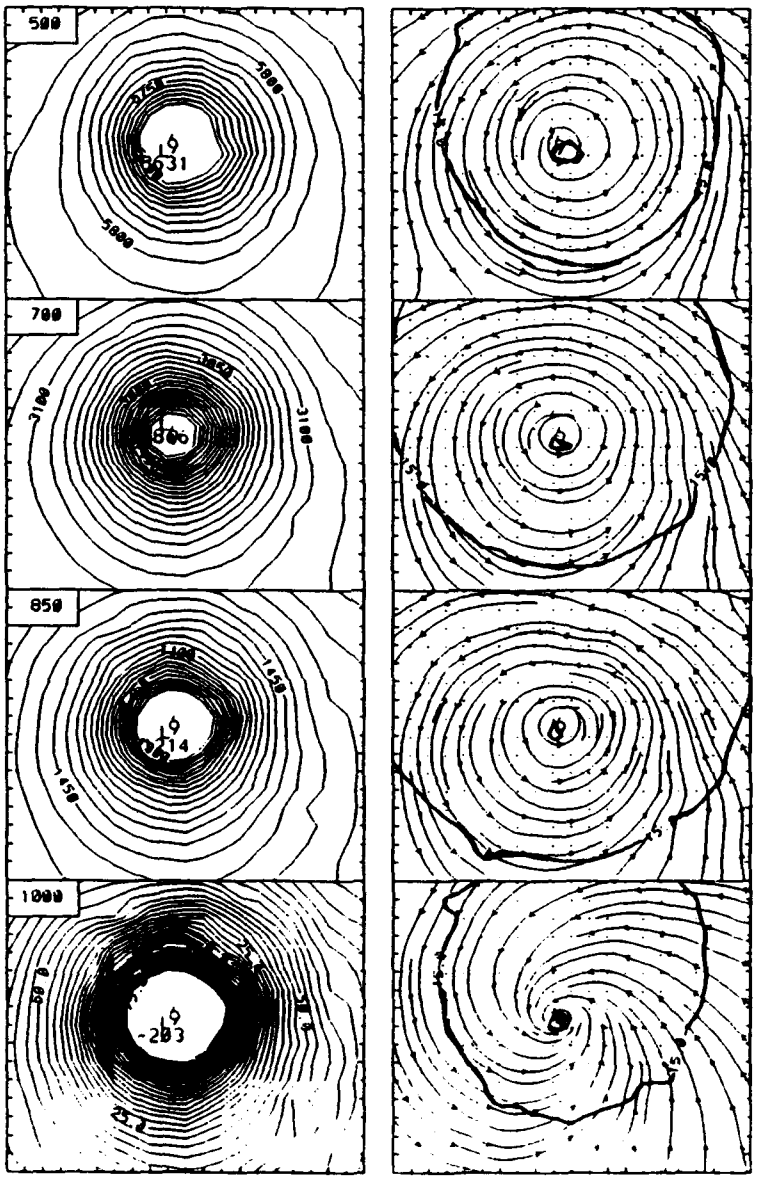

Fig. 6.25 As in Fig. 6.2, except for the geopotential heights (left), and streamlines and isotachs (15 m/s on right) of the intense vortex in the ocean-only simulation (IOC).

a

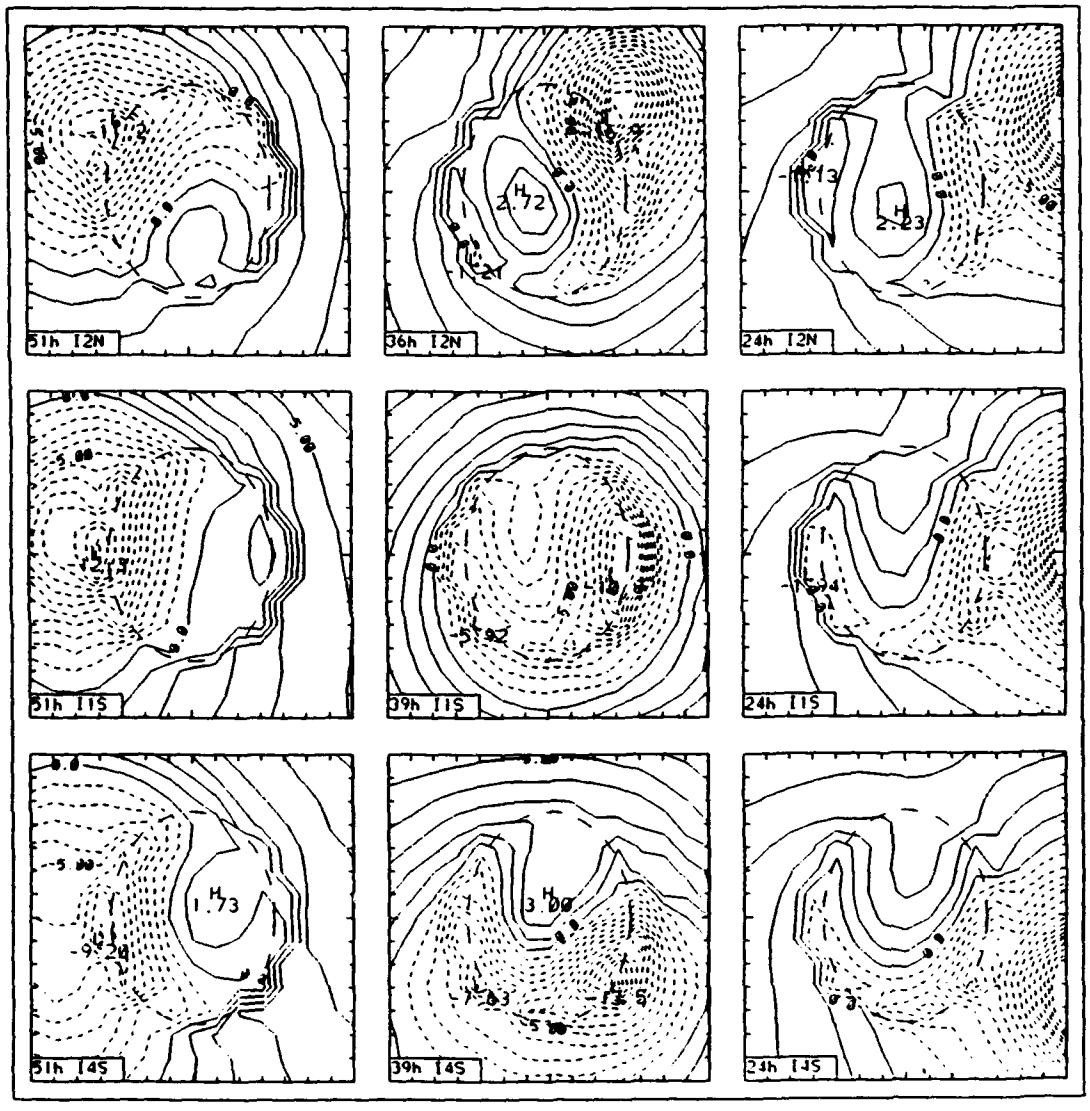

Fig. 6.26 (a) As in Figure 6.5, except for the sea-level pressure anomalies for three intense vortex simulations (I2N, I1S and I4S). (b) As in Figure 6.7, except for the surface streamlines and isotachs corresponding to (a).

b

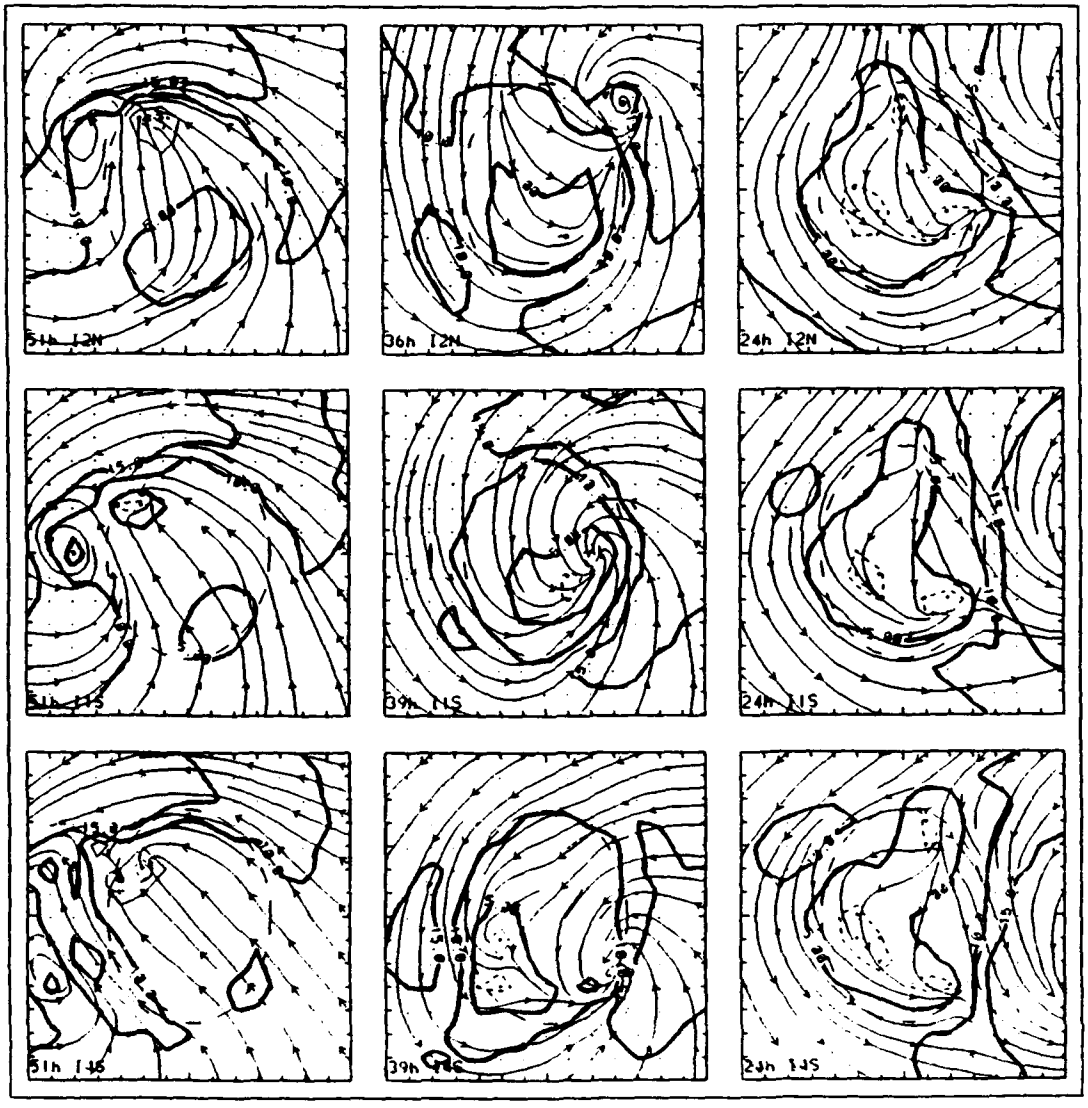

Fig. 6.26 (Continued)

vortex location. A consideration of the full range of larger pressure gradients in the intense vortex to the smaller pressure gradients from the weak vortex simulation (Fig. 6.5 and Fig. 6.22a) would be representative of an averaged pressure distribution over the barrier that would be closer to the observations (Fig. 5.4).

Secondary lows are found in several panels of Fig. 6.26a. Similar to the other simulations, the secondary lows do not move away from the barrier but are locked over the barrier. A secondary low is formed over the west coast when the vortex in the I2N simulation approaches the northern portion of the barrier (Fig. 6.26a). This secondary low does not develop, but is dissipated as the vortex moves farther to the west at 39 h (not shown). The vortex in the I2N simulation follows a continuous track to pass the barrier along the northern coast.

Smaller upstream track deflections are shown in Chapter IV when the intense vortex approaches the barrier. The vortices in both the I1S and I4S simulations have not been significantly slowed before they make landfall near 39 h. Meanwhile, a secondary low has formed over the western coast. As the low-level vortex centers become blocked on the east side of the barrier, the secondary lows become the dominant centers near 42 h (e.g., Fig. 6.27). After the system has passed the barrier, notable terrain-modified structures as in Fig. 6.5 remain over the barrier at 51 h (Fig. 6.26a).

The flow deflections (Fig. 6.26b) near and over the barrier are similar to the weak vortex simulations (Fig. 6.7) when the intense vortex is still far from the barrier at 24 h. The barrier slows the impinging flow and induces a calm wind area on the upwind slope. Most of the the flow is deflected to pass around two sides, which results in strong

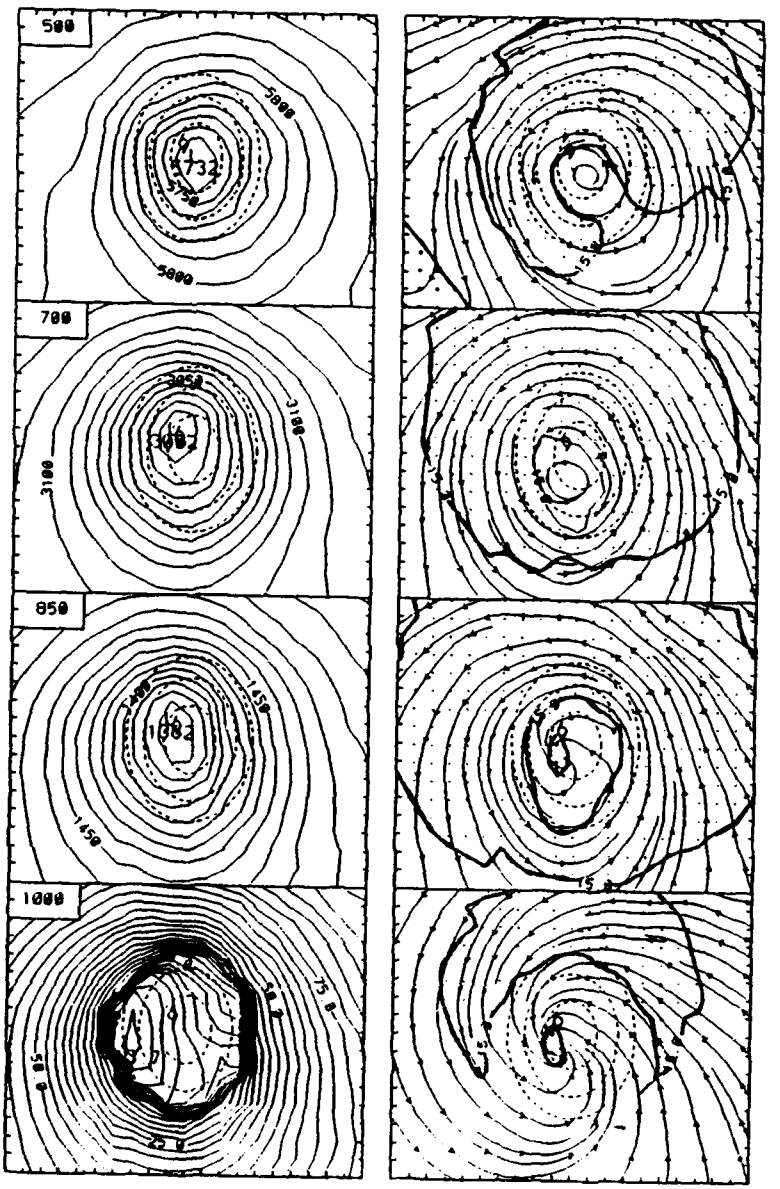

Fig. 6.27 As in Fig. 6.9, except for the height (left), and streamlines and isotachs (2.5 and 15 m/s, right) for simulation I1S for four levels at 42 h.

flow between the barrier and the vortex and a strong wind shear near the northwestern coast. However, more of the flow on the west side of the barrier can pass around the southern end of the barrier because of the stronger circulation in the intense vortex simulation. A convergence zone that extends from the eastern coast eastward to the vortex center is formed as the flow from the west side of the barrier meets the flow deflected around the east side of the barrier.

The flow structures near and over the barrier have relatively larger differences from the weak vortex simulations (Fig. 6.7) as the intense vortex moves closer to the barrier (i.e., left and central columns of Fig. 6.26b). The impinging surface flow just offshore is more than 5 m/s stronger than in the corresponding weak vortex simulation when the intense vortex is near the eastern coast (central column of Fig. 6.26b). As the Froude number is increased, more flow is able to move over the barrier, which maintains almost smooth streamline circles around the center even though the flow is slowed. Significant flow deflections are limited to a rather small area. A large curvature of the flow near the southwestern coast is not found in the I1S simulation whereas a secondary vortex had been produced in the W1S simulation. The leeside vortex in the W6S simulation is also not formed in the I4S simulation.

When the vortex moves to the west of the barrier (left column of Fig. 6.26b), calm areas are found on both the upwind and leeside slopes. A convergence zone extends from the barrier to north of the vortex center. These patterns are similar to the weak vortex simulations. Because of the stronger circulation in the intense vortex, the flow near and over the barrier is less deflected.

Previous sections have shown the upper-level vortex structure is relatively little modified for a weak vortex encountering a barrier. The barrier-induced, upper-level structure changes are even less in the intense vortex simulations. The center blocking in the I1S simulation is limited to a very shallow layer. Centers above 850 mb move over the barrier without significant deflections at 39 h (not shown). As the upper-level center moves continuously westward over the barrier, a secondary low develops near the west coast. The 1000 mb secondary low becomes the dominant center at 42 h (Fig. 6.27) when the original center is dissipated over the southeastern barrier. Whereas the lower-level height center appears to move discountinously from the east slope to the western coast, the 1000 mb wind center moves continuously across the barrier co-located with other higher-level centers. Significant flow distortions are not found at any of the levels in Fig. 6.27. Nearly circular isobars around the center are simulated above 850 mb. The terrain modification of the intense vortex structure in the I1S simulation is relatively insignificant.

More severe structure modifications occur when the intense vortex approaches the southern portion of the barrier due to the vortex circulation directly impinging on the long-axis of the barrier. When the secondary low in the I4S simulation is present on the west coast at 39 h (Fig. 6.26a), the asymmetric vortex structure extends through a deep layer (Fig. 6.28). A trough is found up to at least 500 mb. The 700 mb circulation is also elongated in the northeast-southwest direction, and the cyclonic flow is significantly slowed in the southwestern quadrant. More significant flow deflections occur below 850 mb over the southwestern barrier and the nearby ocean, since the flow is slowed and

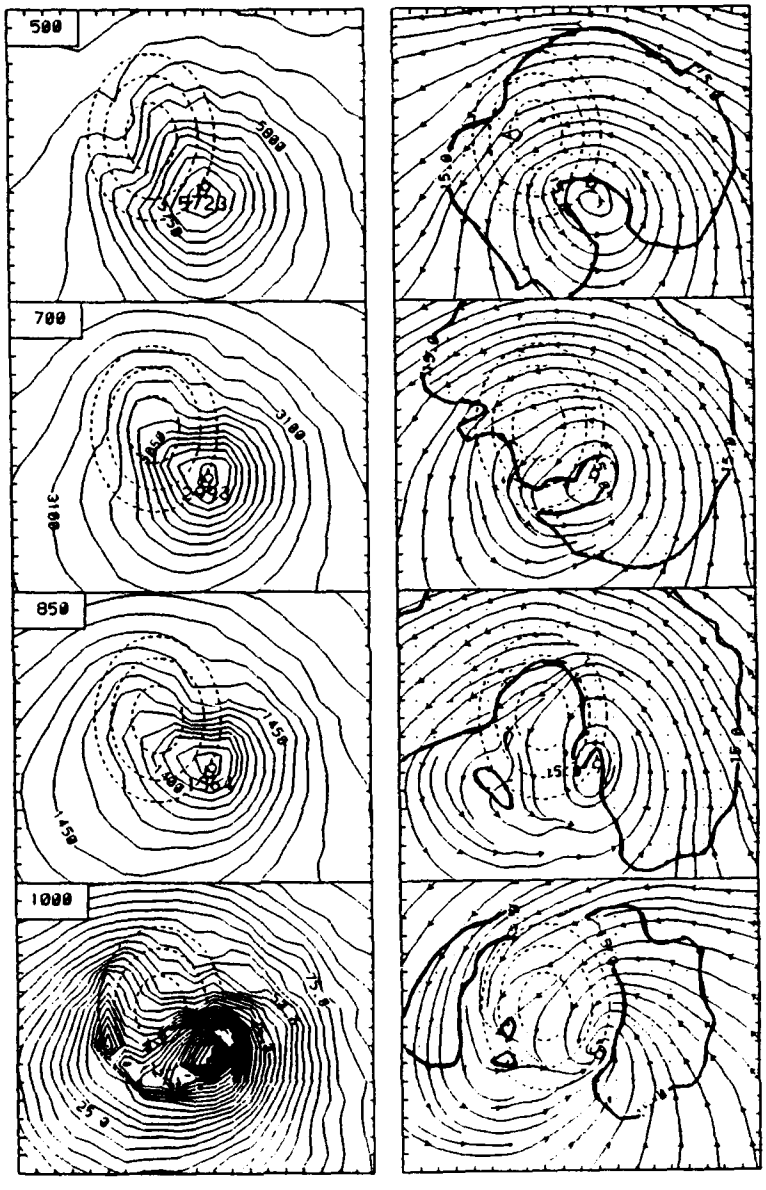

Fig. 6.28 As in Fig. 6.9, except for the height (left), and streamlines and isotachs (2.5 and 15 m/s, right) for simulation I4S for four levels at 39 h.

deviates considerably from a circular track around the center. However, both the wind center and the height center in Fig. 6.28 are vertically stacked despite those flow modifications.

Although the low-level height and wind fields become separated after the I4S vortex moves over the barrier, a separation of the wind and height centers is not noted above 900 mb. The weakening 1000 mb height center is deflected southward when a secondary low on the west coast becomes the dominant center at 42 h (Fig. 6.29). However, the secondary low is only found in a very shallow layer. Meanwhile, the 1000 mb wind center moves over the barrier to the south of the mountain peak close to the 700 mb center. Significant vortex circulation distortions are found in the lower troposphere, especially in the southwestern quadrant. The curvature of the flow to the southwest of the barrier is increased.

The 1000 mb streamline center is found to the southwest of the barrier at 45 h where the large curvature of the flow was located 3 h previously (Fig. 6.29). A well-organized 850 mb circulation center is also found north of the 1000 center where the large curvature of the flow was also indicated in Fig. 6.29. As a result, both centers are accelerated to pass the barrier and the 1000 mb center is deflected southward.

Whereas the other height centers move westward to pass the barrier, the 1000 mb height center is locked near the western coast. The movement of the 1000 mb and 850 mb wind centers is also slowed after passing the barrier. The 1000 mb wind center shifts northwestward while the 850 mb center shifts southwestward. Center positions at 850 mb and 1000 mb are shown in Fig. 6.29. A third low is found separated from the

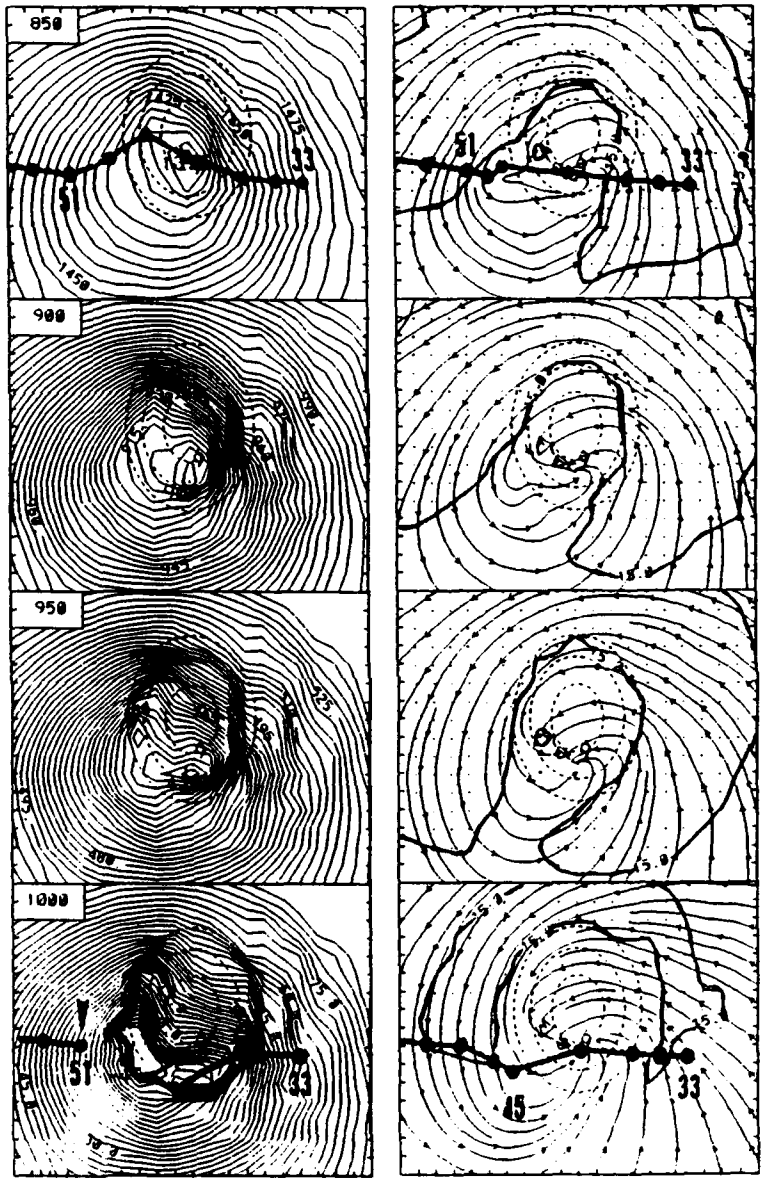

Fig. 6.29 As in Fig. 6.19, except for the height (left), and streamlines and isotachs (2.5 and 15 m/s, right) for simulation I4S at 42 h. Three hourly height and wind center locations at 850 mb and 1000 mb are also indicated. Location of the third low that formed at 51 h is indicated on the 1000 mb height field.

terrain-locked secondary low at 1000 mb when the centers are closer together at 51 h (not shown). The balanced wind-height system then shifts westward with a slight intensification, although notable structure modifications are continuing over the barrier.

F. SUMMARY

Numerical model simulations have been employed to study the CMR-like barrier effect on typhoon structure. The simulations are the same as in Chapter IV with a simplified typhoon structure represented by a 'spun-up' vortex and an isolated barrier slightly larger and lower than the CMR.

Many observed CMR-induced surface features have been reproduced from the idealized simulations. These features include the formation of troughs and the secondary low, enhancement of the precipitation on the upwind slope, and generation of downslope warm and dry foehn winds. Significant flow deflections such as the formation of the secondary vortex, production of calm wind areas on the upwind and downwind sides, increased flow speed between the barrier and the typhoon, and an induced convergence zone near the vortex center are also simulated. Both the model simulation and observational (Chapter V) results show these barrier-induced structure changes mainly depend on the location of the vortex relative to the barrier.

Because complete three-dimensional observations have not been collected when typhoons have encountered Taiwan, the upper-air CMR-modified typhoon structure has not been studied in detail before. These simulations indicate significant displacements of the low-level center from the upper-level center are possible when the vortex moves

close to the barrier. The upper-level vortex structure is less modified, but notable structure changes can extend to a deep layer higher than the mountain peak. As the vortex is significantly distorted, the intensity of the vortex is weakened before it moves over the barrier.

The terrain-induced height (pressure) and wind fields are generally not in a simple balanced relationship, especially for areas close to the barrier. For example, the secondary low center and the secondary vortex center are not co-located. The secondary low is generally located near the central-western coast, and the secondary vortex is southwest of the barrier or it is shedding westward from the western coast. A clear distinction between the height (pressure) field and the wind field is required in determining the storm track.

The 1000 mb height tendency analysis shows the barrier-induced leeside subsidence warming is the dominant term contributing to the formation of the secondary low. Subsidence warming is also found on the downwind slope from the vortex cyclonic circulation where the trough is formed. The secondary low does not move away from the barrier as the strong terrain-induced subsidence warming is locked near the barrier.

The secondary vortex is formed via a different mechanism from the secondary low. Long-lasting easterlies are directly impinging on the long-axis of the barrier when a weak vortex is slowed as it approaches the southern portion of the barrier. A leeside vortex is formed near the central-western coast in a similar way as the leeside vortex forms when a barrier is embedded in a simple zonal flow (e.g., Smolarkiewicz and Rotunno 1989). However, the secondary vortex has a smaller scale and is located closer to the

barrier. A paired anticyclonic vortex also is not produced because of the large curvature of the low-level flow west of the barrier. The secondary vortex is shed westward as the upstream low-level vortex is blocked and distorted by the barrier.

The secondary vortex may also form near the southwestern coast as the low-level southwesterly flow on the west side of the barrier is blocked and deflected onto the southwest slope. This type of secondary vortex is not shed westward.

The vortex structure is less distorted when it passes or moves over the northern barrier. Although the secondary low and the secondary vortex may be formed, they are not developed when the vortex moves close to the barrier. The vortex passes the northern barrier continuously. More severe structure modifications occur when the vortex landfalls on the central or southern barrier. A discontinuous track is found when the low-level height (pressure) center is blocked on the east slope and a secondary low becomes the dominant center. These tracks are generally consistent with the observational study (Fig. 5.20) in which the secondary low develops when the typhoon is located to the southeast of Taiwan.

A track discontinuity also appears in the low-level wind field. As the low-level wind center associated with the original vortex is dissipated over the eastern slope, the secondary vortex is gradually organized to become the dominant circulation center. However, the movement of the wind center does not necessarily follow the height (pressure) center. This study suggests attention must be focused on the wind field as the wind field is more coherent in time and the height (pressure) field is considerably modified by the local temperature distribution over the barrier. Notice that the

precipitation and temperature distribution also are determined by the wind circulation. The height (pressure) field seems to adjust to the wind field as the system gradually moves away from the barrier.

Vortex reorganization occurs on the west side of the barrier. When the vortex is blocked or severely distorted by the barrier, a secondary vortex develops gradually and sheds westward as the new vortex. A third low center developing from low levels upward is found associated with the secondary vortex. Vortex reorganization also occurs when a secondary vortex is formed on the west side, but the upper-level system and remnants of the low-level circulation have moved over the barrier. In this situation, the secondary vortex shifts to the location near the upper-level center and a third low is formed in association with the circulation from the upper levels downward. In both types of secondary vortex formation, the newly formed mass-wind balanced system moves westward as the vortex center. However, notable structure modifications may still occur over the barrier.

The barrier effect on vortex structure depends on the vortex translation speed. The vortex is less distorted when the translation speed increases from 5 m/s to 10 m/s. Dual centers on the west of the barrier are simulated as the vortex passes over the southern tip of the barrier and induces a westward-shedding secondary vortex on the west side. A vortex in a 2.5 m/s flow may be able to survive a severe terrain distortion if the center is gradually deflected to pass around the end of the barrier at a lower altitude.

The barrier effect on vortex structure also depends on the vortex intensity. The central pressure is filled and the maximum wind speed is decreased more when a more

intense vortex approaches the barrier than occurs for a weaker vortex. However, the wind and height centers at different levels in the intense vortex are relatively closer together and are less distorted than in the weak vortex simulation. The secondary low and the secondary vortex are less likely to form, or will be limited to a shallower layer for the intense vortex.

VII. SUMMARY AND CONCLUSIONS

This study examines the effects of steep terrain on typhoon motion and structure. The terrain selected is the island of Taiwan because of its high mountain range with a horizontal scale comparable to the center core of a typhoon, its location in the main path of western North Pacific typhoons, and its good coverage of a surface station network over and near the island. Both observational data analyses and numerical model simulations have been carried out.

The observational studies of the terrain effects on the typhoon motion examine the along-track speed and cross-track deflections of westward-moving typhoons that struck Taiwan from 1947 to 1990. A 20-year (1971-1990) data set from 22 surface stations is also used to describe the effects of the Taiwan orography on the surface structure of typhoons. Simulations using the Limited-Area Weather Prediction Model of the Naval Research Laboratory with 16 levels in the vertical and a 45 km resolution are employed to compare with and extend the results from the observational studies. The finite difference model is of second-order accuracy in both time and space. Chang et al. (1989) and Holt et al. (1990) demonstrated that the model produces good forecasts for real data simulations with S1 scores (defined as in Anthes 1983, with a value of 30 representing a 'perfect' forecast and a value of 80 representing a relatively useless forecast) are approximately 40. Less than 10 % errors on the calculation of the amplitude and speed of the major Taiwan-terrain induced systems are expected.

The along-track speeds are referenced to a second-order polynomial curve fitted to the 6-h best-track positions analyzed by the Joint Typhoon Warning Center in Guam. For the 53 westward-moving typhoons, a downstream acceleration is documented with along-track speed increases from about 4.5 m/s at 72 h prior to landfall to about 6 m/s at landfall. However, this rather steady downstream along-track acceleration is likely to be due to environmental flow changes rather than to the interaction with the topography of Taiwan because similar along-track accelerations are observed for typhoons entering an ocean area without terrain effects. Evidence of along-track decelerations from about 48 h prior to landfall is only observed for the weaker and the slower-moving storms.

The cross-track deflections are calculated as the displacements of the center locations from the second-order polynomial curve fitted to the two ends of the above mentioned best-track positions from -72 h to -54 h prior to landfall and from 6 h to 18 h after leaving Taiwan. The first cross-track deflections upstream of the barrier are generally consistent with the blockage of the low-level steering flow around the island. The vortex turns back toward the island prior to landfall.

The simulations demonstrate similar terrain effects on the vortex motion, and show that the superposition of the outer storm circulation on the basic flow accentuates the blocking effect of the barrier. As the storm moves closer to the barrier, the terrain-induced asymmetric gyres account for the vortex motion deviating from the simple barrier-blocking effect.

The upstream track deflections depend on both the vortex translation speed and the intensity. Smaller track deflections are simulated for more intense or faster-moving

typhoons. However, the terrain effect extends to farther upstream as the size of the vortex is increased.

The observational analyses show that significant structure distortions occur when a typhoon moves over or is located in the vicinity of Taiwan. Most of the observed terrain-induced surface features such as the formation of secondary low, secondary vortex, foehn winds and enhanced precipitation on upwind slopes have been reproduced from the numerical model simulations of this study. From the observational analysis, the lee trough is found to be the dominant mode of the terrain-induced pressure structure. A secondary low center in southwestern Taiwan is enhanced when a local pressure ridge is induced on the southern portion of the lee trough by the southwesterly return flow impinging on the southwest slope of CMR. A 1000 mb height tendency analysis of the simulations shows that the terrain-induced subsidence warming is the dominant term contributing to the formation of the lee trough and thus the terrain-locked secondary low. The occurrence of a secondary low mainly depends on the typhoon center position. The most favorable condition for a secondary low formation is when a typhoon moves into a region that covers southeastern Taiwan and extends east-southeastward to include an ocean area of approximately 2° long. x 1° lat. offshore.

The simulations show that terrain-modified pressure and wind fields are generally not in a simple balance relationship. For example, the secondary vortex is formed about 90 km to the south of the secondary low when a weak vortex approaches the central barrier. The simulations suggest that a center-following algorithm focused on the wind field would be more representative because the wind patterns are more coherent in time.

Track discontinuities are simulated when the low-level wind center associated with the original vortex is dissipated over the eastern slope and a secondary vortex is formed downstream and gradually becomes the dominant circulation center.

Two types of vortex reorganization on the west side of the barrier are simulated. When the vortex is blocked or severely distorted by the barrier, a secondary vortex develops gradually from low levels upward on the west side of the barrier. Vortex reorganization also occurs in a secondary vortex to the southwest of the barrier as the upper-level system and remnants of the low-level circulation move over the barrier. In this situation, the secondary vortex shifts to the location under the upper-level center and a third low is formed downward in association with the circulation from the upper levels.

Although the general barrier effect on the vortex structure change depends mainly on the vortex location relative to the barrier, variations attributed to the steering flow are also found. For example, the simulated vortex is less distorted when the translation speed is increased from 5 m/s to 10 m/s. Dual centers on the west side of the barrier are simulated as the vortex passes over the southern tip of the barrier and induces a westward-shedding secondary vortex on the west side. A dependence of structure changes on vortex intensity is also simulated. The secondary low and the secondary vortex are less likely to form, or will be limited to a shallower layer, in a more intense vortex.

The precipitation heating is the main energy source to increase or maintain the vortex intensity. The barrier significantly modifies the precipitation pattern as the rainfall is enhanced on the upwind slope. However, the track change and vortex

circulation change due to the enhanced latent heating effect are less than 20 % of the changes associated with the dynamical effects of the terrain interaction with the vortex. More studies are required to advance the understanding of how the asymmetric precipitation heating contributes to the vortex motion and structure change.

In this study, the Taiwan orography has been greatly simplified. Nevertheless, the main features of the terrain-induced typhoon motion and structure changes have been simulated. The sensitivity of these changes to the detailed terrain features needs to be further investigated by improving the model resolution and including a more detailed orography to represent Taiwan island.

The lack of dense upper-level observations over the Taiwan area is a serious obstacle for studying the details of the terrain effects on typhoon motion and structure change. The simulations suggest that upper-level processes and changes in structure are contributing to the formation of the secondary low or secondary vortex. These upper-level features also determine how the system is re-organized after the vortex passes the barrier. The analysis of secondary vortex is difficult because it is located west of the barrier and over the Taiwan Strait where few observations exist. Case studies using data from special field experiments, such as the Tropical Cyclone Motion Experiment 1990 and the Taiwan Area Typhoon Experiment 1990, may overcome these problems to some extent.

This study has not examined about half of the total typhoons that approach the Taiwan island from directions other than a general westward approach. Further study is required to advance the understanding of the sensitivity of the terrain effect as a

function of the vortex approach direction. Many interesting terrain-induced structures such as the strong wind shears near the barrier, convergence zones extending from the barrier to the vortex, strong negative relative vorticity produced southwest of barrier, etc. also have not been studied in detail. How those structures may cause significant weather phenomena should be included in future studies.

LIST OF REFERENCES

Anthes, R.. A., 1977: A cumulus parameterization scheme utilizing a one-dimensional cloud model. *Mon. Wea. Rev.*, **105**, 270-286.

--------, 1982: *Tropical cyclones: their evolution, structure and effects*. Meteor. Monographs, Vol. 19, Amer. Meteor. Soc., Boston, MA (ISBN 0-033876-54-8), 208 pp.

--------, 1983: Regional models of the atmosphere in middle latitudes. *Mon. Wea. Rev.*, **111**, 1306-1335.

Bender, M. A., R. E. Tuleya and Y. Kurihara, 1987: A numerical study of the effect of island terrain on tropical cyclones. *Mon. Wea. Rev.*, **115**, 130-155.

Blackada, A. K., 1976: Modeling the nocturnal boundary layer. Preprints, Third Symposium on Atmospheric Turbulence, Diffusion and Air Quality. Raleigh, Amer. Meteor. Soc., 46-49.

Brand, S., and J. Blelloch, 1974: Changes in the characteristics of typhoons crossing the island of Taiwan. *Mon. Wea. Rev.*, **102**, 708-713.

Brown, J. A., Jr., and K. A. Campana, 1978: An economical time-differencing system for numerical weather prediction. *Mon. Wea. Rev.*, **106**, 1125-1136.

Carr, L. E., III, and R. T. Williams, 1989: Barotropic vortex stability to perturbations from axisymmetry. *J. Atmos. Sci.*, **46**, 3177-3196.

Chan, J. C.-L., 1984: An observational study of the physical processes responsible for tropical cyclone motion. *J. Atmos. Sci.*, **41**, 1036-1048.

--------, and R. T. Williams, 1987: Analytical and numerical studies of the beta-effect in tropical cyclone motion. Part I: Zero mean flow. *J. Atmos. Sci.*, **44**, 1257-1265.

Chang, C.-P., and J. M. Chen, 1992: A statistical study of northeasterly cold surges and the large-scale equatorial divergence during the northern winter monsoon. *J. Met. Soc. Japan*, **70**, 287-302.

Chang, S. W., 1979: An efficient parameterization of convective and non-convective planetary boundary layers for use in numerical models. *J. Appl. Meteor.*, **18**, 1205-1215.

--------, 1982: The orographic effects induced by an island mountain range on propagating tropical cyclones. *Mon. Wea. Rev.*, **110**, 1255-1270.

--------, K. Brehme, R. Madala and K. Sashegyi, 1989: A numerical study of the East Coast snowstorm of 10-12 February 1983. *Mon. Wea. Rev.*, **117**, 1766-1776.

Elsberry, R. L., 1987: Tropical cyclone motion. Chap. 4 in *A global view of tropical cyclones*, R. L. Elsberry, Ed., Office of Naval Research, 189 pp.

Fiorino, M., and R. L. Elsberry, 1989: Some aspects of vortex structure related to tropical cyclone motion. *J. Atmos. Sci.*, **46**, 975-990.

Frank, W. M., 1977: The structure and energetics of the tropical cyclone, I: Strom structure. *Mon. Wea. Rev.*, **105**, 1119-1135.

Haltiner, G. J., and R. T. Williams, 1980: *Numerical prediction and dynamic meteorology*, second edition. John Wiley and Sons Inc., 477pp.

Hirschberg, P. A., and J. M. Fritsch, 1991: Tropopause undulations and the development of extratropical cyclones. Part II: Diagnostic analysis and conceptual model. *Mon. Wea. Rev.*, **119**, 518-550.

Holland, G. J., 1987: Mature structure and structure change. Chap. 2 in *A global view of tropical cyclones*, R. L. Elsberry, Ed., Office of Naval Research, 189 pp.

--------, and M. Lander, 1991: On the meandering nature of tropical cyclones. *J. Atmos. Sci.*, (submitted).

Holt, T., S. W. Chang and S. Raman, 1990: A numerical study of the coastal cyclogenesis in GALE IOP 2: Sensitivity to PBL parameterizations. *Mon. Wea. Rev.*, **118**, 234-257.

Holton, J. R., 1979: *An Introduction to Dynamic Meteorology*. Academic Press, Inc., 391 pp.

Hsu, Y. C., 1960: The problems of typhoon forecasting over Taiwan and its vicinity. Proc. U. S. Asian Military Weather Sympos., 9-12 Feb. 1960.

Jones, R. W., 1987: A simulation of hurricane landfall with a numerical model featuring latent heating by the resolvable scale. *Mon. Wea. Rev.*, **115**, 2279-2297.

Kuo, H. L., 1974: Further studies of the parameterization of the influence of cumulus convection on a large-scale flow. *J. Atmos. Sci.*, **31**, 1232-1240.

Lee, C.-S., 1992: The analysis of two typhoons when making landfall on Taiwan. Proceedings, The Second International Conference on East Asia and Western Pacific Meteorology and Climate. 7-10 September 1992, Hong Kong Meteorological Society, Hong Kong. (in preparation)

Li, P. C., 1963: Terrain effects on typhoons approaching Taiwan. Proc. U. S. Asian Military Weather Sympos., 3-7 Feb. 1963.

Li, S.-W., 1992: A three-dimensional study of the influence of mountains on a front. Ph.D. Dissertation. Naval Postgraduate School, Monterey, CA, 142 pp.

Madala, R. V., 1981: Efficient time integration schemes for atmospheric and ocean models. *Finite Difference Techniques for Vectorized Fluid Dynamics*, D. L. Book, Ed. Springer-Verlay, 56-74.

--------, S. W. Chang, U. C. Mohanty, S. C. Madan, R. K. Paliwal, V. B. Sarin, T. Holt and S. Raman, 1987: Description of the Naval Research Laboratory limited area dynamical weather prediction model. NRL technical report No. 5992, Washington, D.C., 131 pp.

Merrill, R. T., 1984: A comparison of large and small tropical cyclones. *Mon. Wea. Rev.*, **112**, 1408-1418.

Perkey, D. J., and C. W. Kreitzberg, 1976: A time-dependent lateral boundary scheme for limited-area primitive equation model. *Mon. Wea. Rev.*, **104**, 744-755.

Phillips, N. A., 1957: A coordinate system having some special advantage for numerical forecasting. *J. Meteor.*, **14**, 184-185.

Powell, M. D., 1982: The transition of the Hurricane Frederic boundary-layer wind field from the open Gulf of Mexico to landfall. *Mon. Wea. Rev.*, **110**, 1912-1932.

--------, 1987: Changes in the low-level kinematic and thermodynamic structure of Hurricane Alice (1983) at landfall. *Mon. Wea. Rev.*, **115**, 75-99.

Smolarkiewicz, P. K., R. M. Rasmussen and T. L. Clark, 1988: On the dynamics of Hawaiian cloud bands: Island forcing. *J. Atmos. Sci.*, **45**, 1872-1905.

Smolarkiewicz, P. K., and R. Rotunno, 1989: Low Froude number flow past three dimensional obstacles. Part I: Baroclinically generated lee vortices. *J. Atmos. Sci.*, **46**, 1154-1164.

Sun, W.-Y., J.-D. Chern, C.-C. Wu and W.-R. Hsu, 1991: Numerical simulation of mesoscale circulation in Taiwan and surrounding area. *Mon. Wea. Rev.*, **119**, 2558-2573.

Tuleya R. E., and Y. Kurihara, 1978: A numerical simulation of the landfall of tropical cyclones. *J. Atmos. Sci.*, **35**, 242-257.

--------, M. A. Bender and Y. Kurihara, 1984: A simulation study of the landfall of tropical cyclones using a movable nested-mesh model. *Mon. Wea. Rev.*, **112**, 124-136.

Wang, S. T., 1980: Prediction of the behavior and strength of typhoons in Taiwan and its vicinity (in Chinese). Res. Rep. 108, Chinese National Science Council, Taipei, Taiwan, 100 pp.

--------, S.-T., C.-Y. Tsai and M.-S. Lin, 1992: An analysis of the secondary flows in the typhoon circulation introduced by the Central Mountain Range in Taiwan (in Chinese, English abstract included). Proceedings, Conference on Weather Analysis and Forecasting, 23-25 April 1992, Central Weather Bureau, Taipei, Taiwan, 209-241.

Williams, R. T., M. S. Peng and D. A. Zankofski, 1992: Effects of topography on fronts. *J. Atmos. Sci.*, **49**, 287-305.

Willoughby, H. E., 1990: Temporal changes of the primary circulation in tropical cyclones. *J. Atmos. Sci.*, **47**, 242-264.

--------, 1992: Linear motion of a shallow-water barotropic vortex as an initial value problem. *J. Atmos. Sci.*, **49**, 2015-2031.

INITIAL DISTRIBUTION LIST

		No. Copies
1.	Defense Technical Information Center Cameron Station Alexandria, VA 22304-6145	2
2.	Library, Code 052 Naval Postgraduate School Monterey, CA 93943-5000	2
3.	Chairman (Code MR/Hy) Department of Meteorology Naval Postgraduate School Monterey, CA 93943-5000	1
4.	Professor R.L. Elsberry (Code MR/Es) Department of Meteorology Naval Postgraduate School Monterey, CA 93943-5000	1
5.	Professor C.-P. Chang (Code MR/Cp) Department of Meteorology Naval Postgraduate School Monterey, CA 93943-5000	1
6.	Professor R.T. Williams (Code MR/Wu) Department of Meteorology Naval Postgraduate School Monterey, CA 93943-5000	1
7.	Professor C.-H. Lee (Code EC/Le) Department of Electrical and Computer Engineering Naval Postgraduate School Monterey, CA 93943-5000	1

8.	Professor N. C. Rowe (Code CS/Rp) Department of Computer Science Naval Postgraduate School Monterey, CA 93943-5000	1
9.	Dr. Chi-Sann Liou Naval Research Laboratory Monterey, CA 93943	1
10.	Professor M.S. Peng (Code MR/Pg) Department of Meteorology Naval Postgraduate School Monterey, CA 93943-5000	2
11.	Commanding Officer Fleet Numerical Oceanography Center Naval Postgraduate School Monterey, CA 93943-5000	1
12.	Commanding Officer US NAVOCEANCOMCEN COMNAVMAR Box 12 FPO San Francisco, CA 96630-2926	1